CARDIFF UNIVERSITY

Cardiff University School of Engineering

Establishing the material parameters of the neonatal porcine ventricular myocardium

A Thesis submitted to Cardiff University for the

Degree of Doctor of Philosophy

By

Faizan Ahmad

June 2018

Changes between the original and amended version of the thesis

Changes were made in chapter 8 – Appendix from pages 272 - 371, to remove the comments and suggestions made by the reviewers of journals. Instead, the DOI links of published articles were provided to avoid the publication of private & confidential contents. These changes can be found on pages 272-273 of the amended version of the thesis.

DECLARATION

This work has not been submitted in substance for any other degree or award at this or any other university or place of learning, nor is being submitted concurrently in candidature for any degree or other award.

Signed ……(candidate) Date……..……..……

STATEMENT 1

This thesis is being submitted in partial fulfillment of the requirements for the degree of ……(insert MCh, MD, MPhil, PhD etc, as appropriate)

Signed …….. (candidate) Date ……..……

STATEMENT 2

This thesis is the result of my own independent work/investigation, except where otherwise stated, and the thesis has not been edited by a third party beyond what is permitted by Cardiff University's Policy on the Use of Third Party Editors by Research Degree Students. Other sources are acknowledged by explicit references. The views expressed are my own.

Signed ……..… (candidate) Date ……..……..…

STATEMENT 3

I hereby give consent for my thesis, if accepted, to be available online in the University's Open Access repository and for inter-library loan, and for the title and summary to be made available to outside organisations.

Signed ……(candidate) Date ……

THESIS SUMMARY

Neonatal heart disorders represent a major clinical challenge and congenital heart disease alone affects 36,000 new-borns annually within the European Union. Engineering-based computational modelling is increasingly used in adult cardiology to simulate normal and pathophysiological conditions, leading to the development of new clinical interventions. However, the application of such technologies to advance care in young patients is limited by the need to characterise the structural and biomechanical properties of *neonatal tissue* in estimating the material parameters. Consequently, this research aims to establish the first material parameters that describe neonatal cardiac tissue.

A porcine model was used to perform the microstructural and biomechanical analysis. Established (histology) and emerging—two-photon excited fluorescence and second-harmonic generation (TPEF/SHG) and diffusion tensor magnetic resonance imaging (DT-MRI)—imaging methodologies enabled quantification of the in-plane and out-plane cardiomyocytes' and collagen fibrils' orientation and dispersion, in addition to the cardiomyocytes' architecture and regional fractional anisotropy. The biomechanical analysis was performed via uniaxial tensile, biaxial and simple shear tests.

The analyses identified the regional variations within the anterior and posterior aspects of both ventricles. The surface area analysis quantified the greater ratio of collagen to cardiomyocytes in the posterior wall in both ventricles. TPEF/SHG identified the greater cardiomyocytes rotation in the posterior wall of both ventricles. The anterior ventricular walls were stiffest. The one-day-old porcine tissue was identified as exhibiting one-half the stiffness of adult porcine tissue in uniaxial testing, one-third in biaxial testing, and one-fourth

stiffness in simple shear testing. Finally, these data were used with the structurally-based Holzapfel–Ogden model of the myocardium to establish the material parameters. The estimated material parameters in this study will enable a simulation that specifically reflects neonatal ventricular tissue behaviour. This will ultimately create new opportunities for researchers, bioengineers and clinicians to identify novel treatments and interventions of neonatal heart diseases.

ACKNOWLEDGEMENTS

I would like to acknowledge and thank the following people for all their help, encouragement, support and guidance over the course of my PhD, without whom it would not have been possible to complete my thesis.

Firstly, I would like to thank Dr Peter Theobald and Dr Shwe Soe for supervising my project and providing excellent guidance, continuous support and for their invaluable contributions to the project. Without the great supervision provided by both and the sharing of their expertise and expansive knowledge, this project would not have developed or progressed as it has done.

Also, I would like to thank the research office for providing guidance and help throughout my PhD.

Finally, I must thank my family, especially my mother, brother and sister for their support and encouragement throughout my PhD.

TABLE OF CONTENTS

DECLARATION II

THESIS SUMMARY III

ACKNOWLEDGEMENTS V

TABLE OF CONTENTS VI

LIST OF FIGURES XI

LIST OF TABLES XXVI

LIST OF ABBREVIATIONS XXX

1. INTRODUCTION **1**

1.1. Research rationale 1

1.2. Neonatal vs. adult heart physiology 2

1.3. Research aims and objectives 4

1.4. Published outcomes 7

Refereed journal articles 7

Peer-reviewed conference abstracts 7

1.5. Thesis structure 8

2. LITERATURE REVIEW **11**

2.1. Cardiac anatomy 11

2.2. Cardiac tissue structure 14

2.2.1. Cardiomyocytes 14

2.2.2. The extracellular matrix (ECM) 15

2.2.3. Cardiomyocyte–collagen interaction 17

2.3. Techniques for imaging tissue microstructure 19

2.3.1. Two-dimensional microstructural analyses of adult and neonatal tissue 20

2.3.1.1 Histological and immunohistochemical analysis 20

2.3.2. Three-dimensional microstructural analyses of adult and neonatal tissue 21

2.3.2.1. TPEF/SHG and Confocal microscopy 21

2.3.2.2. DT-MRI and micro-CT imaging 23

2.4. Cardiac tissue function 25

2.4.1. Uniaxial tensile properties 27

2.4.2. Biaxial extension properties 27

2.4.3. Simple shear properties 31

2.4.4. Energy dissipation 32

2.4.5. Stress softening 33

2.5. Application of structural and function data of cardiac tissue 35

2.5.1. Computational modelling of neonatal heart diseases 37

2.5.2. Constitutive modelling of the myocardium 38

2.6. Surrogate animal models in biomedical research 42

2.7. Research motivations 44

2.8. Research aims and objectives 45

3.0. MATERIALS AND METHODS 48

3.1. Materials 49

3.1.1. Heart dissection 49

3.1.2. Microstructural analyses 52

3.1.2.1. Histological sample preparation 53

3.1.2.2. TPEF/SHG sample preparation 54

3.1.2.3. DT-MRI sample preparation 54

3.1.3. Biomechanical analyses 57

3.1.3.1. Sample preparation of biomechanical testing of neonatal porcine ventricles 57
Uniaxial tensile test 57
Biaxial tensile test 58
Simple shear test 58
3.2. Experimental methods 62

3.2.1. Microstructural analyses 62

3.2.1.1. Histological analysis 62
Staining 62
Experimental microscope setup and image acquisition settings 62
Data analysis 63
3.2.1.2. TPEF/SHG analysis 64
Experimental microscope setup and image acquisition settings 64
Data analysis 67
3.3.1.3. DT-MRI analysis 67
DT-MRI imaging protocols 67
Data analysis 68
Statistical analysis 73
3.2.2. Biomechanical testing 73

3.2.2.1. Uniaxial extension test 73
Experimental setup 73
Pilot study: defining the experimental procedures in uniaxial testing 73
Uniaxial testing 74
Data analysis 74
3.2.2.2. Biaxial extension test 79
Experimental setup 79
Pilot study: defining the experimental procedures in biaxial testing 79
Neonatal porcine myocardial tissue 80
Data analysis 82
3.2.2.3. Simple shear test 85
Data analysis 86
Statistical analysis 87
3.3. Myocardial constitutive modelling 87

3.3.1. Mathematical methods 88

3.3.1.1. Extracting parameters from uniaxial test data 88
3.3.1.2. Extracting parameters from the biaxial extension test 95
3.3.1.3. Extracting parameters from a simple shear test 100

4.0. RESULTS 102

4.1. Microstructural analyses 102

4.1.1. Histological analysis 102

4.1.2. TPEF / SHG analyses 113

4.1.3. DT–MRI analysis 135

4.1.3.1. Fractional anisotropy and fibre tractography 135

4.2. Biomechanical analyses 139

4.2.1. Uniaxial tensile behaviour 139

4.2.2. Biaxial extension behaviour 152

4.2.3. Simple shear behaviour 163

4.2.4. Neonatal heart tissue behaviour under uniaxial tensile, biaxial tensile and simple shear loading modes 175

4.4. Estimating the material parameters of neonatal ventricular myocardium 179

4.4.1. Objective function 179

4.4.2. Fitting results with the HO model of myocardium 179

5. DISCUSSION 201

5.1.Anterior and posterior LVFW 202

5.1.1. Structure analysis 202

5.1.2. Functional analysis 209

5.2.Anterior and posterior RVFW 213

5.2.1. Structural analysis 213

5.2.2. Functional analysis 217

5.3.Structural and biomechanical differences in neonatal and adult ventricular tissue..

..... ……220

5.4. Enabling more accurate neonatal cardiac simulations 222

5.4.1 Translating experimental data to numerical parameters 223

5.4.2. Estimating the uniaxial tensile, biaxial tensile and simple shear material parameters with HO model 223

5.5. Clinical implications 224

5.6. Limitations 226

6. CONCLUSIONS 228

6.1. Research conclusions 228

6.2. Future work 230

6.2.1 Development of modified HO model 230

6.2.2 Establishing a new model that encompasses growth and remodelling 230

6.2.2.1. Aims and objectives of future work 231

7. REFERENCES 233

8. APPENDIX 261

A.1. Masson's Trichrome stained histological images of the anterior and posterior aspects in the LVFW and RVFW 261

A.2. Matlab code for fitting the experimental data with the HO model of the myocardium 270

A.2. Refereed journal article - I 272

A.3. Refereed journal article - II 273

A.4. Peer-reviewed conference abstract - I 274

A.5. Peer-reviewed conference abstract – II 276

A.6. Peer-reviewed conference abstract – III 278

LIST OF FIGURES

Figure 2.1: Heart anatomy. Copied from [1]……13

Figure 2.2: Cardiac myocytes composed of myofibrils, each of which contains myofilaments. The sarcomere lies between two Z – lines. Copied from [1]……15

Figure 2.3: Schematic of the arrangement of muscle and collagen fibres and the surrounding matrix: (a) unloaded structure; (b) structure under tensile load in the muscle fibre direction, showing decreased inter-fibre separation so that the collagen network bears load primarily in the muscle fibre direction; (c) structure under compressive load in the muscle fibre direction, showing the muscle fibres buckled and lateral extension of the collagen network. Copied from [2]...……...16

Figure 3.1: One-day-old deceased Yorkshire piglet……..50

Figure 3.2: The chest is cut open through an incision in the thorax-region, to harvest the heart……51

Figure 3.3: A three-dimensional schematic model of the neonatal porcine heart. (a) Anterior view: LVFW = Grey region, RVFW = Yellow region, Left atrium = Green region, Right atrium = Maroon region. (b) Posterior view: LVFW = blue region, RVFW = pink region Left atrium = Green region, Right atrium = Maroon region. Squares representing the equatorial region of the LVFW and RVFW anteriorly and posteriorly. Left and right atria (green and maroon regions) are not relevant to this study……..55

Figure 3.4: Samples (2 x 2 mm) were dissected from the (a) anterior and (b) posterior wall of LVFW and RVFW, to perform histological and TPEF/SHG analyses. Scale bar = 12 mm……...56

Figure 3.5: Schematic representation of the samples harvested from the neonatal porcine heart. Samples were dissected aligned to the 'mean fibre direction' (MFD) and 'cross fibre direction' (CFD), determined by observing the external features of the organ. (a) Uniaxial CFD samples are dissected from the anterior aspect of the LVFW and RVFW. (b) & (c) Uniaxial MFD samples extend from the anterior to posterior aspect of the LVFW and RVFW. (d) & (e) Biaxial (square) samples extended from the anterior to posterior aspects of the LVFW and RVFW. (f) & (g) Simple shear samples were dissected from the equatorial region of both the anterior and posterior aspects of the LVFW and RVFW. Scale bar = 12 mm……...61

Figure 3.6: The anterior (a) and posterior (b) aspects of the neonatal porcine heart. The helical cardiomyocyte architecture of neonatal porcine heart before being processed; anterior view (c) and posterior view (d). The cardiomyocyte architecture of neonatal porcine heart after being processed; anterior view (e) and posterior view (f). Scale bar = 8 mm……...71

Figure 3.7: The anterior (a) and posterior (b) aspects of neonatal porcine heart. The cardiomyocyte architecture of neonatal porcine heart after being processed; anterior view (c) and posterior view (d). Anterior view identifying the regions of interest used to calculate the fractional anisotropy (FA) for the base (1), equator (2) and apex (3) of the right and left ventricles (c). Scale bar = 8 mm……...72

Figure 3.8: Representing passive 'uniaxial behaviour' of LVFW until failure (a); demonstrating passive 'uniaxial behaviour' of RVFW until failure (b). The slipping of myocardial tissue through the clamps are highlighted using the circle symbol……75

Figure 3.9: Representing passive 'uniaxial behaviour' of LVFW until failure (a); demonstrating passive 'uniaxial behaviour' of RVFW until failure (b). The slipping of myocardial tissue through the clamps are highlighted using the circle symbol……76

Figure 3.10: Representing passive 'uniaxial behaviour' of LVFW until failure (a); demonstrating passive 'uniaxial behaviour' of RVFW until failure (b). The slipping of myocardial tissue through the clamps are highlighted using the circle symbol……77

Figure 3.11: Representing passive 'uniaxial behaviour' of LVFW until failure (a); demonstrating passive 'uniaxial behaviour' of RVFW until failure (b). The slipping of myocardial tissue through the clamps are highlighted using the circle symbol……78

Figure 3.12: Biaxial testing setup, comprising four stepper motors, two load cells, and physiological saline bath. In-house Labview code (National Instrument, Version 6, Austin, TX) was used to control the stepper motors and record the applied forces and tissue strain……81

Figure 3.13: (a) Representing passive 'biaxial behaviour' in the circumferential direction of the LVFW; (b) demonstrating passive 'biaxial behaviour' in the longitudinal direction of the LVFW. The myocardial tissue was uniformly deformed and

high-quality results were obtained, using surgical sutures…….....83

Figure 3.14: (a) Representing passive 'biaxial behaviour' in the circumferential direction of the RVFW; (b) demonstrating passive 'biaxial behaviour' in the longitudinal direction of the RVFW. The myocardial tissue was uniformly deformed and high-quality results were obtained, using surgical sutures……..84

Figure 3.15: Experimental design in simple shear. Epicardium is fixed when endocardium is moving in the positive and negative shear, indicating the experiments measure the shear in MFD and CFD…….86

Figure 3.16: Uniaxial sample in MFD (the left panel) and CFD (the right panel)…….....89

Figure 3.17: Fibre rotation Θ along the depth……91

Figure 3.18: Effective area when fibre direction is Θ……93

Figure 3.19: Effective area when fibre direction is Θ…….....94

Figure 3.20: Effective fibre distribution area…….....95

Figure 3.21: Biaxial sample…….....97

Figure 3.22: Transformation of a shear amount based on image…….....98

Figure 4.1: Masson's trichrome staining images of the neonatal porcine ventricles, sectioned in the plane perpendicular to the transmural direction (i.e. in-plane), and viewed at × 20 and × 40 magnification. (a - b) LVFW anterior, demonstrating circumferentially aligned fibres. (c - d) LVFW posterior, describing longitudinally aligned fibres. Principal or preferred fibre angles are detailed in

table.4.1. Scale bar at **×20** =100 µm and at **×40** =50µm, respectively. ……104

Figure 4.2: Masson's trichrome staining images of the neonatal porcine ventricles, sectioned in the plane perpendicular to the transmural direction (i.e. in-plane), and viewed at × 20 and × 40 magnification. (a - b) LVFW anterior, demonstrating circumferentially aligned fibres. (c - d) LVFW posterior, describing longitudinally aligned fibres. Principal or preferred fibre angles are detailed in table.4.1. Scale bar at **×20** =100 µm and at **×40** =50µm, respectively. ……...105

Figure 4.3: Masson's trichrome staining images of the neonatal porcine ventricles, sectioned in the plane perpendicular to the transmural direction (i.e. in-plane), and viewed at × 20 and × 40 magnification. (a - b) LVFW anterior, demonstrating circumferentially aligned fibres. (c - d) LVFW posterior, describing longitudinally aligned fibres. Principal or preferred fibre angles are detailed in table.4.1. Scale bar at **×20** =100 µm and at **×40** =50µm, respectively. ……...106

Figure 4.4: Masson's trichrome staining images of the neonatal porcine ventricles, sectioned in the plane perpendicular to the transmural direction (i.e. in-plane), and viewed at × 20 and × 40 magnification. (a - b) LVFW anterior, demonstrating circumferentially aligned fibres. (c - d) LVFW posterior, describing longitudinally aligned fibres. Principal or preferred fibre angles are detailed in table.4.1. Scale bar at **×20** =100 µm and at **×40** =50µm, respectively. ……107

Figure 4.5: Masson's trichrome staining images of the neonatal porcine ventricles, sectioned in the plane perpendicular to the transmural direction (i.e. in-plane), and viewed at × 20 and × 40 magnification. (a - b) RVFW anterior, demonstrating circumferentially aligned fibres. (c - d) RVFW posterior, describing longitudinally aligned fibres. Principal or preferred fibre angles are detailed in table.4.1. Scale bar at **×20** =100 µm and at **×40** =50µm, respectively. ……108

Figure 4.6: Masson's trichrome staining images of the neonatal porcine ventricles, sectioned in the plane perpendicular to the transmural direction (i.e. in-plane), and viewed at × 20 and × 40 magnification. (a - b) RVFW anterior, demonstrating circumferentially aligned fibres. (c - d) RVFW posterior, describing longitudinally aligned fibres. Principal or preferred fibre angles are detailed in table.4.1. Scale bar at **×20** =100 µm and at **×40** =50µm, respectively. ……...109

Figure 4.7: Masson's trichrome staining images of the neonatal porcine ventricles, sectioned in the plane perpendicular to the transmural direction (i.e. in-plane), and viewed at × 20 and × 40 magnification. (a - b) RVFW anterior, demonstrating circumferentially aligned fibres. (c - d) RVFW posterior, describing longitudinally aligned fibres. Principal or preferred fibre angles are detailed in table.4.1. Scale bar at **×20** =100 µm and at **×40** =50µm, respectively. ……...110

Figure 4.8: Masson's trichrome staining images of the neonatal porcine ventricles, sectioned in the plane perpendicular to the transmural direction (i.e. in-plane), and viewed at × 20 and × 40 magnification. (a - b) RVFW anterior, demonstrating

circumferentially aligned fibres. (c - d) RVFW posterior, describing longitudinally aligned fibres. Principal or preferred fibre angles are detailed in table.4.1. Scale bar at **×20** =100 µm and at **×40** =50µm, respectively. ……111

Figure 4.9: In-plane TPEF/SHG images of the anterior LVFW. (a) The anterior view of one-day-old neonatal porcine heart; (b) SHG-channel was displayed in green, to identify the collagen fibril distribution; (c) TPEF-channel was shown in red, to specify the cardiomyocyte distribution; (d) Both channels were merged to demonstrate the collagen-cardiomyocyte overlapping. Scale bar measures 100 µm……...115

Figure 4.10: In-plane TPEF/SHG images of the anterior RVFW. (a) The anterior view of one-day-old neonatal porcine heart; (b) SHG-channel was displayed in green, to identify the collagen fibril distribution; (c) TPEF-channel was shown in red, to specify the cardiomyocyte distribution; (d) Both channels were merged to demonstrate the collagen-cardiomyocyte overlapping. Scale bar measures 100 µm……...116

Figure 4.11: In-plane TPEF/SHG images of the posterior LVFW. (a) The anterior view of one-day-old neonatal porcine heart; (b) SHG-channel was displayed in green, to identify the collagen fibril distribution; (c) TPEF-channel was shown in red, to specify the cardiomyocyte distribution; (d) Both channels were merged to demonstrate the collagen-cardiomyocyte overlapping. Scale bar measures 100 µm……...117

Figure 4.12: In-plane TPEF/SHG images of the posterior RVFW. (a) The anterior view of one-day-old neonatal porcine heart; (b) SHG-channel was displayed in green,

to identify the collagen fibril distribution; (c) TPEF-channel was shown in red, to specify the cardiomyocyte distribution; (d) Both channels were merged to demonstrate the collagen-cardiomyocyte overlapping. Scale bar measures 100 µm……...118

Figure 4.13: TPEF/SHG microscopy was used to quantify the mean in-plane and out–plane cardiomyocyte and collagen fibril microstructural parameters of the anterior LVFW. (a) in-plane preferred orientation; (b) out-plane preferred orientation. (c) in-plane dispersion; (d) out-plane dispersion. (e) in-plane amount; (f) out-plane amount. In-plane and out-plane image-stacks were acquired through the depth of 200-and 1022 µm respectively…….121

Figure 4.14: TPEF/SHG microscopy was used to quantify the mean in-plane and out–plane cardiomyocyte and collagen fibril microstructural parameters of the anterior RVFW. (a) in-plane preferred orientation; (b) out-plane preferred orientation. (c) in-plane dispersion; (d) out-plane dispersion. (e) in-plane amount; (f) out-plane amount. In-plane and out-plane image-stacks were acquired through the depth of 200-and 1022 µm respectively……..124

Figure 4.15: TPEF/SHG microscopy was used to quantify the mean in-plane and out–plane cardiomyocyte and collagen fibril microstructural parameters of the posterior LVFW. (a) in-plane preferred orientation; (b) out-plane preferred orientation. (c) in-plane dispersion; (d) out-plane dispersion. (e) in-plane amount; (f) out-plane amount. In-plane and out-plane image-stacks were acquired through the depth of 200-and 1022 µm respectively……..127

Figure 4.16: TPEF/SHG microscopy was used to quantify the mean in-plane and out–plane cardiomyocyte and collagen fibril microstructural parameters of the posterior RVFW. (a) in-plane preferred orientation; (b) out-plane preferred orientation. (c) in-plane dispersion; (d) out-plane dispersion. (e) in-plane amount; (f) out-plane amount. In-plane and out-plane image-stacks were acquired through the depth of 200-and 1022 µm respectively……..130

Figure 4.17: The helical cardiomyocyte architecture of one-day-old neonatal porcine heart. (a) Anterior view identifying the regions of interest within the base (1), equator (2) and apex (3) in the right and left ventricles. (b) Posterior view. The anterior (c) and posterior (d) aspects of LVFW and RVFW. Scale bar = 12 mm……..136

Figure 4.18: The anterior and posterior aspects of the one-day-old neonatal porcine heart. Fibre bundles were coloured to demonstrate the mean-fibre orientation, using 50% fibre density; anterior view (a) and posterior view (b). 25% fibre density; anterior view (c) and posterior view (d). 15% fibre density; anterior view (e) and posterior view (f) respectively……..137

Figure 4.19: Representing the uniaxial tensile behaviour of the LVFW in the MFD and CFD. The sample I (a), sample II (b), sample III (c), sample IV (d) and sample V (e)…….143

Figure 4.20: Representing the uniaxial tensile behaviour of the RVFW in the MFD and CFD. The sample I (a), sample II (b), sample III (c), sample IV (d) and sample V (e)……146

Figure 4.21: Uniaxial cyclic behaviour of LVFW (a) and RVFW (b) in CFD. (c) Average ‘uniaxial behaviour’ of LVFW & RVFW until failure (n = 5). (d) Representing

passive 'uniaxial behaviour' of LVFW until failure. Mean curves of the LVFW (e) and RVFW (f) (n = 5). (g) Column plots indicate mean failure stress in the anterior and posterior aspect of LVFW & RVFW, for MFD and CFD. Standard deviation indicated by error bars……150

Figure 4.22: Representing the biaxial tensile behaviour of the LVFW in the MFD and CFD. The sample I (a), sample II (b), sample III (c), sample IV (d) and sample V (e)……...155

Figure 4.23: Representing the biaxial tensile behaviour of the RVFW in the MFD and CFD. The sample I (a), sample II (b), sample III (c), sample IV (d) and sample V (e)……158

Figure 4.24: 'Average biaxial behaviour' of LVFW (a) and RVFW (b) (n = 5). Mean 'biaxial' curves of the LVFW (c) and RVFW (d) (n = 5). (e) Columns plot specifying the average peak Engineering stress of the LVFW and RVFW in the MFD and CFD (n = 5). Error bars describe the standard deviation……161

Figure 4.25: Demonstrating passive 'simple shear' behaviour of the anterior and posterior aspects of the LVFW & RVFW in the MFD and CFD, at increments of 0.3 (blue curve), 0.4 (orange curve) and 0.5 (black curve). (a) LVFW – anterior. (b) LVFW – posterior. (c) RVFW – anterior. (d) RVFW – posterior……..166

Figure 4.26: 'Mean simple shear behaviour' of anterior and posterior aspect of the LVFW (a) and the RVFW (b), in the MFD and CFD at increments of 0.1, 0.2, 0.3, 0.4 & 0.5 (n = 5). LVFW anterior (c) and posterior (d) in MFD and CFD, at an increment of 0.5. RVFW anterior (e) and posterior (f) in MFD and CFD at an

increment of 0.5. (g) – (i) Column plots indicate average peak shear stress in the anterior and posterior aspects of both ventricles at increments of 0.3, 0.4 and 0.5 respectively (n = 5). (j) Column plots demonstrating mean hysteresis areas in the anterior and posterior aspect of LVFW & RVFW, for MFD and CFD at an increment of 0.5 (n = 5). Error bars represent standard deviation……171

Figure 4.27: (a) Mean curves of the LVFW (n = 5), demonstrating the mechanical behaviour under uniaxial tensile, biaxial tensile and simple shear loading modes in MFD. (b) Mean curves of the LVFW (n = 5), identifying the mechanical behaviour under uniaxial tensile, biaxial extension and simple shear loading modes in CFD……176

Figure 4.28: (a) Mean curves of the RVFW (n = 5), demonstrating the mechanical behaviour under uniaxial tensile, biaxial tensile and simple shear loading modes in MFD. (b) Mean curves of the RVFW (n = 5), identifying the mechanical behaviour under uniaxial tensile, biaxial extension and simple shear loading modes in CFD……177

Figure 4.29: Fit based on HO model under different assumptions between experimental data noted by Experimental-and calculating data, and noted by calculations in three types of LVFW experiments respectively. (a),(b) and (c) show the fitting when assuming there is no fibre rotation in the experimental samples; (d),(e) and (f) are the results after considering fibre rotation but no effective area; (g),(h) and (i) adopt fibre rotation and effective area. (j) is a comparison among different conditions. NRNE considers no fibre rotation and no effective area; RNE considers only fibre rotation and RE considers both fibre rotation and effective

area. UM presents Uni-axial tension in MFD; UC presents Uni-axial tension in CFD; BM presents Bi-axial tension in MFD; BC presents Bi-axial tension in CFD; SM presents shear amount in MFD and SC presents shear amount in CFD……..186

Figure 4.30: Fit based on general HO models under different fitting couples of LVFW. (a),(b) and (c) show the results by only fitting uni-axial and then apply the parameters to bi-axial and simple shear; (d),(e) and (f) are only fitting bi-axial data; (g),(h) and (i) fitting simple shear only. (j) is the area error comparison among different conditions. UM presents Uni-axial tension in MFD; UC presents Uni-axial tension in CFD; BM presents Bi-axial tension in MFD; BC presents Bi-axial tension in CFD; SM presents shear amount in MFD and SC presents shear amount in CFD……192

Figure 4.31: Fit based on general HO model under different fitting couples of LVFW. (a),(b) and (c) show applying the parameters gotten by only fitting uni-axial and biaxial data to simple shear; (d),(e) and (f) are fitting uni-axial and simple shear and then applying the parameters to bi-axial data; (g),(h) and (i) fit the biaxial and simple shear data only. (j) is area error comparison among different couples. UM presents Uni-axial tension in MFD; UC presents Uni-axial tension in CFD; BM presents Bi-axial tension in MFD; BC presents Bi-axial tension in CFD; SM presents shear amount in MFD and SC presents shear amount in CFD……....198

LIST OF TABLES

Table 4.1: The average in-plane principal fibre orientation parameter and coefficient of determination R^2 'goodness of fit' for RVFW and LVFW in the anterior (n = 16) and posterior (n = 16) aspects. Histological specimens were examined in the direction perpendicular to the transmural plane, i.e. epicardium towards endocardium using Fourier-component image analysis method (n = 32)……112

Table 4.2: The average surface area ratio of collagen to myocyte for RVFW and LVFW in the anterior (n = 16) and posterior (n = 16) aspects. Histological specimens were examined in transmural – plane, i.e. epicardium towards endocardium (n = 32) using custom MATLAB code……..112

Table 4.3: In-plane cardiomyocyte rotation, dispersion and amount through the LVFW and RVFW, across 200 µm depth of the anterior (A) and posterior (P) aspects…….131

Table 4.4: Out-plane cardiomyocyte rotation, dispersion and amount through the LVFW and RVFW, across 1022 µm depth in the anterior (A) and posterior (P) aspects……..……...131

Table 4.5: In-plane collagen fibril rotation, dispersion and amount through the LVFW and RVFW, across 200 µm depth in the anterior (A) and posterior (P) aspects…….132

Table 4.6: Out-plane collagen fibril rotation, dispersion and amount through the LVFW and RVFW, across 1022 µm depth in the anterior (A) and posterior (P) aspects…….132

Table 4.7: Statistical data describing the significance of difference in cardiomyocyte rotation (1 – 4) and dispersion (5 – 8) between the anterior (A) and posterior (P) aspects of the LVFW and RVFW for: (1) LVFW (A & P) in-plane; (2) RVFW (A & P) in-plane; (3) LVFW (A & P) out-plane; (4) RVFW (A & P) out-plane. (5) LVFW (A & P) in-plane; (6) RVFW (A & P) in-plane; (7) LVFW (A & P) out-plane; and (8) RVFW (A & P) out-plane……133

Table 4.8: Statistical data describing the significance of difference in collagen fibril rotation (1 – 4) and dispersion (5 – 8) between the anterior (A) and posterior (P) aspects of the LVFW and RVFW for: (1) LVFW (A & P) in-plane; (2) RVFW (A & P) in-plane; (3) LVFW (A & P) out-plane; (4) RVFW (A & P) out-plane. (5) LVFW (A & P) in-plane; (6) RVFW (A & P) in-plane; (7) LVFW (A & P) out-plane; and (8) RVFW (A & P) out-plane……134

Table 4.9: The total number of fibre tracks and regional fractional anisotropy (FA) in the anterior LVFW……138

Table 4.10: The total number of fibre tracks and regional fractional anisotropy (FA) in the anterior RVFW……..138

Table 4.11: Average hysteresis area (J/m^3) of neonatal porcine LVFW and RVFW for uniaxial testing at 10% strain in MFD and CFD……...151

Table 4.12: Average failure stress values (KPa) for neonatal LVFW and RVFW for uniaxial testing; the specimens were stretched until failure……151

Table 4.13: Average hysteresis area (J/m^3) of neonatal porcine LVFW and RVFW for biaxial testing at (30:30) N / m in MFD and CFD……..162

Table 4.14: Average peak engineering stress values (KPa) for neonatal porcine LVFW and RVFW for biaxial testing at (30:30) N / m in MFD and CFD……162

Table 4.15: Average hysteresis area (J/m^3) of neonatal porcine LVFW and RVFW in the anterior and posterior aspects for simple shear testing at 0.5 increments in MFD and CFD……172

Table 4.16: Average peak shear stress values (KPa) for the neonatal LVFW in the anterior (A) and posterior (P) aspects for simple shear testing at 0.3, 0.4, 0.5 increments in MFD and CFD modes……173

Table 4.17: Average peak shear stress values (KPa) for the neonatal RVFW in the anterior (A) and posterior (P) aspects for simple shear testing at 0.3, 0.4, 0.5 increments in MFD and CFD modes……173

Table 4.18: Statistical analysis (One way ANOVA along with Tukey HSD post hoc test) data for LVFW and RVFW in the anterior (A) and posterior (P) aspects represent: (1) LVFW (anterior & posterior) for MFD – CFD; (2) RVFW (anterior & posterior) for MFD – CFD; (3) LVFW (A) and RVFW (A) for MFD – CFD; and (4) LVFW (P) and RVFW (P) for MFD – CFD respectively. A p-value less than 0.05 considered statistically significant……174

Table 4.19: Material parameters in figure 4.37. RE considers both fibre rotation and effective area; RNE considers only fibre rotation and NRNE considers no fibre rotation and no effective area…….....199

Table 4.20: Material parameters in figure 4.38, for uniaxial tensile, biaxial tensile and simple shear data……...199

Table 4.21: Material parameters in figure 4.39, under different fitting couples……...199

Table 4.22: Area error values in figure 4.37. RE considers both fibre rotation and effective area; RNE considers only fibre rotation and NRNE considers no fibre rotation and no effective area. UM presents Uni-axial tension in MFD; UC presents Uni-axial tension in CFD; BM presents Bi-axial tension in MFD; BC presents Bi-axial tension in CFD; SM presents shear amount in MFD and SC presents shear amount in CFD……...200

Table 4.23: Area error values in figure 4.38, for uniaxial tensile, biaxial tensile and simple shear data. UM presents Uni-axial tension in MFD; UC presents Uni-axial tension in CFD; BM presents Bi-axial tension in MFD; BC presents Bi-axial tension in CFD; SM presents shear amount in MFD and SC presents shear amount in CFD…….200

Table 4.24: Area error values in figure 4.39, under different fitting couples. UM presents Uni-axial tension in MFD; UC presents Uni-axial tension in CFD; BM presents Bi-axial tension in MFD; BC presents Bi-axial tension in CFD; SM presents shear amount in MFD and SC presents shear amount in CFD……...200

LIST OF ABBREVIATIONS

BM	Biaxial tension in mean-fibre direction
BC	Biaxial tension in cross-fibre direction
CHD	Congenital heart disease
CFD	Cross-fibre direction
CT	computed tomography
DT – MRI	Diffusion-weighted magnetic resonance imaging
ECM	Extracellular matrix
FA	Fractional anisotropy
G & R	Growth and Remodelling
HO model	Holzapfel Ogden constitutive model of myocardium
LVFW	Left ventricle free-wall
MFD	Mean-fibre direction
NRNE	No fibre rotation and no effective area
RE	Both fibre rotation and effective area
RNE	Only fibre rotation
RVFW	Right ventricle free-wall
SC	Simple shear in cross-fibre direction
SHG	Second-harmonic generation
SM	Simple shear in mean-fibre direction
TPEF	Two-photon excitation fluorescence
UC	Uniaxial tension in cross-fibre direction
UM	Uniaxial tension in mean-fibre direction

1. INTRODUCTION

1.1. Research rationale

Heart-related diseases are the leading cause of mortality in the world [3]. It is estimated that Europe alone spends about €196 billion per year on heart-related medical treatments [4]. Cardiovascular disease (CVD) is the leading cause of mortality, accounting for more than 161,000 deaths in the UK each year. The British Heart Foundation estimate that CVD causes a £19bn annual economic impact when considering the cost of premature death, lost productivity, hospital treatment and prescriptions [5]. CVD typically affects older patients, who attract the majority of research efforts and innovations. However, congenital heart defects (CHDs) are strikingly different and they necessitate clinical intervention from birth, through childhood and adolescence, and into adulthood. CHD describes a series of structural cardiac disorders, including ventricular and atrial septal defects, which annually affect 36,000 new-borns within the European Union [6, 7]. In addition, in the European Union, 3000 children who are annually diagnosed with CHD die as a termination of pregnancy for fetal abnormality (TOFPA), early neonatal death, or late fetal death [7]. CHDs affect 9-in-1000 births and they are one of the UK's most common congenital disabilities. CHD patients account for over 100,000 UK hospital bed-days per annum [5].

Understanding the behaviour of biological tissues is a critical step in performing biomechanical, computer-based investigations into complex clinical problems. Engineering-based computational modelling is increasingly used in adult cardiology to understand the behaviour of structural components. They enable the simulation of normal and

pathophysiological conditions, and they can lead to new interventions [8-15]. However, the application of these technologies to advance care in younger cardiology patients is limited by the need to better understand the structure and underlying biomechanical behaviour of *neonatal* cardiac tissue. Unfortunately, to date, there are no experimental data available that quantitatively describe the neonatal cardiac tissue structure and biomechanical behaviour. This data is also valuable to estimate the material parameters and the development of age-specific material models. Holzapfel and Ogden [13] have identified that the shortage of experimental data to estimate material parameters is a key limitation for developing constitutive models. Neonatal computational simulations that adopt, or scale, adult data, are at risk of incorporating an unknown level of error [16-19]. Consequently, this shortage of relevant data currently limits the value of computational modelling, and prevents a better understanding of the underlying neonatal ventricular mechanics and, potentially, the identification of novel interventions.

1.2. Neonatal vs. adult heart physiology

The neonatal mammalian heart functions differently to the adult heart, working at relatively higher rates and nearer maximal capacity to achieve the greater oxygen demands of the young [21, 22]. The ventricular wall functionality also differs between the neonatal and adult heart because the former can only increase the cardiac output by increasing the heart rate (although only limited), while the adult heart can also increase stroke volume [21, 22]. The neonatal heart also undergoes dramatic adaptive remodelling immediately after birth, which continues to eventually generate the structure and functionality typical of adult tissue [21-23]. Structural changes begin immediately postnatal, with the rapid closing of the ductus

arteriosus and foramen ovale, and reliance on pulmonary circulation [24, 25]. These morphological and physiological changes contribute to an immediate increase in left ventricle workload, which stimulates left ventricle cardiomyocyte hypertrophy, hyperplasia and extracellular collagen deposition [23, 26]. In studies of neonatal porcine, the left ventricular free-wall increases in mass 4.5-fold within two weeks, cell volume increases 3.5-fold, and cellular proliferation increases 0.28-fold [23]. During this same period, previous studies have shown a rapid increase in the deposition of interstitial collagen, peaking 15–20 days postnatal [26]. The neonate heart also has a greater fraction of fibrous tissue to contractile tissue than an adult [21, 22], while there is variation in the collagen fibril density, and mono-nucleated and bi-nucleated cell concentrations [27-29]. Increasing age is also associated with changes in the cardiac matrix, and with an increase in collagen fibril crosslinking and assembly [19].

Currently, despite knowledge of these rapid changes, there are no experimental data of neonatal mammalian tissue describing the precise structure and behaviour of *neonatal* heart tissue. The unavailability of experimental data can limit the effectiveness of computational simulations in defining the clinical solutions that are targeted at repairing neonatal cardiac diseases [16-19].

1.3. Research aims and objectives

This research aimed to establish the material parameters that for the first time specifically describe neonatal ventricular myocardium. These material parameters will enable a simulation that more accurately reflects neonatal ventricular myocardium behaviour. This will ultimately create new opportunities for researchers, bioengineers and clinicians to identify novel treatments and interventions in cases of abnormal neonatal heart functionality. To achieve the aim of this research study, a complete set of microstructural and biomechanical data is needed for the estimation of the material parameters. Consequently, this research study systematically characterises the microstructure and biomechanical parameters of neonatal left and right ventricle 'free-walls' (LVFW and RVFW, respectively). Recognising the different physiological roles of the ventricles and, by comparison to the adult heart, the front and back walls, this study will investigate these four different regions (LVFW anterior and posterior; RVFW anterior and posterior). An experimental protocol was followed to systematically analyse the microstructure and biomechanical behaviour, using an accepted porcine animal model [30-37]. Two-dimensional Masson's trichrome staining histology was consolidated with three-dimensional TPEF/SHG microscopy to quantify the cardiomyocytes and collagen fibrils structure and organisation. Three-dimensional diffusion tensor magnetic resonance imaging (DT-MRI) was used to assess the cardiomyocyte architecture of the intact heart, describing the directional coherence of cardiomyocytes orientation. Biomechanical analyses were then performed via uniaxial tensile, biaxial tensile and simple shear loading modes. Finally, these data were used with the structurally-based Holzapfel–Ogden (HO) model of the adult myocardium [38], to establish the material parameters that more accurately describe neonatal ventricular tissue behaviour. The following goals were identified to achieve these aims:

1. To understand the fundamental structural differences between neonatal and adult cardiac tissue by performing histological analysis on the anterior and posterior aspects of RVFW and LVFW. This enabled identification of the two-dimensional cardiomyocytes and collagen fibrils distribution. The cardiomyocytes preferred orientation and surface area ratio of collagen to myocyte fibres were also quantified.

2. To identify the in-plane and out-plane cardiomyocytes and collagen fibrils preferred orientation (°) and angular dispersion (°) through the ventricular walls (RVFW, LVFW). The anterior and posterior aspects of both ventricles were microscopically investigated using the TPEF/SHG imaging techniques.

3. To describe the macroscopic directional coherence of cardiomyocytes orientation in the intact neonatal porcine heart, three-dimensional diffusion tensor magnetic resonance imaging (DT-MRI) was performed. This indicated the macroscopic directional coherence of the cardiomyocytes' orientations. The *regional* fractional anisotropy (FA) was also evaluated in the anterior aspect of LVFW and RVFW.

4. To describe the uniaxial preconditioning behaviour, biomechanical behaviour (stress vs. strain), hysteresis area (energy dissipation) and mean failure stresses of one-day-old porcine ventricles, a uniaxial tensile mechanical testing was performed in the mean-fibre direction (MFD) and cross-fibre direction (CFD) of both ventricles.

5. To describe the biaxial biomechanical behaviour (stress vs. stretch), hysteresis area (energy dissipation) and mean peak stresses of one-day-old porcine ventricles; biaxial tensile mechanical testing was performed in the MFD and CFD of both ventricles.

6. To describe the simple shear preconditioning behaviour, biomechanical behaviour (stress vs. strain), hysteresis area (energy dissipation) and mean peak shear stresses of one-day-old porcine ventricles, simple shear tests were performed on the anterior and posterior aspects of both ventricles in the MFD and CFD.

7. Finally, the microstructural and biomechanical data were used with the structurally-based HO model of the adult myocardium [38] to establish material parameters that more accurately describe neonatal ventricular tissue behaviour via computational simulations.

1.4. Published outcomes

Refereed journal articles

Faizan Ahmad, R. Prabhu, Jun Liao, Shwe Soe, Michael D Jones, Jonathan Miller, Parker Berthelson, Daniel Enge, Katherine M. Copeland, Samar Shaabeth, Richard Johnston, Ian Maconochie, Peter S.Theobald. **'**Biomechanical properties and microstructure of neonatal porcine ventricles', *Journal of the Mechanical Behavior of Biomedical Materials.* .

Faizan Ahmad, S Soe, N White, R Johnston, I Khan, J Liao, M Jones, R Prabhu, I Maconochie, P Theobald. 'Characterising the region-specific microstructure of neonatal porcine ventricles', *Annals of Biomedical Engineering*.

Sian Morgan, Yadan Zhang, **Faizan Ahmad**, Andreas Gazze. Muhammad Javed, Zita Jessop, Peter Theobald, Lewis Francis, Ian Whitaker, Ilyas M Khan. 'Differences in the biochemical and biomechanical properties of immature and mature mammalian auricular cartilages', *Cellular and Molecular Bioengineering*, under consideration.

Debao Guan, **Faizan Ahmad**, Peter Theobald, Shwe Soe, Hao Gao, Xiaoyu Luo 2018. 'Fitting Various Experimental Data from Neonatal Porcine Myocardium Based on the HO Model', *Computer Methods in Biomechanics and Biomedical Engineering*, under consideration.

Peer-reviewed conference abstracts

Faizan Ahmad, S Soe, P Skacel, R Johnston, I Maconochie, P Theobald 2016. 'Biaxial and shear properties of immature porcine heart tissue', 2nd Workshop on Soft Tissue Modelling, Glasgow.

Faizan Ahmad, S Soe, P Skacel, R Johnston, I Maconochie, P Theobald 2016. 'The use of additive manufacturing to enhance infant CPR', 1st Welsh International Symposium on Emergency Medicine, Cardiff.

Debao Guan, **Faizan Ahmad**, Peter Theobald, Shwe Soe, Hao Gao, Xiaoyu Luo 2018. 'Fitting Various Experimental Data from Neonatal Porcine Myocardium Based on the HO

Model', Frontiers of simulations and experimentation for personalised cardiovascular management and treatment, London.

Amanda Davies, **Faizan Ahmad,** Peter Theobald, Richard Hugtenburg, Richard Johnston 2018. 'A Novel MRI Method for Vertebral Strength', British Renal Society, Winchester.

1.5. Thesis structure

This thesis is structured to first appreciate the existing science surrounding neonatal heart tissue before describing the experimental approach adopted to investigate its structural and biomechanical characteristics for the estimation of material parameters. Chapter 2 describes the cardiac tissue structure and function. The two-and three-dimensional techniques for imaging tissue microstructure are described in this chapter, including a description of the applications of such techniques in the context of the current literature of the adult and neonatal cardiac tissue. This chapter further describes the cardiac tissue function, including the procedures that are used to systematically characterising the biomechanical properties of the heart tissue. Emphasis will be placed on the literature that describes the biomechanical properties of the adult mammalian heart. The application of structural and functional data of cardiac tissue in developing constitutive models, estimating material parameters and performing engineering-based computational simulations in defining new interventions to target neonatal cardiac diseases are also detailed in this chapter. The connection between the gaps in the literature and this research aim are also highlighted.

Chapter 3 describes the experimental protocol that is used to systematically analyse the microstructure and biomechanical behaviour by using an accepted porcine animal model. Two-dimensional Masson's trichrome staining histology is consolidated with three-dimensional

two-photon excited fluorescence and second-harmonic generation TPEF/SHG microscopy to quantify the cardiomyocytes and collagen fibrils structure and organisation. Three-dimensional diffusion tensor magnetic resonance imaging (DT-MRI) is used to assess the cardiomyocyte architecture of the intact heart, describing the directional coherence of the cardiomyocytes' orientation. Biomechanical analyses are then performed using uniaxial tensile, biaxial tensile and simple shear loading modes. Finally, these data are used with the structurally-based HO model of the adult myocardium to establish the material parameters that more accurately describe neonatal ventricular tissue behaviour. These material parameters will enable increased accuracy when performing computational simulations of neonatal ventricular tissue.

Chapter 4 describes two-and three-dimensional microstructural data for the neonatal porcine cardiac tissue within the anterior and posterior aspects of the left and right ventricle free-wall. The biomechanical properties of the neonatal porcine cardiac tissue are demonstrated in uniaxial tensile, biaxial tensile and simple shear loading modes. The obtained microstructural and biomechanical data are then used with the structurally-based HO constitutive model of the myocardium to estimate the material parameters of the neonatal porcine left ventricular myocardium.

Chapter 5 discusses the key findings of this research and it compares the regional variations of structural and biomechanical properties in the anterior and posterior aspects of the LVFW and RVFW. The one-day neonatal porcine microstructural and biomechanical data was also compared with an adult, indicating the structural and biomechanical changes that occur during maturation. This chapter also describes the potential impact of this research in establishing the material parameters that, for the first time, specifically describe neonatal ventricular

myocardium and will enable simulation that more accurately reflect ventricular tissue behaviour. The clinical implications and limitations of this research study will also be discussed.

Finally, Chapter 6 summarises the principal findings of this research and it gives some directions for future research in the field of cardiac mechanics.

2. LITERATURE REVIEW

2.1. Cardiac anatomy

The cardiovascular system consists of the heart, blood vessels, and blood. Continuous blood circulation is essential to sustain life and, therefore, blood is continually driven through the cardiovascular system by the heart (Figure 2.1). The heart is the most important muscular organ in the body and normal heart function is vital for a healthy life. The heart is divided into right and left sides, and each side consists of an atrium and a ventricle. Blood circulation involves pulmonary circulation and systemic circulations [37]. The pulmonary capillary network surrounds the lung alveoli, allowing the exchange of CO_2 and O_2. Pulmonary circulation transports oxygen-poor blood from the right ventricle to the lungs, where it is oxygenated in the capillaries and then returned, enriched with oxygen, to the left atrium. Systemic circulation transports oxygen- and nutrient-rich blood from the left ventricle to various systems in the body and it returns deoxygenated blood to the right atrium of the heart. The coronary arteries, which are situated on the heart's surface, are responsible for the heart's blood circulation [28, 32].

Four valves (the tricuspid, pulmonary, mitral and aortic valves) regulate blood flow. The tricuspid valve is located between the right atrium and the right ventricle. The pulmonary valve is located between the right ventricle and the pulmonary artery. The mitral valve is located between the left atrium and the left ventricle. The aortic valve is located between the left ventricle and the aorta. All of these valves, except for the mitral valve, have three flaps

that open in only one direction due to pressure generated during heart contraction and relaxation phases. The mitral has only two flaps [14].

The heart pumping cycle is associated with changes in arterial and ventricular pressure. The cycle is split into four phases: filling, isovolumetric contraction, expulsion, and isovolumetric relaxation. The isovolumetric contraction and filling phases are known as systole, and the isovolumetric relaxation and expulsion phases are known as diastole. Controlled by periodic electrical impulses, the pacemaker function for the mechanical contraction of the heart begins with excitation of the sinoatrial node [14]. The propagation of an electrical potential in the heart generates an active contraction, which is determined by the underlying mechanical structure. In particular, the cardiomyocytes' contraction influences the membrane potential and the duration of the action potential, this phenomenon is known as mechano-electric feedback [39]. Cardiac mechanics and electrophysiology are, thus, interlinked in performing the overall cardiac function. The passive stiffness of the myocardium significantly contributes to performing the diastolic and systolic functions of the heart [40, 41]. Moreover, the relative sliding/shearing of adjacent myocardial layers in the left ventricle wall significantly contribute to wall thickening during systole and wall thinning during diastole [42, 43]. Consequently, an enhanced knowledge of the *myocardium* structure and underlying mechanical behaviour is of utmost importance in understanding the heart function.

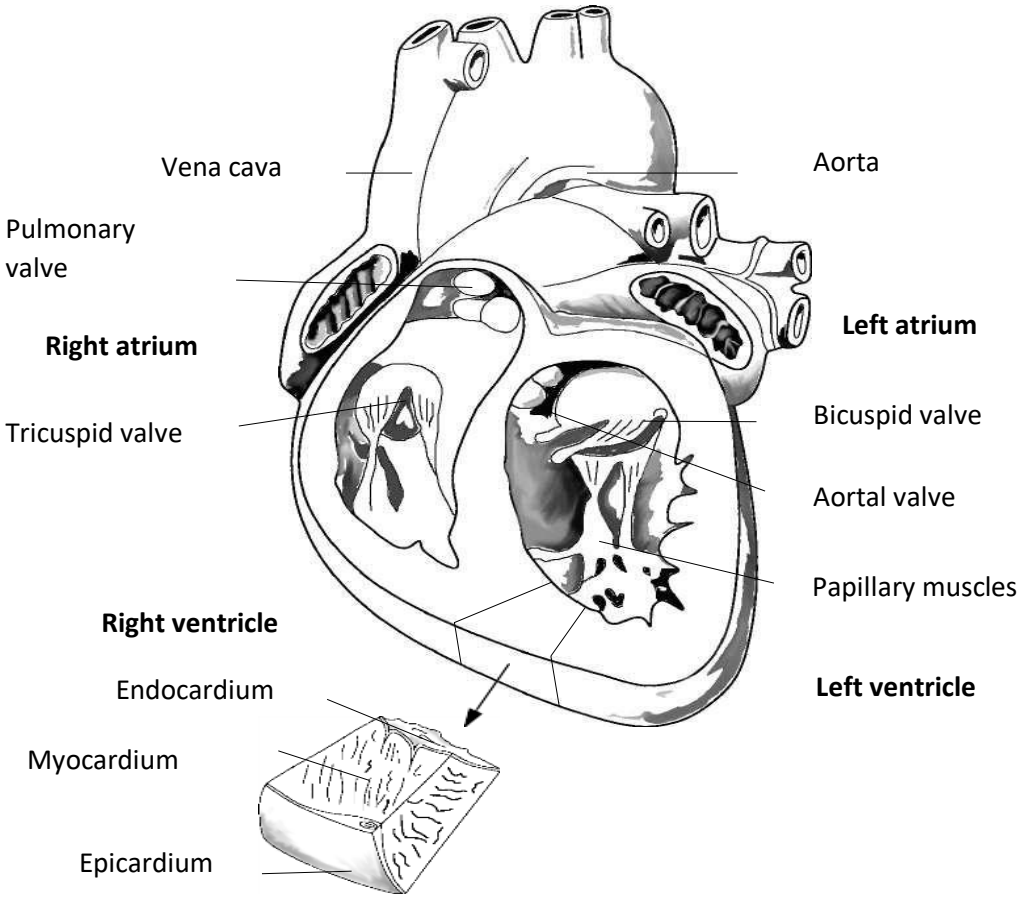

Figure 2.1: *Heart anatomy. Source: [1].*

2.2. Cardiac tissue structure

The myocardium of the heart is arranged within a hierarchically organised extracellular matrix (ECM), which consists of: epimysium, a fibro-elastic sheath surrounding the muscle; perimysium, a sheath of connective tissue that encloses bundles of cardiomyocytes; and the endomysium, a loose connective tissue with areolar configuration around individual cardiomyocytes.

2.2.1. Cardiomyocytes

Cardiomyocytes are the muscle cells that are responsible for generating contractile force in the intact heart. Each myocardial cell contains bundles of myofibrils. The myofibrils have distinct repeating micro-anatomical units, which are termed sarcomeres and which represent the basic contractile units of the myocyte. The sarcomere is defined as the region of myofilament structures between two Z-lines (Figure 2.2). The sarcomere is composed of thick and thin filaments—myosin and actin, respectively (Figure 2.2). Chemical and physical interactions between the actin and myosin cause the sarcomere length to shorten and, therefore, the myocyte to contract during the process of excitation-contraction coupling. The interactions between actin and myosin serve as the basis for the sliding filament theory of muscle contraction [44]. The cardiomyocytes are not perfectly aligned in the myocardial tissue [45]. Their orientation is typically described by the ‘fibre direction’, while their disorganisation is referred to as the ‘angular dispersion’. Cardiomyocyte orientation and angular dispersion changes in the orthogonal direction of cardiac tissue, which influences its biomechanical behaviour. Their orientation and angular dispersion are essential to maintain the myocardial stiffness and anisotropy during the cardiac cycle. The influence of

cardiomyocyte orientation and dispersion has previously been highlighted in adult studies, which have identified the significant effects of these parameters on the passive and active behaviour of myocardial tissue [10, 46].

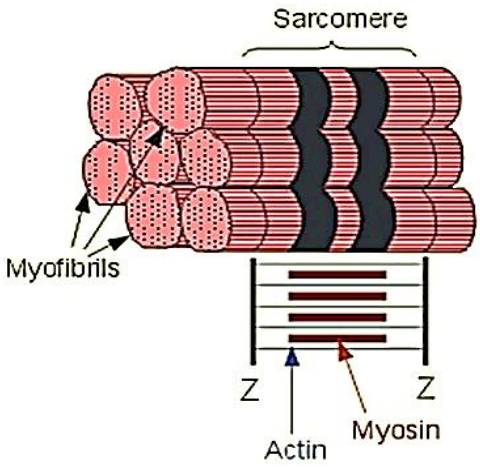

Figure 2.2: *Cardiac myocytes composed of myofibrils, each of which contains myofilaments. The sarcomere lies between two Z – lines. Source: [1].*

2.2.2. The extracellular matrix (ECM)

The ECM's three-dimensional supporting structure comprises primarily of collagen types I and III, elastin, proteoglycans and glycoproteins, within which cardiomyocytes, fibroblasts, endothelial and smooth muscle cells are arranged. The collagen architecture is one of the major factors that define the biomechanical properties of heart tissue and affects contraction of the whole tissue at the macroscopic level. The intermediate region of connective tissue, which is also known as the interstitial matrix and which is predominantly composed of perimysial collagen, is a major contributor to the tissue's mechanical properties (Figure 2.3) [47]. The perimysium is physically anchored to the basement membrane and it forms a functional unit that, by providing mechanical resistance and structural support to the

myocardium, preserves the shape and wall thickness during diastole and systole [48, 49]. The cardiomyocytes are embedded within this matrix (Figure 2.3) [50].

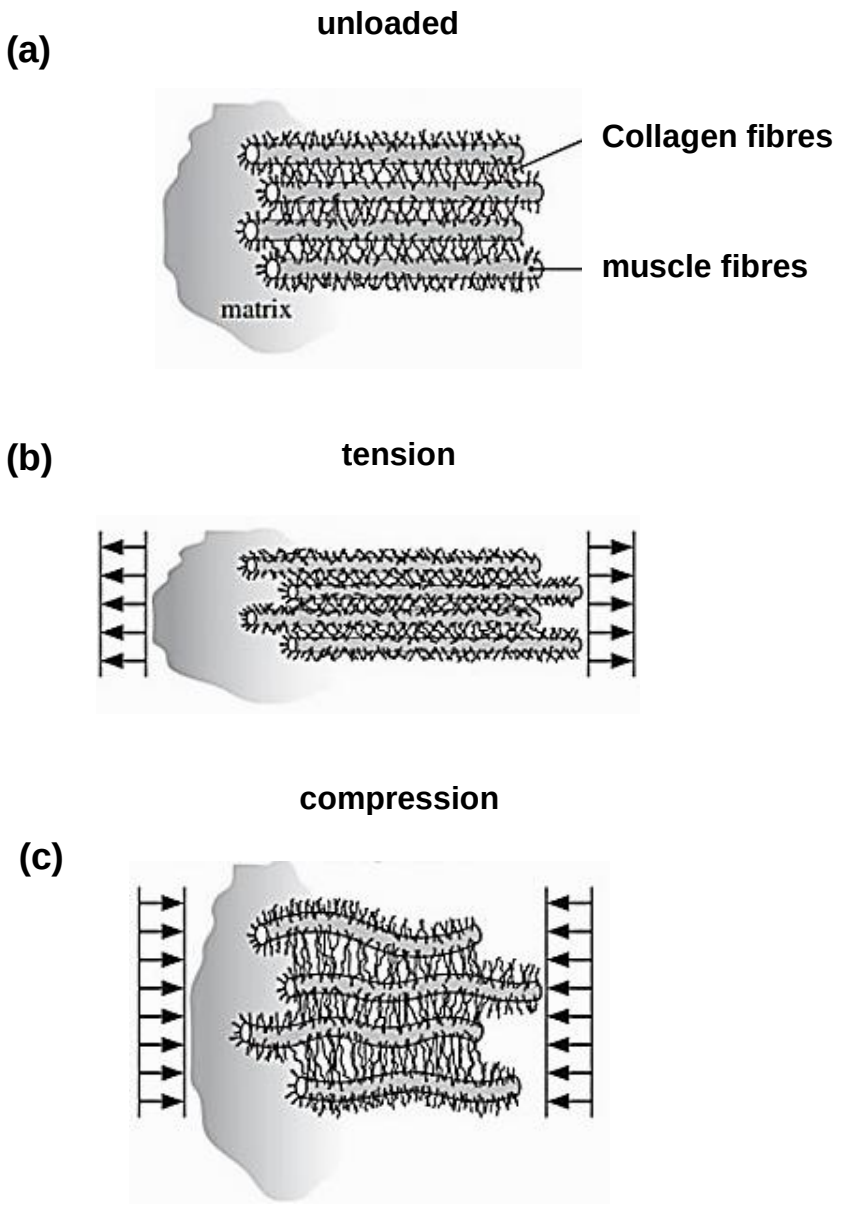

Figure 2.3: *Schematic of the arrangement of muscle and collagen fibres and the surrounding matrix:* ***(a)*** *unloaded structure;* ***(b)*** *structure under tensile load in the muscle fibre direction, showing decreased inter-fibre separation so that the collagen network bears load primarily*

in the muscle fibre direction; ***(c)*** *structure under compressive load in the muscle fibre direction, showing the muscle fibres buckled and lateral extension of the collagen network. Source: [2].*

2.2.3. Cardiomyocyte–collagen interaction

The interaction between cardiomyocytes and collagen fibrils ensembles has been reported to provide myocardial mechanical stiffness, serving to resist the overextension of myocardial tissue during the cardiac cycle (Figure 2.3) [51]. However, at low strains, the myocardial mechanical response has been identified to govern by cardiomyocytes alone, without any coupling between different cardiomyocytes ensembles [51]. Meanwhile, at higher strains, the cardiomyocytes' and collagen fibrils' coupling significantly contributes to the mechanical strength and distensibility of the myocardium, as described in a previous study [51]. This mechanical coupling between cardiomyocytes and collagen fibrils ensembles has been reported to occur as a consequence of the existence of a dense network of fine collagen fibrils, which run across the cardiomyocytes and large collagen fibrils (Figure 2.3) [51, 52].

Previous studies have identified the significant mechanical role that is played by the perimysial collagens during the diastolic function of the heart. The collagen network has been reported to work as a strain-locking system, which limits the overextension of the cardiomyocytes in both ventricles during diastole to prevent a ventricular aneurysm and rupture [48, 49]. A similar function of this collagen was previously reported in the adventitia of arteries [53-55]. The interaction between cardiomyocytes and collagen fibrils has also been reported to significantly contribute to the regional non-homogeneous behaviour of the heart.

During the diastolic phase, the lack of homogeneity in the distensibility of different regions in LVFW has previously been reported, which was due to the difference in the cardiomyocytes' and collagen fibrils' interactions within the anterior and posterior wall [56]. This attribute has been noted in the mammalian heart, which has specified the greater distensibility in the posterior wall compared to the anterior wall in both ventricles [56]. These differences suggest that the posterior wall might make a greater contribution to diastolic filling than the anterior wall [56]. During systolic phase, the nonhomogeneity in regional shortening has previously been reported in the mammalian heart. This identified the greater contribution of the anterior wall in systolic contraction due to the regional differences in cardiomyocytes and collagen fibrils interactions, causing the relative change in substrate stiffness (ECM) and providing the mechanical force to eject the blood [57].

Unfortunately, to date, no such data have been reported describing the cardiomyocytes' and perimysium collagen fibrils' orientation and dispersion for the neonatal mammalian heart. With this microstructural data, *age-specific material models* and *associated material parameters* can be defined for the description of the mechanical behaviour of the ventricular myocardium in neonates. These models will lead to accurate computational simulations to better understand the fundamental underlying neonatal ventricular mechanics. This step will lead to the improvement of the medical treatment of neonatal heart diseases.

2.3. Techniques for imaging tissue microstructure

A number of technologies exist that provide an opportunity for the two and three-dimensional microstructural analyses of heart tissue. For example, the histological and immunohistochemical methods have commonly been used to perform two-dimensional microstructural analysis of heart tissue. However, these techniques require invasive extraction of tissue samples, thin slicing by microtomes (1–10 microns sections), embedding, fixation, and staining procedures [58, 59]. Even though these methods allow the cardiomyocytes and collagen fibrils to be clearly distinguished, they only provide a qualitative assessment from a thin layer of the sample, giving a limited understanding of the myocardial tissue structure. In addition, sample processing, such as tissue dissection and staining, can introduce artefacts, thus limiting the use of these methods [60]. Three-dimensional imaging is required to perform the quantitative analysis of the cardiomyocytes and collagen fibrils. Recently, nonlinear optical microscopy has evolved into a robust tool for non-invasive imaging of thick specimens [61, 62]. In particular, two-photon excitation (TPE), second-harmonic generation (SHG), and confocal microscopy have been used to perform quantitative analysis of the structure of cardiomyocytes and collagen fibrils [43, 63, 64]. In addition, three-dimensional diffusion tensor MRI (DT-MRI) and micro-computed tomography imaging (micro - CT) provide a platform to assess the helical cardiomyocyte architecture of the intact heart. Both imaging modalities have been used as non-destructive methods for the assessment of the cardiomyocytes' architecture [65-71].

2.3.1. Two-dimensional microstructural analyses of adult and neonatal tissue

2.3.1.1 Histological and immunohistochemical analysis

Masson's trichrome staining histology has been used in adult mammalian cardiac tissue, which allows us to identify cardiomyocytes and collagen fibrils for assessment [71-73]. In the study of the adult ovine model, Masson's trichrome staining histology has been used to systematically evaluate the surface area ratio of collagen to myocyte fibres in both atria and ventricles of the heart [72]. In addition, Masson's trichrome staining histology has previously been performed in the adult porcine heart to specify the relative alterations of cardiomyocytes and collagen fibrils in both healthy and infarcted myocardium [71]. Moreover, the orientations of the collagen fibrils have been reported in the study of adult rat infarcted myocardium by using Masson's trichrome histology [73]. Histological data has also been used to determine the preferred cardiomyocytes' orientation of the left and right ventricle in adult porcine heart studies [74, 75].

The current understanding of the microstructure of neonatal cardiac tissue is predominantly derived from histological and immunohistochemical analyses [76-82]. Both of these methods provide the opportunity to microscopically examine tissue structure, although they typically limit investigators to a qualitative analysis as a consequence of the two-dimensional representation. The required tissue dissection will also likely disrupt the microstructure, if not directly as a consequence of cutting the tissue then potentially as a result of relieving residual tissue stress. Histological analysis has previously been performed to investigate the possible histopathological myocardial changes in the young mammalian heart after dexamethasone treatment [77]. Myocardial histological study has also been performed to identify the

myocardial alterations after cardiopulmonary bypass of neonatal piglet heart [81]. Immunohistochemical analysis has previously been used to characterise neonatal cardiac pericytes to provide a novel cellular option for tissue engineering in congenital heart disease [76]. Histological analysis has also been consolidated with the immunohistochemical study to investigate the cardiac myopathies in the neonatal mammalian heart [79]. A similar approach has previously been adopted to investigate the normal and pathological conditions in the neonatal mammalian heart during developmental defects and excessive apoptosis [82]. Most of these studies have provided a two-dimensional qualitative representation of the tissue, although they lack three-dimensional quantitative analysis.

2.3.2. Three-dimensional microstructural analyses of adult and neonatal tissue

2.3.2.1. TPEF/SHG and Confocal microscopy

Several microscopic techniques have been used to describe the three-dimensional architecture of cardiomyocytes and collagen fibrils in the adult mammalian heart, which mainly come from two-photon excited fluorescence and second-harmonic generation (TPEF/SHG), and confocal microscopy [52, 63, 83]. Three-dimensional imaging of the entire organ provides a route to overcome the need for tissue dissection, which could be responsible for disrupting the microstructure—if not directly as a consequence of cutting the tissue, then potentially as a result of relieving residual tissue stress. Hence, evolving techniques such as two-photon excitation (TPEF) and SHG provide the ability to optically section thick specimens [61, 62, 84-87]. SHG provides a deeper insight into those molecules that lack a centre of symmetry (e.g. collagen, microtubules and myosin), while TPEF can image elastin and myocytes by exciting endogenous fluorophores [88-91]. When used in tandem, these two techniques can

provide a microscopic, three-dimensional representation of the interplay between key proteins within biological samples. They also negate the need for disruptive tissue dissection or staining, which is a common source of artefact [63]. Whereas in confocal microscopy, an additional confocal pinhole is supplementary to reject out-of-focus background fluorescence and it can produce thin (i.e. less than 1 micrometre), unblurred optical sections.

TPEF/SHG microscopy has previously been used to identify the biomolecular arrays in cells, tissues and organisms [88]. TPEF/SHG is also an ideal method for producing live cell images thanks to its high resolution of nonlinear optical microscopy, and enhanced ability to reduce photobleaching and phototoxicity effects [89]. In particular, SHG microscopy of collagen generates extremely strong and robust signals, which is a consequence of the collagen fibrils nonlinear susceptibility. This provides a novel platform for imaging tissue structure at optimum resolution, as reported in previous studies [90, 91].

TPEF/SHG microscopy has been reported to be a robust imaging modality that can be used to investigate the quantitative changes in cardiomyocytes and collagen fibril architecture in pathological conditions, including fibrosis and connective tissue disorders [61]. TPEF/SHG microscopy is also an effective tool for visualising the development and remodelling of neonatal mammalian cardiomyocytes during the dynamic myofibrillogenesis [85, 86]. In addition, TPEF/SHG microscopy has been used to determine the effect of fetal mammalian cardiac ECM on the expansion of cardiomyocytes. It has also been used to develop biomaterials that mimic developmental cues to stimulate or maintain cardiomyocyte proliferation for tissue engineering or regenerative medicine approaches for treating Congenital heart defects (CHD) [87]. Recently, Sommer et al. have used TPEF/SHG to

systematically quantify the in-plane and out-plane cardiomyocytes' preferred orientation and dispersion in the adult human left ventricle [52]. Similarly, Pope et al. have used extended volume confocal microscopy to describe the three-dimensional quantitative representation of cardiomyocytes and perimysial collagen in the adult mammalian heart [92].

The cardiomyocytes' and collagen fibrils orientation and angular dispersion changes in the orthogonal direction of cardiac tissue influence its biomechanical behaviour. Their orientation and angular dispersion are essential to maintain myocardial stiffness and anisotropy during the cardiac cycle. The influence of cardiomyocyte orientation and dispersion has previously been highlighted in adult studies, which have identified the significant effects of these parameters on the passive and active behaviour of myocardial tissue [10, 46].

2.3.2.2. DT-MRI and micro-CT imaging

Three-dimensional diffusion tensor magnetic resonance imaging (DT-MRI) has been established as a robust non-destructive method that can be used to assess the cardiomyocyte architecture of intact mammalian heart [93-95]. Three-dimensional DT-MRI has also been used to identify the cardiomyocyte architectural plasticity in fetal, neonatal, and adult mammalian hearts [70]. In addition, three-dimensional DT-MRI has increasingly been used to evaluate the post-infarct remodelling in the myocardium, where it has indicated the altered tissue integrity in the adult mammalian heart [69, 96-100]. In most of these studies, tractography (which is a method specific to tracking fibre directionality) has been performed within a filter framework using a discrete mixture of Gaussian tensors to model the signal.

Starting from a seed point, each fibre was traced using an unscented Kalman filter, which propagates in the most consistent direction to approximate the local structure along the fibre; as described in detail elsewhere [101]. Fractional anisotropy (FA) is a quantitative measure of water diffusion anisotropy and it has previously been computed for neonatal and adult mammalian hearts, which reflects the directional coherence of cardiomyocytes orientation [70, 71, 102, 103].

Three-dimensional DT-MRI has been used to provide an enhanced ability to track the cardiomyocyte architectural plasticity with increasing age, as demonstrated in a previous study of fetal, neonatal and adult porcine hears [70]. Zhang et al. performed three-dimensional DT-MRI on fetal, neonatal and adult porcine hearts, to identify the postnatal changes of cardiomyocyte architecture from P1 to P14, which predominantly occurred in the septum and RVFW [70]. These authors also identified the shift in the volume ratio of LVFW vs RVFW, which was associated with the cardiomyocytes' architecture. Moreover, they also indicated the relative decrease in the fibre rotation of RVFW, due to the change of stress within the tissue after birth. In addition, they reported the substantial structural changes that occurred as a consequence of the increased workload and altered cardiac mechanical function after birth [70].

FA is an index that is used to calculate water diffusion anisotropy, which has previously been used to identify alterations in the cardiomyocyte's architecture. In particular, FA measures have previously been used to highlight alterations in the cardiomyocytes in healthy and pathological heart conditions for both neonatal and adult porcine hearts [70, 71]. Meanwhile, Zhang et al. described the greater FA in neonatal porcine hearts than adults. McGill et al.

reported the regional FA in healthy human hearts, which was found to be non-homogeneous and it varied significantly transmurally and regionally. These authors suggested that the marked heterogeneity in FA may be related to several factors, such as variations in the cardiac microstructure, partial volume effects and strains [102].

The DT-MRI technique is now gaining in prominence because of its ability to non-destructively derive the cardiomyocytes' architecture. Meanwhile, an alternative non-destructive method such as the micro-CT is largely disregarded due to the poor soft-tissue contrast. In some studies, iodine base staining has been used to enhance the contrast, which has enabled the assessment of the cardiomyocytes' architecture. However, this technique is limited to investigations of small regions in the heart [65-67].

2.4. Cardiac tissue function

The biomechanical properties of the myocardial tissue have previously been characterised using biaxial extension tests, which mainly come from the adult mammalian heart [104-109]. Unfortunately, to date, there are no biomechanical data of neonatal heart tissues available for material parameter estimation and the development of sophisticated age-specific constitutive models for neonates is lacking. Holzapfel and Ogden have identified that the problem in developing the constitutive models is the shortage of experimental data for estimating the material parameters [110]. Constitutive models and their corresponding material parameters can be defined for the description of the mechanical behaviour of the ventricular myocardium. These models will lead to accurate computational simulations that are able to

better understand the fundamental underlying neonatal ventricular mechanics, which will improve the medical treatment of neonatal heart diseases.

The heart undergoes a complex pattern of deformations during the cardiac cycle, such as tension, compression, and shearing. In particular, shearing deformation or relative sliding of myocardial layers has been found to play an important role in the mechanical function of the heart during both diastole and systole. This mechanism has previously been reported to facilitate left ventricle ejection by contributing to subendocardial wall thickness during systole [111]. In addition, relative shearing also contributes to the myocardium wall thinning during passive ventricular filling [112]. Hence, biaxial tests alone are not sufficient to characterise the passive behaviour of the myocardial tissue [110]. In previous adult studies, biaxial extension tests have mostly been used to characterise the biomechanical properties of adult cardiac tissue; however, uniaxial tensile and simple shear tests have also been performed in a few adult mammalian heart studies [52, 104-109, 113, 114].

The FSN-coordinate system in LVFW and RVFW has previously been identified based on the local laminar architecture and morphology of the myocardium [2, 39, 113]:

- The fibre axis (F), which is defined as the mean-fibre direction (MFD) as observed by the external surface texture;
- The sheet axis (S), which is defined as the direction transverse to the fibre axis within the layer;
- The sheet-normal axis (N), which is defined as the direction perpendicular to both the fibres and layers, this is also referred as the cross-fibre direction (CFD).

2.4.1. Uniaxial tensile properties

Uniaxial tensile tests have previously been performed to characterise the biomechanical properties of the adult mammalian heart [104, 114]. In most studies, uniaxial tests have been performed in the MFD and CFD of adult mammalian cardiac tissue, which are predominantly orthogonal to each other. Previous uniaxial studies have identified nonlinear, anisotropic, and viscoelastic mechanical behaviour of adult mammalian cardiac tissue [104, 114]. In adult canine and bovine studies, myocardial specimens exhibited large deformation, pronounced nonlinearity and the formation of hysteresis with stiffer behaviour and larger hysteresis in MFD than the CFD. Other soft tissues possess large deformations with nonlinear stress-strain behaviour, anisotropy, and small hysteresis; as documented in the previous studies [115-119]. Demer et al. described the different interpretations for the uniaxial and biaxial tensile tests on the adult canine myocardium, identifying the influence of boundary conditions on tissue behaviour [104]. In addition, Hamid et al. performed uniaxial tensile tests on specimens taken from the LVFW and RVFW of the adult bovine myocardium, demonstrating the hyperelastic and viscoelastic behaviour of the tissue [114].

2.4.2. Biaxial extension properties

In the literature, biaxial extension tests have mostly been used to systematically quantify the biomechanical properties of the adult mammalian myocardium, which mainly come from the canine and bovine hearts [104-109, 114]. In most of these studies, equibiaxial tests have been performed to characterise the biomechanical properties of the adult mammalian myocardium. Only Yin et al. performed non-equibiaxial extension tests with different ratios in the MFD and CFD on the adult canine myocardium [109]. Recently, Sommer et al. have performed the

biaxial tests on the LVFW of the adult human myocardium. A strong correlation between the microstructure and mechanical behaviour of the adult human myocardium has been reported in this study [39]. Sommer et al. have also endorsed to use experimental data in estimating the material parameters and the development of sophisticated material models, which could be used for computational simulations [39]. In studies of adult canine, bovine and the human hearts, myocardium specimens have demonstrated large deformation, pronounced nonlinearity and the formation of hysteresis with stiffer behaviour and larger hysteresis in MFD than the CFD [39, 104-109, 114]. Other soft tissues exhibiting large deformations with nonlinear stress-strain behaviour, anisotropy, and small hysteresis have been reported in previous studies [115-119].

Demer et al. identified the significant differences in the material parameters for the uniaxial tensile and biaxial extension tests during the mechanical characterisation of the isolated adult canine myocardium [104]. This indicates the influence of boundary conditions on the passive behaviour of the adult mammalian myocardium. Humphrey et al. performed biaxial tests on thin sheets of the adult canine myocardium to develop a constitutive model for the passive myocardium [106]. In this study, myocardium was assumed to be transversely isotropic material, and therefore transversely isotropic constitutive model with five material parameters was developed.

Biaxial tests have also been performed on the passive RVFW myocardium. Sacks et al. demonstrated the passive biaxial mechanical properties of the adult canine RVFW myocardium [108]. This study reported that the RVFW myocardium exhibited anisotropic behaviour with a greater stiffness in the MFD than the CFD. Moreover, a regional variation

in the anisotropy was highlighted and a comparison was made to the similar region of LVFW, which specified that the RVFW myocardium was stiffer than the LVFW in the MFD. In addition, RVFW myocardium was found to possess greater anisotropy than the LVFW, as documented by the Sacks et al. [108]. Biaxial tests have been performed to evaluate the transmural differences in the mechanical behaviour of the adult canine myocardium. Novak et al. performed biaxial tests on the outer, middle, and inner regions of the adult LVFW canine myocardium, and they reported the following findings: (1) a three-dimensional constitutive model could be used to describe the nonlinear and anisotropic behaviour in the three regions equally well; (2) all three regions exhibited the similar extent of anisotropy; (3) specimens from inner and outer regions possessed greater stiffness when compared to those from the middle region of the LVFW. This study suggested that the mechanical properties of the adult mammalian heart were qualitatively similar to region-to-region but quantitatively different [107].

Inflation test has also been performed to characterise the biaxial properties of adult murine RVFW. Hill et al. identified the strong correlation between the microstructure and mechanical behaviour of this tissue [105]. In particular, the cardiomyocytes' and collagen fibrils' orientation has been reported to significantly contribute to the mechanical behaviour of the myocardial tissue, in both healthy and pathological conditions. Moreover, Hill et al. described that the cardiomyocytes and collagen fibrils interaction was essential for maintaining myocardial stiffness and mechanical anisotropy [105].

Biaxial tests have also been performed on the isolated epi and endocardium of the adult mammalian heart, and they have described the biomechanical behaviour of both membranes

[120-123]. Humphrey et al. performed biaxial extension tests on the epicardium excised from the RVFW and LVFW of adult canine hearts [120]. Humphrey et al. demonstrated that the epicardium possessed highly nonlinear stress-stretch and anisotropic behaviour. Interestingly, epicardium exhibited strain-dependent behaviour. At low strains, it was very complaint but it then became very stiff near the limits of its extensibility [120]. Moreover, epicardium demonstrated isotropic behaviour at low strains but became markedly anisotropic upon rapid stiffening. In the same study, specimens from both ventricles appeared to behave similarly qualitatively but possessed different quantitative mechanical behaviour. Despite having a thin membrane, the epicardium could withstand significant in-plane loads. This allows it to considerably contribute to the local and global cardiac mechanics and physiology, as reported in a previous study [120]. Kang et al. performed a biaxial study to compare the mechanical properties of the adult bovine isolated endo and epicardium [121]. Their study reported that the endo and epicardium behaved differently: the endocardium possessed the greater stiffness in the low-strain range, while epicardium was more complaint in the low-strain, although it exhibited greater stiffness towards the limit of its extensibility. Moreover, Kang et al. identified that the endocardium behaviour could be described by a seven-parameter strain-energy function, whereas the epicardium required a four-parameter strain-energy function [121]. Recently, a new approach has been developed to determine the shear deformation or in-plane compression for the epicardium, in which suction is applied locally to the intact passive adult canine LVFW epicardium [122]. The resulting deformation was measured throughout the region of interest using magnetic resonance tagging. In the same study, the transversely isotropic constitutive model was used to estimate the material parameters for the intact passive canine LVFW epicardium [122].

2.4.3. Simple shear properties

Shearing deformation or relative sliding of myocardial layers has been identified to significantly contribute to the mechanical function of the heart during both diastole and systole. This mechanism has previously been reported to facilitate left ventricle ejection by contributing to subendocardial wall thickness during systole [111]. In addition, the relative shearing also contributes to the myocardium wall thinning during passive ventricular filling [112]. Hence, uniaxial and biaxial tests alone are not sufficient to characterise the passive behaviour of the myocardial tissue [110].

Simple shear tests have previously been performed to quantify the biomechanical properties of adult mammalian LVFW, which mainly come from the porcine and human myocardium [39, 113]. Dokos et al. defined the local laminar architecture and morphology of the myocardium, based on a right-handed orthogonal set of reference axes. The three orthogonal axis were identified to obtain the FSN-coordinate system, which related to the MFD or fibre axis (F); the direction transverse to the fibre axis, arranging the myocardial layers, which is referred to as the sheet axis (S); and, the direction perpendicular to both the fibres and layers, which is referred to as the sheet-normal axis (N) [113]. In both studies, simple shear tests have been performed in the six possible modes of simple shear deformation, comprising different orientations [39, 113]. Previous simple shear studies have specified nonlinear, anisotropic, viscoelastic and heterogeneous behaviour during a simple shear test [39, 113]. Shear strains ranging (0.1– 0.5) were used to cover the physiological deformations, as reported for the beating heart in a previous study [113]. In studies of adult porcine and human myocardium, hysteresis formation (energy dissipation) was prominently evident throughout the cyclic shearing behaviour, while LVFW demonstrated increased shear. MFD exhibited the greater energy dissipation and large hysteresis than the other directions, as demonstrated

in previous studies [39, 113]. Dokos et al. described that the LVFW myocardium was least resistant to simple shear displacements imposed in the sheet-direction (S), while myocardium exhibited the greater stiffness in the plane producing an extension of the myocyte axis (MFD) [113]. Anisotropy was predominantly evident in all six modes of shearing, as demonstrated in previous studies [39, 113].

2.4.4. Energy dissipation

The energy dissipation or formation of hysteresis has previously been reported in uniaxial and biaxial adult mammalian heart studies [39, 104, 114]. Studies of other soft tissue have also identified the energy dissipation during the biomechanical testing [115-119]. Energy dissipation has been reported to occur as a consequence of the interaction between cardiomyocytes and collagen fibrils ensembles, which provides myocardial mechanical stiffness and serves to resist the overextension of ventricles during the cardiac cycle [51]. However, at low strains, the myocardial mechanical response is governed by the cardiomyocytes alone, without any coupling between different cardiomyocytes ensembles [51]. Meanwhile, at higher strains, the cardiomyocyte and collagen fibril coupling significantly contribute to the mechanical strength and distensibility of the myocardium [51]. This mechanical coupling between cardiomyocytes and collagen fibrils ensembles occurs as a consequence of the existence of a dense network of fine collagen fibrils, which run across that cardiomyocytes and large collagen fibrils. This may contribute to causing the energy dissipation in both ventricles [39, 51].

Energy dissipation has also been reported during simple shear tests on LVFW myocardium [39, 113]. Hysteresis was more pronounced during shearing in myocardial tissue than during

uniaxial tensile and biaxial extension testing, as reported in previous studies [52, 113]. This attribute has been reported to occur as a consequence of the relatively high water content of myocardium (~ 80% wet weight) and it is affected by the muscle presence [40]. In addition, changes in water content, such as edema, may contribute to causing alternations in the passive stiffness and viscoelasticity of the myocardium [40]. Moreover, the giant protein titin, which connects the Z line to the M line in the sarcomere, may contribute to the passive properties of the myocardium during shear deformations; as reported in previous studies [124-126]. Alternatively, the actin-myosin interaction might be partly responsible for causing the hysteresis formation, as suggested in previous studies [127, 128]. These interactions between all solid and liquid within the intra and extracellular components in the myocardium may contribute to the hysteresis formation, but to what extent is currently unknown.

2.4.5. Stress softening

Stress softening has previously been reported during the uniaxial and biaxial cyclic preconditioning of adult mammalian myocardium, which mainly comes from canine, bovine and human hearts [39, 104, 114]. In these studies, the greatest change in the stress was noticed during the first two preconditioning cycles. This stress-softening behaviour is also referred as the Mullins effect [129]. It has previously been suggested that stress softening in myocardial tissue may cause due to the disruption of perimysial collagen network, which is a consequence of the excessive shearing between adjacent myocardial muscle layers [130]. Moreover, the softening may occur due to the changes in the collagen matrix where the cardiomyocytes are embedded [131]. In addition, stress softening may occur due to the damage to endomysial collagen, which is a consequence of excessive stretch of the tissue [132]. Alternatively, disruption of myofilaments such as titin, actin and myosin may partly

contribute to the stress softening of myocardial tissue; as described in the previous studies [125, 133].

Strain softening has also been identified during the simple shear tests on the adult LVFW myocardium [39, 113]. In these studies, strain softening was briefly observed with increased shear. This may be caused by a disruption of perimysial collagen during cyclic shearing, which is a consequence of excessive shearing between adjacent myocardial muscle layers [130, 134, 135]. A similar damage in perimysial fibres has previously been identified during the inflation test [130, 134]. Moreover, strain softening has been reported in both cardiomyocytes and individual cardiac myofibrils, during axial extensions larger than 3 µm [133, 136, 137]. However, myocardial tissue did not possess softening at stains lower than 2.3 µm, as reported in the previous studies [138-140]. Hence, it has been suggested that the myocardial tissue would possess strain softening at extensions larger than 3 µm.
Alternatively, the softening observed in the adult mammalian myocardium may be due to the rearrangement of the extracellular connective tissue, which is a consequence of the increased mechanical loadings [39]. Strain softening was more pronounced during shearing than during uniaxial tensile and biaxial extension tests, as highlighted in previous studies [39, 104, 113, 114]. This has been reported to occur as a consequence of the relative damage within the intra and extracellular components in the myocardium during shearing in the tissue [39].

2.5. Application of structural and function data of cardiac tissue

Congenital heart disease (CHD) describes a series of structural cardiac disorders, including ventricular and atrial septal defects, which annually affects 36,000 new-borns within the European Union [6, 7]. In addition, in the European Union, 3000 children who are diagnosed with CHD die annually as a termination of pregnancy for fetal abnormality (TOFPA), early neonatal death, or late fetal death [7]. CHDs affect 9-in-1000 births and they are one of the UK's most common birth defects. CHD patients account for over 100,000 UK hospital bed-days per annum [5].

Cardiovascular surgical interventions are necessary to repair CHD, without which, in most circumstances, the patients could endure several pathological heart conditions, such as volume overload, cyanosis, and congestive heart failure. Surgical treatment entails the use of biocompatible implants to patch up CHD [141-143]. To date, the most widely used material conduit are biocompatible synthetic polymers; however, these materials are associated with several short and long-term limitations, which could potentially lead to thromboembolisation, calcification, infection and stenosis [16-18]. In particular, for paediatric cardiovascular applications, it is quite recurrent for patients to outgrow their grafts because these materials lack growth potential; hence, leading to reoperation, which is related with adversely higher rates of mortality and morbidity than first-time sternotomies [144, 145]. Rates of failure for grafts that composed of synthetic materials in paediatric cardiac surgery can be distinguished into three categories—(a) Early, (b) midterm and, (c) long-term—the published 5 years patency rates are between 65%–90% for early and midterm; 70%–100% for the long-term graft failure at 10–15 years [146]. Therefore, despite significant developments in surgical procedures for CHD which have occurred in the last 30 years, the verdict on an ideal vascular graft stays is still open to contest.

Resolving the limitations associated with currently used graft materials will significantly reduce mortality and morbidity in children born with CHD, which is a crucial step towards improving their postoperative quality of life [20]. An ideal and promising method for the creation of the ideal vascular conduit is to bioengineer tissue utilising (pluripotent or multipotent) stem cells, which is commonly known as tissue-engineered vascular graft (TEVG) [147]. Interestingly, selecting a scaffold material used for TEVG creation is a critical and defining step in designing successful constructs for vascular engineering. Its selection predominantly depends on three important factors: (a) biocompatibility, (b) biomechanical properties, and (c) rate of biodegradation [20]. Stem cells differentiate into different lineages, depending on the mechanical properties of the matrix material [148]. Hence, an appropriate biomechanical microenvironment for stem cells might provide an ideal platform for correctly differentiated cells [149]. It is of *utmost* importance to ensure compliance between the mechanical properties of the engineered cardiac patch and native heart wall to enhance the mechanical stimulation between the native myocardial environment to the stem cells during the diastolic and systolic functions of the heart [147, 149, 150]. However, an acute lack of data describing the biomechanical behaviour of *neonatal cardiac tissue*, twinned with the structural changes to the tissue during *maturating*, potentially limits the effectiveness of these novel techniques.

Unfortunately, to date, no study has attempted to systematically quantify the microstructure and underlying biomechanical behaviour of the *neonatal cardiac tissue*. In addition, simply adopting or scaling adult data risks incorporating an unknown level of error, which may contribute to the short, medium and long-term failure of synthetic and biological scaffolds [20, 147]. Hence, enhanced knowledge of *neonatal tissue behaviour* to achieve more effective designs has the potential to positively influence CHD mortality and morbidity [20].

2.5.1. Computational modelling of neonatal heart diseases

Engineering-based computational simulations provide robust tools to perform patient-specific cardiovascular simulations, and so predict the consequence and effectiveness of surgical interventions. Computational modelling is increasingly used in adult cardiology to understand the behaviour of structural components, which enables the simulation of normal and pathophysiological conditions and leads to new interventions [8, 10-13, 15]. Recent advances in the development of constitutive models and computing power have enabled computational simulations to gain greater clinical acceptance. In adult cardiology, patient-specific computational modelling provides a novel platform to enhance the understanding of cardiac mechanics, which assists researchers, bioengineers and clinicians to develop new interventions and, thus, improve the postoperative lives of patients [151-153]. A similar approach for simulation adoption could be used in paediatric clinical applications. However, an acute lack of quantitative data, describing the *neonatal tissue structure* and *biomechanical behaviour* limits the widespread use and effectiveness of sophisticated techniques to investigate neonatal cardiac disorders. Moreover, the lack of validation through experimental data potentially limits the use of computational simulations in a wide range of paediatric and CHDs. Hence, experimental data is needed to describe the mechanical and structural behaviour of *neonatal tissue* in estimating the material parameters, which will allow the widespread use of these simulations in both modelling methodology and clinical applications. Holzapfel and Ogden have identified that the problem in developing the constitutive models is the shortage of experimental data for estimating the material parameters [110]. Therefore, the strong demand for mechanical data, combined with their underlying microstructural data, sophisticated age-specific material models and associated material parameters can be help in the description of the mechanical behaviour of the ventricular myocardium in neonates.

These models will lead to accurate computational simulations that will allow us to better understand the fundamental underlying ventricular mechanics, which is a necessary step in the improvement of the medical treatment of neonatal heart diseases [110].

2.5.2. Constitutive modelling of the myocardium

As discussed in Section 2.4, the myocardium has nonlinear, anisotropic, viscoelastic and heterogeneous mechanical behaviour. A number of different approaches have been used in the literature to model the myocardium, including constitutive models to estimate the material parameters of the highly nonlinear myocardium for computational simulations. In particular, a realistic description of the three-dimensional geometry and microstructure of the myocardium along with its biomechanical data is required to develop a sophisticated constitutive model of the myocardium, as described in the previous study reported by Holzapfel et al. [110]. The myocardium undergoes a complex pattern of deformations during the cardiac cycle, such as tension, compression, and shearing. Specifically, shearing deformation or relative sliding of myocardial layers has been found to play an important role in the mechanical function of the heart during both diastole and systole. This mechanism has previously been reported to facilitate left ventricle ejection by contributing to subendocardial wall thickness during systole [111]. Moreover, relative shearing also contributes to the myocardium wall thinning during passive ventricular filling [112]. Hence, the biaxial tests alone are insufficient to characterise the passive behaviour of the myocardial tissue and, hence, to develop the enhanced constitutive models [110].

A general nonlinear elasticity theory framework has previously been used to develop constitutive models for the myocardium [154]. The structural features of the myocardium and its mechanical properties have been accounted within the theoretical framework of the existing constitutive models.

A number of transversely isotropic models have been proposed, including Humphrey et al., who described the strain-energy function as the sum of two exponentials, one in I_1 and one in I_4,

$$\Psi = c\{\exp[b(I_1 - 3)] - 1\} + A\{\exp[a(\sqrt{I_4} - 1)^2] - 1\}, \quad \text{(Eqn 2.1)}$$

which contains four material parameters: c, b, A and a. This model was the first to include anisotropic invariant and it accounted for the fibre structure [155]. Another transversely isotropic model, based on the invariants I_1 and I_4 was proposed by Humphrey et al., which has the form

$$\Psi = c_1(\sqrt{I_4} - 1)^2 + c_2(\sqrt{I_4} - 1)^3 + c_3(I_1 - 3) + c_4(I_1 - 3)(\sqrt{I_4} - 1) + c_5(I_1 - 3)^2$$

(Eqn 2.2)

which contains five material constants: c_1,c_2,..,c_5 [156]. The estimated values of these parameters were obtained from biaxial test data from the middle portion of the inter-ventricular septum, and the inner, middle and outer layers of the passive canine ventricular myocardium, as reported in a previous study [107].

These models were based on the assumption of incompressibility but another transversely isotropic model was proposed by Kerckhoffs et al. that was based on the assumption of compressibility, which has the form

$$\Psi = a_0[\exp(a_1\hat{I}_1^2 + a_2\hat{I}_2) - 1] + a_3[\exp(a_4 E_{\mathrm{ff}}^2) - 1] + a_5(I_3 - 1)^2, \quad \text{(Eqn 2.3)}$$

which contains six material parameters: a_0, a_1, …, a_5, where $\hat{I}_1$ and $\hat{I}_2$ are the principal invariants of **E** and E_{ff} is the Green–Lagrange strain in the fibre direction [157]. Other transversely isotropic models were constructed by Guccione et al. and Costa et al., which did not include the morphology and structure of the of the myocardium [158, 159]. Furthermore, Horowitz et al. proposed the transversely isotropic model that was based on the microstructure to potentially capture the micro-mechanical behaviour of the myocardium [160]. Although all of these models considered the myocardium as a transversely isotropic material, LeGrice et al. and Dokos et al. identified the myocardium as an orthotropic material. Hence, an orthotropic constitutive model is needed to adequately estimate the material parameters of the myocardium [43, 113].

In the literature, several orthotropic models have been proposed, in which some models are inappropriate for modelling myocardial tissue—including Bischoff et al.'s Langevin eight-chain based model, which does not account for the morphology and structure of the myocardium [161]. Costa et al. developed an orthotropic model, using the Fung-type exponential strain-energy function, which has the form

$$\Psi = \tfrac{1}{2}a(\exp Q - 1),$$

$$、\ Q = b_{\mathrm{ff}}E_{\mathrm{ff}}^2 + b_{\mathrm{ss}}E_{\mathrm{ss}}^2 + b_{\mathrm{nn}}E_{\mathrm{nn}}^2 + 2b_{\mathrm{fs}}E_{\mathrm{fs}}^2 + 2b_{\mathrm{fn}}E_{\mathrm{fn}}^2 + 2b_{\mathrm{sn}}E_{\mathrm{sn}}^2, \quad \text{(Eqn 2.4)}$$

which contains seven material parameters: a and b_{ij}, where i, j representing the fibre (f), sheet (s), and normal (n) directions in the myocardium [162]. Moreover, Schmid et al. also proposed the Fung-type orthotropic model, which has the form

$$\Psi = \tfrac{1}{2}a_{\mathrm{ff}}[\exp(b_{\mathrm{ff}}E_{\mathrm{ff}}^2)-1] + \tfrac{1}{2}a_{\mathrm{fn}}[\exp(b_{\mathrm{fn}}E_{\mathrm{fn}}^2)-1] + \tfrac{1}{2}a_{\mathrm{fs}}[\exp(b_{\mathrm{fs}}E_{\mathrm{fs}}^2)-1] + \tfrac{1}{2}a_{\mathrm{nn}}[\exp(b_{\mathrm{nn}}E_{\mathrm{nn}}^2)-1] + \tfrac{1}{2}a_{\mathrm{ns}}[\exp(b_{\mathrm{ns}}E_{\mathrm{ns}}^2)-1] + \tfrac{1}{2}a_{\mathrm{ss}}[\exp(b_{\mathrm{ss}}E_{\mathrm{ss}}^2)-1].$$

(Eqn 2.5)

which contains 12 material parameters, which also used the components E_{ij}, where i, j describe the fibre (f), sheet (s), and normal (n) directions in the myocardium [163].

Recently, Holzapfel et al. proposed the structurally-based orthotropic model for the passive myocardium, which has the form

$$\Psi = \frac{a}{2b}\exp[b(I_1-3)] + \sum_{i=f,s}\frac{a_i}{2b_i}\{\exp[b_i(I_{4i}-1)^2]-1\} + \frac{a_{\mathrm{fs}}}{2b_{\mathrm{fs}}}[\exp(b_{\mathrm{fs}}I_{8\mathrm{fs}}^2)-1]$$

(Eqn 2.6)

where a, b, a_f, a_s, b_f, b_s , a_{fs} and b_{fs} are eight positive material constants, the *a* parameters possess the stress dimension, while the *b* parameters are dimensionless. This consists of the isotropic term in I_1, the transversely isotropic terms in $I_{4\,f}$ and $I_{4\,s}$ and the orthotropic term in $I_{8\,fs}$.

In the general theory of nonlinear elasticity, I_1, I_2, and I_3 are defined as isotropic invariants. However, if the material has a preferred direction in the reference configuration, then this

introduces anisotropy, specifically transverse isotropy, which is defined by two additional (transversely isotropic) invariants denoted by I_4 and I_5. Subsequently, if there are two preferred directions in a material, then this further introduces the invariants I_6 and I_7 associated with it and, additionally, a coupling invariant, denoted by I_8.

Unfortunately, to date, there are no available experimental data that quantitatively describe the neonatal cardiac tissue structure and biomechanical behaviour. This data is valuable to estimate the material parameters and the development of age-specific material models. Such a model will lead to more accurate computational simulations in understanding the fundamental underlying neonatal ventricular mechanics.

2.6. Surrogate animal models in biomedical research

Several surrogate animal models have been used in human-related cardiac research, which mainly comprised of the canine and porcine. In the biomechanical and microstructural studies, canine and porcine animal models were mostly used as the surrogates of the humans [104, 107, 108, 113, 135]. Until the mid-1980s, canines were used extensively in cardiac research. In general, canines and human's cardiovascular functions are similar. However, there are considerable differences in the size and anatomical shape of the heart, which may potentially affect the outcome. Porcine animal surrogates have been used to investigate chronic ischaemia, therapeutic angiogenesis, hypertrophic cardiomyopathy and CPR research. In particular, porcine cardiac anatomy, coronary arteries and physiology resemble closely those of humans [164-166]. They are also available at a lower cost than canines, which provides a wider availability of uniform sizes and ages for all stages of experimental modelling [90]. In addition, myocardial histology is similar in swine and humans [167]. After

induction of myocardial ischaemia, both porcine and human myocardium biochemical and metabolic response is similar [168, 169].

The porcine model has increasingly been used in performing human-related biomedical research due to its anatomical and physiological resemblance to humans [30-37]. The adult porcine model has a wide range of applications in biomedical research, such as in cardiovascular, dental, pancreatic and chronic toxicological studies [31, 170-172]. In particular, the research on fetal and neonatal porcine models has provided a novel platform, in performing numerous investigative studies for the perinatal biology. The fetal and neonatal porcine models have been selected to emphasise the usefulness of these models in prenatal and postnatal studies to human biology and medicine, as described in the previous studies [33, 170]. Neonatal porcine models have commonly been utilised in several areas of biomedical research, including cardiology, embryology, nutrition, metabolism, teratology and immunology [33]. In addition, these models have been adopted in the studies of both spontaneous and iatrogenic pathological conditions in human infants [33]. When compared with the other young animal models that are commonly used in biomedical research, such as the canine, the neonatal porcine model has been identified to be most like the new-born human infant [33]. The resemblances in cardiovascular, respiratory, renal and haematological systems have been highlighted in a previous study [173]. Moreover, the large litter size, two or three litters per sow per year and the relatively low cost of piglets make it an ideal animal model in defining human infants in biomedical research studies [173].

The process of translating innovative discoveries from biomedical research into clinically applicable novel therapies is commonly described as translational medicine [174].

Appropriate animal models are critical when evaluating the efficacy and safety of new drugs and novel interventions for the success of translational research. In the past, rodent models were widely used for the translational research [30]. Recently, transgenic pigs have comprehensively been documented as large animal models for selected human pathologies, including cardiovascular, cystic fibrosis, diabetes mellitus and neurodegenerative diseases [30]. The techniques related to genetic modification of pigs have precisely been documented to facilitate the generation of tailored disease models [30, 175-177]. Previous studies have also identified the resemblance between the transgenic neonatal porcine models and human infants for the healthy and pathological conditions, which specified the future reliance on such models for improving the analysis of the pathogenesis and development of new treatment and surgical interventions for cardiovascular, cystic fibrosis, diabetes mellitus and neurodegenerative diseases [30, 174].

Although the porcine model was adopted as the neonatal and adult organs are commonly used to simulate human performance for both the healthy and pathological conditions, given their relatively similar structure and dimensions, there are still significant differences that should be taken in account during the applicability of these data [178]. Therefore, caution should be exercised when applying these data to human scenarios given these differences.

2.7. Research motivations

Engineering-based computational modelling is increasingly used in adult cardiology to understand the behaviour of structural components, enabling the simulation of normal and pathophysiological conditions, and leading to new interventions [8-15]. However, there is a lack of experimental data that quantitatively describes the neonatal cardiac tissue structure

and biomechanical behaviour, which limits our ability to estimate the material parameters in performing computational simulations. However, neonatal computational simulations that simply adopt, or scale, adult data, risk incorporating an unknown level of error [16-19]. Hence, this shortage of relevant data is currently limiting the value of computational modelling and it prevents a better understanding of the underlying neonatal ventricular mechanics and, potentially, the identification of novel treatments and surgical interventions, which is a necessary step in the improvement of medical treatment of neonatal heart diseases [110].

2.8. Research aims and objectives

This research aimed to establish the material parameters that for the first time specifically describe neonatal ventricular myocardium. These material parameters will enable a simulation that more accurately reflects neonatal ventricular myocardium behaviour. This will ultimately create new opportunities for researchers, bioengineers and clinicians to identify novel treatments and interventions in cases of abnormal neonatal heart functionality. To achieve the aim of this research study, a complete set of microstructural and biomechanical data is needed for the estimation of the material parameters. Consequently, this research study systematically characterises the microstructure and biomechanical parameters of neonatal left and right ventricle 'free-walls' (LVFW and RVFW, respectively). Recognising the different physiological roles of the ventricles and, by comparison to the adult heart, the front and back walls, this study will investigate these four different regions (LVFW anterior and posterior; RVFW anterior and posterior). An experimental protocol was followed to systematically analyse the microstructure and biomechanical behaviour, using an accepted porcine animal model [30-37]. Two-dimensional Masson's trichrome staining histology was consolidated with three-dimensional TPEF/SHG microscopy to quantify the

cardiomyocytes and collagen fibrils structure and organisation. Three-dimensional diffusion tensor magnetic resonance imaging (DT-MRI) was used to assess the cardiomyocyte architecture of the intact heart, describing the directional coherence of cardiomyocytes orientation. Biomechanical analyses were then performed via uniaxial tensile, biaxial tensile and simple shear loading modes. Finally, these data were used with the structurally-based Holzapfel–Ogden (HO) model of the adult myocardium [38], to establish the material parameters that more accurately describe neonatal ventricular tissue behaviour. The following goals were identified to achieve these aims:

1. To understand the fundamental structural differences between neonatal and adult cardiac tissue by performing histological analysis on the anterior and posterior aspects of RVFW and LVFW. This enabled identification of the two-dimensional cardiomyocytes and collagen fibrils distribution. The cardiomyocytes preferred orientation and surface area ratio of collagen to myocyte fibres were also quantified.

2. To identify the in-plane and out-plane cardiomyocytes and collagen fibrils preferred orientation (°) and angular dispersion (°) through the ventricular walls (RVFW, LVFW). The anterior and posterior aspects of both ventricles were microscopically investigated using the TPEF/SHG imaging techniques.

3. To describe the macroscopic directional coherence of cardiomyocytes orientation in the intact neonatal porcine heart, three-dimensional diffusion tensor magnetic resonance imaging (DT-MRI) was performed. This indicated the macroscopic directional coherence

of the cardiomyocytes' orientations. The *regional* FA was also evaluated in the anterior aspect of LVFW and RVFW.

4. To describe the uniaxial preconditioning behaviour, biomechanical behaviour (stress vs. strain), hysteresis area (energy dissipation) and mean failure stresses of one-day-old porcine ventricles, a uniaxial tensile mechanical testing was performed in the MFD and CFD of both ventricles.

5. To describe the biaxial biomechanical behaviour (stress vs. stretch), hysteresis area (energy dissipation) and mean peak stresses of one-day-old porcine ventricles; biaxial tensile mechanical testing was performed in the MFD and CFD of both ventricles.

6. To describe the simple shear preconditioning behaviour, biomechanical behaviour (stress vs. strain), hysteresis area (energy dissipation) and mean peak shear stresses of one-day-old porcine ventricles, simple shear tests were performed on the anterior and posterior aspects of both ventricles in the MFD and CFD.

7. Finally, the microstructural and biomechanical data were used with the structurally-based HO model of the adult myocardium [38] to establish material parameters that more accurately describe neonatal ventricular tissue behaviour via computational simulations.

3.0. MATERIALS AND METHODS

In this chapter, an experimental protocol was followed to systematically characterise the microstructure and biomechanical behaviour of neonatal porcine ventricles [30-37], in obtaining a complete set of data for estimating the material parameters of the neonatal ventricular myocardium. Two-dimensional Masson's trichrome staining histology was consolidated with three-dimensional two-photon excited fluorescence and second-harmonic generation TPEF/SHG microscopy to quantify the cardiomyocytes' and collagen fibrils' structure and organisation. Three-dimensional diffusion tensor magnetic resonance imaging (DT-MRI) was used to assess the cardiomyocyte architecture of the intact heart, describing the directional coherence of the cardiomyocytes' orientation. Biomechanical analyses were then performed using uniaxial tensile, biaxial tensile and simple shear loading modes. Finally, these data were used with the structurally-based Holzapfel–Ogden (HO) model of adult myocardium [38] to establish the material parameters that specifically describe neonatal ventricular tissue behaviour. These material parameters will enable increased accuracy when performing computational simulations of neonatal porcine ventricular myocardium.

3.1. Materials

Ethical constraints and a lack of appropriate experimental facilities prevented this work from investigating human neonatal cardiac tissue. Such constraints are commonplace across the field of biomechanics—especially when opening a new research area, with donor animal models instead serving as a frequent source of tissue. In this instance, the neonatal pig has previously been used as the young animal model in the microstructural and biomechanical studies [70, 179]. Compared with the other young animal models that are commonly used in biomedical research, such as the canines, the neonatal porcine model has been identified to be the most like the new-born human infant [33]. The resemblances in cardiovascular, respiratory, renal and haematological systems have been highlighted in a previous study [173]. Moreover, the large litter size, two or three litters per sow/ per year and the relatively low cost of piglets make it an ideal animal model in defining human infants when performing biomedical research studies, as discussed in detail in Chapter 2 (Section 2.6) [173]. Hence, it was adopted as the model to be used through this study.

3.1.1. Heart dissection

All hearts were harvested from the one-day-old deceased Yorkshire piglets (mass: 2.1-2.4 kg, length: 0.38-0.51m), which were then used to perform microstructural and biomechanical analyses. The deceased piglets were acquired from local breeding farms. The piglets were most likely to have died from hypoxia, meaning that they were accidentally suffocated by the sow soon after birth. The piglets were collected within the hours of their natural death and transported to the laboratory at 4^{o}C. An image of a deceased pig is provided to enable an appreciation of the gross anatomy in Figure 3.1.

Scalpel dissection (size 10 blade) was initially performed to remove the skin from the thorax-region. A scalpel size 15 blade was then used to make an incision through the rib-cage. The protective membrane of the pericardium was dissected using a scalpel size 10 blade (Figure 3.2). A pipette was used to remove the excess blood from the heart. The connective pulmonary veins and arteries were isolated from the heart, using surgical scissors. The aorta was then dissected from the heart, also using surgical scissors. The heart was then promptly harvested and stored in Ringer's solution (Oxoid; Thermo Scientific, UK) at 4°C, to minimise any shrinkage in the tissue.

***Figure 3.1**: One-day-old deceased Yorkshire piglet.*

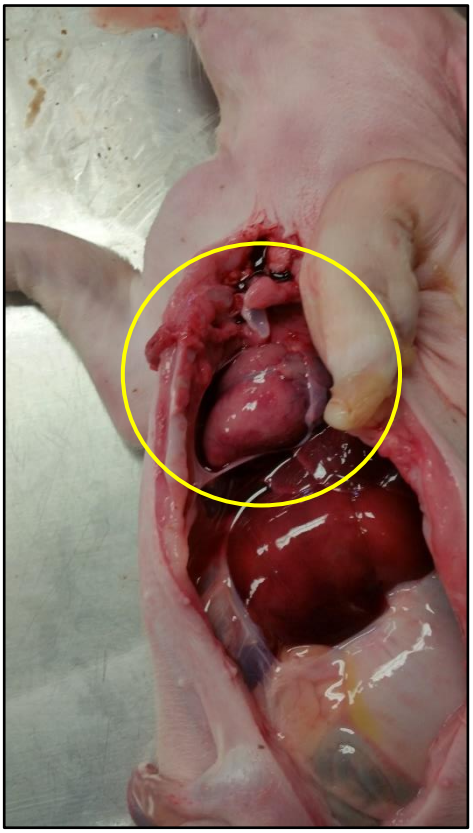

***Figure 3.2**: The chest is cut open through an incision in the thorax-region, to harvest the heart.*

3.1.2. Microstructural analyses

Microstructural analyses were performed using three imaging modalities:

- Two-dimensional histology, which was used to describe the cardiomyocytes preferred orientation (although only limited) and surface area ratio of collagen to cardiomyocyte fibres, within the anterior and posterior aspects of LVFW and RVFW.

- Three-dimensional TPEF/SHG, which quantified both in-plane and out-plane preferred orientation and angular dispersion of the cardiomyocytes and collagen fibrils, within the anterior and posterior aspects of LVFW and RVFW.

- Three-dimensional DT-MRI, which was used to identify the helical cardiomyocyte architecture of the intact heart, seeking correlation between the microstructure and biomechanical behaviour, and to describe the directional coherence of cardiomyocyte orientation [70, 71].

The anterior and posterior aspects of the LVFW and RVFW were identified based on the local laminar architecture and morphology of the myocardium (Figure 3.3). The FSN-coordinate system was then identified as follows [2, 39, 113]:

The fibre axis (F), which is defined as the mean-fibre direction as observed by the external surface texture;

The sheet axis (S), which is defined as the direction transverse to the fibre axis within the layer; and

The sheet-normal axis (N), which is defined as the direction perpendicular to both the fibres and layers.

In this study, the fibre axis (F) is described as the 'mean-fibre direction' (MFD), and sheet-normal axis (N) is defined as the 'cross-fibre direction' (CFD) [52] (Figures 3.4 and 3.5). These reference axes were used to accurately identify the sample orientation, and a suture was placed to mark the orientation during dissection of myocardial tissue in performing all the analyses.

3.1.2.1. Histological sample preparation

Evans blue dye was used to label the heart equator and to demarcate the anterior and posterior aspects of LVFW and RVFW, as shown in Figure 3.3. A reference axis was then defined as that passing through the apex and base, with the edge of a square cutter kept parallel to this axis when dissecting the tissue samples (2 x 2 mm). Eight hearts were used for histological analysis (Figure 3.4). Thirty-two cubic samples (2 × 2 × 2 mm) were dissected using a square-shaped cutter from the equatorial regions of the anterior and posterior aspects of LVFW and RVFW (Figure 3.4). A pre-defined coordinate system was used to ensure consistent orientation of the cutter throughout the histological specimen preparations. Hence, the cutter was always aligned with the vertical axis of the heart, which is defined as passing through the apex and base. All samples were immersed in Ringer's solution throughout to minimise tissue shrinkage.

3.1.2.2. TPEF/SHG sample preparation

Evans blue dye was used to label the heart equator and to demarcate the anterior and posterior aspects of LVFW and RVFW, as shown in the Figure 3.3. Ten hearts were used for TPEF/SHG analysis (Figure 3.4). Samples (2 × 2 mm) were dissected using a square-shaped cutter from the equatorial regions of the anterior and posterior aspects of LVFW and RVFW (Figure3.4). A reference axis was then defined as that passing through the apex and base, with the edge of a square cutter kept parallel to this axis when dissecting tissue samples (2 x 2 mm). The first five hearts were used to dissect the tissue samples through the thickness of the ventricle walls, with five collected from around the equator in the anterior and posterior aspects of the LVFW and RVFW, as described in Figure 3.4. These 20 samples were used for in-plane (x, y) TPEF/SHG analysis. A further 20 samples were collected from an additional five hearts using an identical technique, for out-plane (x, z) analysis. A pre-defined coordinate system was used to ensure consistent orientation of the cutter throughout the TPEF/SHG specimen preparations. Hence, the cutter was always aligned with the vertical axis of the heart, which is defined as passing through the apex and base. All of the samples were immersed in Ringer's solution throughout to minimise tissue shrinkage.

3.1.2.3. DT-MRI sample preparation

The hearts were used in their as-dissected state for DT-MRI imaging.

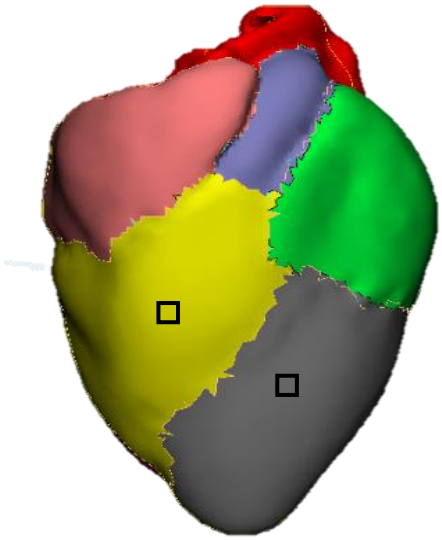

(a) Anterior–view

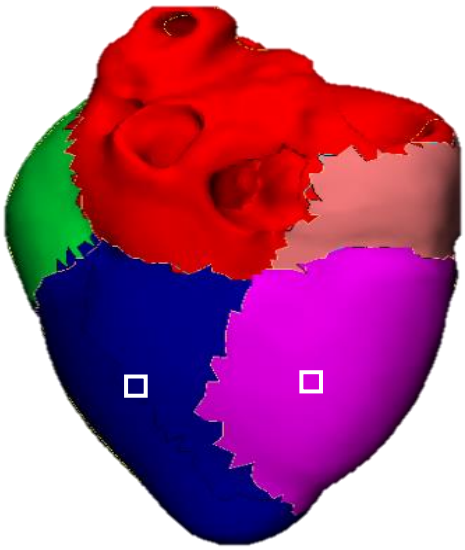

(b) Posterior–view

Figure 3.3*: A three-dimensional schematic model of the neonatal porcine heart.* ***(a)*** *Anterior view: LVFW = Grey region, RVFW = Yellow region, Left atrium = Green region, Right atrium = Maroon region.* ***(b)*** *Posterior view: LVFW = blue region, RVFW = pink region Left atrium = Green region, Right atrium = Maroon region. Squares representing the equatorial region of the LVFW and RVFW anteriorly and posteriorly. The left and right atria (green and maroon regions) are not relevant to this study.*

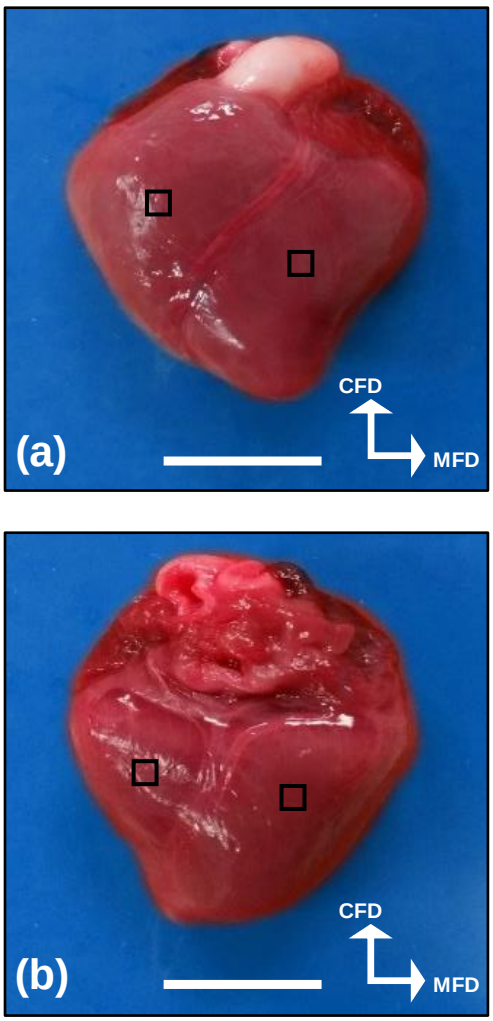

***Figure 3.4**: Samples (2 x 2 mm) were dissected from the (a) anterior and (b) posterior wall of LVFW and RVFW to perform histological and TPEF/SHG analyses. Scale bar = 12 mm.*

3.1.3. Biomechanical analyses

The heart undergoes a complex pattern of deformations such as tension, compression, and shearing during the cardiac cycle. Therefore, in this study, the directional anisotropy of the LVFW and RVFW tissue was investigated at different deformation states, using three independent protocols. This study would provide the baseline data that describes the biomechanical behaviour from four regions of the neonatal heart. All biomechanical tests were completed within 12h of donor piglet birth to produce data from fresh tissue. Common protocols were followed to ensure that the tissues remained hydrated.

3.1.3.1. Sample preparation of biomechanical testing of neonatal porcine ventricles

Uniaxial tensile test

Uniaxial tensile testing samples were dissected from 20 hearts. The 10 randomly selected hearts had samples of dimensions 20mm (l) x 10mm (w) x 3mm (t) dissected, with the longest dimension aligned to the MFD. Meanwhile, the MFD was judged based on the external surface texture and observed fibre direction. The remaining 10 hearts were used to harvest samples in the CFD, which is broadly perpendicular to the MFD and was again defined by external tissue features (Figures 3.5 (a), (b) and (c)). This method is inherently subjective, although was performed in a manner consistent with previous studies [52, 113]. All 20 samples were then trimmed using a cutting punch, achieving a traditional dog-bone shape and a 5mm minimum width.

Biaxial tensile test

For biaxial extension analysis, five samples (15 x 15 x 3mm) were dissected using a square-shaped cutting punch from the LVFW, and a further five hearts used for RVFW samples (Figures 3.5 (d) and (e)). Each sample was dissected such that the presumed MFD and CFD were consistent with the x- and y-axes of the cutter.

Simple shear test

A similar approach although with a smaller cutter (3 x 3 mm) was adopted to dissect tissue for shear analysis. These tissues were collected from the anterior and posterior aspects of the LVFW and RVFW, and they were dissected from the equatorial regions of five hearts (Figures 3.5 (f) and (g)).

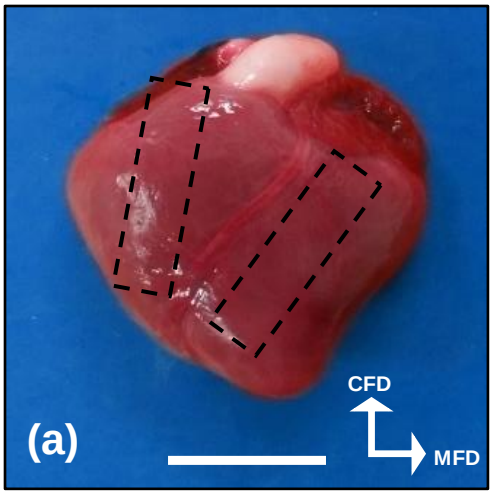
CFD
MFD
(a)

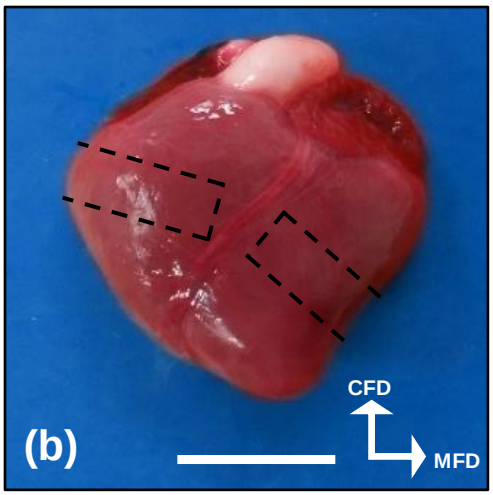
CFD
MFD
(b)

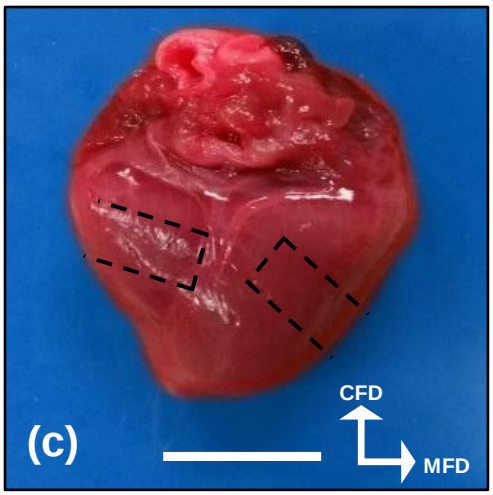
CFD
MFD
(c)

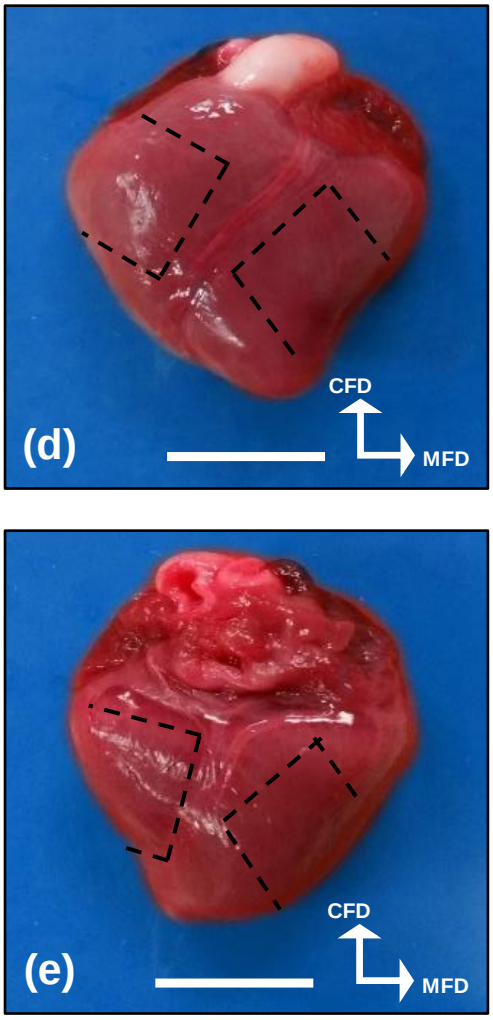
(d)
CFD
MFD
(e)
CFD
MFD

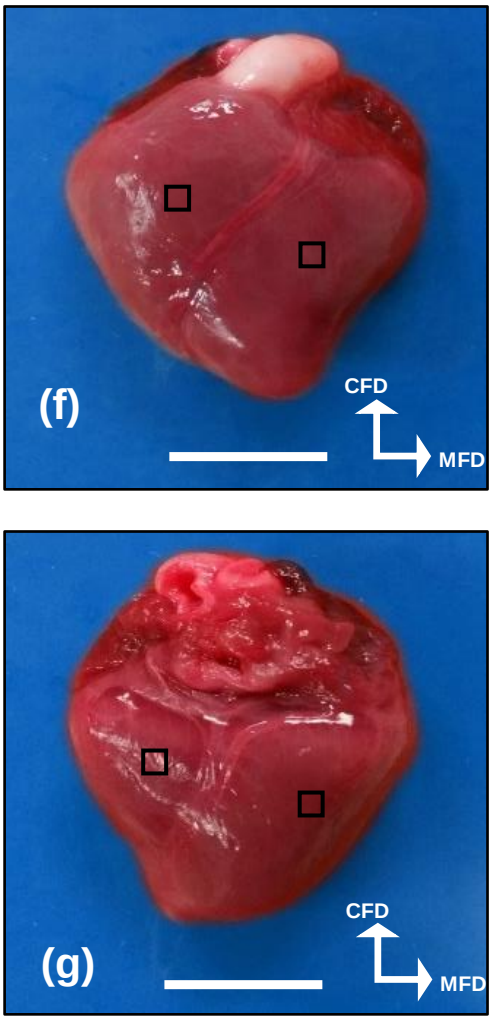

***Figure 3.5**: Schematic representation of the samples harvested from the neonatal porcine heart. Samples were dissected aligned to the MFD and CFD, determined by observing the external features of the organ. **(a)** Uniaxial CFD samples are dissected from the anterior aspect of the LVFW and RVFW. **(b)** and **(c)** Uniaxial MFD samples extend from the anterior to posterior aspect of the LVFW and RVFW. **(d)** and **(e)** Biaxial (square) samples extended from the anterior to posterior aspects of the LVFW and RVFW. **(f)** and **(g)** Simple shear samples were dissected from the equatorial region of both the anterior and posterior aspects of the LVFW and RVFW. Scale bar = 12 mm.*

3.2. Experimental methods

3.2.1. Microstructural analyses

3.2.1.1. Histological analysis

Staining

The histological sectioning and staining was performed by a third-party company Histoserv, Inc., during a research sabbatical at Mississippi State University. They followed a standard protocol, where all samples were fixed in 4% paraformaldehyde for 48h and then in 70% glutaraldehyde. The samples were then processed through a standard histological preparation protocol, including being dehydrated in graded alcohol, cleared with xylene and then embedded within paraffin wax. The block was then processed in a plane perpendicular to the transmural direction (i.e. epicardium towards endocardium). A standard Masson's trichrome staining protocol was then performed, with the samples finally mounted with Permount. The Masson's trichrome stain identified muscle fibres in red and collagen fibres light blue.

Experimental microscope setup and image acquisition settings

The histological slides were then returned from the third-party for analysis. The anterior and posterior aspects of both ventricles were viewed at ×20 and x40 magnification using a biological microscope (Nikon YS100, Japan), which was fitted with a camera to enable digital capturing of the images. The optimal focus settings were adjusted at each viewing level to enhance the image quality. Two optical powers were used to provide a better understanding of the cardiomyocytes' and collagen fibrils' interaction.

Data analysis

Fiji/Image J (NIH, USA) software was used to evaluate the preferred fibre orientation of the myocyte fibres. In-plane (x, y) images were pre-processed in two dimensions using selected computational filters (unsharp mask, Gaussian blur 3D and Kuwahara). The images were then analysed using the Fourier components method [180]. This method is based on Fourier spectrum analysis. For a square image, structures with a preferred orientation generate a periodic pattern at +90º orientation in the Fourier transform of the image when compared to the direction of the objects in the input image [180]. This approach enabled quantification of fibre distribution. Using the ImageJ plugin 'Directionality', data from all images were then used to generate a histogram. This enabled identification of the 'preferred' fibre orientation direction (i.e. the histogram peak). This plugin is used to infer the preferred orientation of the structures that are present in the input image. It computes a histogram that indicates the amount of structures in a given direction. Images with completely isotropic content are expected to give a flat histogram, whereas images in which there is a preferred orientation generate a histogram peak at that orientation. This peak was then fitted by a Gaussian function, this method is consistent with other studies [181-185]. The output included: (1) the preferred fibre orientation direction (°), as defined by the centre of the Gaussian distribution; (2) the angular dispersion (°), as defined as the standard deviation (std) of the Gaussian distribution; (3) the amount parameter, as defined as the sum of the histogram from minus 1 std to plus 1 std, divided by the total sum of the histogram; and (4) goodness of fit (R^2). Fiji/Image J (NIH, USA) software was adopted to quantify the surface area ratio of collagen to myocyte fibres, using image thresholding based on RGB (red, green and blue) values [72].

3.2.1.2. TPEF/SHG analysis

Experimental microscope setup and image acquisition settings

TPEF/SHG images were acquired by non-linear microscopy (NLM) using a laser scanning microscope (LSM880 NLO, Carl Zeiss, Ltd. Cambridge, UK) equipped with an ultrafast-pulsed near-infrared (NIR) TiS laser illumination system (Chameleon Vision II, Coherent Lasers, Cambridge, UK). Laser excitation at 900nm and approximately 140fs pulse width were used for all NLM imaging, which was passed to the specimen and separated from returning emissions by a 690nm short-pass primary dichroic reflector.

All NLM imaging was carried out with a 'dipping' water immersion objective lens, which is designed for use without a cover glass (W Plan-Apochromat 20x/1.0NA, Carl Zeiss). Backwards propagating TPEF and SHG light from the specimen was collected by the objective and detected in the reflected light (epi-) pathway of the microscope, using the internal spectrometer to select the desired wavelengths. SHG (at half the excitation wavelength) was detected at 450+/-10nm and TPEF at all wavelengths longer than 470nm.

Two channel (TPEF and SHG) 8-bit images were acquired simultaneously at serial focal positions to build up a 3D (volume) stack of optical section images. These comprised the in-plane (x,y) and out-plane (x,z) total volumes of 425 µm x 425 µm x 202µm and 425 µm x 425 µm x 1022 µm, collected at 1.52µs intervals. Each line of every 2D optical section was scanned 8 times and the average signal recorded. Heart tissue scatters laser light significantly (even at NIR wavelengths), so the illumination power available for image generation is much

reduced deeper in the tissue than at the surface and TPEF and SHG signals are attenuated even more as they pass out of the tissue. To partially compensate for these effects, the laser power was increased automatically, according to a pre-set pattern for each specimen, as the optical section series progressed deeper into the tissue. Tissue samples were fixed into a plastic petri dish using medical glue and immersed in the medium (Ringers solution–Oxoid; Thermo Scientific, UK) into which the objective lens was dipped for NLM imaging.

The backward SHG signal that is generated by the cardiac tissue arose from both collagen and myosin, at the same wavelength; however, the different localization within the myocardial tissue enabled discrimination between the two signals. The backward SHG generated by myosin required higher laser intensity at 900nm than the collagen. Moreover, the myosin-SHG signal can be neglected within the power range 10 to 20 mW because it contributed to less than 5% of the total while retaining the good signal quality and noise ratio for the collagen-SHG collection. Hence, all of the NLM imaging on cardiac tissue were performed at 10–12 mW, which in turn also limits the induction of photodamage.

The SHG-collagen directionality is highly dependent on the ionic strength of the medium solution, in which the objective lens dipped for NLM imaging [63]. Preliminary studies were performed using different concentrations of sodium chloride (NaCl) to indicate the optimum medium (Ringers solution–Oxoid; Thermo Scientific, UK) and maximise the backward SHG collection on myocardial tissue. Analysis indicated that the four-quarter strength ringers solutions would provide the maximum backward SHG signal collection for the myocardial tissue. Hence, four ¼ strength ringers solution tablets were used to make 500 ml of four-quarter strength ringers solutions, which in turn gave the maximum backward SHG collection

for the myocardial tissue. Thus, the medium-ionic strength was optimised to enhance the NLM imaging signal collection.

The SHG signal intensity has been reported to be the dependent on the angle between the collagen fibrils and the polarization of incident light [63]. Therefore, preliminary studies were performed to identify the optimal imaging conditions and to evaluate the effect of the polarization angle by rotating the microscope stage in 10-degree steps and in an increment of 1-degree stepper time. The variations in the SHG intensity at different polarization angles were found to be consistent with those found in previous studies [63, 90, 186]. In this study, the directional effects of polarization were determined to define the finest experimental conditions to increase the strength and quality of the Backward SHG signal. For consistency, all of the myocardial specimens were imaged in the same orientation under the microscope.

The intensity of the backward SHG signal is limited by penetration depth. Bulk optical properties such as the absorption coefficient, scattering, refractive index are among the key parameters in determining the optimal depth of the material. In this study, the excitation light at the range of 450+/-10nm wavelengths was used, which limits the penetration depth of 200 µm (in-plane) and 1022 µm (out-plane) for the cardiac tissue specimens. A rapid decay in the backward SHG light was observed within the first 100 µm for the cardiac tissue specimens. It has previously been reported that the clearing agents and the adaptive optics could be used to improve the penetration depth [63]. Therefore, a 50% glycerol treatment was applied to all of the cardiac tissue samples prior to imaging to increase the maximum penetration depth of 200 µm (in-plane) and 1022 µm (out-plane), respectively. As an added precaution, cardiac tissue

specimens were prepared with a consistent thickness to improve our quantitative analysis, which would impose similar scattering and attenuation effects on all of the samples.

Data analysis

This process is the same as that described in Section 3.2.1.1, with the exception of the three-dimensional analysis. In-plane (x, y) and out-plane (x, z) image-stacks were pre-processed in three dimensions using selected computational filters (unsharp mask, Gaussian blur 3D and Kuwahara). These 'image-stacks' were then analysed using the Fourier components analysis method, as described in detail in Section 3.2.1.1 [180]. The output included: (1) the preferred fibre orientation direction (°), as defined by the centre of the Gaussian distribution; (2) the angular dispersion (°), as defined as the standard deviation (std) of the Gaussian distribution; (3) the amount parameter, as defined as the sum of the histogram from minus 1 std to plus 1 std, divided by the total sum of the histogram; and (4) goodness of fit (R^2).

3.3.1.3. DT-MRI analysis

DT-MRI imaging protocols

Diffusion-weighted images were acquired with a Bruker MRI scanner, 9.4 Tesla small bore MRI and magnetic resonance spectroscopy (MRS) system. Custom-built loop-gap coils (1 ~ 5 cm diameter) were used to constrain the neonatal porcine heart, which was then placed in conical centrifuge plastic tubes. The conical centrifuge plastic tubes were filled with Ringer's solution (Oxoid; Thermo Scientific, UK) to prevent any shrinkage in the tissue during the scans. A data volume of 96 x 96 x 36 mm was acquired with a voxel size of 1.17 x 1.17 x 2.6 mm. The GE diffusion tensor imaging protocol was used with two b values (0, 1000) and 55

gradient directions. The following imaging parameters were also used: repetition time, 2 s; echo time, 34 ms; diffusion gradient strength, 10 Gauss/cm; diffusion time, 20 ms; gradient pulse duration, 5 ms; gradient factor, 784 s/mm^2; slice thickness, 1 mm; and in-plane resolution, 156 × 156 μm^2 f. The total acquisition time for each heart was _2 h. This method is consistent with a previous study that described the structure of neonatal and adult porcine heart [70].

Data analysis

Fibre tractography and fractional anisotropy

The 3D Slicer software plugin 'SlicerDMRI' was used to perform unscented Kalman filter (UKF) tractography and scalar measurements. Diffusion-weighted images (DWI) were used to calculate the diffusion tensor. The diffusion tensor D in each voxel was visualised as a diffusion ellipsoid. The eigenvectors were used to specify the directions of the principal axes and the ellipsoidal proportional to the square root of the eigenvalues. The size and shape of the diffusion tensor were described by rotationally invariant eigenvalues λ_1, λ_2, λ_3. Diffusion tensor imaging (DTI) was used to evaluate the trace (D) and fractional anisotropy (FA). Trace and FA are scaler measures that are intrinsic to tissue and which are independent of fibre orientation, and diffusion sensitizing gradient directions. Trace was used to calculate the size of the tensor, whereas fractional anisotropy characterised the shape (degree of 'out of roundness') of the diffusion ellipsoid, ranging from 0 (low FA) to 1 (high FA). FA is a quantitative measure of water diffusion anisotropy that is used to describe the directional coherence of cardiomyocytes orientation for the neonatal porcine heart. The Tractography Interactive seeding module was then used on the FA map to track the cardiomyocytes.

Undesirable tracks were removed to obtain the required heart profile, as demonstrated in Figure 3.6. This method is consistent with that described in detail in a previous study [101]. The 'SlicerDMRI' plugin was also used to select the fibre bundles in each region, which were used to label the map and quantifying the regional-specific FA, within the anterior aspect of both ventricles (Figure 3.7).

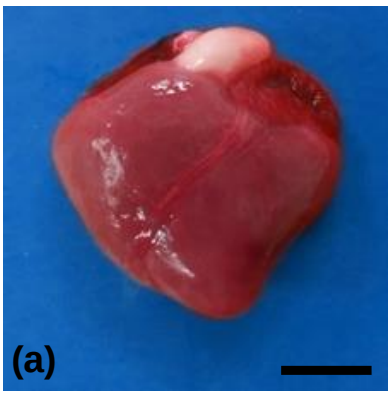
(a)

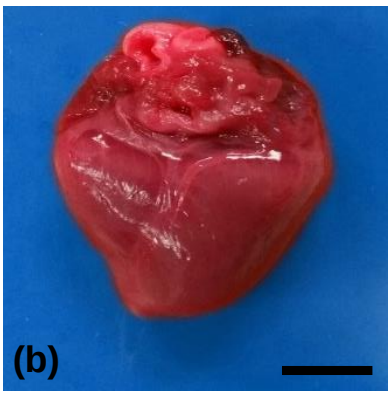
(b)

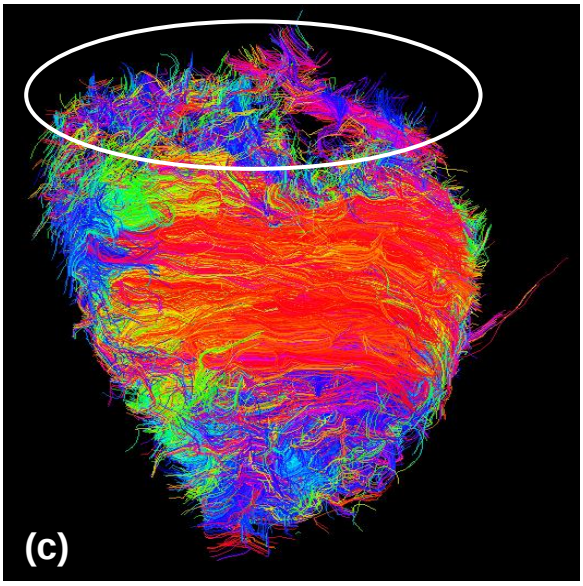
(c)

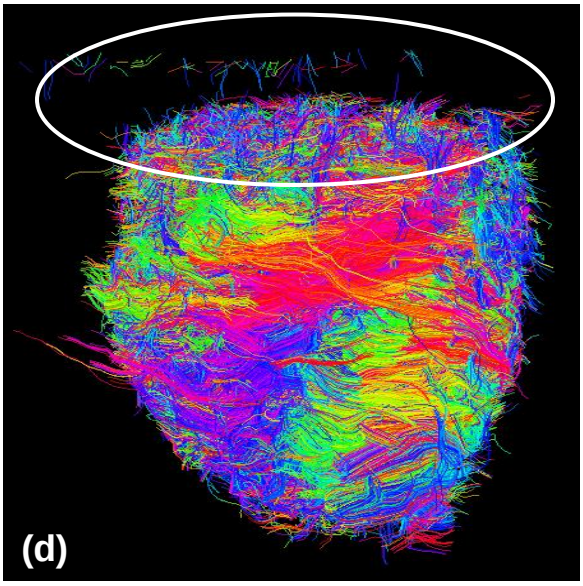
(d)

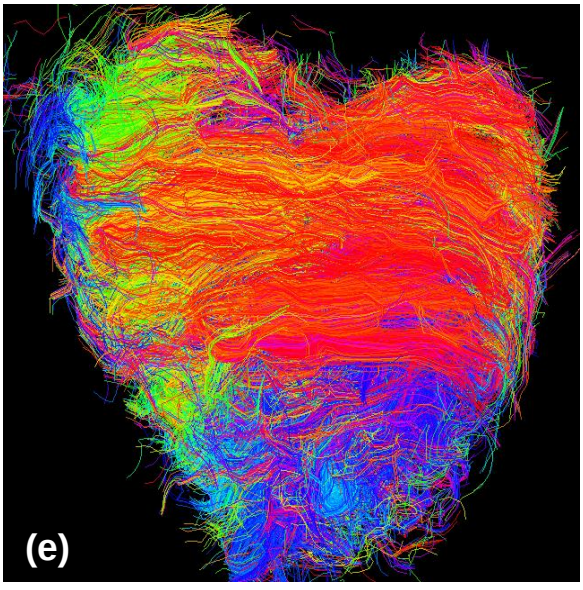
(e)

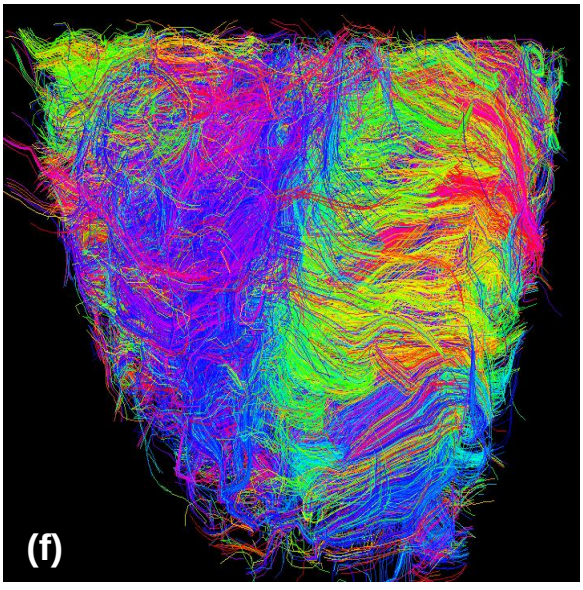
(f)

***Figure 3.6**: The anterior **(a)** and posterior **(b)** aspects of the neonatal porcine heart. The helical cardiomyocyte architecture of neonatal porcine heart before being processed; anterior view **(c)** and posterior view **(d)**. The cardiomyocyte architecture of neonatal porcine heart after being processed; anterior view **(e)** and posterior view **(f)**. Fibre bundles were coloured to enable visualisation of the mean fibre orientation on the anterior **(e)** and posterior **(f)** aspects of both ventricles. Scale bar = 8 mm.*

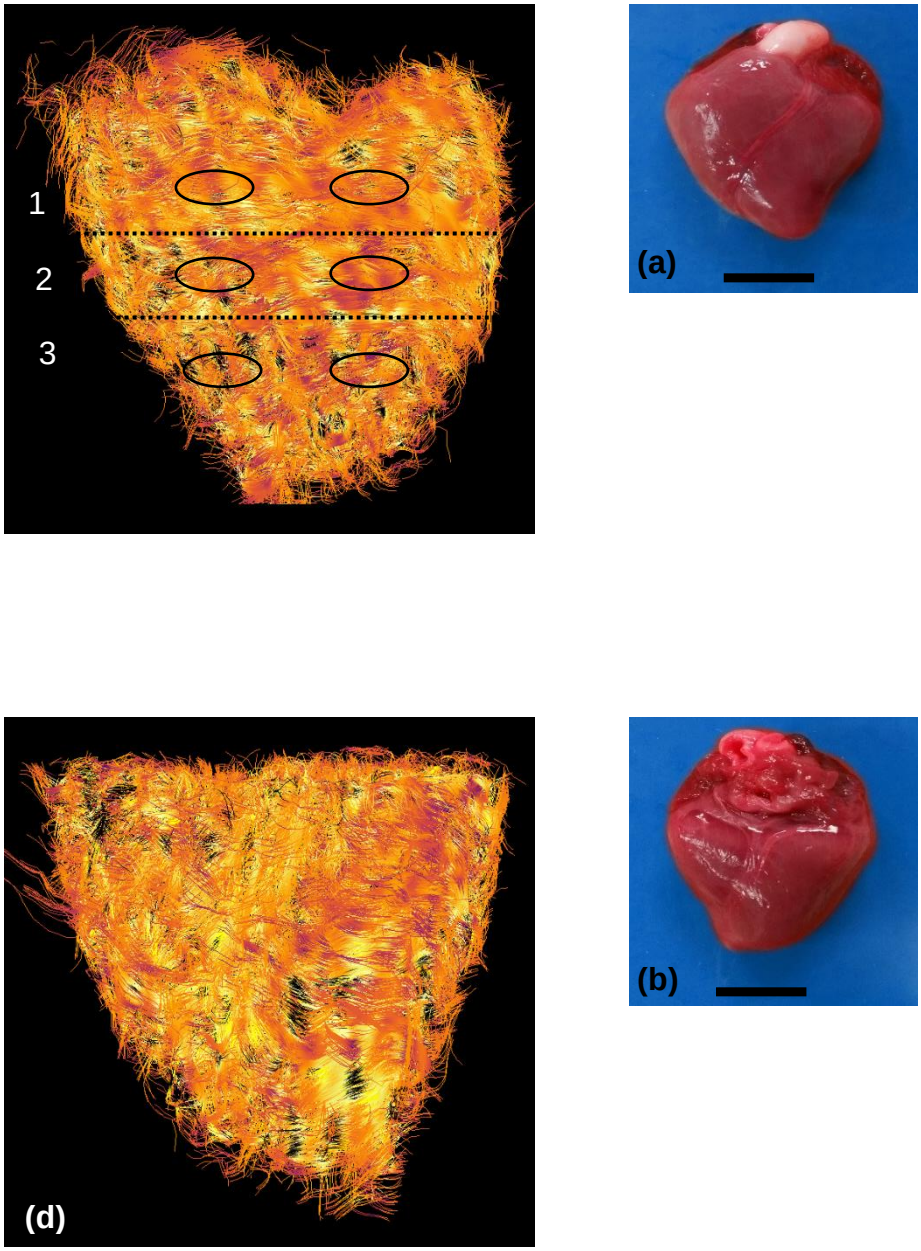

***Figure 3.7**: The anterior (a) and posterior (b) aspects of neonatal porcine heart. The cardiomyocyte architecture of neonatal porcine heart after being processed; anterior view (c) and posterior view (d). Anterior view identifying the regions of interest used to calculate the FA for the base (1), equator (2) and apex (3) of the right and left ventricles (c). Scale bar = 8 mm.*

Statistical analysis

All of the values were reported as mean ± standard deviation (SD), where statistical significance given to values less than 0.05. One-way analysis of variances (ANOVA) was performed along with Tukey HSD post hoc test to quantify the statistical significance of the anterior and posterior aspects of both ventricles. All of the statistical analyses were conducted in SPSS 20.0.

3.2.2. Biomechanical testing

3.2.2.1. Uniaxial extension test

Experimental setup
Pilot study: defining the experimental procedures in uniaxial testing

An initial study was important to determine the optimal conditions to successfully perform uniaxial tensile testing, particularly in respect to clamping. This pilot study evaluated the optimum technique to clamp the myocardial tissue to avoid any slipping near the clamping of the samples, which is the common phenomenon during the biomechanical tests of soft biological tissues. Initial/pilot data demonstrated slipping when the tissue samples were clamped directly into the stainless steel grips of a uniaxial testing machine (Mach-1; Biosyntech, MN) (Figures 3.8–3.11); hence, both ends of the dog-bone-shaped samples were then wrapped in emery paper.

Uniaxial testing

Sample preparation is described above, with each having dimensions of approximately 15mm (l) x 5mm (w) x 3mm (t), and with five measurements taken with digital callipers. The testing method that was adopted is consistent with the previous uniaxial studies on biological tissue [187, 188]. Each sample was preconditioned with 10 cycles at 10% strain, accounting for the viscoelastic behaviour of the myocardial tissue, before being loaded to failure at 1.5 mm s^{-1} ramp speed. This rate was used as it represented 10% of the specimen's gauge length. Engineering stress was computed by normalising the applied force to the initial cross-sectional area and engineering strain was calculated by normalising the displacement to the initial gauge length. It was observed that the results were influenced by pre-loading. Therefore, for reproducibility of results, 0.05N was applied as a preload to each myocardial sample [52]. Mean peak stress, which describes the stress of failure, was then calculated from these data for the MFD and CFD samples. The last preconditioning cycle was used to quantify the myocardial hysteresis (to account for energy dissipation due to the viscoelastic behaviour) by dividing the area enclosed by the loading and unloading curves (energy dissipation) by the area beneath the loading curve (energy input) as demonstrated in Figures 4.21 (a) & (b).

Data analysis

Engineering stresses in MFD (σ_{11}) and CFD (σ_{22}) are calculated as the ratio of the applied force and the initial cross-sectional area. Strains in the MFD (ε_1) and CFD (ε_2) are computed as the ratio of the displacement and the initial gauge length.

$$\sigma_{11} = \frac{f_1}{A_1}, \qquad \sigma_{22} = \frac{f_2}{A_2}, \qquad \text{(Eqn 3.1)}$$

$$\varepsilon_1 = \frac{x_1}{X_1}, \qquad \varepsilon_2 = \frac{x_2}{X_2},$$

where (x_1, x_2) are the displacements; (X_1 , X_2) are the initial gauge lengths.

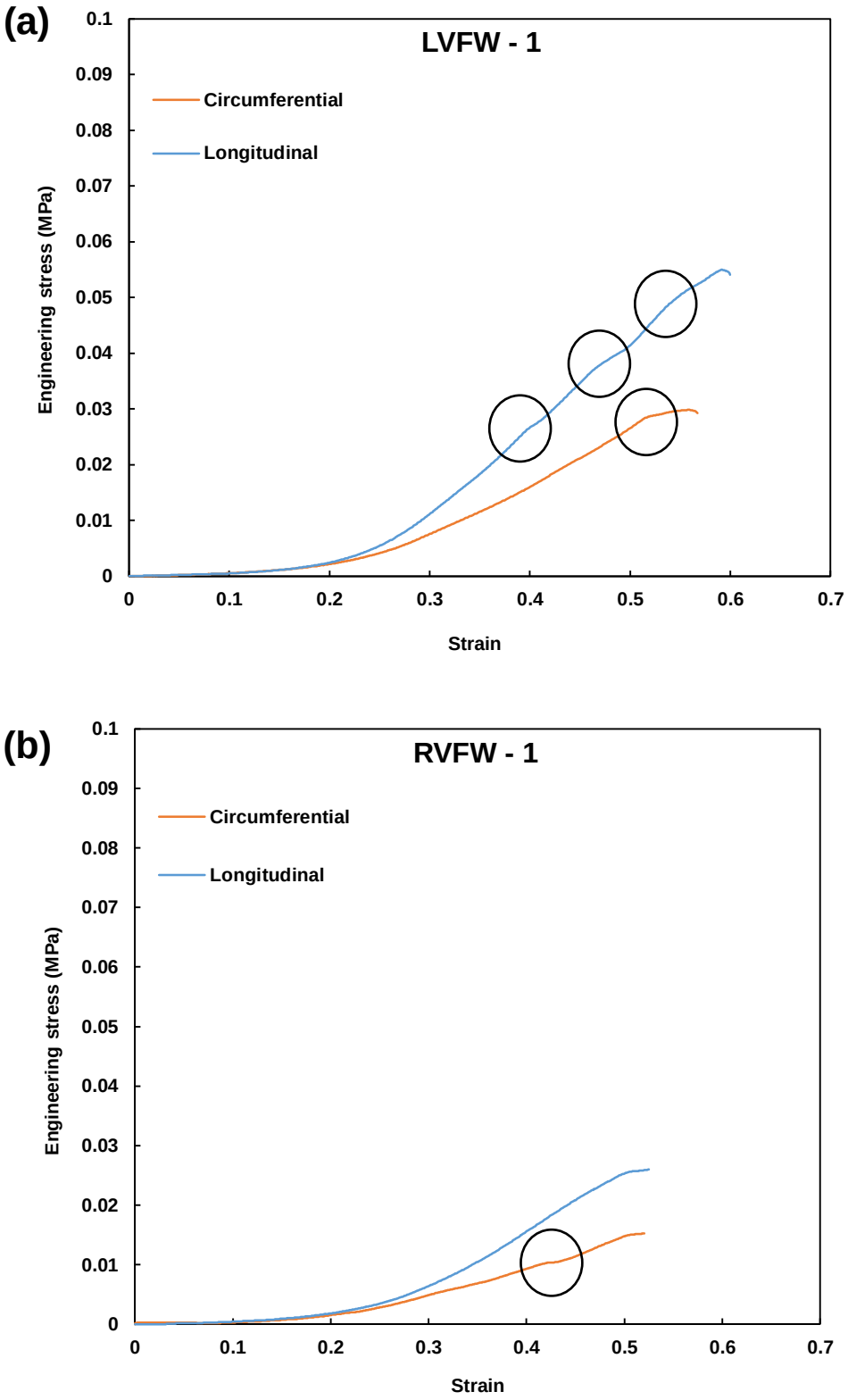

***Figure 3.8**: Representing passive 'uniaxial behaviour' of LVFW until failure (a) demonstrating passive 'uniaxial behaviour' of RVFW until failure (b). The slipping of myocardial tissue through the clamps is highlighted using the circle symbol.*

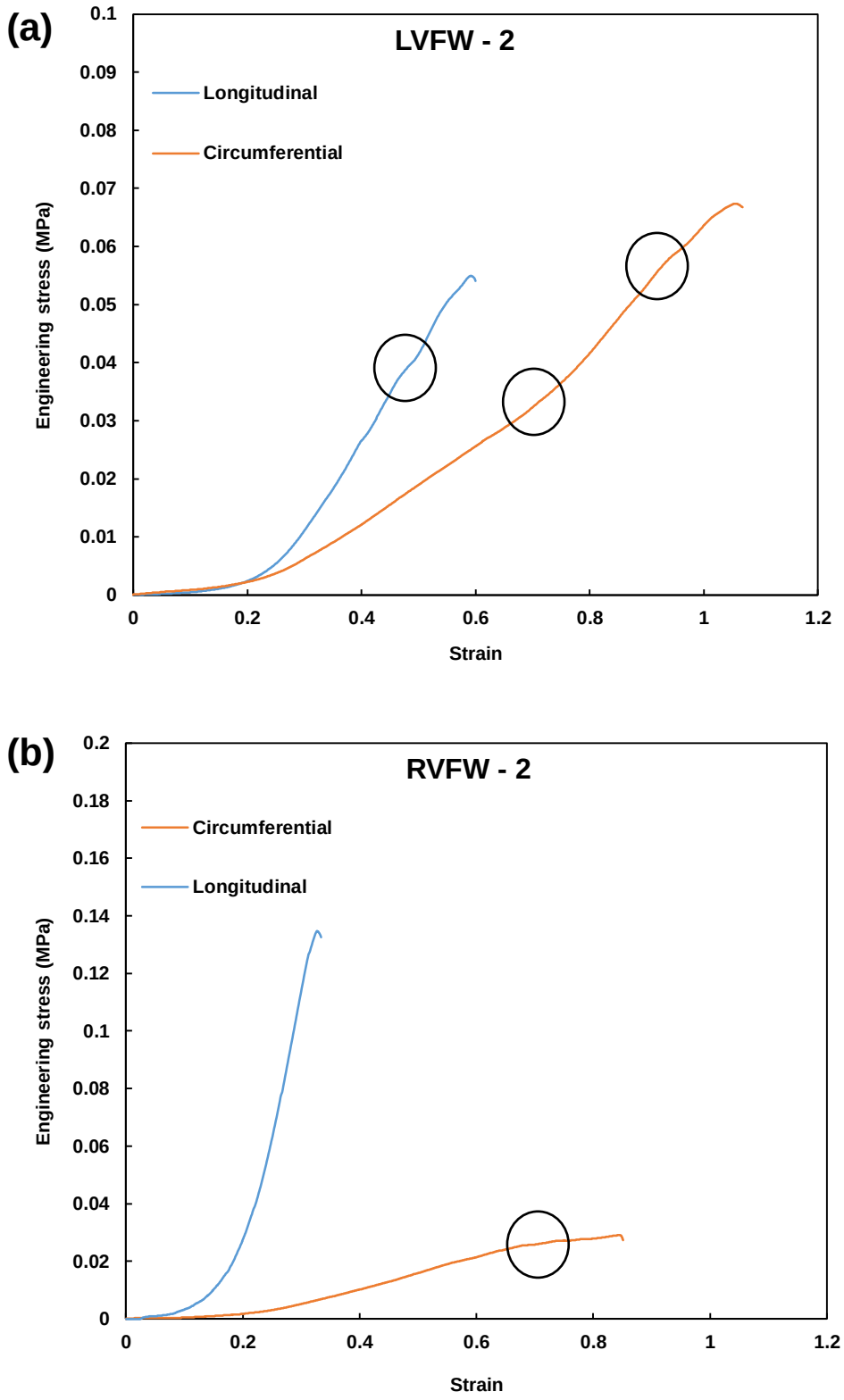

***Figure 3.9**: Representing passive 'uniaxial behaviour' of LVFW until failure (a); demonstrating passive 'uniaxial behaviour' of RVFW until failure (b). The slipping of myocardial tissue through the clamps is highlighted using the circle symbol.*

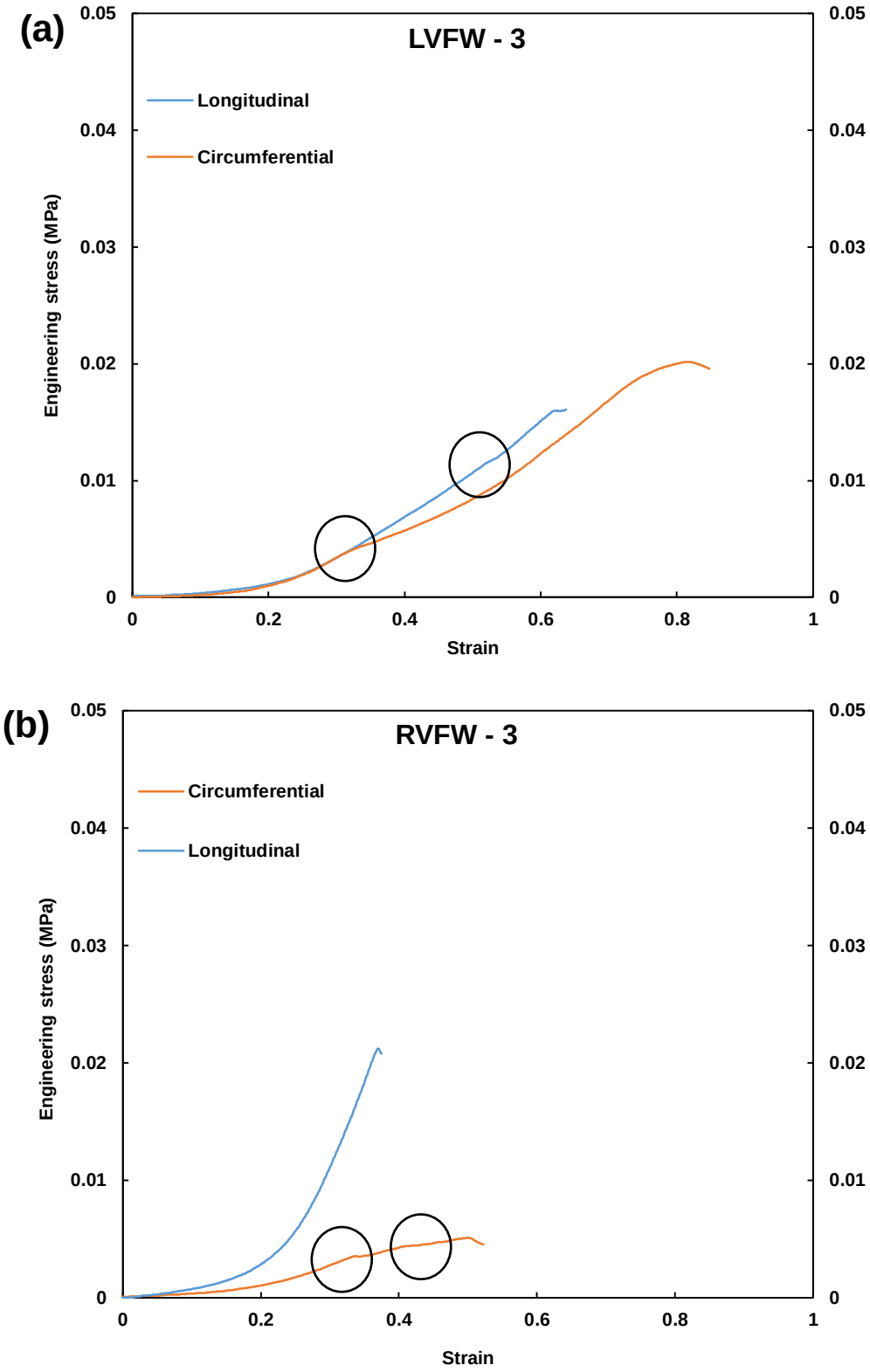

***Figure 3.10**: Representing passive 'uniaxial behaviour' of LVFW until failure (a); demonstrating passive 'uniaxial behaviour' of RVFW until failure (b). The slipping of myocardial tissue through the clamps is highlighted using the circle symbol.*

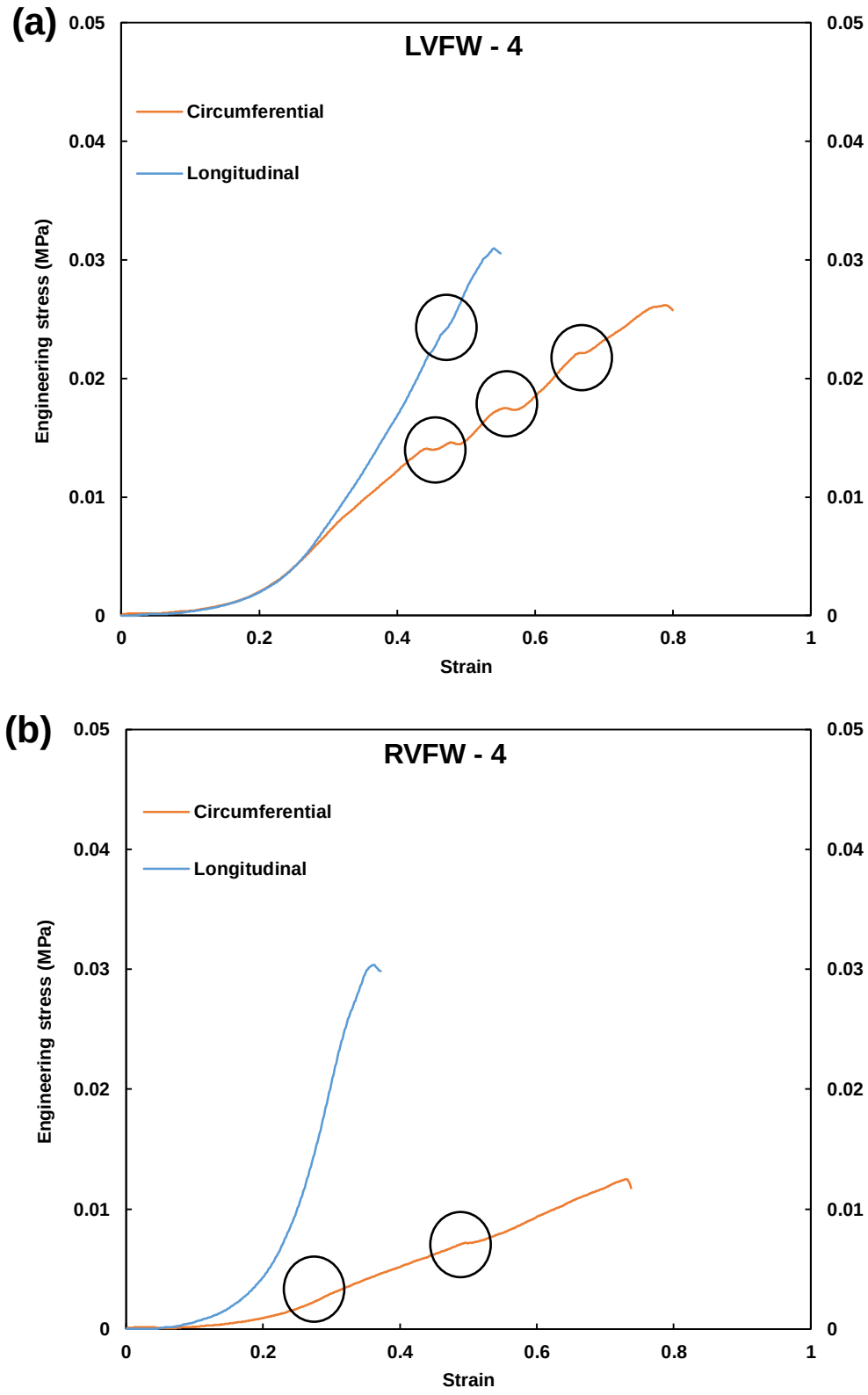

***Figure 3.11**: Representing passive 'uniaxial behaviour' of LVFW until failure (a); demonstrating passive 'uniaxial behaviour' of RVFW until failure (b). The slipping of myocardial tissue through the clamps is highlighted using the circle symbol.*

3.2.2.2. Biaxial extension test

Experimental setup
Pilot study: defining the experimental procedures in biaxial testing

A pilot study was performed to define the experimental parameters for the biaxial testing. Commercially available adult porcine myocardial tissue was used for this study. A video extensometer was used to precisely determine the high deformation measurements of the tissue. Four markers were placed towards the centre of the specimen using microporous tape. Tests were conducted at a strain rate of 0.5 mms^{-1} with the applied forces measured from the load cells. An initial study was important to determine the optimal conditions to successfully perform biaxial tensile testing, particularly in respect to clamping. This pilot study evaluated the optimum technique to clamp the myocardial tissue. In addition, the peak tension ratio was identified to perform all of the tests to avoid any rupture near the clamping area of the samples, which is the common phenomenon during the biomechanical tests of soft biological tissues. Different clamping techniques have previously been used, mainly using clips and surgical sutures [104-106, 114, 135]. Both clamping systems were used to identify the optimum method for mounting the myocardial tissue. Experiments were performed in different configurations using clips and surgical sutures. The biaxial mechanical properties were investigated using a custom-built biaxial testing system, consisting of four stepper motors, two load cells and a physiological saline bath; as described in detail elsewhere (Figure 3.12) [189, 190]. Tissue deformation was measured via a charge-coupled device camera (National Instrument, IMAQ CCD, Austin, TX), which tracked the relative position of four reference points placed in a 2 × 2 array. In-house Labview code (National Instrument, Version 6, Austin, TX) was used to control the stepper motors, and to record the applied forces and tissue strain. Although tissue slipping was observed in the clips during the biaxial tests, the myocardial tissue was uniformly deformed and high-quality results were obtained

using surgical sutures; as demonstrated in Figures 3.13 and 3.14. Hence surgical sutures are adopted hereafter to mount the myocardial tissue during the biaxial tests.

Neonatal porcine myocardial tissue

The square samples that had been dissected with the observed MFD and CFD aligned with the x- and y-axes were then mounted onto the machine using surgical sutures, as described in Section 3.1.3.3. Five thickness measurements were collected at different locations using a digital calliper to determine an average dimension. The samples were then immersed in 37ºC phosphate buffered saline (PBS). A preload of 0.05N was applied to each myocardial sample to ensure the reproducibility of results [52]. A total of 10 preconditioning cycles were performed, accounting for the viscoelastic behaviour of the myocardial tissue, before the stress-stretch data were collected. The last preconditioning cycle was used to quantify the myocardial hysteresis (to account for energy dissipation due to the viscoelastic behaviour), dividing the area enclosed by the loading and unloading curves (energy dissipation) by the area beneath the loading curve (energy input). The specimens were stretched by applying a 30 N/m tension in the MFD (T_{MFD}) and CFD (T_{CFD}) at 0.5 mms^{-1}. Tissue deformation was measured via a charge-coupled device camera (National Instrument, IMAQ CCD, Austin, TX), tracking the relative position of four reference points placed in a 2 × 2 array. In-house Labview code (National Instrument, Version 6, Austin, TX) was used to control the stepper motors, and to record the applied forces and tissue strain.

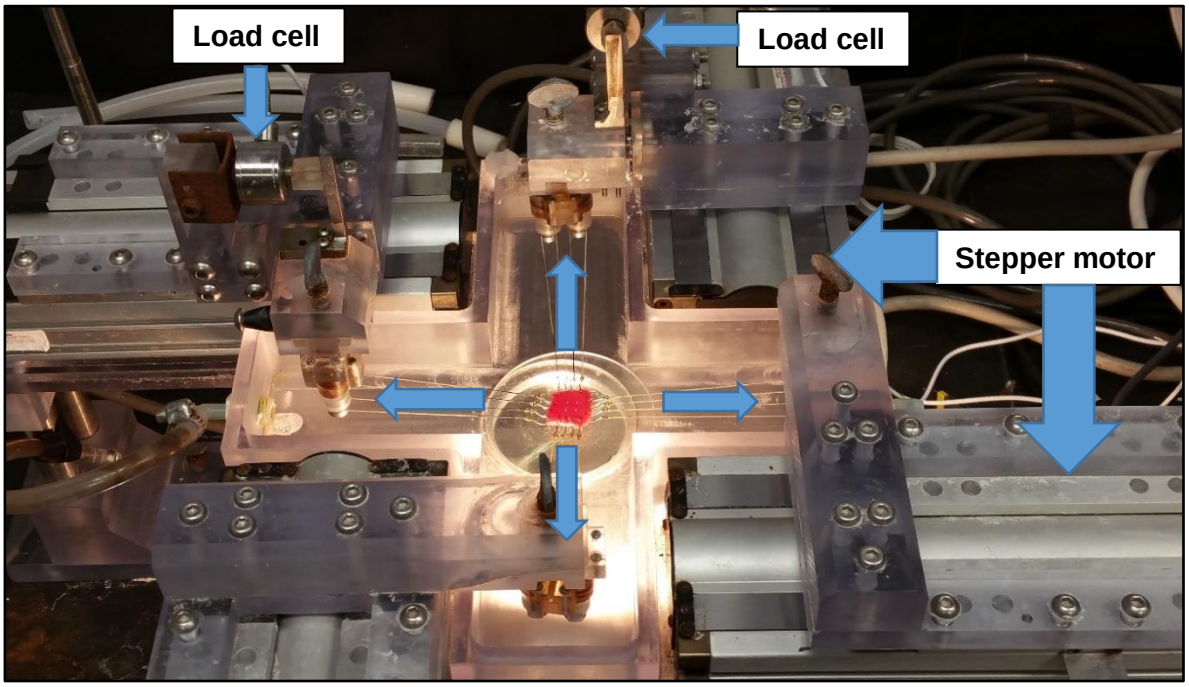

***Figure 3.12**: Biaxial testing setup, comprising four stepper motors, two load cells, and physiological saline bath. In-house Labview code (National Instrument, Version 6, Austin, TX) was used to control the stepper motors and record the applied forces and tissue strain.*

Data analysis

Soft biological tissue is typically considered to be an incompressible material when performing biomechanical analysis [104], allowing the Cauchy stresses in MFD (σ_{11}) and CFD (σ_{22}) to be computed from the first Piola-Kirchhoff stresses (MFD : P_{11} ; CFD :P_{22}) as [191]:

$$\sigma_{11} = \lambda_1 P_{11} = \lambda_1 \frac{f_1}{TL_2}, \qquad \sigma_{22} = \lambda_2 P_{22} = \lambda_2 \frac{f_2}{TL_1}, \qquad \text{(Eqn 3.2)}$$

where $\lambda_1 = \frac{x_1}{X_1}$ and $\lambda_2 = \frac{x_2}{X_2}$ characterise the tissue stretches in both directions, respectively; (x_1, x_2) represents the marker distances in a loaded configuration; (X_1 , X_2) represents the marker distance in an unloaded configuration; the applied forces in each directions are symbolised as f_1 andf_2; T is the average thickness measured in unloaded configurations; and, L_1 and L_2 are the measured side lengths of the tissue sample in the undeformed states, for the MFD fibre and CFD. For incompressible material $\lambda_1\lambda_2\lambda_3$ = 1, which can be used to calculate the λ_3, given the $\lambda_1\lambda_2$ are known.

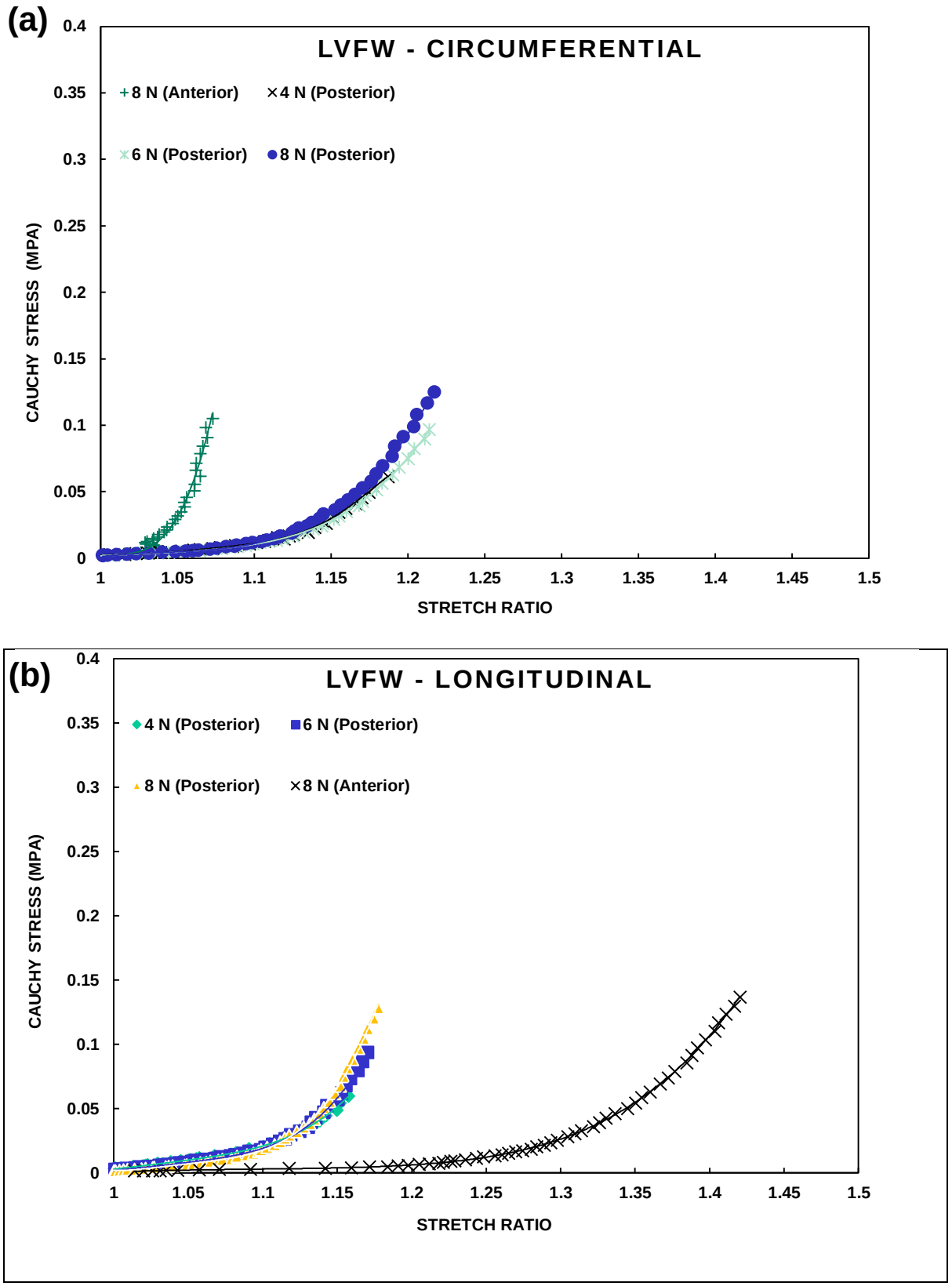

***Figure 3.13**: **(a)** Representing passive 'biaxial behaviour' in the circumferential direction of the LVFW; **(b)** demonstrating passive 'biaxial behaviour' in the longitudinal direction of the LVFW. The myocardial tissue was uniformly deformed and high-quality results were obtained using surgical sutures.*

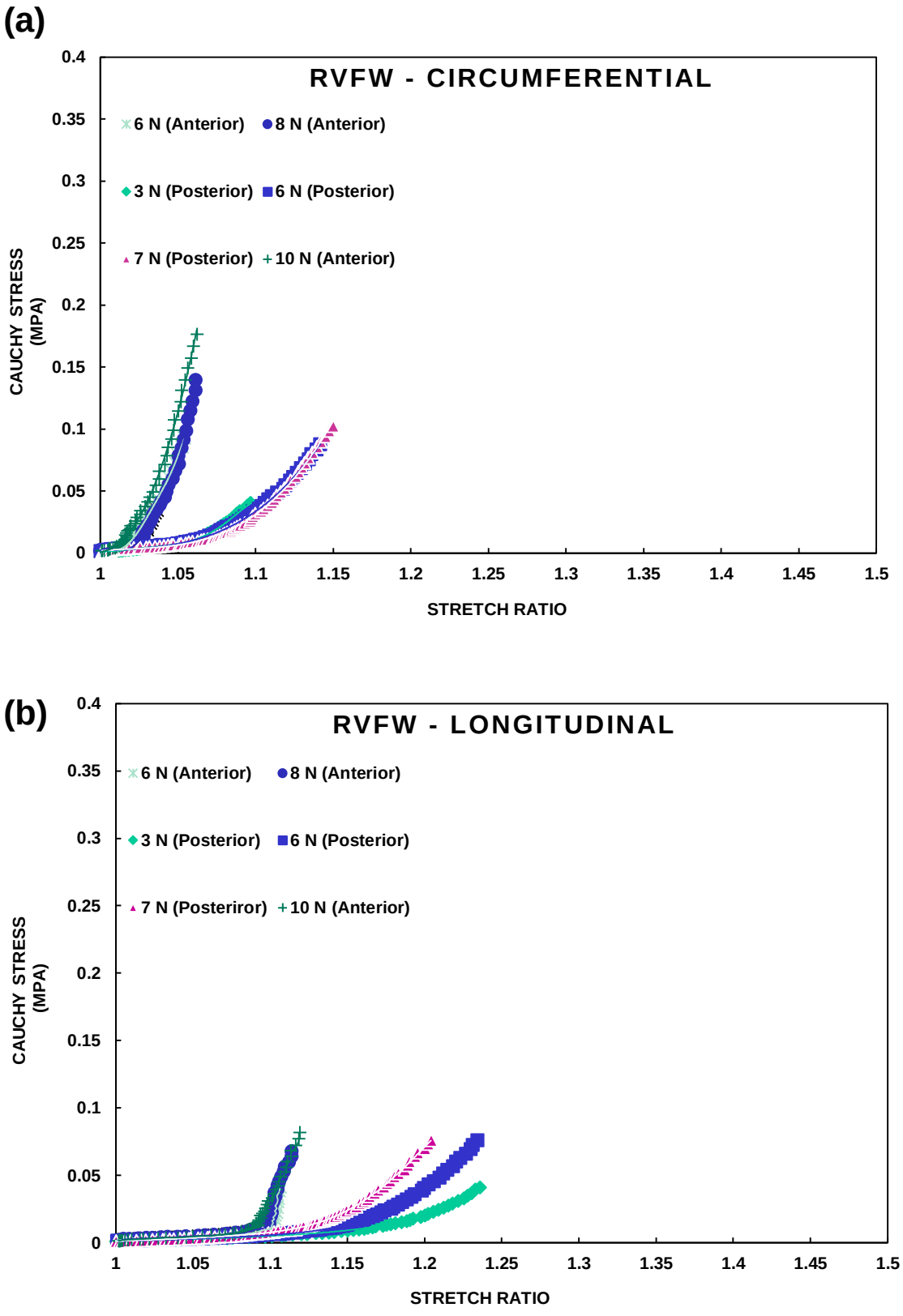

***Figure 3.14**: **(a)** Representing passive 'biaxial behaviour' in the circumferential direction of the RVFW; **(b)** demonstrating passive 'biaxial behaviour' in the longitudinal direction of the RVFW. The myocardial tissue was uniformly deformed and high-quality results were obtained using surgical sutures.*

3.2.2.3. Simple shear test

The simple shear tests focused on the relative shearing and sliding of the myocardial tissues, this feature is critical for effective blood ejection during systole [111] and wall thinning during diastole [42]. Simple shear tests involved mounting the tissue in custom-built shear plates, which were mounted in the Mach 1 testing machine (Biosyntech, MN); as demonstrated in Figure 3.15. Regional anisotropy was investigated using 3 × 3 x 3 mm cubic specimens that had been dissected so that the MFD and CFD were consistent with the x and y-axes. Tissue samples were mounted between the two shear plates using minimal cyanoacrylate before being tested in the MFD and CFD. Evans blue dye was used to label the specimen orientation during testing [113]. The tissue was exposed to positive and negative amount of shear at 10% and then incrementally increased to a maximum 50%, at a loading rate of 0.02 mms^{-1}. Positive cyclic shearing was used to quantify the myocardial hysteresis (to account for energy dissipation due to the viscoelastic behaviour), dividing the area enclosed by the loading and unloading curves (energy dissipation) by the area beneath the loading curve (energy input). This protocol is consistent with a previous study that examined adult porcine heart tissue, which enabled a direct comparison of the data [113].

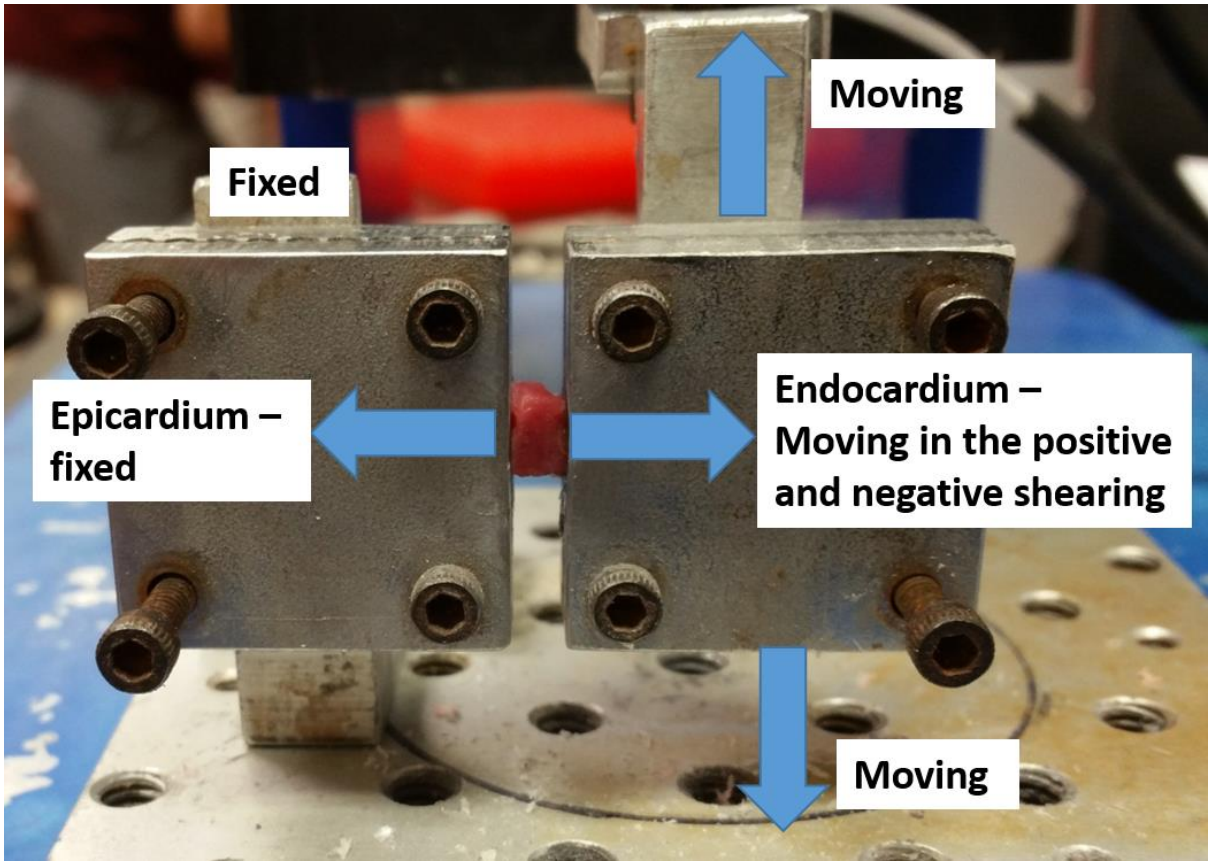

***Figure 3.15**: Experimental design in simple shear. Epicardium is fixed when endocardium is moving in the positive and negative shear, indicating that the experiments are able to measure the shear in MFD and CFD.*

Data analysis

Shear stress (τ) is the ratio of the shear force f and the shear area $= L^2$; hence, this calculation represents the relative in-plane displacement of two parallel layers of this cubic specimen. The amount of shear γ ranges from 0.1–0.5 in increments of 0.1, while the separation distance (side length) for the cubic specimen was L ~ 3 mm:

$$\gamma = \frac{\Delta L}{\mathrm{L}}, \qquad \tau = \frac{f}{L^2}, \qquad \text{(Eqn 3.3)}$$

where ΔL represents the shear displacement.

Statistical analysis

All of the values are reported as the mean ± SD, where a *p*-value less than 0.05 was considered to be statistically significant. One-way analysis of variances (ANOVA) was performed along with Tukey HSD post hoc test to quantify the statistical significance of the anterior and posterior aspects of both ventricles. All of the statistical analyses were conducted in SPSS 20.0.

3.3. Myocardial constitutive modelling

The structurally-based Holzapfel–Ogden (HO) model was used to fit the microstructural (i.e. mean-fibre rotation) and biomechanical (i.e. uniaxial tensile, biaxial tensile and simple shear) data that are used to estimate the material parameters of the neonatal porcine myocardium. The strain energy function of HO model is

$$\Psi = \frac{a}{2b}\exp[b(I_1-3)] + \sum_{i=f,s}\frac{a_i}{2b_i}\{\exp[b_i(I_{4i}-1)^2]-1\} + \frac{a_{\mathrm{fs}}}{2b_{\mathrm{fs}}}[\exp(b_{\mathrm{fs}}I_{8\mathrm{fs}}^2)-1]$$

(Eqn 3.4)

where a, b, a_f, a_s, b_f, b_s , a_{fs} and b_{fs} are eight positive material constants, the *a* parameters possessing the stress dimension, while the *b* parameters are dimensionless. This consists of the isotropic term in I_1, the transversely isotropic terms in $I_{4\,f}$ and $I_{4\,s}$ and the orthotropic term in $I_{8\,fs}$.

Correspondingly, the Cauchy stress for the incompressible material is

$$\boldsymbol{\sigma} = -p\mathbf{I} + a\exp[b(I_1 - 3)]\mathbf{B} + 2a_f(I_{4\mathrm{f}} - 1)\exp\left[b_f(I_{4\mathrm{f}} - 1)^2\right]\mathbf{f}\otimes\mathbf{f} + 2a_s(I_{4\mathrm{s}} - 1)\exp\left[b_s(I_{4\mathrm{s}} - 1)^2\right]\mathbf{s}\otimes\mathbf{s} + a_{\mathrm{fs}}I_{8\mathrm{fs}}\exp\left(b_{\mathrm{fs}}I_{8\mathrm{fs}}^2\right)(\mathbf{f}\otimes\mathbf{s} + \mathbf{s}\otimes\mathbf{f})$$

(Eqn 3.5)

3.3.1. Mathematical methods

3.3.1.1. Extracting parameters from uniaxial test data

Engineering stresses in MFD, denoted by direction 1) (σ_{11}) is calculated as the ratio of the applied force f_1 and the initial cross-sectional area A_1. The strain is computed as the ratio of the displacement and the initial gauge length:

$$T_{11}^{\mathrm{Exp}} = \frac{f_1}{A_1}, \quad \varepsilon_1 = \frac{dx_1}{X_1}$$

(Eqn 3.6)

where the dx_1 is the displacement and X_1 is the initial gauge length. Therefore, the stretch and Cauchy stress are as follows:

$$\lambda_1^{\mathrm{Exp}} = \frac{x_1 + X_1}{X_1} = 1 + \varepsilon_1, \quad \sigma_{11}^{\mathrm{Exp}} = \frac{f_1}{A_1}\lambda_1^{\mathrm{Exp}}.$$

(Eqn 3.7)

Similarly, the Cauchy stress in CFD, denoted by direction 2). Please note that the CFD actually is the normal direction.

$$\lambda_2^{\mathrm{Exp}} = \frac{dx_2 + X_2}{X_2} = 1 + \varepsilon_2, \quad \sigma_{22}^{\mathrm{Exp}} = \frac{f_2}{A_2}\lambda_2^{\mathrm{Exp}}.$$

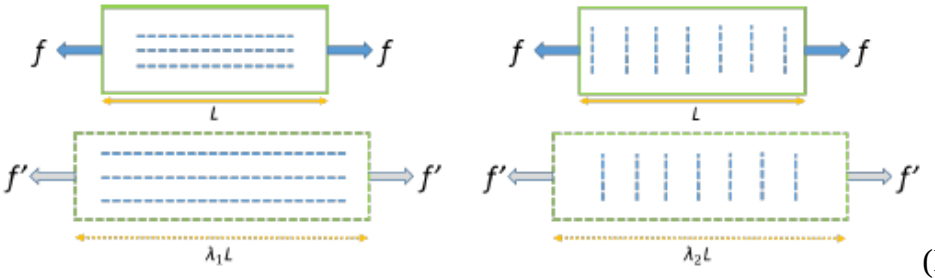

(Eqn 3.8)

***Figure 3.16**: Uniaxial sample in MFD (the left panel) and CFD (the right panel)*

Given that the analysis in MFD and CFD are the same, the detailed analysis was performed in the MFD. Assuming the first principle direction is along the MFD, the other two principle directions are in the cross-section area and, thus, the deformation gradient tensor is:

$$\mathbf{F} = \begin{bmatrix} \lambda_1 & 0 & 0 \\ 0 & \lambda_2 & 0 \\ 0 & 0 & \lambda_3 \end{bmatrix}$$

The deformation gradient F is assumed to be homogeneous throughout the whole experimental sample and λ_1, λ_2, and λ_3 denote the principle stretches in the 1, 2 and 3 directions, in which 1, 2 and 3 represents MFD, CFD and sheet direction, respectively.

Furthermore, f_0 = (1, 0, 0) denotes MFD, and n_0 = (0; 1; 0) denotes CFD. In addition, $\lambda_2 = \lambda_3$ were assumed to be the same. Under incompressible constrain (detF = 1),

$$\mathbf{F} = \begin{bmatrix} \lambda_1 & 0 & 0 \\ 0 & \frac{1}{\sqrt{\lambda_1}} & 0 \\ 0 & 0 & \frac{1}{\sqrt{\lambda_1}} \end{bmatrix}$$

and,

$$\mathbf{C} = \mathbf{F}^T\mathbf{F} = \begin{bmatrix} \lambda_1^2 & 0 & 0 \\ 0 & \frac{1}{\lambda_1} & 0 \\ 0 & 0 & \frac{1}{\lambda_1} \end{bmatrix}, \quad \mathbf{B} = \mathbf{F}\mathbf{F}^T = \begin{bmatrix} \lambda_1^2 & 0 & 0 \\ 0 & \frac{1}{\lambda_1} & 0 \\ 0 & 0 & \frac{1}{\lambda_1} \end{bmatrix}$$

Where, by definition, **C** is the right Cauchy-Green Strain and **B** is the left Cauchy-Green Strain respectively. **C** is defined in and associated with the reference configuration (un-deformed-state), acting on vectors in the reference configuration. Whereas, **B** is defined in the current configuration (deformed-state).

The invariants are

$$\begin{aligned} I_1 &= \mathrm{tr}\mathbf{C} = \lambda_1^2 + \frac{2}{\lambda_1} \\ I_{4\mathrm{f}} &= \mathbf{C} : (\mathbf{f}_0 \otimes \mathbf{f}_0) = \lambda_1^2 \\ I_{4\mathrm{s}} &= \mathbf{C} : (\mathbf{s}_0 \otimes \mathbf{s}_0) = \frac{1}{\lambda_1} \\ I_{8\mathrm{fs}} &= \mathbf{C} : (\mathbf{f}_0 \otimes \mathbf{s}_0) = 0 \end{aligned} \qquad \text{(Eqn 3.9)}$$

Because the fibre cannot resist compression, the I_{4f} and I_{4s} were redefined as

$$I_{4f}^{*} = \max(I_{4f}, 1), \text{and} \quad I_{4s}^{*} = \max(I_{4s}, 1)$$

Here, it is important to note that fibres rotate from epicardium to endocardium by about -30 ^{0} to +30 ^{0}, which suggests that the fibre rotation should be considered at different depths of the experimental sample, as demonstrated in Figure 3.17.

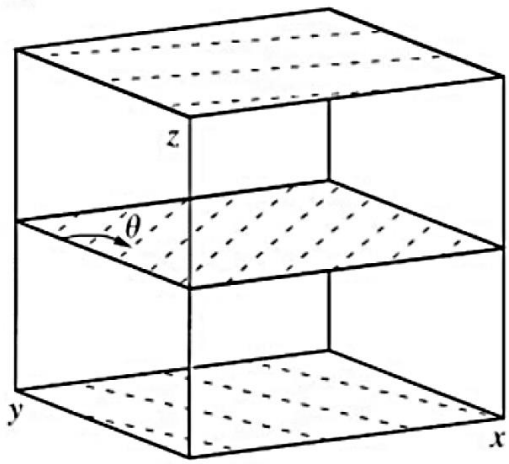

***Figure 3.17**: Fibre rotation θ along the depth*

To express the fibre rotation, a global coordinate system at the surface of the sample was defined, in which the x axial aligns with the MFD, the y axial aligns the CFD, and the z axial is the depth direction (transmural direction) of the sample. In addition, the fibre direction was assumed to rotate with the depth linearly, increasing from 0 ^{o} to 60 ^{o} and defined as f_0 = (cos θ, sin θ, 0), s_0 = (0, 0, 1) and n_0 = (- sin θ, cos θ, 0), in which θ is the angle between the x axial and fibre direction. In the current configuration, f = Ff_0, and s = Fs_0. Finally, the expressions of the invariants can be rewritten as follows

$$
\begin{aligned}
I_{4\mathrm{f}} &= \lambda_1^2 \cos^2\theta + \frac{\sin^2\theta}{\lambda_1}, \\
I_{4\mathrm{s}} &= \frac{1}{\lambda_1}, \\
I_{8\mathrm{fs}} &= 0, \\
I_{4\mathrm{f}}^* &= \max(I_{4\mathrm{f}}, 1), \\
I_{4\mathrm{s}}^* &= \max(I_{4\mathrm{s}}, 1).
\end{aligned}
$$

(Eqn 3.10)

Then, the Cauchy stress is

$$
\begin{aligned}
\boldsymbol{\sigma} = -p\mathbf{I} + a\exp[b(I_1 - 3)]\mathbf{B} + 2a_{\mathrm{f}}(I_{4\mathrm{f}}^* - 1)\exp\left[b_{\mathrm{f}}(I_{4\mathrm{f}}^* - 1)^2\right]\mathbf{f}\otimes\mathbf{f} \\
+ 2a_s(I_{4\mathrm{s}}^* - 1)\exp\left[b_s(I_{4\mathrm{s}}^* - 1)^2\right]\mathbf{s}\otimes\mathbf{s}
\end{aligned}
$$

(Eqn 3.11)

Because σ_{33} is zero (i.e. the stress is in the sheet's direction), equation 3.11 can be solved for the Lagrangian multiplier p. In terms of the fibre directions at different depths, assuming it changes linearly with depth value (t),

$$
\theta = f(t) = \frac{\theta_{\max}}{T_0}\, t
$$

(Eqn 3.12)

where T_0 is the thickness of the sample, and θmax is the maximum fibre rotation as shown in Figure 3.18. Analysis of the stress of the whole specimen has revealed that not all of the fibre contributes to stress. In other words, there is an effective area in which the fibres provide stress while the excluding has no effect. Figure 3.19 schematically shows an experimental sample under uniaxial stretch. Given that there are two family fibres (denoted as f and n) at each depth, either f or n will contribute to the total stress as long as they are stretched. Thus, for f, if it runs from the most left side to the most right side, then those fibres along f can potentially contribute to the total Cauchy stress along the x-axis; as shown in the Figure 3.19 in the region enclosed by the two dashed lines.

An effective area coefficient $\mathcal{E}_\theta$ was defined for stress in every fibre direction, which is denoted by

$$\epsilon_\theta = \begin{cases} 1 - 3|\tan(\theta)| & \text{for} \quad 0 < \theta < \theta_1 \quad or \quad \pi - \theta_1 < \theta < \pi \\ 1 - 3|\cot(\theta)| & \text{for} \quad \frac{\pi}{2} - \theta_1 \leq \theta \leq \frac{\pi}{2} + \theta_1 \\ 0 & \text{for} \quad \text{others} \end{cases}$$

(Eqn 3.13)

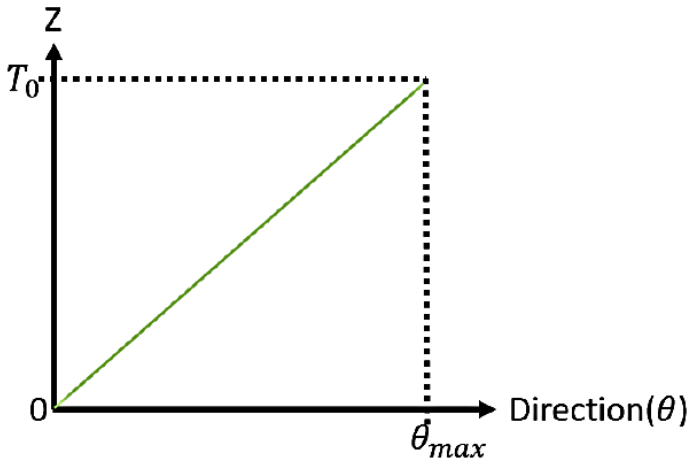

***Figure 3.18**: Effective area when fibre direction is θ*

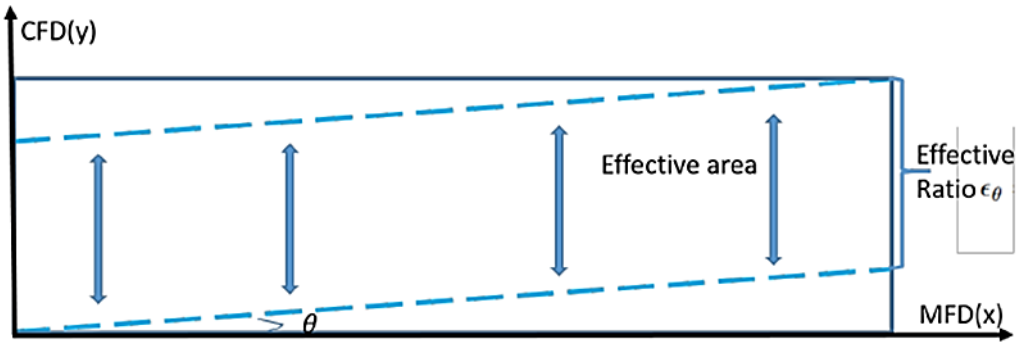

***Figure 3.19**: Effective area when fibre direction is θ*

where θ_1 = arctan H_0 / L_0, H_0 = 5mm and L_0 = 15mm are the height and length of the sample, respectively. Figure 3.20 shows f angle distribution, which will contribute to σ_{ff} uniaxial stretch.

Finally, the effective stress σ^{θ} at a specific angle θ is

$$\boldsymbol{\sigma}^{\theta} = -p\mathbf{I} + a\exp[b(I_1-3)]\mathbf{B} + \epsilon_\theta\, 2a_{\mathrm{f}}(I_{4\mathrm{f}}^{*}-1)\exp\left[b_{\mathrm{f}}(I_{4\mathrm{f}}^{*}-1)^2\right]\mathbf{f}\otimes\mathbf{f} + \epsilon_\theta\, 2a_{\mathrm{s}}(I_{4\mathrm{s}}^{*}-1)\exp\left[b_{\mathrm{s}}(I_{4\mathrm{s}}^{*}-1)^2\right]\mathbf{s}\otimes\mathbf{s}$$

(Eqn 3.14)

Then, the effective stress for the whole sample is derived as follows

$$\sigma_{11}^{E} = \frac{1}{T_0}\int_0^{T_0} \sigma_{11}^{\theta}\, dt \quad \text{(Eqn 3.15)}$$

Then, σ^{E}_{11} can be fitted using measured σ^{Exp}_{11} and λ_1^{Exp}. A similar approach was used to obtain the σ^{E}_{22} fitted by σ^{Exp}_{22} and λ_2^{Exp}.

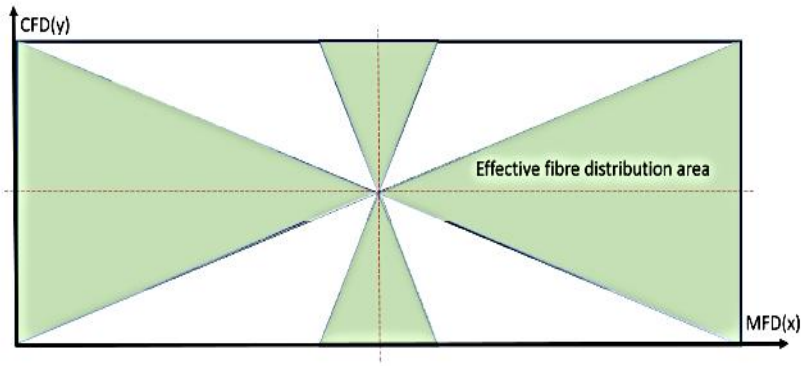

***Figure 3.20**: Effective fibre distribution area*

3.3.1.2. Extracting parameters from the biaxial extension test

All loads are applied normal to the specimen edge and are symbolised as f_1 and f_2 in MFD and CFD, respectively. In accordance with the numerical model analysis, 1 and 2 characterise the tissue stretches in both directions, respectively. Meanwhile, t is the average thickness measured in unloaded configurations, and l1 and l2 are the lengths of the sample in the undeformed states for the MFD and CFD. The first Piola-Kirchhoff stress can be obtained as

$$T_{11} = \frac{f_1}{tl_2}, \qquad T_{22} = \frac{f_2}{tl_1}.$$

To compute the Cauchy stresses, the following relationship was used

$$\boldsymbol{\sigma} = \frac{1}{J}\mathbf{T}\,\mathbf{F}.$$

For incompressible materials, J = 1, thus, the expression of experimental Cauchy stresses can be calculated as

$$\sigma_{11}^{\mathrm{Exp}} = \lambda_1^{\mathrm{Exp}}\frac{f_1}{t\,l_2}, \qquad \sigma_{22}^{Exp} = \lambda_2^{\mathrm{Exp}}\frac{f_2}{t\,l_1} \qquad \text{(Eqn 3.16)}$$

A homogeneous deformation was assumed throughout the sample, where λ1, λ2 and λ3 denote the normal stretch in the 1, 2 and 3 directions, and γ_{21} and γ_{12} as the shearing deformation in the 1 and 2 directions, but there is no shear in the 1-3 and 2-3 planes. Therefore, the final deformation gradient tensor is

$$\mathbf{F} = \begin{bmatrix} \lambda_1 & \gamma_{12} & 0 \\ \gamma_{21} & \lambda_2 & 0 \\ 0 & 0 & \lambda_3 \end{bmatrix}$$

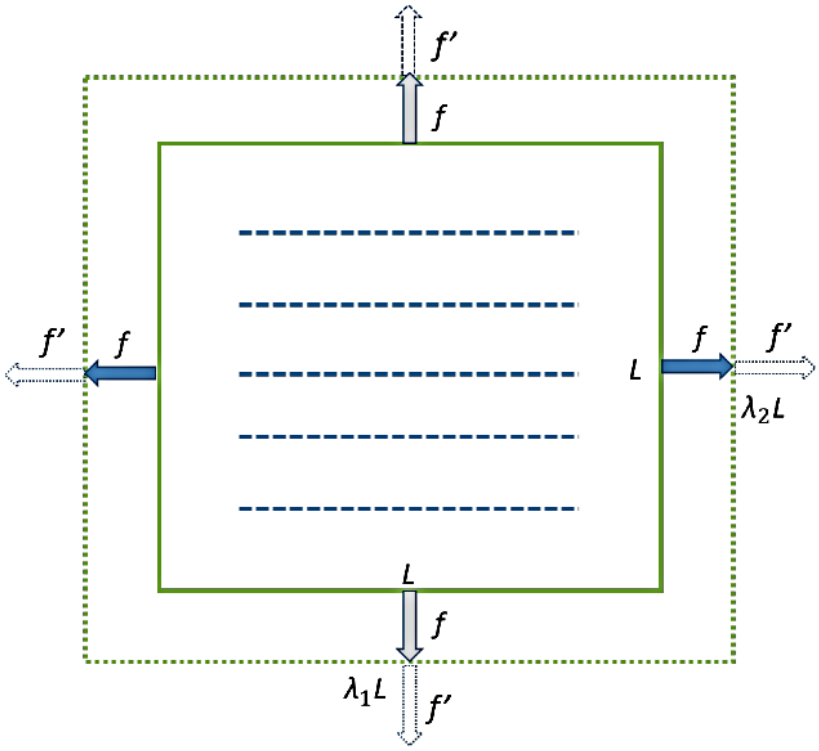

***Figure 3.21**: Biaxial sample*

To ensure that the model structure between different types of experiments is consistent, the fraction of fibre rotation θ was introduced from the top to the bottom of the sample. Although there should theoretically be no shear in biaxial tension experiments, the image that records the experimental process demonstrates an apparent shear deformation.

For the experimental data, the specific values for λ1 and λ2 can be obtained. However, there is no data for shear amount γ_{12} and γ_{21}, which did happen during experiments and which significantly contributes to fitting the data. Therefore, the amount of shear was calculated based on the image by measuring the shape transformation in the individual coordinate. In Figure 3.22, the coordinate values of four corner points were measured in the individual

coordinate to get the value of the amount of shear that is not affected by coordinate and to set new individual coordinate for convenience.

The transformed coordinate values, $M'_1(x'_1, y'_1)$, $M'_2(x'_2, y'_2)$, $M'_3(x'_3, y'_3)$ and $M'_4(x'_4, y'_4)$, are enough to deduce the shear angle α_1, α_2, α_3 and α_4.

$$\tan\alpha_1 = \frac{(x'_2 - x'_1)}{(y'_2 - y'_1)} \qquad \tan\alpha_2 = \frac{(y'_4 - y'_1)}{(x'_4 - x'_1)} \quad \text{(Eqn 3.17)}$$

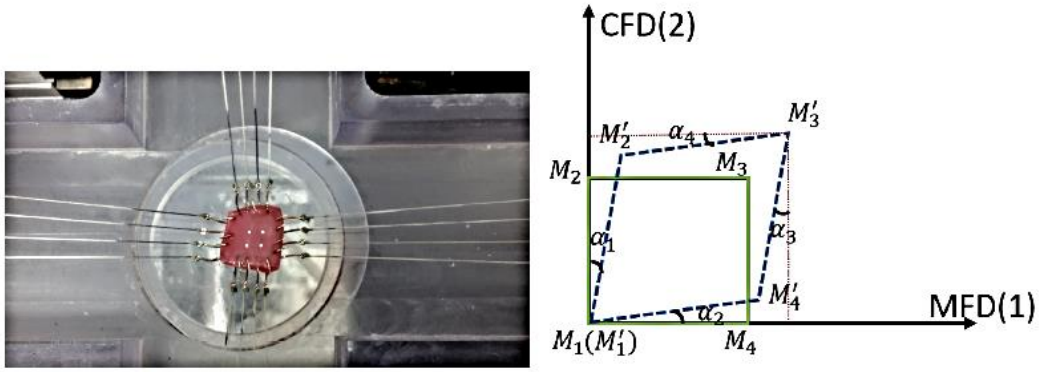

***Figure 3.22**: Transformation of a shear amount based on image*

$$\tan\alpha_3 = \frac{(x'_3 - x'_4)}{(y'_3 - y'_4)} \qquad \tan\alpha_4 = \frac{(y'_3 - y'_2)}{(x'_3 - x'_2)} \quad \text{(Eqn 3.18)}$$

In addition, the shear transformation was assumed to be theoretically symmetrical, i.e. α_1=α_2 = α_3 = α_4. To reduce the error resulting from the experiment behaviour and measurement, the average value of those measuring angles was taken as the shear angle α_i.

$$\tan\alpha_1^{'} = \tan\alpha_2^{'} = \tan\alpha_3^{'} = \tan\alpha_4^{'} = \frac{\tan\alpha_1 + \tan\alpha_2 + \tan\alpha_3 + \tan\alpha_4}{4}$$

(Eqn 3.19)

$$\gamma_{12} = \tan\alpha_1^{'} + \tan\alpha_2^{'} = \gamma_{21} = \tan\alpha_3^{'} + \tan\alpha_4^{'}$$ (Eqn 3.20)

By substituting equations 3.18 and 3.19 into the equation 3.20, we get:

$$\gamma_{12} = \gamma_{21} = \frac{\frac{(x_2^{'}-x_1^{'})}{(y_2^{'}-y_1^{'})} + \frac{(y_4^{'}-y_1^{'})}{(x_4^{'}-x_1^{'})} + \frac{(x_3^{'}-x_4^{'})}{(y_3^{'}-y_4^{'})} + \frac{(y_3^{'}-y_2^{'})}{(x_3^{'}-x_2^{'})}}{2}$$

(Eqn 3.21)

After measuring, γ_{12}^{max} ~ 0.15, a function should be designed to express the the pattern of its change, as in equation 3.22

$$\gamma_{12} = \gamma_{21} = (\frac{\lambda_1 - 1}{\lambda_2} + \frac{\lambda_2 - 1}{\lambda_1})k$$

(Eqn 3.22)

where k is coefficient that makes the γ_{12}^{max} ~ 0.15, k ~ 1.3

In the biaxial experiment, four sides are stretched in two directions. This indicates that all of the fibres in the sample contribute to Cauchy stress σ_{ff}, i.e. $\mathcal{E}_{\Theta}$= 1; I_{8fs} = 0. Therefore, the stress function should be

$$\boldsymbol{\sigma}^{\theta} = -p\mathbf{I} + a\exp[b(I_1 - 3)]\mathbf{B} + 2a_{\mathrm{f}}(I_{4\mathrm{f}}^{*} - 1)\exp\left[b_{\mathrm{f}}(I_{4\mathrm{f}}^{*} - 1)^2\right]\mathbf{f}\otimes\mathbf{f} + 2a_{\mathrm{s}}(I_{4\mathrm{s}}^{*} - 1)\exp\left[b_{\mathrm{s}}(I_{4\mathrm{s}}^{*} - 1)^2\right]\mathbf{s}\otimes\mathbf{s}$$

$$\sigma_{11}^{E} = \frac{1}{T_0}\int_0^{T_0}\sigma_{11}^{\theta}\,dt = \frac{1}{T_0}\int_0^{T_0}\sigma_{11}\,dt$$

$$\sigma_{22}^{\theta}\,dt = \frac{1}{T_0}\int_0^{T_0}\sigma_{22}\,dt$$

Meanwhile, σ_{22}^{E} can be calculated and compared with the measured σ_{11}^{Exp}, σ_{22}^{Exp}, λ_1^{Exp} and λ_2^{Exp}.

3.3.1.3. Extracting parameters from a simple shear test

The simple shear tests focus on the relative shearing and sliding of the myocardial tissues. Regional anisotropy was investigated using cubic specimens whose MFD and CFD were consistent with the x and y-axes. Shear stress (τ), the ratio of the shear force f and the shear area $a = l^2$, and the amount of shear are

$$\tau = \frac{f}{l^2}, \qquad \gamma = \frac{\Delta l}{l}$$

where Δl represents the shear displacement.

The f_0 and n_0 unit vectors are used to denote the MFD and CFD. The shear in MFD is the relative movement of endocardium in the mean-fibre direction while keeping the epicardium fixed with almost zero displacements. Similarly, the shearing in CFD is the relative movement of endocardium in the cross-fibre direction while keeping the epicardium fixed with almost zero displacements, as demonstrated in the Figure 3.15.

The deformation gradient tensors are as follows:

$$\mathbf{F} = \begin{bmatrix} 1 & 0 & \gamma \\ 0 & 1 & 0 \\ 0 & 0 & 1 \end{bmatrix}, \quad \text{and} \quad \mathbf{F} = \begin{bmatrix} 1 & 0 & 0 \\ 0 & 1 & \gamma \\ 0 & 0 & 1 \end{bmatrix}$$

for shear in the MFD and CFD, respectively. Correspondingly the shear stress function is

$$\sigma^{\theta} = -p\mathrm{I} + a\exp[b(I_1 - 3)]\mathrm{B} + \epsilon_{\theta}\, 2a_{\mathrm{f}}(I^{*}_{4\mathrm{f}} - 1)\exp\,[b_{\mathrm{f}}(I^{*}_{4\mathrm{f}} - 1)^2]\mathrm{f}\otimes\mathrm{f} + \epsilon_{\theta}\, 2a_{\mathrm{s}}(I^{*}_{4\mathrm{s}} - 1)\exp\,[b_{\mathrm{s}}(I^{*}_{4\mathrm{s}} - 1)^2]\mathrm{s}\otimes\mathrm{s} + a_{\mathrm{fs}}I_{8\mathrm{fs}}\exp\,(b_{\mathrm{fs}}I^{2}_{8\mathrm{fs}})(\mathrm{f}\otimes\mathrm{s} + \mathrm{s}\otimes\mathrm{f}) \quad \text{(Eqn 3.23)}$$

All of the fibres were assumed to effectively contribute to the simple shear in MFD and CFD, so the $\mathcal{E}_{\theta}$= 1, and then the final effective stress function is

$$\sigma^{E}_{12} = \frac{1}{T_0}\int_0^{T_0} \sigma^{\theta}_{12}\, dt$$

4.0. RESULTS

In this chapter, the microstructural and biomechanical behaviour of neonatal porcine left and right ventricle 'free-wall' (LVFW, RVFW) are demonstrated using the experimental protocol that was described in Chapter 3. These data will then be used with the structurally-based HO model of the adult myocardium to establish the materials parameters that, for the first time, specifically describe neonatal ventricular myocardium and will enable simulation that more accurately reflect ventricular tissue behaviour.

4.1. Microstructural analyses

4.1.1. Histological analysis

Masson's trichrome stain indicated cardiomyocytes in red and collagen fibres light blue. Figures 4.1–4.8 show the overall fibre orientation in the anterior and posterior aspects of the LVFW and RVFW. These samples were collected in alignment to the vertical axis of the heart (defined as passing through the apex and base). These images indicated that the fibre direction in the anterior LVFW was more aligned to the horizontal and posterior to the vertical axes, respectively (Figures 4.1(a) and (b), and Figures 4.4 (a) and (b)). Indeed, the alignment of fibres with either the horizontal or vertical appears stronger in the LVFW than the RVFW (Figures 4.1 and 4.8). The Fourier-components analysis quantified these alignments and confirmed that the fibres in the anterior and posterior LVFW were more aligned to the horizontal and vertical axes of the heart (Figures 4.1–4.4 and Table 4.1). Conversely, fibres in the anterior and posterior RVFW were aligned nearer diagonally, though the former had less extracellular space (Figures 4.5–4.8 and Table 4.1). Surface area

analysis revealed the greater concentration of collagen in the posterior wall when compared to the anterior wall in both ventricles (Table 4.2). LVFW specified the greater ratio of collagen to myocyte fibres than the RVFW (Table 4.2). Moreover, the ratio of collagen to myocyte fibres was highest in the LVFW–posterior and lowest in the RVFW–anterior regions (Table 4.2). The average in-plane (x, y) principal (preferred) fibre orientation of the LVFW and RVFW are stated in Table 4.1.

In both ventricles, the anterior aspects exhibited the strong alignment of muscle fibres with less intercellular space (Figures 4.1–4.8). The greater dispersion of muscle fibres were observed in the posterior wall of both ventricles (Figures 4.1–4.8), which may serve to accommodate the greater concentration of collagen reported in Table 4.2. The relative differences of the collagen fraction within the anterior and posterior aspects provide an indication of the different extent of remodelling in the front and back walls of the one-day-old neonatal porcine ventricles post-natal (Table 4.2). The anterior and posterior aspects of both ventricles did not possess any abrupt disruption in the muscle fibre alignment, providing an indication of the structural integrity of the myocardial tissue (Figures 4.1–4.8). Cardiomyocytes and collagen fibrils demonstrated the nearly planar interaction in the anterior and posterior aspects of both ventricles (Figures 4.1–4.8). This interaction may provide the structural support to maintain the normal heart function during diastole and systole. The marked interstitial concentration of collagen may also serve to arrange the cardiomyocytes architecture into the higher order of laminar sheet layers (Figures 4.1–4.8).

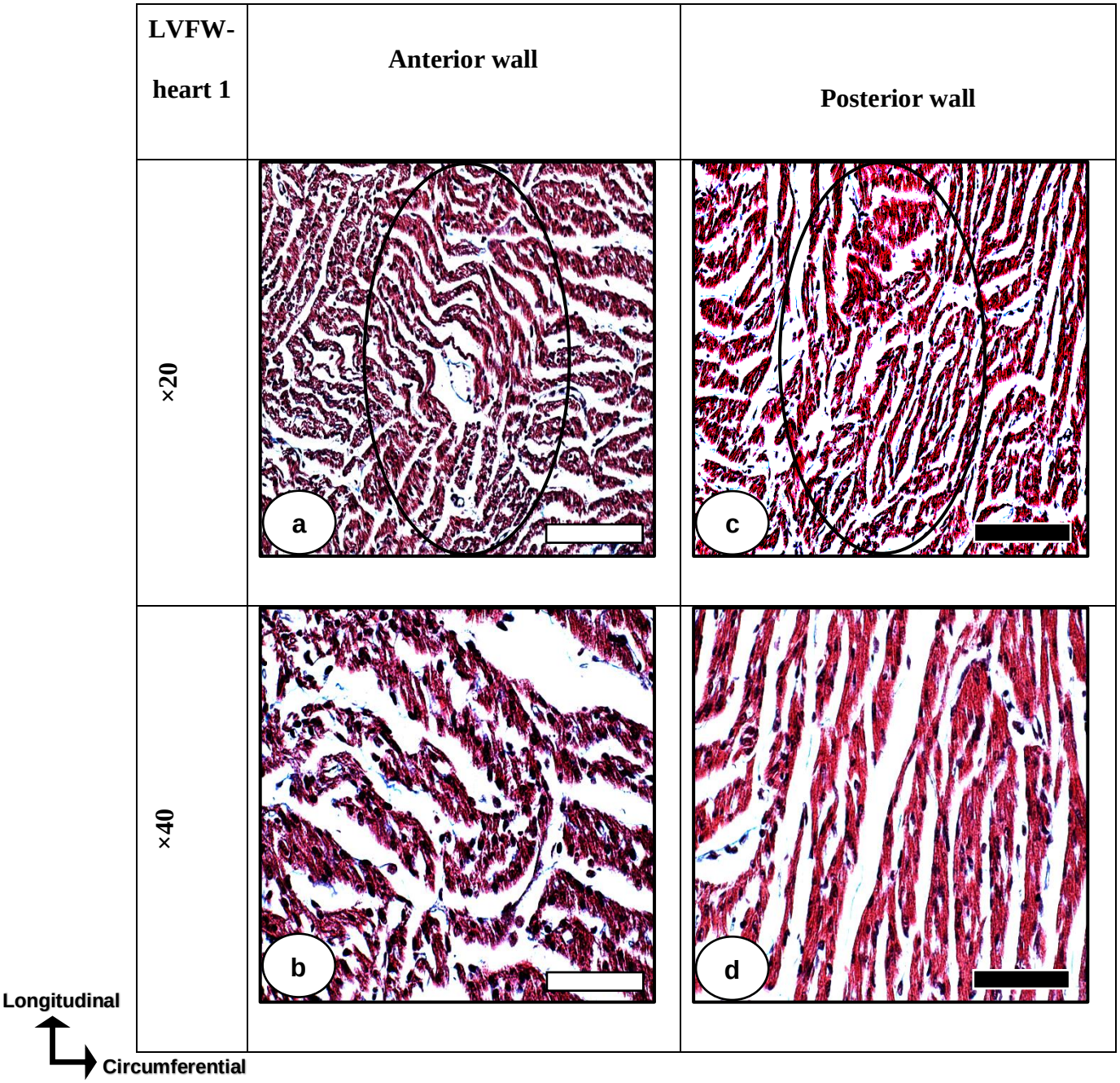

Figure 4.1: *Masson's trichrome staining images of the neonatal porcine ventricles, sectioned in the plane perpendicular to the transmural direction (i.e. in-plane), and viewed at × 20 and × 40 magnification.* ***(a–b)*** *LVFW–anterior, demonstrating circumferentially aligned fibres.* ***(c–d)*** *LVFW–posterior, describing longitudinally aligned fibres. Principal or preferred fibre angles are detailed in Table 4.1. Scale bar at* ***×20*** *=100 µm and at* ***×40*** *=50µm, respectively.*

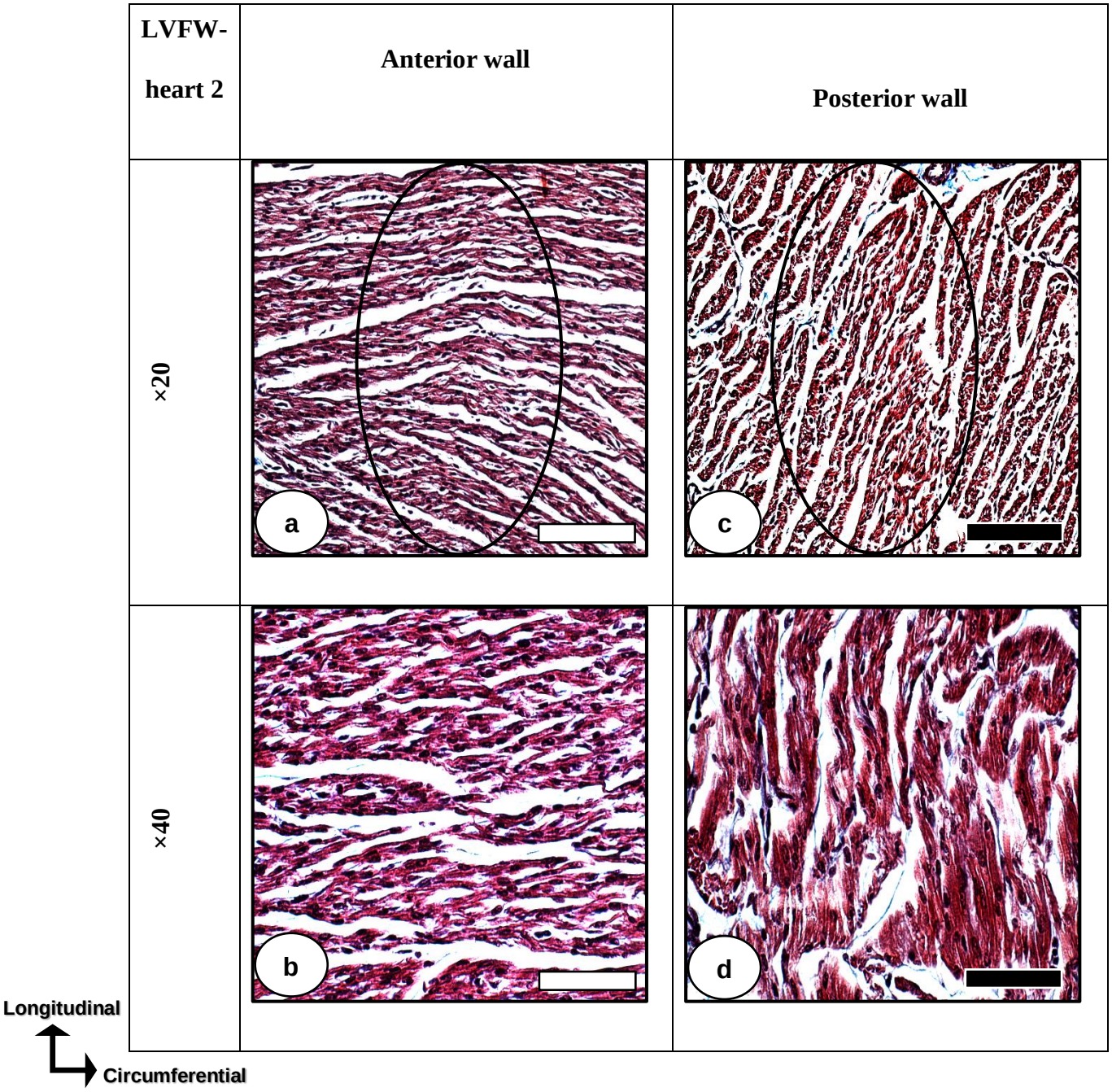

Figure 4.2: *Masson's trichrome staining images of the neonatal porcine ventricles, sectioned in the plane perpendicular to the transmural direction (i.e. in-plane), and viewed at × 20 and × 40 magnification.* ***(a–b)*** *LVFW–anterior, demonstrating circumferentially aligned fibres.* ***(c–d)*** *LVFW–posterior, describing longitudinally aligned fibres. Principal or preferred fibre angles are detailed in Table 4.1. Scale bar at* ***×20*** *=100 µm and at* ***×40*** *=50µm, respectively.*

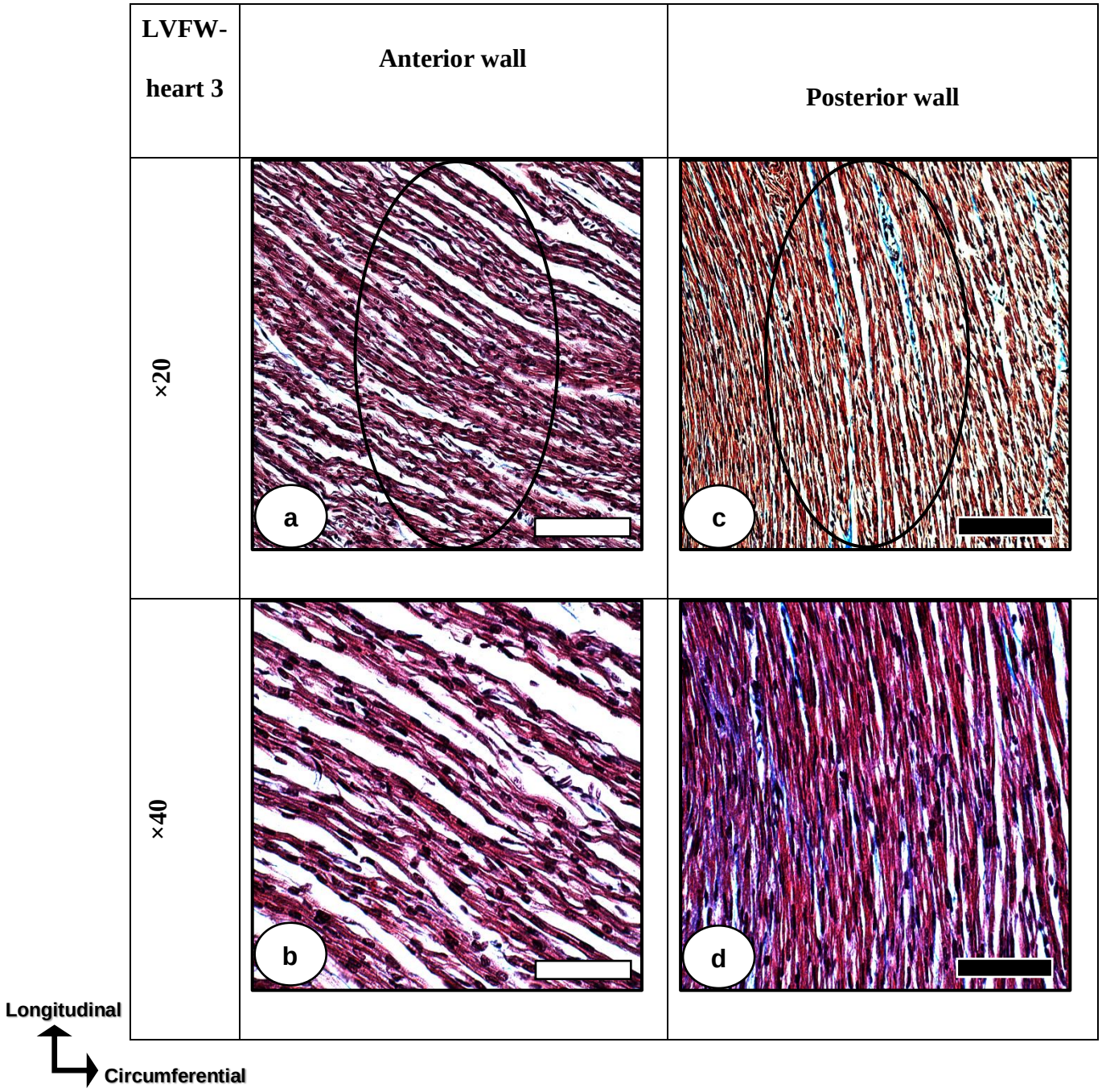

Figure 4.3: *Masson's trichrome staining images of the neonatal porcine ventricles, sectioned in the plane perpendicular to the transmural direction (i.e. in-plane), and viewed at × 20 and × 40 magnification.* ***(a–b)*** *LVFW–anterior, demonstrating circumferentially aligned fibres.* ***(c–d)*** *LVFW–posterior, describing longitudinally aligned fibres. Principal or preferred fibre angles are detailed in Table 4.1. Scale bar at* ***×20*** *=100 µm and at* ***×40*** *=50µm, respectively.*

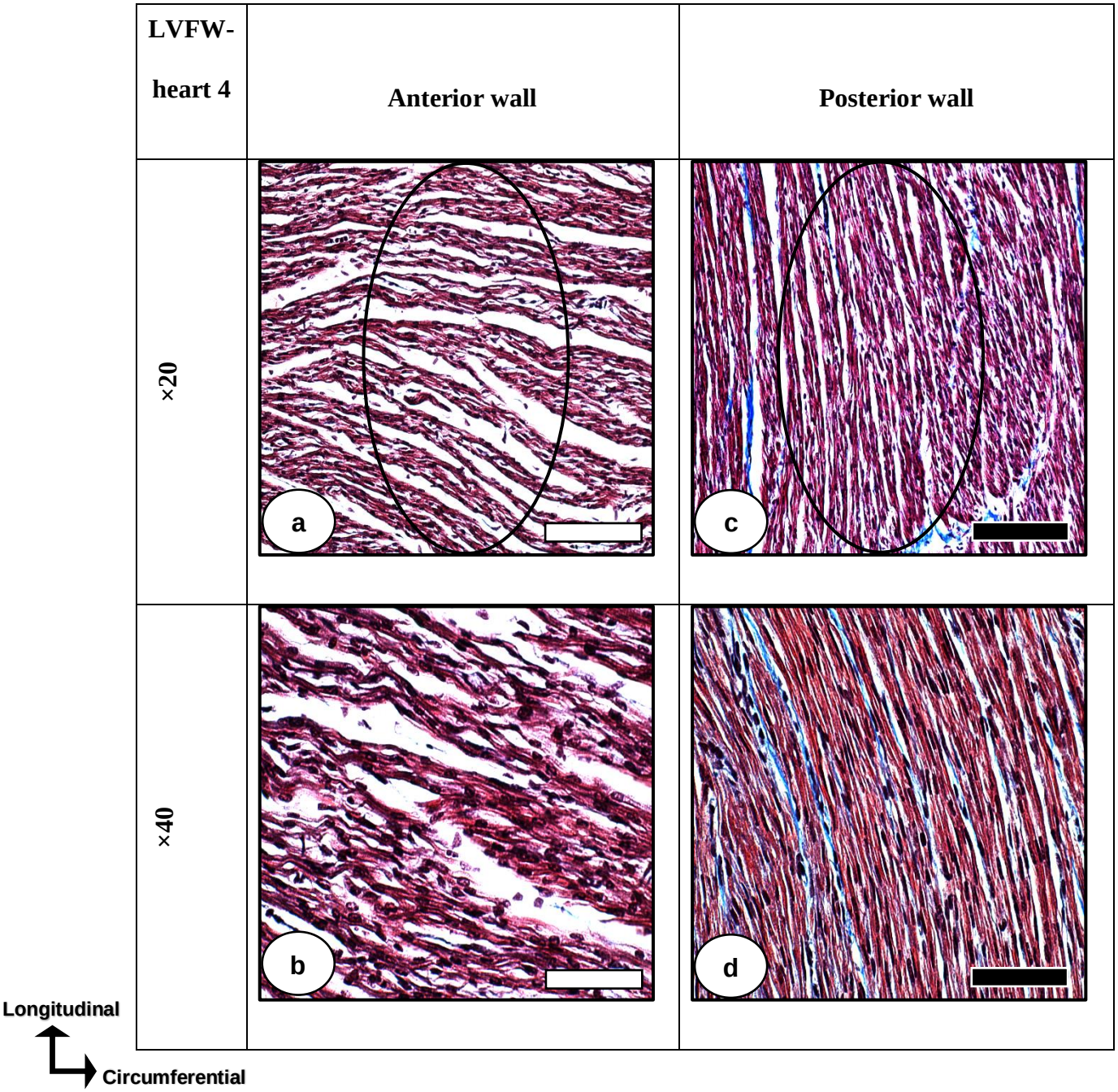

Figure 4.4: *Masson's trichrome staining images of the neonatal porcine ventricles, sectioned in the plane perpendicular to the transmural direction (i.e. in-plane), and viewed at × 20 and × 40 magnification.* ***(a–b)*** *LVFW–anterior, demonstrating circumferentially aligned fibres.* ***(c–d)*** *LVFW–posterior, describing longitudinally aligned fibres. Principal or preferred fibre angles are detailed in Table 4.1. Scale bar at* ***×20*** *=100 µm and at* ***×40*** *=50µm, respectively.*

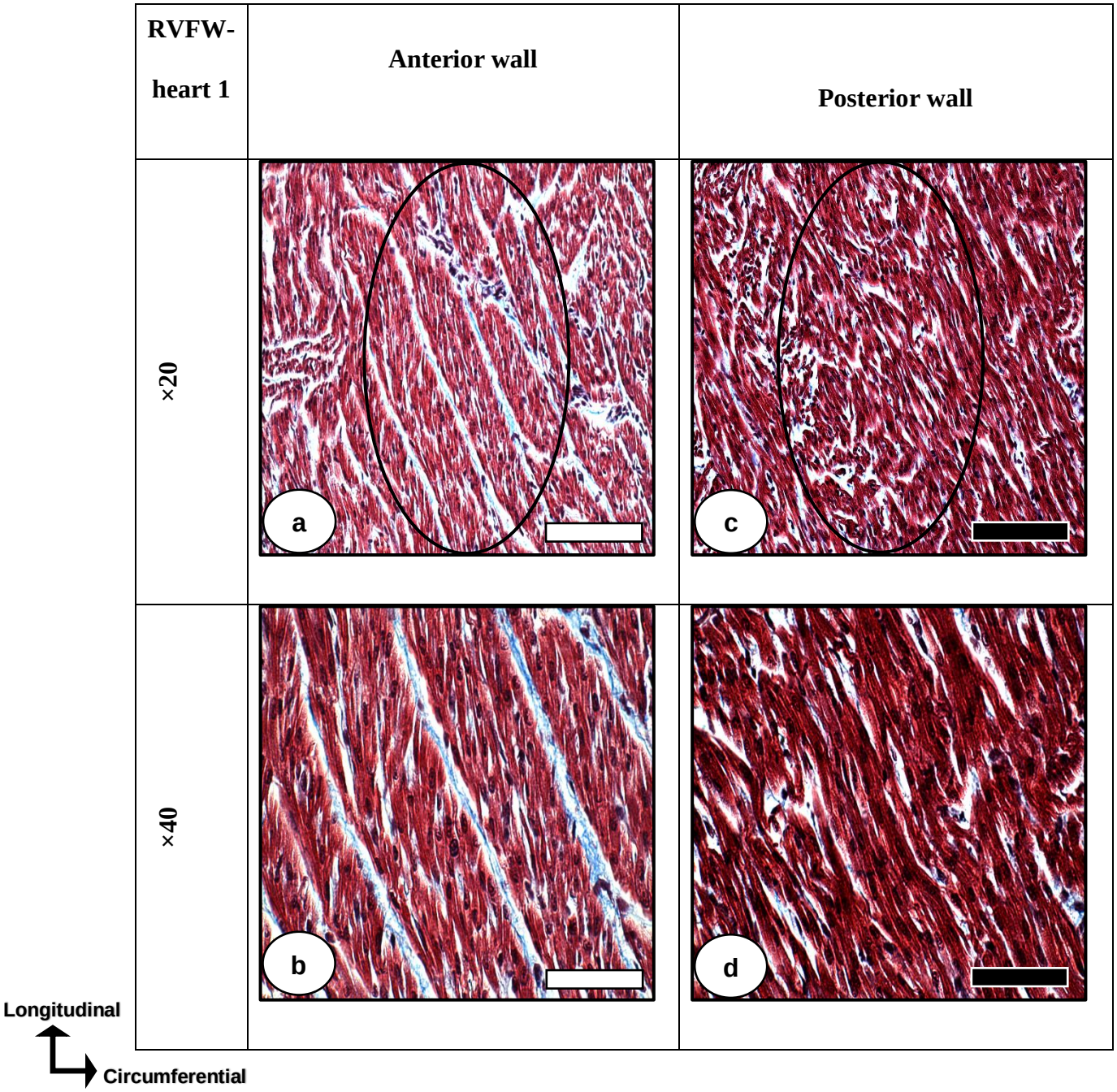

Figure 4.5: *Masson's trichrome staining images of the neonatal porcine ventricles, sectioned in the plane perpendicular to the transmural direction (i.e. in-plane), and viewed at × 20 and × 40 magnification. The RVFW–anterior* ***(a–b)*** *and posterior* ***(c–d)*** *aspects demonstrated almost symmetrical fibre alignment, with the former having greater concentration and alignment of muscle fibres. Principal or preferred fibre angles are detailed in Table 4.1. Scale bar at* ***×20*** *=100 µm and at* ***×40*** *=50µm, respectively.*

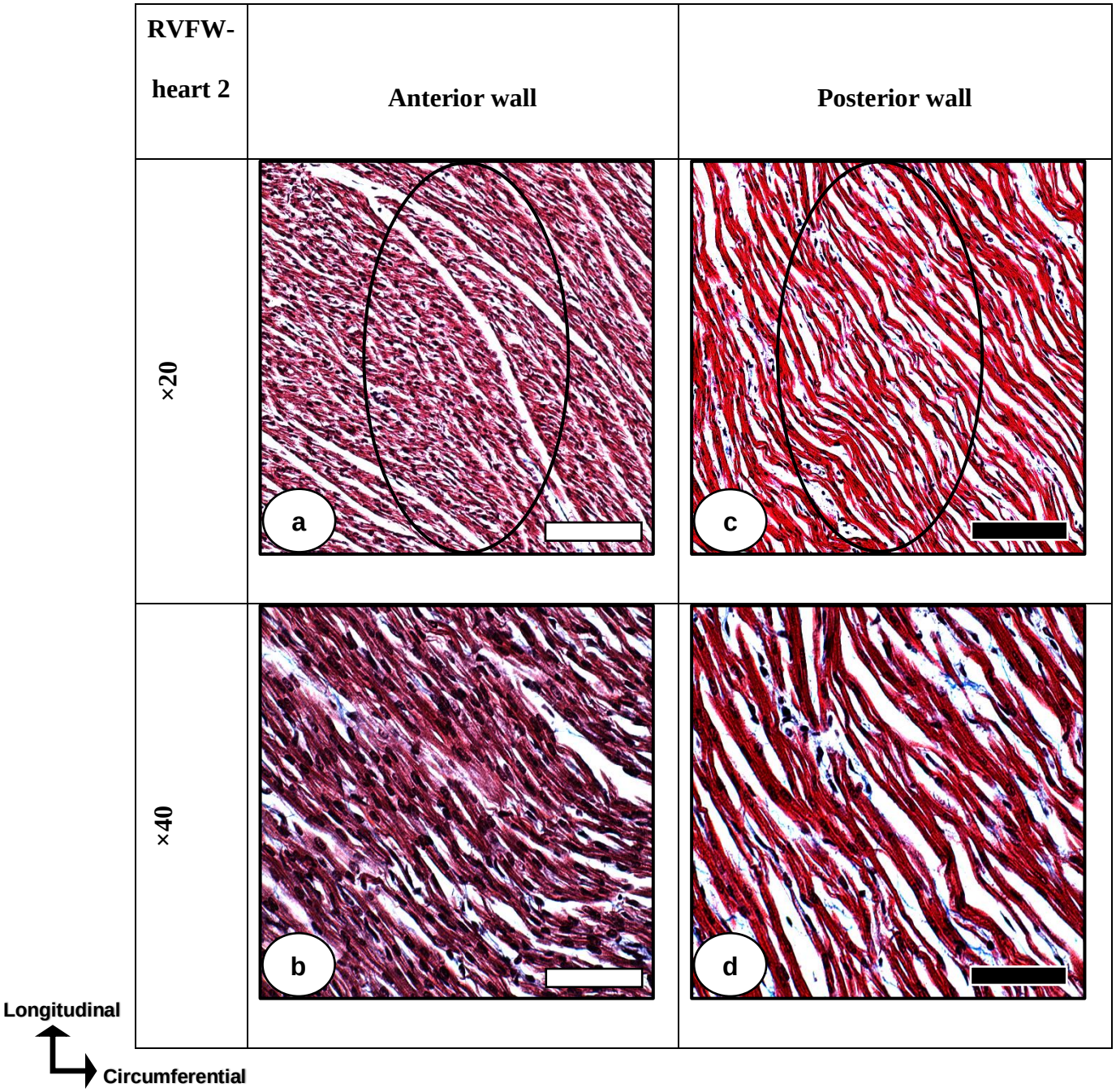

Figure 4.6: *Masson's trichrome staining images of the neonatal porcine ventricles, sectioned in the plane perpendicular to the transmural direction (i.e. in-plane), and viewed at × 20 and × 40 magnification. The RVFW–anterior* ***(a–b)*** *and posterior* ***(c–d)*** *aspects demonstrated almost symmetrical fibre alignment, with the former having greater concentration and alignment of muscle fibres. Principal or preferred fibre angles are detailed in Table 4.1. Scale bar at* ***×20*** *=100 µm and at* ***×40*** *=50µm, respectively.*

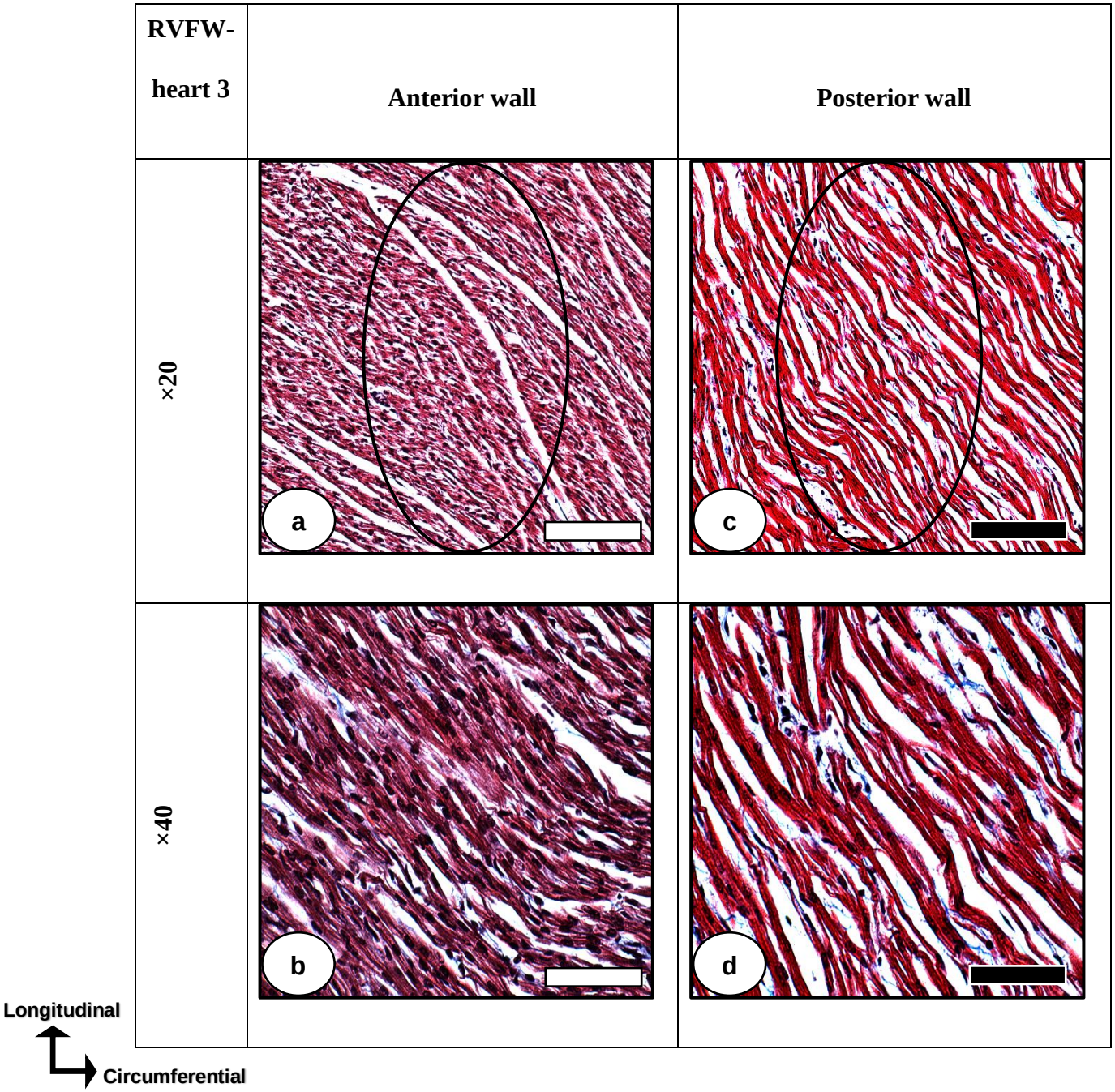

Figure 4.7: *Masson's trichrome staining images of the neonatal porcine ventricles, sectioned in the plane perpendicular to the transmural direction (i.e. in-plane), and viewed at × 20 and × 40 magnification. The RVFW–anterior* ***(a–b)*** *and posterior* ***(c–d)*** *aspects demonstrated almost symmetrical fibre alignment, with the former having greater concentration and alignment of muscle fibres. Principal or preferred fibre angles are detailed in Table 4.1. Scale bar at* ***×20*** *=100 µm and at* ***×40*** *=50µm, respectively..*

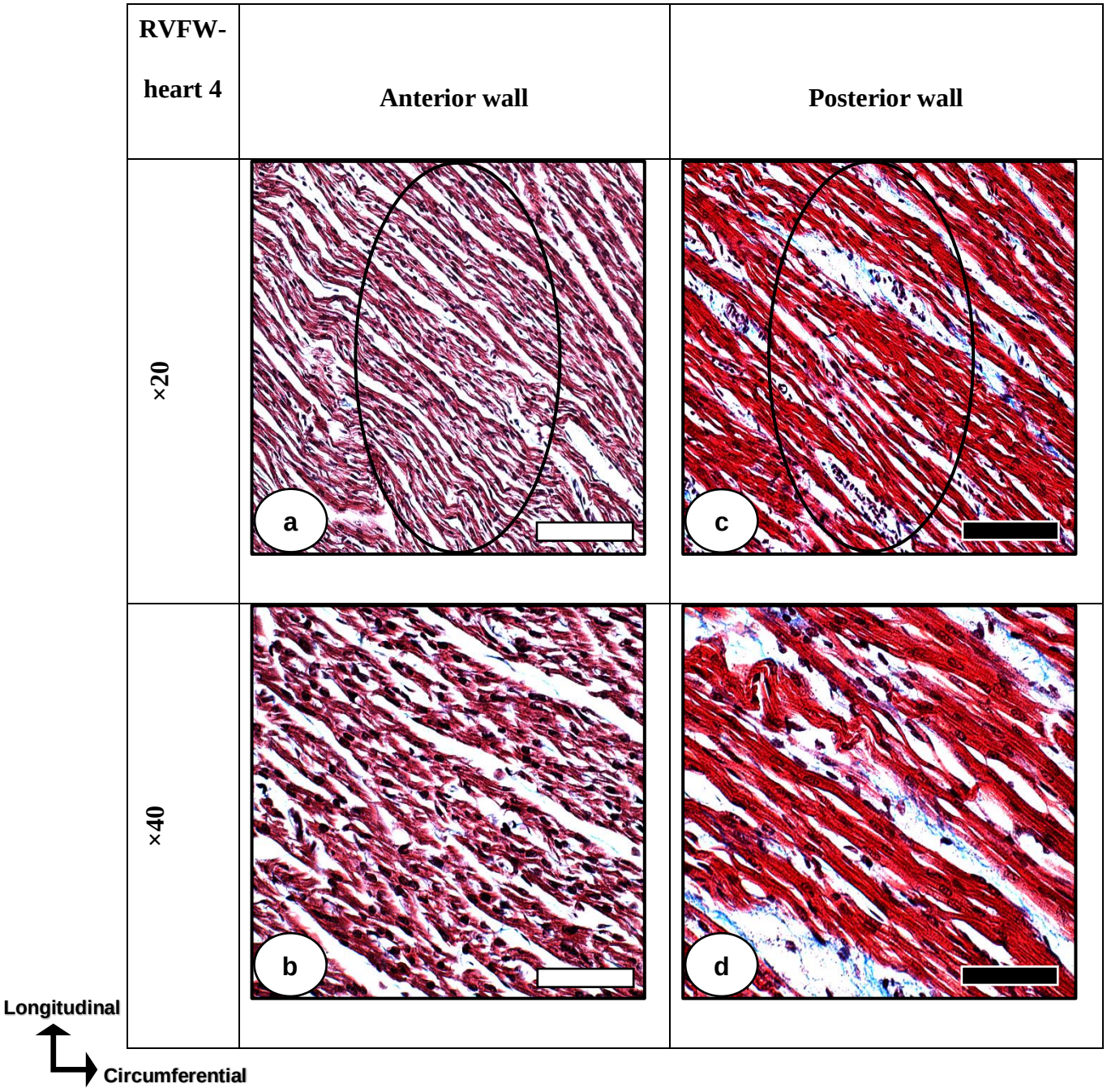

Figure 4.8: *Masson's trichrome staining images of the neonatal porcine ventricles, sectioned in the plane perpendicular to the transmural direction (i.e. in-plane), and viewed at × 20 and × 40 magnification. The RVFW–anterior* ***(a–b)*** *and posterior* ***(c–d)*** *aspects demonstrated almost symmetrical fibre alignment, with the former having greater concentration and alignment of muscle fibres. Principal or preferred fibre angles are detailed in Table 4.1. Scale bar at* ***×20*** *=100 µm and at* ***×40*** *=50µm, respectively.*

Table 4.1

The average in-plane principal fibre orientation parameter and coefficient of determination R^2 'goodness of fit' for RVFW and LVFW in the anterior (n = 16) and posterior (n = 16) aspects. Histological specimens were examined in the direction perpendicular to the transmural plane; i.e., epicardium towards endocardium using Fourier-component image analysis method (n = 32).

Heart regions	Preferred fibre orientation μ (°)	(SD)	Coefficient of determination R^2	(SD)
LVFW (A)	4.19*	(0.6)	0.96	(0.4)
LVFW (P)	-60.98*	(0.7)	0.98	(0.6)
RVFW (A)	-40.77*	(0.2)	0.98	(0.7)
RVFW (P)	-44.01*	(0.4)	0.98	(0.6)

** One-way analysis of variance (ANOVA) revealed statistical significance between the anterior (A) and posterior (P) aspects of both ventricles $p < 0.05$.*

Table 4.2

The average surface area ratio of collagen to myocyte for RVFW and LVFW in the anterior (n = 16) and posterior (n = 16) aspects. Histological specimens were examined in transmural–plane; i.e., epicardium towards endocardium (n = 32) using custom MATLAB code.

Collagen / myocyte	LV (A)	(SD)	LV (P)	(SD)	RV (A)	(SD)	RV (P)	(SD)
Transmural - plane	0.10*	(0.5)	0.20*	(0.6)	0.03*	(0.3)	0.08*	(0.4)

** One-way analysis of variance (ANOVA) revealed statistical significance between the anterior (A) and posterior (P) aspects of both ventricles $p < 0.05$.*

4.1.2. TPEF / SHG analyses

The anterior and posterior aspects of both ventricles were microscopically investigated using the TPEF and SHG imaging techniques to identify the cardiomyocytes and collagen fibrils preferred orientation (°) and angular dispersion (°) through the ventricular walls (Figures 4.9–4.12). In-plane stacks were obtained through 200 µm z-depth, with x-y dimensions 425 × 425 µm. Out-plane stacks were acquired through 1022 µm y-depth, with x-z dimensions 425 × 425 µm. The SHG-channel, which is visualised in green, identifies the collagen fibril distribution, while the TPEF-channel in red, highlights cardiomyocyte distribution (Figures 4.9–4.12). Merging both channels enables the overlaying of these data, demonstrating the interaction between the interstitial collagen and cardiomyocytes (Figures 4.9–4.12). The correlation coefficient R^2 was calculated to determine the 'goodness of fit' between the highest histogram peak (i.e. preferred fibre orientation) and Gaussian function [180, 182, 183]. TPEF/SHG images with correlation > 0.8 were used for further analyses [52].

TPEF/SHG channels were used to measure the in-plane and out-plane cardiomyocyte and collagen fibril preferred orientation direction (°), angular dispersion (°) and amount (i.e. a measure of fibre distribution with the preferred orientation) parameters in the LVFW and RVFW as a function of depth through the stacks (Figures 4.13–4.16). The posterior wall of both ventricles exhibited the greater rate' (i.e. per unit thickness) of in-plane cardiomyocyte rotation and dispersion than the anterior wall (Table 4.3). The out-plane rate of cardiomyocytes rotation and dispersion was more pronounced in the RVFW, compared to the LVFW (Table 4.4). The posterior LVFW possessed the greater rate of in-plane collagen fibril rotation in both ventricles (Table 4.5), while the greatest in-plane collagen fibril dispersion rate was observed in the anterior LVFW (Table 4.5). The anterior RVFW exhibited the

greater rate of out-plane collagen fibril rotation and dispersion in both ventricles (Table 4.6). Overall, cardiomyocytes exhibited greater dispersion rate out-plane (Tables 4.3–4.6), whereas collagen fibril dispersion rate was more pronounced in-plane in both ventricles (Tables 4.3–4.6). Relatively high cardiomyocyte and collagen fibril rotation and dispersion rate were noted in the sub-epicardium region of both ventricles (Figures 4.13–4.16). Interstitial collagen was the greatest fraction in the anterior and posterior LVFW (Figures 4.9–4.12). The in-plane and out-plane cardiomyocytes rotation rates through the stack depth, and the corresponding angular dispersion and amount data, are described in Tables 4.3 and 4.4. The in-plane and out-plane collagen fibril rotation rates through the stack depth, and the equivalent angular dispersion and amount data, are described in Tables 4.5 and 4.6. Variations in the mean in-plane and out-plane cardiomyocyte rotation and dispersion were compared across the anterior and posterior aspects of both ventricles via a one-way analysis of variance (ANOVA) and Tukey HSD post hoc test, as detailed in Table 4.7. An identical approach was also used to assess the average in-plane and out-plane collagen fibril rotation and dispersion, as specified in Table 4.8.

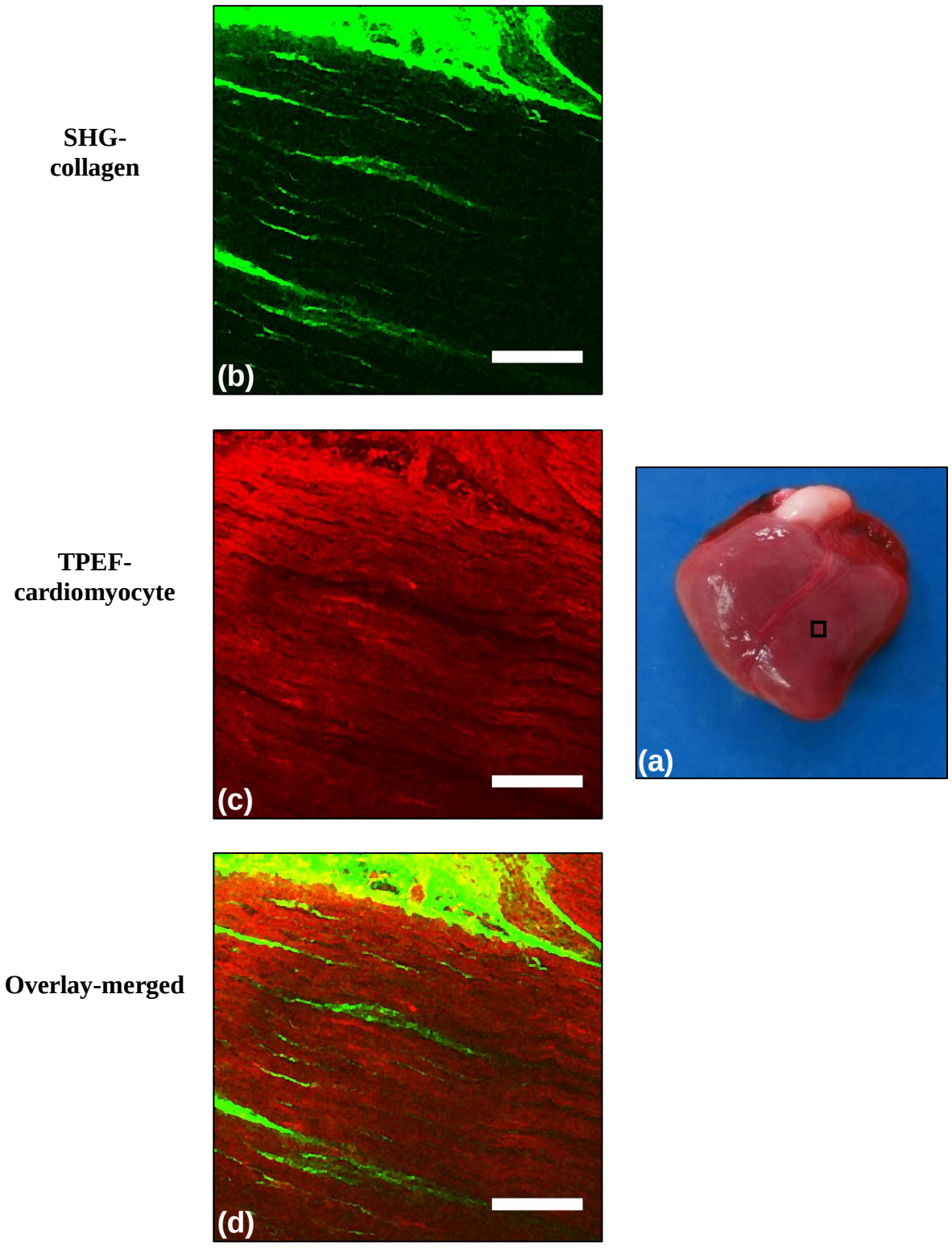

Figure 4.9: *In-plane TPEF/SHG images of the anterior LVFW.* ***(a)*** *The anterior view of one-day-old neonatal porcine heart;* ***(b)*** *SHG-channel was displayed in green, to identify the collagen fibril distribution;* ***(c)*** *TPEF-channel was shown in red, to specify the cardiomyocyte distribution;* ***(d)*** *Both channels were merged to demonstrate the collagen-cardiomyocyte overlapping. Scale bar measures 100 µm.*

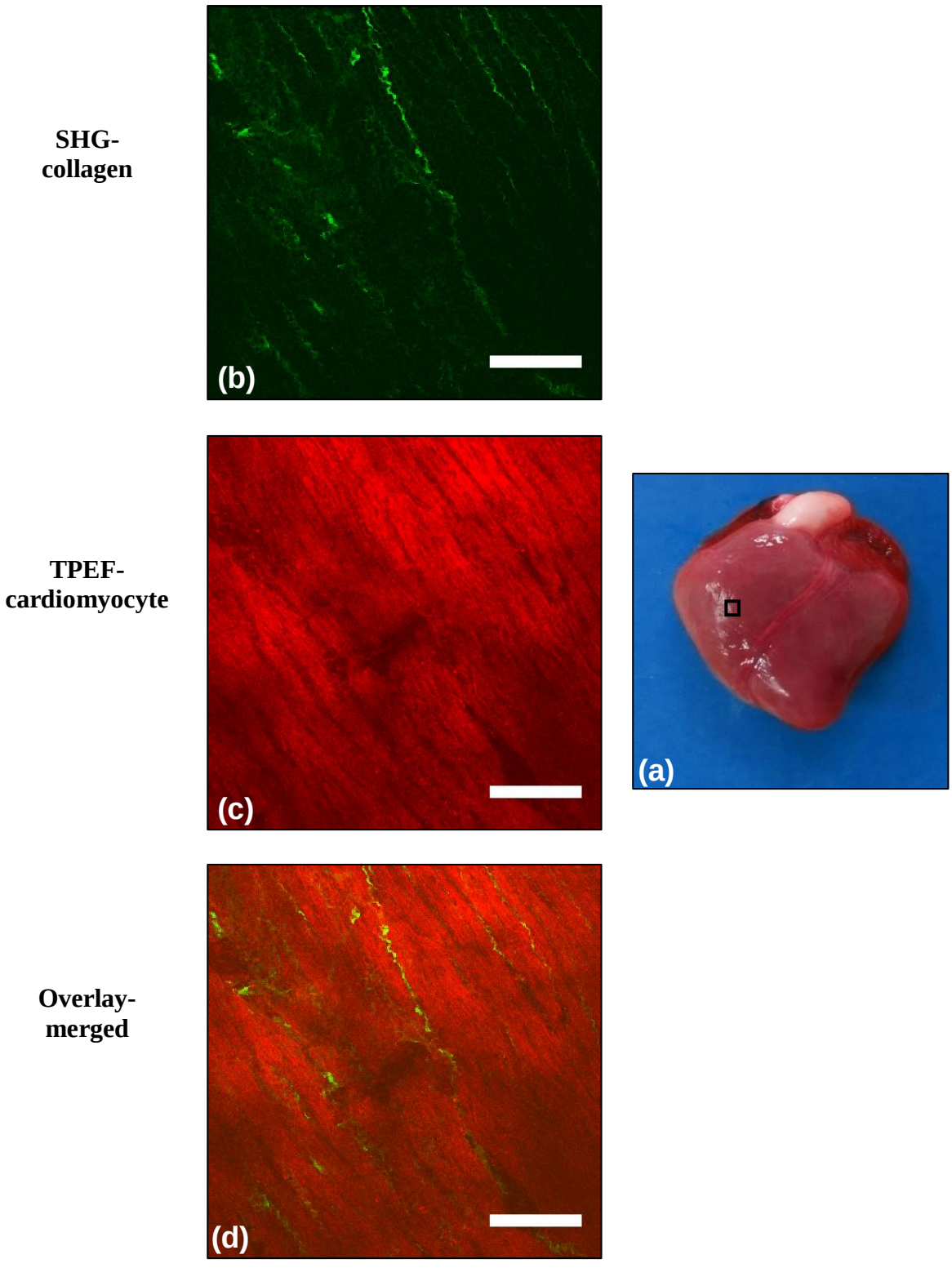

Figure 4.10: *In-plane TPEF/SHG images of the anterior RVFW.* ***(a)*** *The anterior view of one-day-old neonatal porcine heart;* ***(b)*** *SHG-channel was displayed in green, to identify the collagen fibril distribution;* ***(c)*** *TPEF-channel was shown in red, to specify the cardiomyocyte distribution;* ***(d)*** *Both channels were merged to demonstrate the collagen-cardiomyocyte overlapping. Scale bar measures 100 µm.*

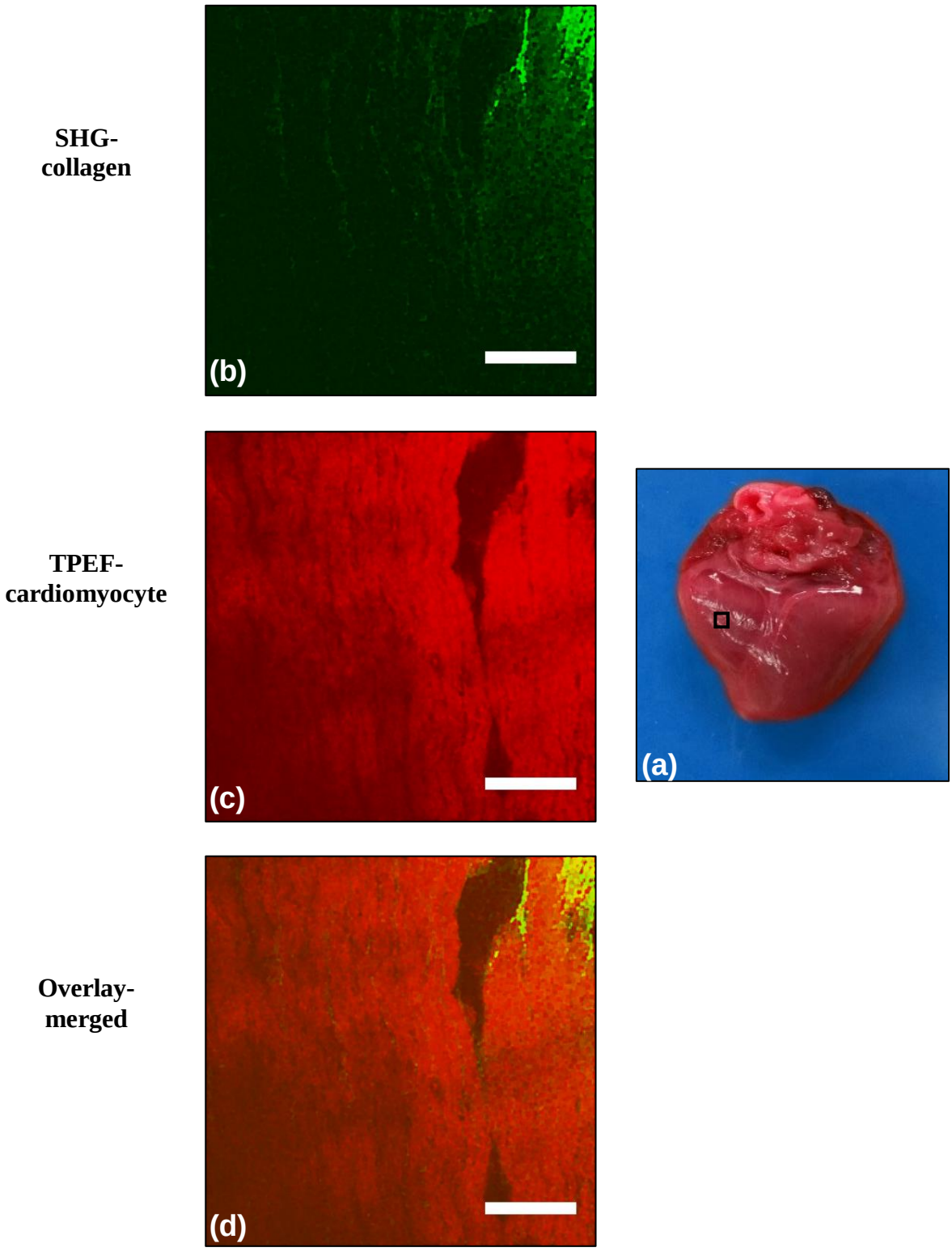

Figure 4.11: *In-plane TPEF/SHG images of the posterior LVFW.* ***(a)*** *The anterior view of one-day-old neonatal porcine heart;* ***(b)*** *SHG-channel was displayed in green, to identify the collagen fibril distribution;* ***(c)*** *TPEF-channel was shown in red, to specify the cardiomyocyte distribution;* ***(d)*** *Both channels were merged to demonstrate the collagen-cardiomyocyte overlapping. Scale bar measures 100 µm.*

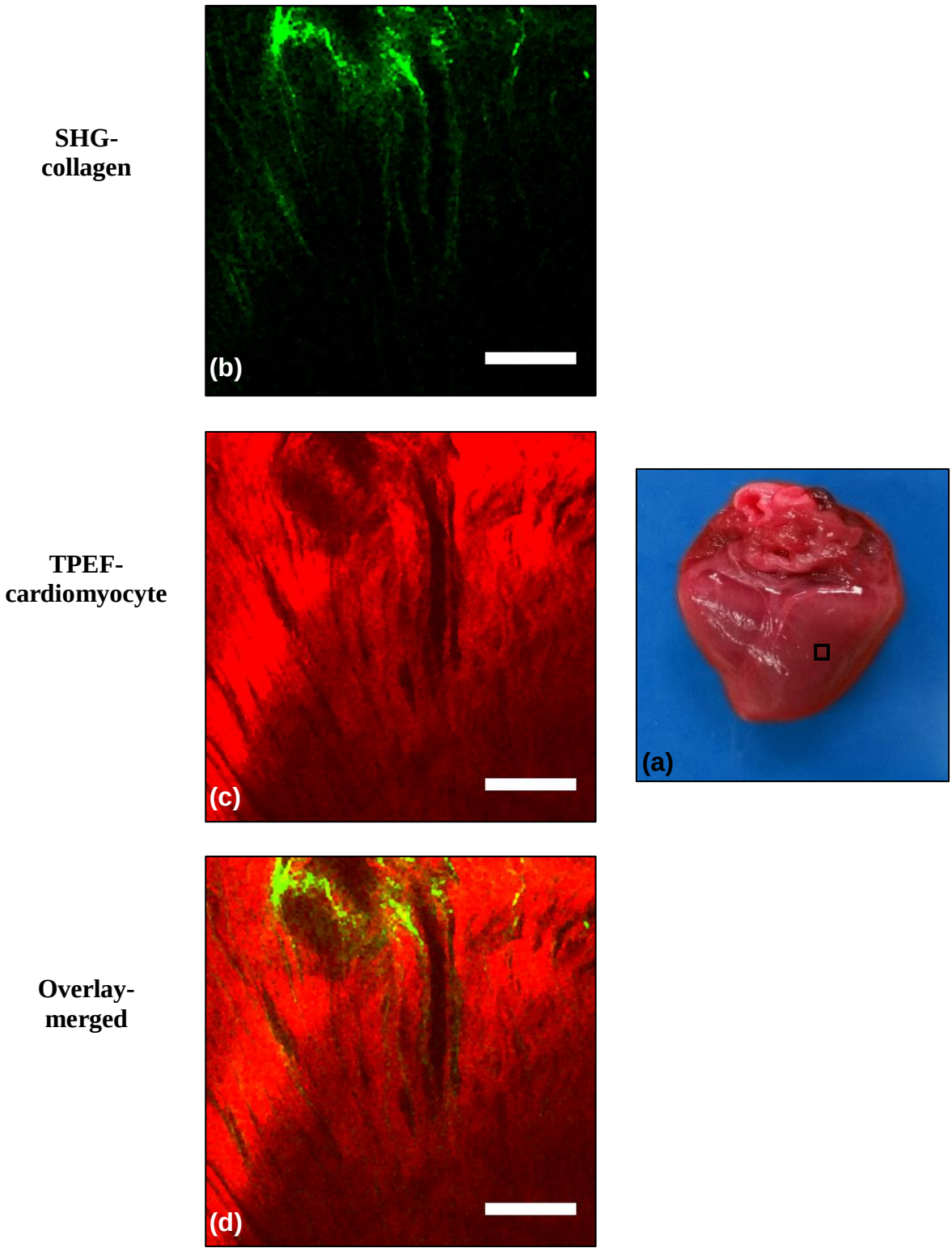

Figure 4.12: *In-plane TPEF/SHG images of the posterior RVFW.* ***(a)*** *The anterior view of one-day-old neonatal porcine heart;* ***(b)*** *SHG-channel was displayed in green, to identify the collagen fibril distribution;* ***(c)*** *TPEF-channel was shown in red, to specify the cardiomyocyte distribution;* ***(d)*** *Both channels were merged to demonstrate the collagen-cardiomyocyte overlapping. Scale bar measures 100 µm.*

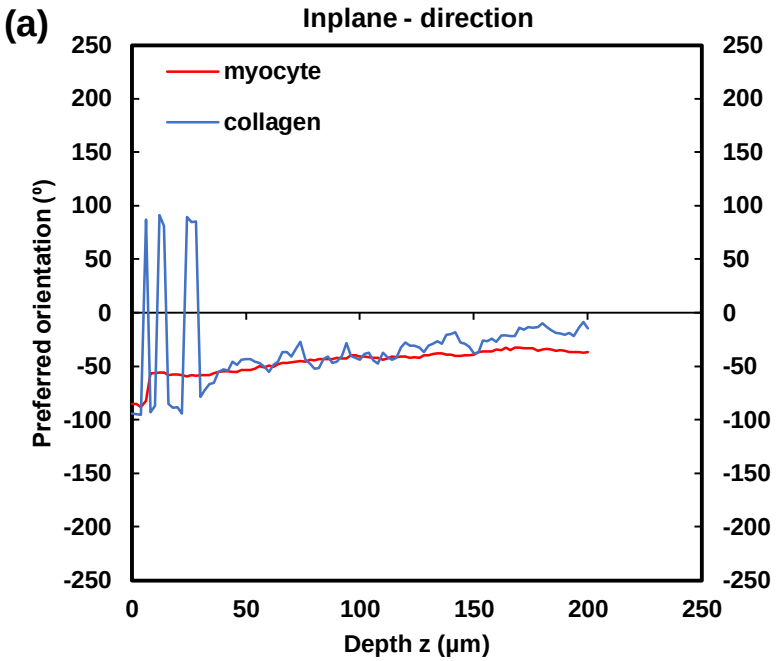
(a)
Inplane - direction
myocyte
collagen
Preferred orientation (°)
Depth z (μm)
250
200
150
100
50
0
-50
-100
-150
-200
-250
0
50
100
150
200
250

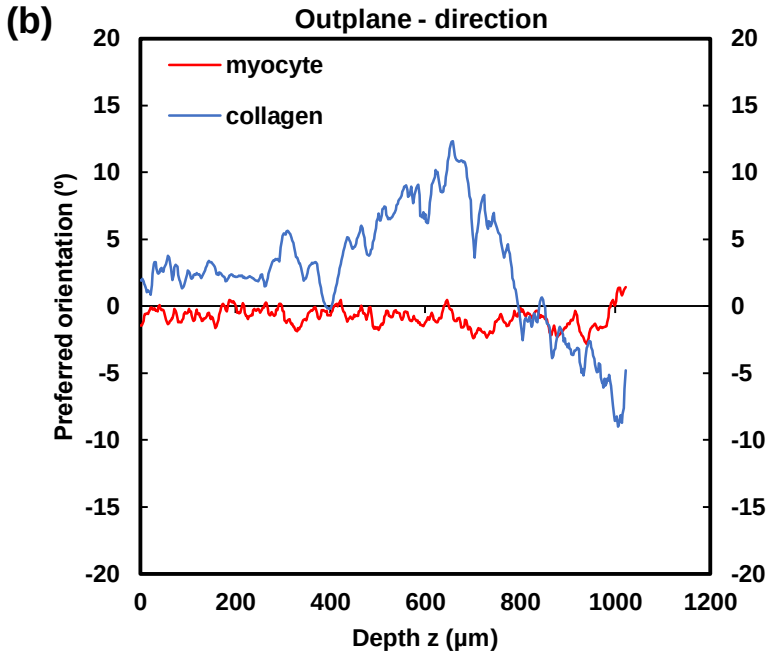
(b)
Outplane - direction
myocyte
collagen
Preferred orientation (°)
Depth z (μm)
20
15
10
5
0
-5
-10
-15
-20
0
200
400
600
800
1000
1200

(c)

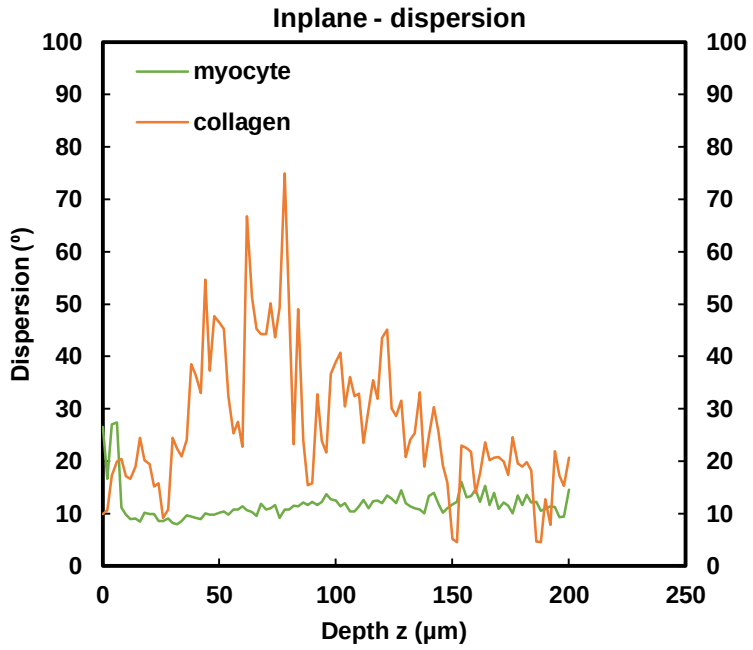
Inplane - dispersion
myocyte
collagen
Dispersion (°)
Depth z (μm)
0
10
20
30
40
50
60
70
80
90
100
0
50
100
150
200
250

(d)

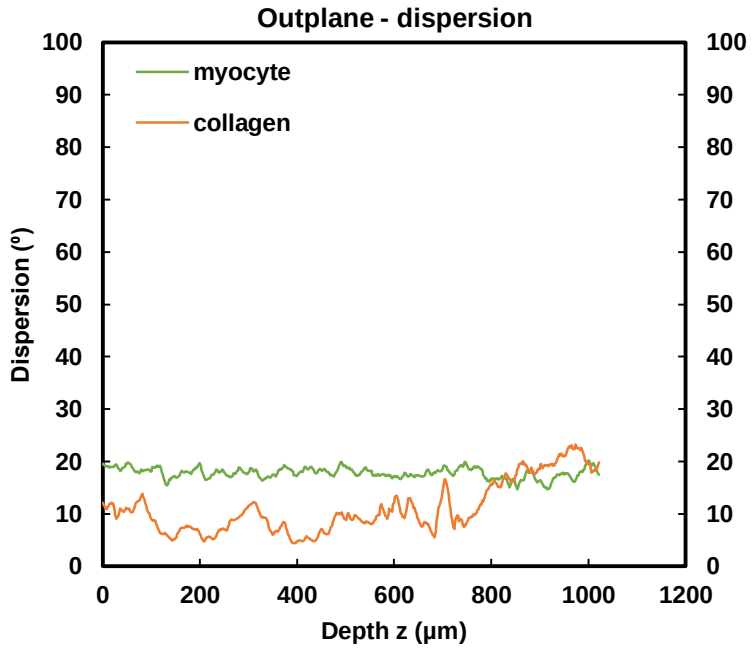
Outplane - dispersion
myocyte
collagen
Dispersion (°)
Depth z (μm)
0
10
20
30
40
50
60
70
80
90
100
0
200
400
600
800
1000
1200

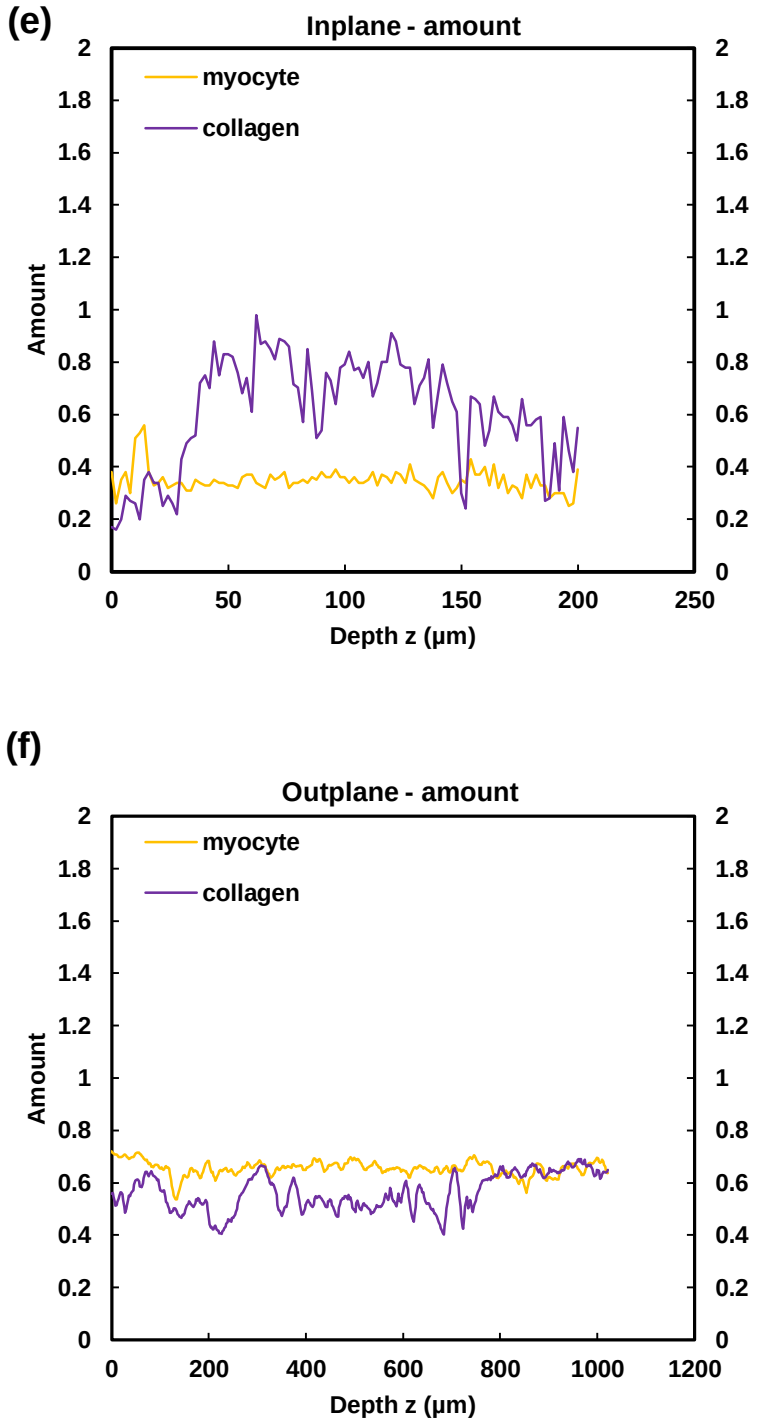

Figure 4.13: *TPEF/SHG microscopy was used to quantify the mean in-plane and out-plane cardiomyocyte and collagen fibril microstructural parameters of the anterior LVFW.* ***(a)*** *in-plane preferred orientation;* ***(b)*** *out-plane preferred orientation;* ***(c)*** *in-plane dispersion;* ***(d)*** *out-plane dispersion;* ***(e)*** *in-plane amount;* ***(f)*** *out-plane amount. In-plane and out-plane image-stacks were acquired through the depth of 200-and 1022 μm, respectively.*

(a)

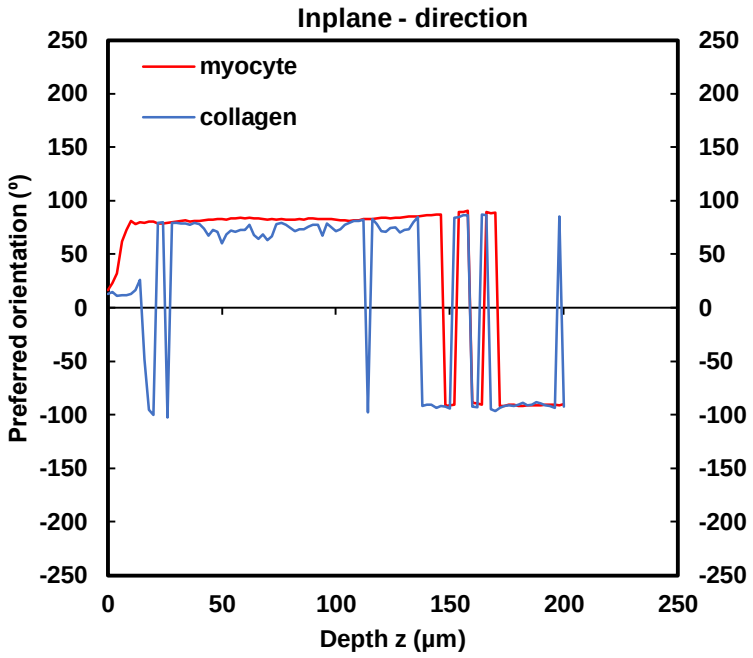
Inplane - direction
myocyte
collagen
Preferred orientation (°)
Depth z (μm)
250
200
150
100
50
0
-50
-100
-150
-200
-250
0
50
100
150
200
250

(b)

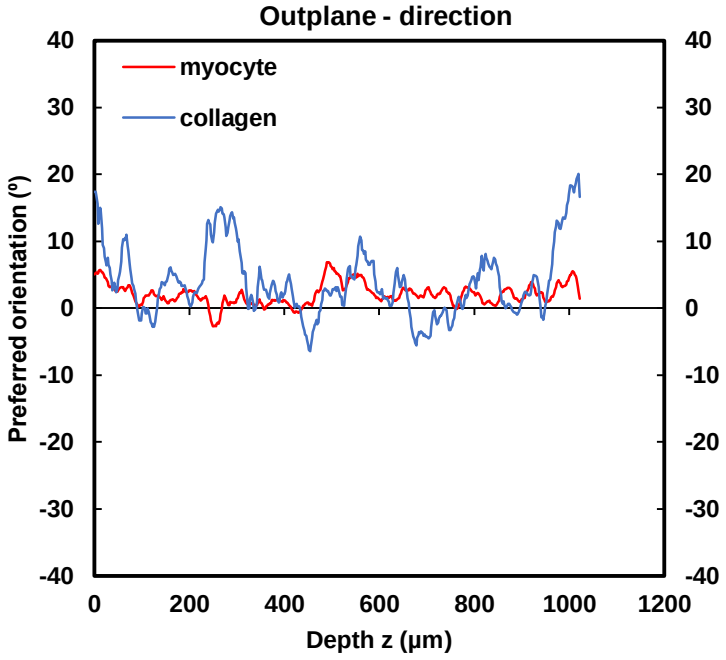
Outplane - direction
myocyte
collagen
Preferred orientation (°)
Depth z (μm)
40
30
20
10
0
-10
-20
-30
-40
0
200
400
600
800
1000
1200

(c)

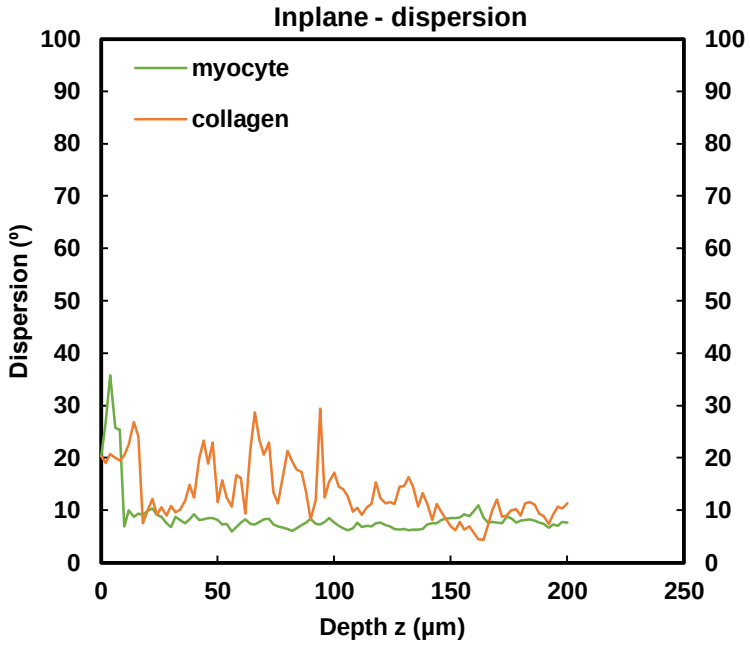
Inplane - dispersion
myocyte
collagen
Dispersion (°)
Depth z (μm)
0
10
20
30
40
50
60
70
80
90
100
0
50
100
150
200
250

(d)

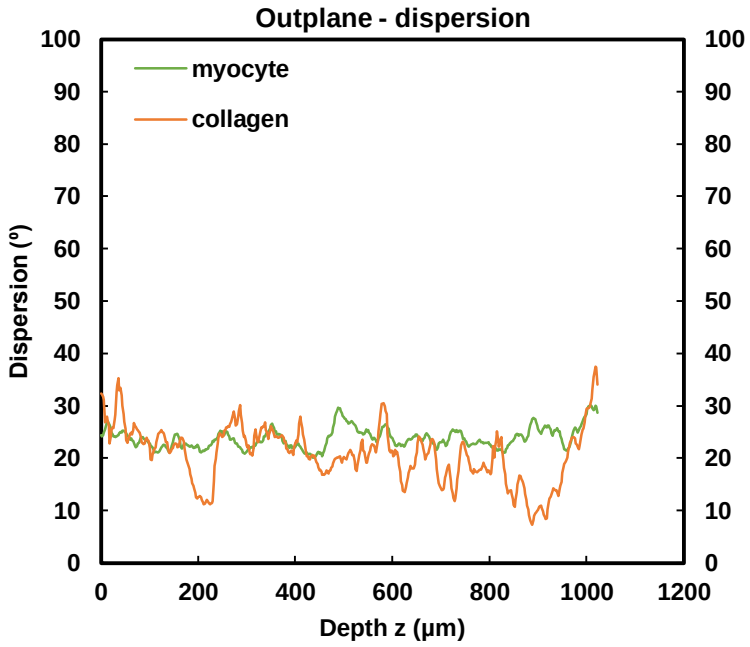
Outplane - dispersion
myocyte
collagen
Dispersion (°)
Depth z (μm)
0
10
20
30
40
50
60
70
80
90
100
0
200
400
600
800
1000
1200

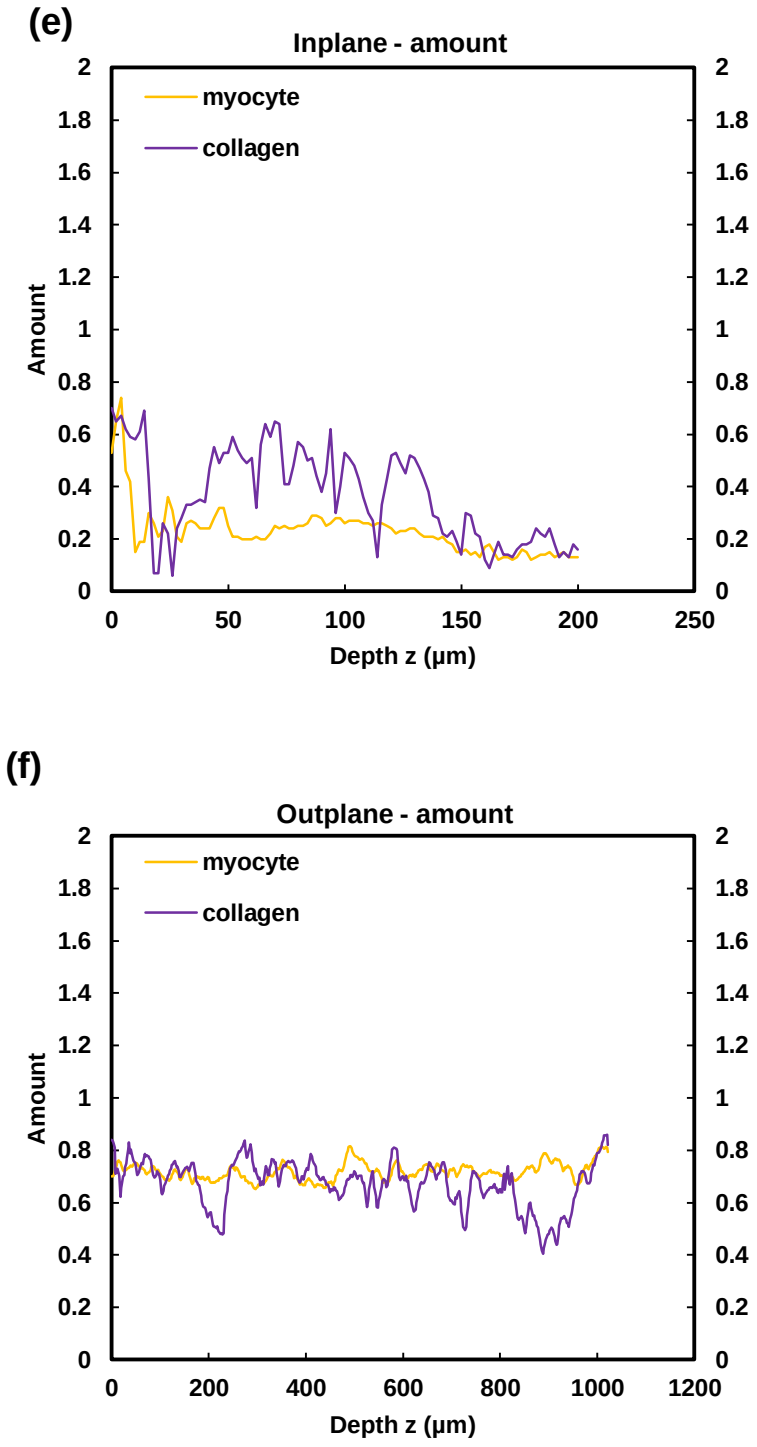

Figure 4.14: *TPEF/SHG microscopy was used to quantify the mean in-plane and out-plane cardiomyocytes and collagen fibrils microstructural parameters of the anterior RVFW.* ***(a)*** *in-plane preferred orientation;* ***(b)*** *out-plane preferred orientation;* ***(c)*** *in-plane dispersion;* ***(d)*** *out-plane dispersion;* ***(e)*** *in-plane amount;* ***(f)*** *out-plane amount. In-plane and out-plane image-stacks were acquired through the depth of 200-and 1022 μm, respectively.*

(a)

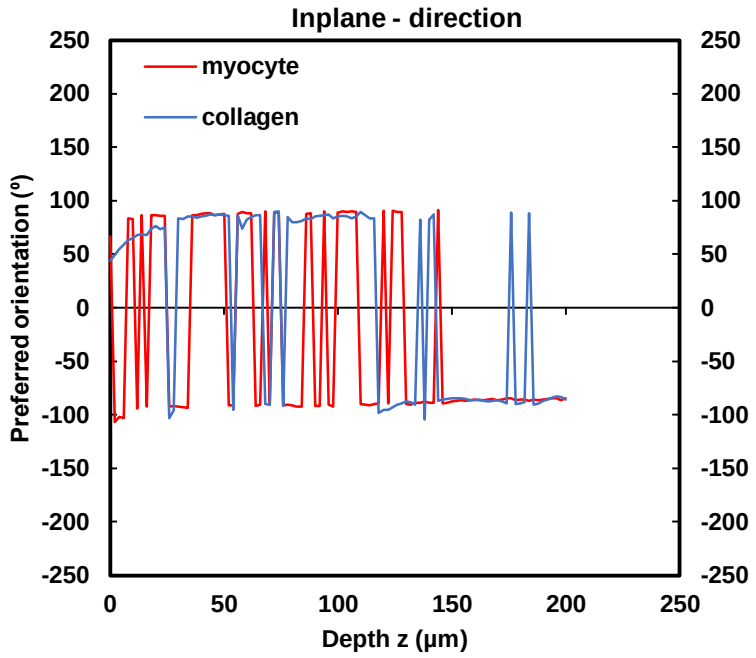
Inplane - direction
myocyte
collagen
Preferred orientation (°)
Depth z (μm)
250
200
150
100
50
0
-50
-100
-150
-200
-250
0
50
100
150
200
250

(b)

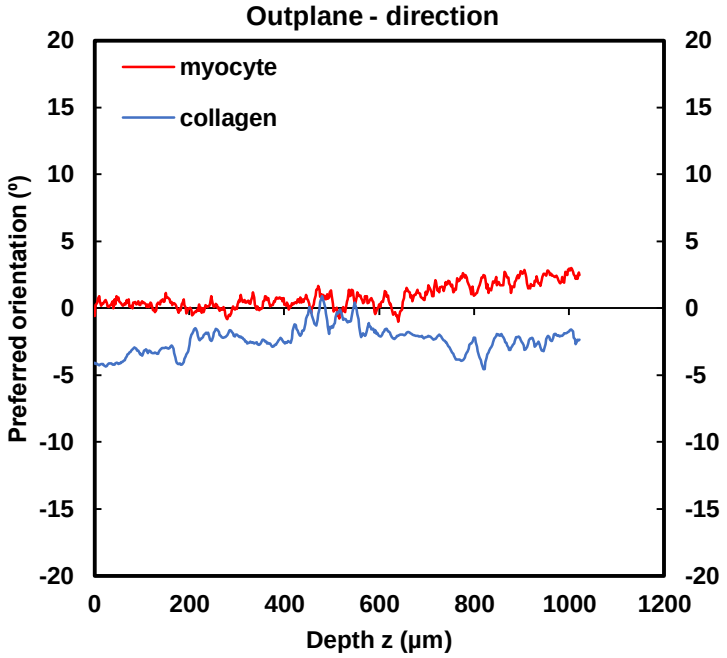
Outplane - direction
myocyte
collagen
Preferred orientation (°)
Depth z (μm)
20
15
10
5
0
-5
-10
-15
-20
0
200
400
600
800
1000
1200

(c)

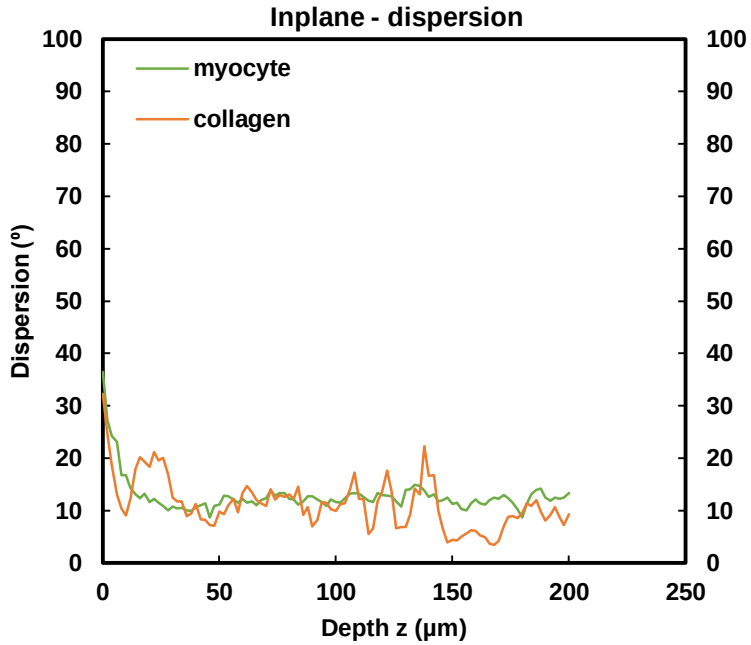
Inplane - dispersion
myocyte
collagen
Dispersion (°)
Depth z (μm)
0
10
20
30
40
50
60
70
80
90
100
0
50
100
150
200
250

(d)

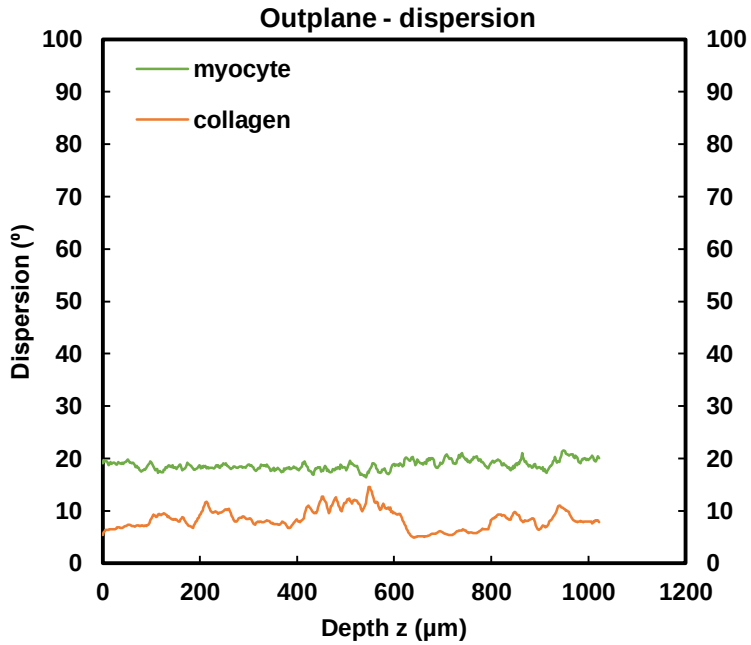
Outplane - dispersion
myocyte
collagen
Dispersion (°)
Depth z (μm)
0
10
20
30
40
50
60
70
80
90
100
0
200
400
600
800
1000
1200

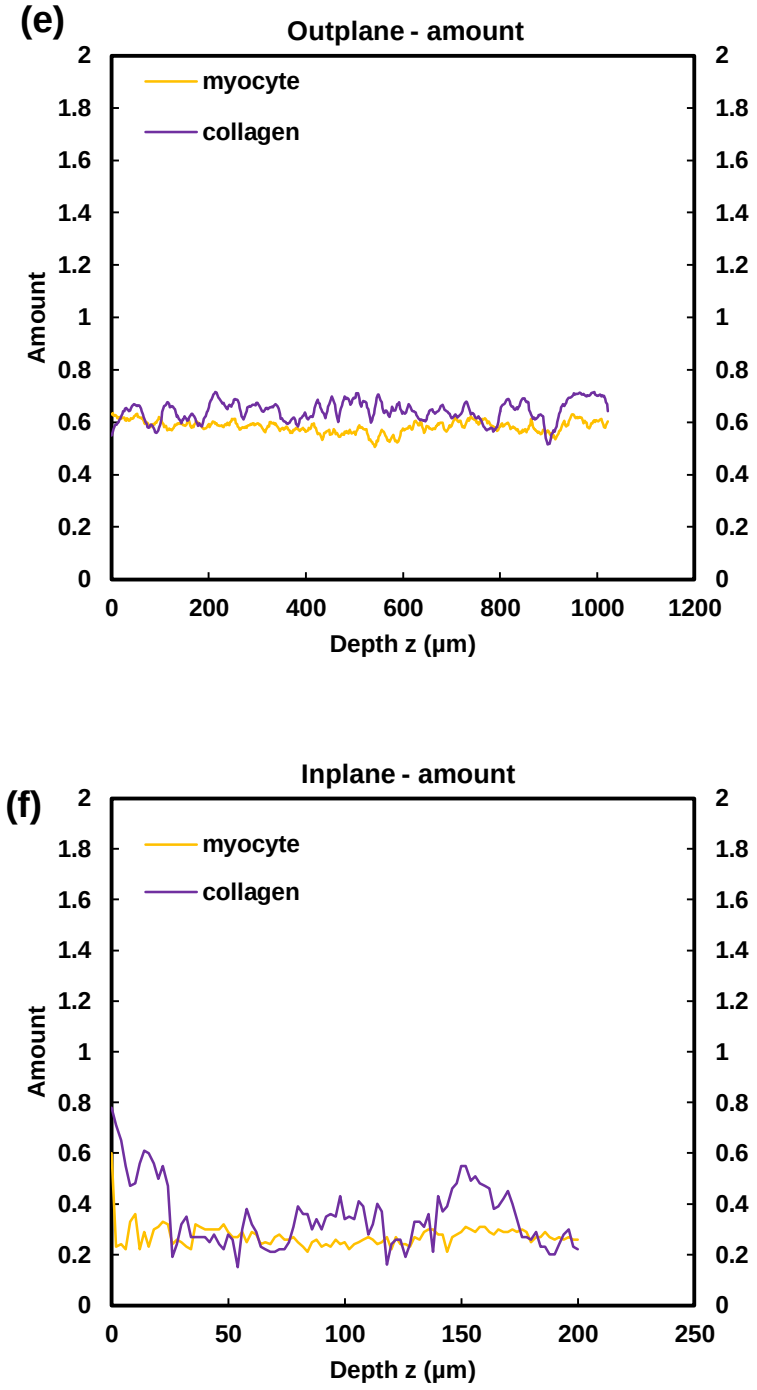

Figure 4.15: *TPEF/SHG microscopy was used to quantify the mean in-plane and out-plane cardiomyocyte and collagen fibril microstructural parameters of the posterior LVFW.* ***(a)*** *in-plane preferred orientation;* ***(b)*** *out-plane preferred orientation;* ***(c)*** *in-plane dispersion;* ***(d)*** *out-plane dispersion;* ***(e)*** *in-plane amount;* ***(f)*** *out-plane amount. In-plane and out-plane image-stacks were acquired through the depth of 200-and 1022 µm, respectively.*

(a)

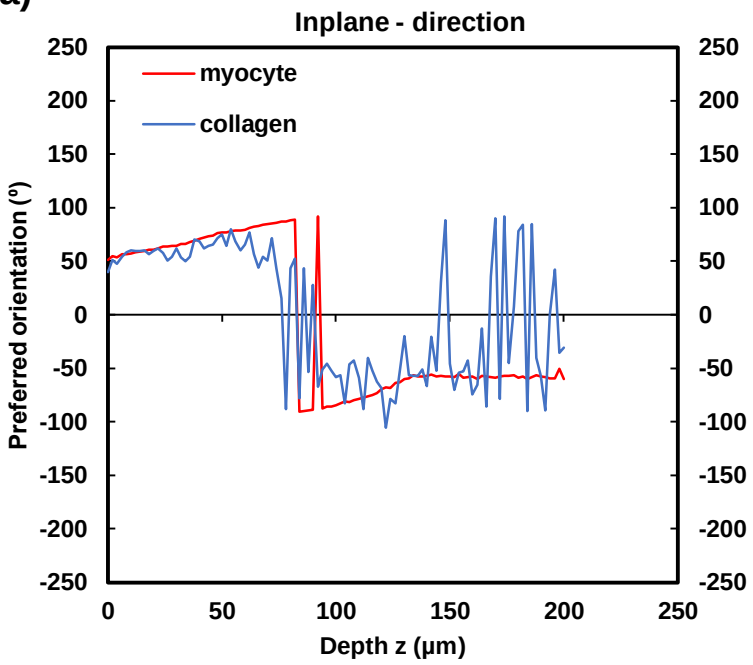
Inplane - direction
myocyte
collagen
Preferred orientation (°)
Depth z (μm)
250
200
150
100
50
0
-50
-100
-150
-200
-250
0
50
100
150
200
250

(b)

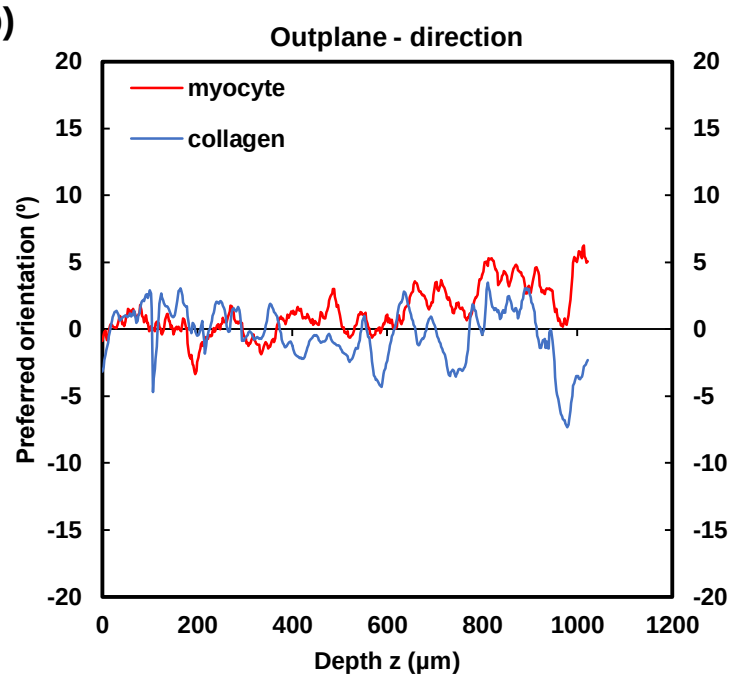
Outplane - direction
myocyte
collagen
Preferred orientation (°)
Depth z (μm)
20
15
10
5
0
-5
-10
-15
-20
0
200
400
600
800
1000
1200

(c)

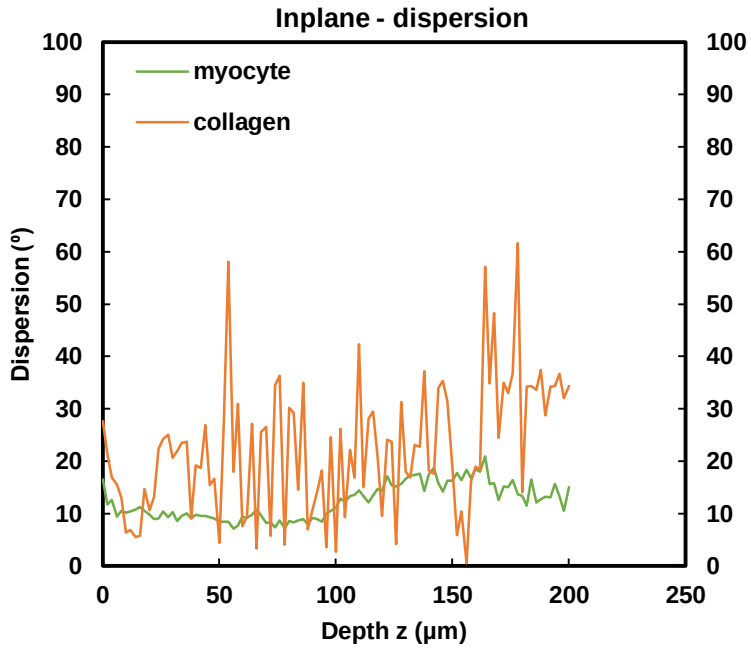
Inplane - dispersion
myocyte
collagen
Dispersion (°)
Depth z (μm)
0
10
20
30
40
50
60
70
80
90
100
0
50
100
150
200
250

(d)

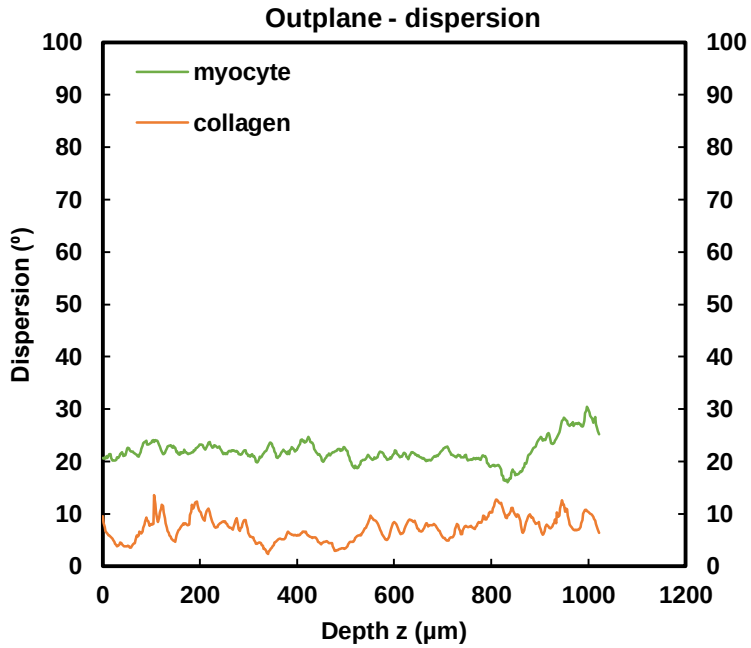
Outplane - dispersion
myocyte
collagen
Dispersion (°)
Depth z (μm)
0
10
20
30
40
50
60
70
80
90
100
0
200
400
600
800
1000
1200

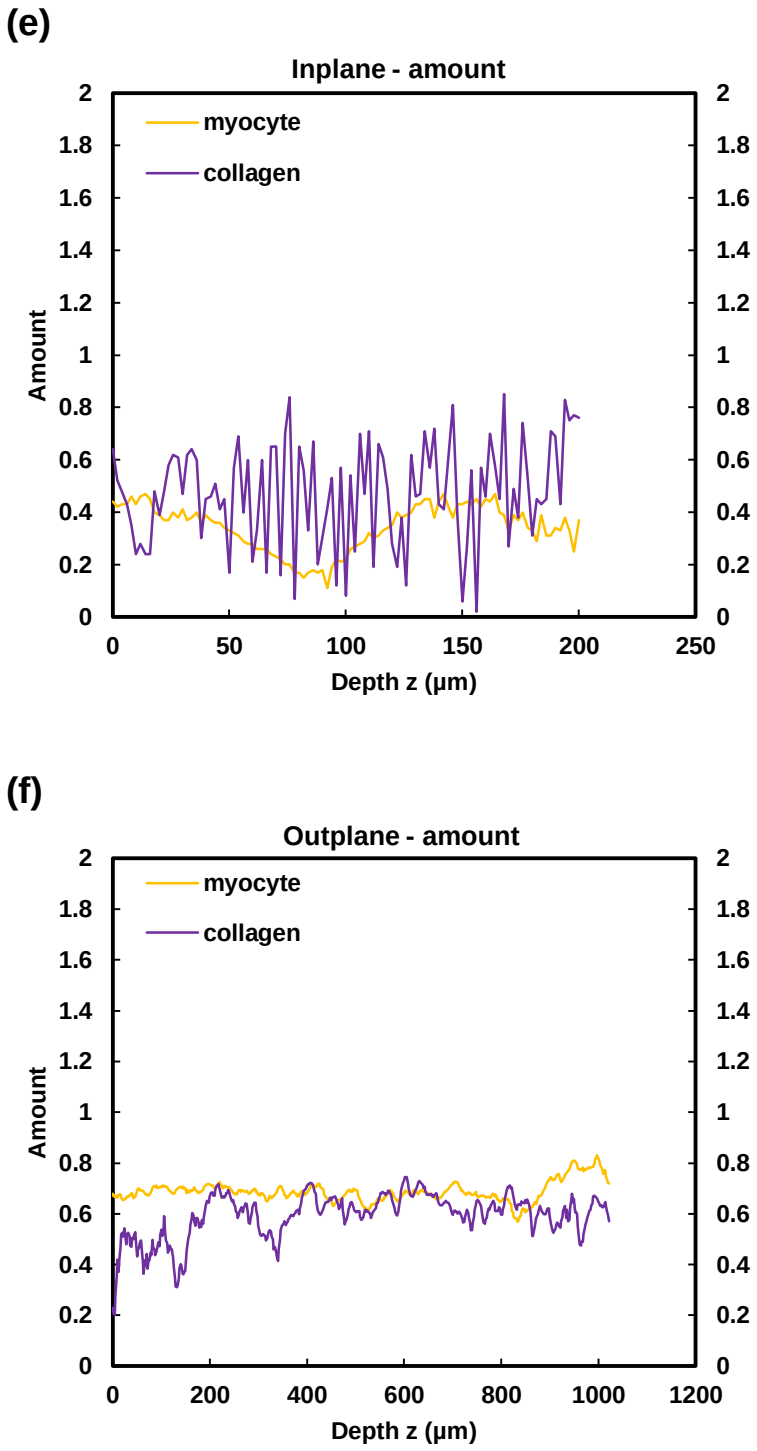

Figure 4.16: *TPEF/SHG microscopy was used to quantify the mean in-plane and out-plane cardiomyocyte and collagen fibril microstructural parameters of the posterior RVFW.* ***(a)*** *in-plane preferred orientation;* ***(b)*** *out-plane preferred orientation;* ***(c)*** *in-plane dispersion;* ***(d)*** *out-plane dispersion;* ***(e)*** *in-plane amount;* ***(f)*** *out-plane amount. In-plane and out-plane image-stacks were acquired through the depth of 200-and 1022 μm, respectively.*

Table 4.3

In-plane cardiomyocyte rotation, dispersion and amount through the LVFW and RVFW, across 200 µm depth of the anterior (A) and posterior (P) aspects.

	Rotation (º)	Dispersion (º)	Amount
LVFW(A)	48 ± 5.3*	11.8 ± 3.0*	0.35 ± 0.04
RVFW(A)	106.7 ± 10.6*	8.7 ± 2.0*	0.23 ± 0.05
LVFW(P)	151.3 ± 9.2*	12.8 ± 1.5*	0.27 ± 0.09
RVFW(P)	111.2 ± 3.2*	12.3 ± 2.3*	0.34 ± 0.05

*Results are expressed as mean ± SD (n=5). * One-way analysis of variance (ANOVA) revealed statistical significance between the anterior (A) and posterior (P) aspects of both ventricles $p < 0.05$.*

Table 4.4

Out-plane cardiomyocyte rotation, dispersion and amount through the LVFW and RVFW, across 1022 µm depth in the anterior (A) and posterior (P) aspects.

	Rotation (º)	Dispersion (º)	Amount
LVFW (A)	3.5 ± 2.8*	17.8 ± 1.9*	0.65 ± 0.03
RVFW (A)	8.4 ± 3.6*	23.9 ± 4.1*	0.72 ± 0.07
LVFW (P)	2.2 ± 2.8*	18.8 ± 1.6*	0.58 ± 0.02
RVFW (P)	6.4 ± 1.2*	22 ± 2.4*	0.69 ± 0.06

Results are expressed as mean ± SD (n=5). One-way analysis of variance (ANOVA) revealed statistical significance between the anterior (A) and posterior (P) aspects of both ventricles $p < 0.05$.

Table 4.5

In-plane collagen fibril rotation, dispersion and amount through the LVFW and RVFW, across 200 µm depth in the anterior (A) and posterior (P) aspects.

	Rotation (º)	Dispersion (º)	Amount
LVFW (A)	41 ± 3.8*	27.1 ± 2.8*	0.61 ± 0.09
RVFW (A)	104.8 ± 6.5*	13.4 ± 4.2*	0.37 ± 0.1
LVFW (P)	129.5 ± 2.9*	14.3 ± 1.8*	0.35 ± 0.08
RVFW (P)	70.7 ± 6.2*	22.4 ± 3.1*	0.48 ± 0.07

*Results are expressed as mean ± SD (n=5). * One-way analysis of variance (ANOVA) revealed statistical significance between the anterior (A) and posterior (P) aspects of both ventricles $p < 0.05$.*

Table 4.6

Out-plane collagen fibril rotation, dispersion and amount through the LVFW and RVFW, across 1022 µm depth in the anterior (A) and posterior (P) aspects.

	Rotation (º)	Dispersion (º)	Amount
LVFW (A)	1.1 ± 1.7*	11.2 ± 2.3*	0.56 ± 0.04
RVFW (A)	2.7 ± 4.1*	20.8 ± 3.8*	0.67 ± 0.02
LVFW (P)	1.8 ± 2.4*	8.4 ± 3.5*	0.64 ± 0.03
RVFW (P)	1.6 ± 4.8*	7.2 ± 3.6*	0.60 ± 0.04

*Results are expressed as mean ± SD (n=5). * One-way analysis of variance (ANOVA) revealed statistical significance between the anterior (A) and posterior (P) aspects of both ventricles $p < 0.05$.*

Table 4.7

Statistical data describing the significance of difference in cardiomyocyte rotation (1–4) and dispersion (5–8) between the anterior (A) and posterior (P) aspects of the LVFW and RVFW for: (1) LVFW (A and P) in-plane; (2) RVFW (A and P) in-plane; (3) LVFW (A and P) out-plane; (4) RVFW (A and P) out-plane. (5) LVFW (A and P) in-plane; (6) RVFW (A and P) in-plane; (7) LVFW (A and P) out-plane; and (8) RVFW (A and P) out-plane.

Configurations	LVFW (A)	LVFW (P)	RVFW (A)	RVFW (P)
1	0.001	0.002	-	-
2	-	-	0.001	0.001
3	0.001	0.002	-	-
4	-	-	0.001	0.001
5	0.001	0.003	-	-
6	-	-	0.001	0.002
7	0.001	0.003	-	-
8	-	-	0.001	0.002

Table 4.8

Statistical data describing the significance of difference in collagen fibril rotation (1–4) and dispersion (5–8) between the anterior (A) and posterior (P) aspects of the LVFW and RVFW for: (1) LVFW (A and P) in-plane; (2) RVFW (A and P) in-plane; (3) LVFW (A and P) out-plane; (4) RVFW (A and P) out-plane. (5) LVFW (A and P) in-plane; (6) RVFW (A and P) in-plane; (7) LVFW (A and P) out-plane; and (8) RVFW (A and P) out-plane.

Configurations	**LVFW (A)**	**LVFW (P)**	**RVFW (A)**	**RVFW (P)**
1	0.002	0.002	-	-
2	-	-	0.003	0.001
3	0.002	0.002	-	-
4	-	-	0.001	0.003
5	0.002	0.003	-	-
6	-	-	0.001	0.002
7	0.003	0.003	-	-
8	-	-	0.002	0.002

4.1.3. DT–MRI analysis

4.1.3.1. Fractional anisotropy and fibre tractography

Unscented Kalman filter (UKF) tractography was used to identify the helical cardiomyocyte architecture of neonatal porcine ventricles, as shown in Figures 4.18 (a)–(f). The detailed methodology used in evaluating fractional anisotropy and performing fibre tractography has been stated in Section 3.3.1.3, Chapter 3. Figure 4.17 (a) highlights the (1) base, (2) equator and (3) apex regions of both ventricles anteriorly, which were used to quantify the scalar measurements of FA. The particular measurement describes the variation in water diffusion anisotropy within these regions. The anterior RVFW exhibited slightly greater FA in all three regions, compared to the LVFW (Tables 4.9 and 4.10). The equatorial region of both ventricles possessed greater FA, with the lowest observed in the apex. The average LVFW and RVFW FA are detailed in Tables 4.9 and 4.10. The greatest cardiomyocyte density was observed in the lower base and equator regions (Figures 4.18 (a)–(f)). Cardiomyocytes were aligned horizontally (relative to the defined vertical axis of the heart, passing through the apex and base) in the anterior surface of both ventricles (Figures 4.18 (a), (c) and (e)). Cardiomyocytes in the posterior surface of the LVFW were diagonally aligned, and horizontal in the RVFW (Figures 4.18 (b), (d) and (f)). Cardiomyocytes were predominantly aligned in parallel towards the lower base and equator regions, although weaker alignment was evident in the apex of both ventricles anteriorly and posteriorly (Figures 4.18 (a)–(f). At one-day post birth, the neonatal RVFW (~ 4 mm) thickness was almost consistent with the LVFW (~ 5 mm).

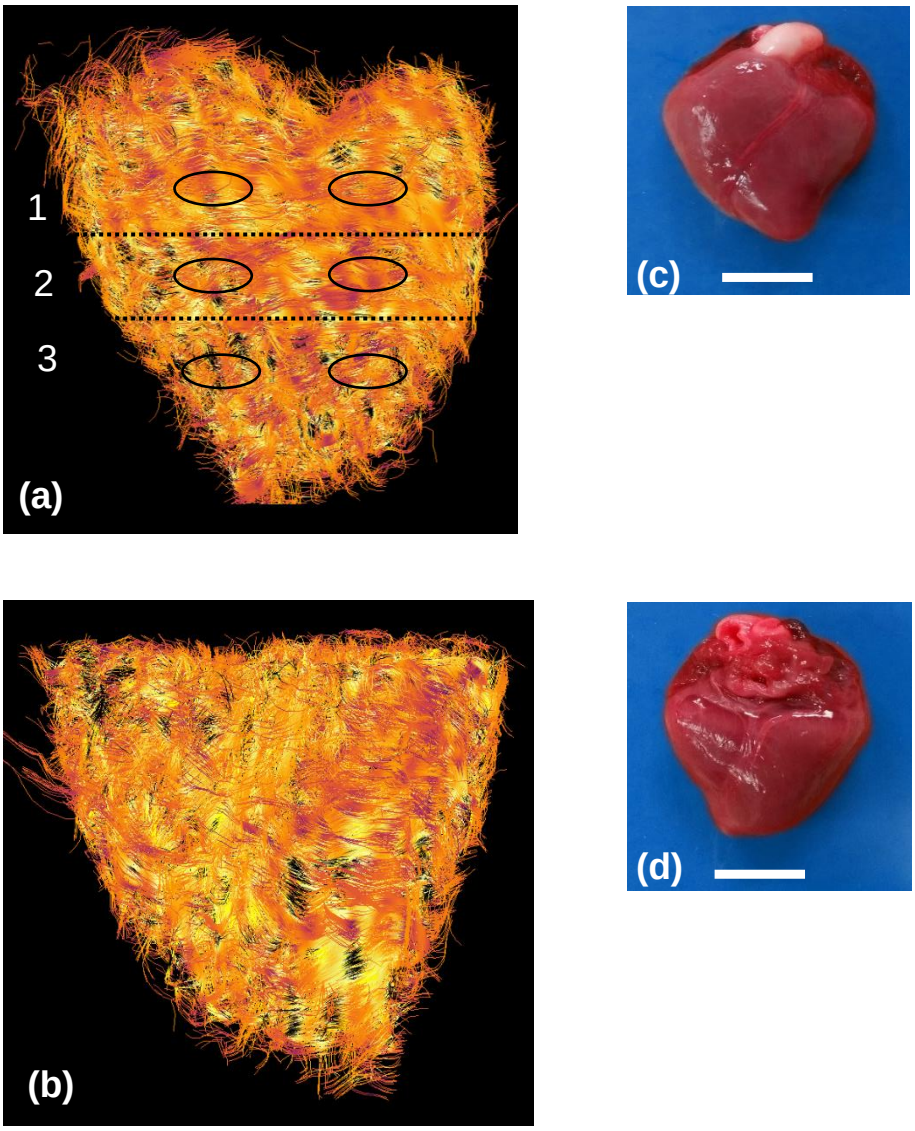

Figure 4.17: *The helical cardiomyocyte architecture of one-day-old neonatal porcine heart.* ***(a)*** *Anterior view identifying the regions of interest within the base (1), equator (2) and apex (3) in the right and left ventricles.* ***(b)*** *Posterior view. The anterior* ***(c)*** *and posterior* ***(d)*** *aspects of LVFW and RVFW. Scale bar = 12 mm.*

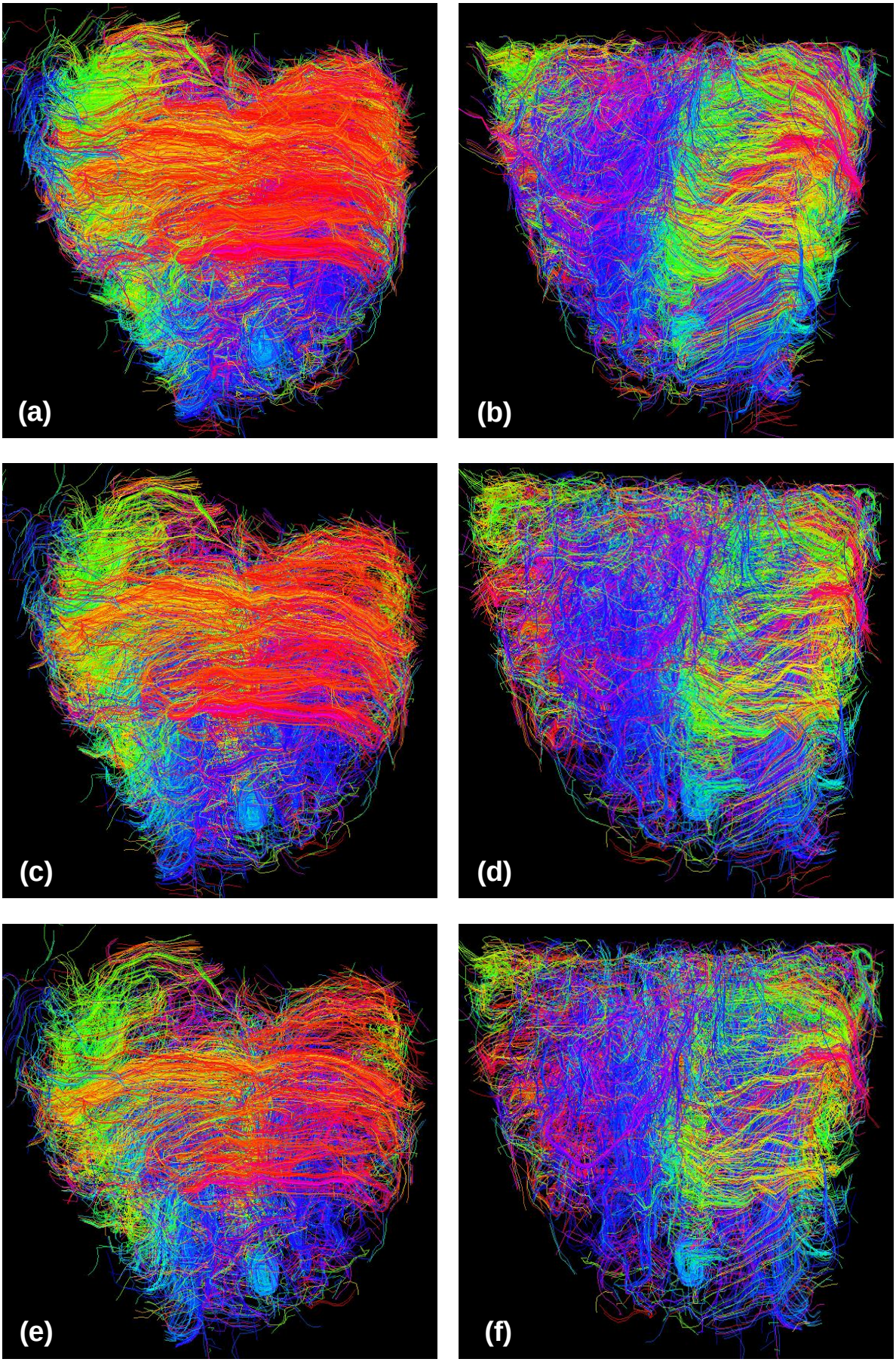
(a)
(b)
(c)
(d)
(e)
(f)

Figure 4.18: *The anterior and posterior aspects of the one-day-old neonatal porcine heart. Fibre bundles were coloured to demonstrate the mean-fibre orientation, using 50% fibre density; anterior view* ***(a)*** *and posterior view* ***(b)****. 25% fibre density; anterior view* ***(c)*** *and posterior view* ***(d)****. 15% fibre density; anterior view* ***(e)*** *and posterior view* ***(f),*** *respectively.*

Table 4.9

The total number of fibre tracks and regional FA in the anterior LVFW.

ROI'S	Fibre number	FA
Base	795	0.72 ± 0.06*
Equator	330	0.75 ± 0.04*
Apex	1284	0.70 ± 0.03*

Results are expressed as mean ± SD.

** One-way analysis of variances (ANOVA) specified statistical significance among ROI's, p < 0.05.*

Table 4.10

The total number of fibre tracks and regional fractional anisotropy (FA) in the anterior RVFW.

ROI'S	Fibre number	FA
Base	339	0.74 ± 0.05*
Equator	169	0.77 ± 0.03*
Apex	789	0.71 ± 0.06*

Results are expressed as mean ± SD.

* One-way analysis of variances (ANOVA) specified statistical significance among ROI's, p < 0.05.

4.2. Biomechanical analyses

4.2.1. Uniaxial tensile behaviour

A total of 10 preconditioning cycles were performed per test to account for the viscoelastic behaviour of the myocardial tissue. During these tests, both the LVFW and RVFW demonstrating the greatest change in behaviour during the first two cycles (Figures 4.21 (a) and (b)). For clarity and easy interpretation, only the first, second, sixth, and tenth cycles were plotted in Figures 4.21 (a) and (b). Both ventricles possessed the repeatable and stable curves, after a few preconditioning cycles. Five to six preconditioning cycles were enough to consider the viscoelasticity of the neonatal porcine heart tissue. The relative change of the maximum stress value was not significant in both ventricles during preconditioning but a prominent decrease of the hysteresis area was noted (Figures 4.21 (a) and (b)). Softening was clearly evident in both ventricles, with a notable softening occurred in the first two preconditioning cycles (Figures 4.21 (a) and (b)). The mean hysteresis area or dissipation energy per unit volume was evaluated at 10% strain in both ventricles by dividing the area enclosed by the loading and unloading curves (energy dissipation) to the area beneath the loading curve (energy input) (Table 4.11). The MFD exhibited the greater energy dissipation than the CFD in both ventricles. The energy dissipation was more pronounced in LVFW when compared to the RVFW. The energy dissipation values for both ventricles are specified in Table 4.11.

The average uniaxial tensile behaviour of the LVFW and RVFW is presented in the Figure 4.21 (c), with the data describing a non–linear, anisotropic, viscoelastic (hysteresis formation) response in all regions. It is evident from Figure 4.21 (c) that the MFD was stiffer than the CFD in the strain range 0 to ~ 0.20 but that the CFD becomes stiffer than the MFD after ~

0.20 for both ventricles. The RVFW is consistently the stiffer of the two ventricles in the MFD and CFD (Figure 4.21 (c)). The LVFW exhibited the greater extensibility than the RVFW in the MFD (Figure 4.21 (c)). Specimen-to-specimen variations have been noted in both ventricles (Figures 4.19 and 4.20) and, therefore, the mean uniaxial tensile stress-strain behaviour of all considered myocardial samples from LVFW (n = 5) and RVFW (n = 5) was plotted with the error bars, specifying standard deviation in Figures 4.21 (e) and (f). Both ventricles exhibited identical behaviour (nonlinearity, anisotropy, hysteresis formation), even though they had different quantitative properties (Figures 4.19 and 4.20). Hence, the failure stresses of both ventricles were computed to perform the quantitative comparison in both ventricles. The failure stress values of both ventricles are summarised in Table 4.12 and Figure 4.21 (g). The data in the Figure 4.21 (c) demonstrate similar trends, although there is a significant difference between the RVFW and LVFW peak stresses ($p = 0.001$) and between MFD and CFD ($p = 0.0001$).

(a)

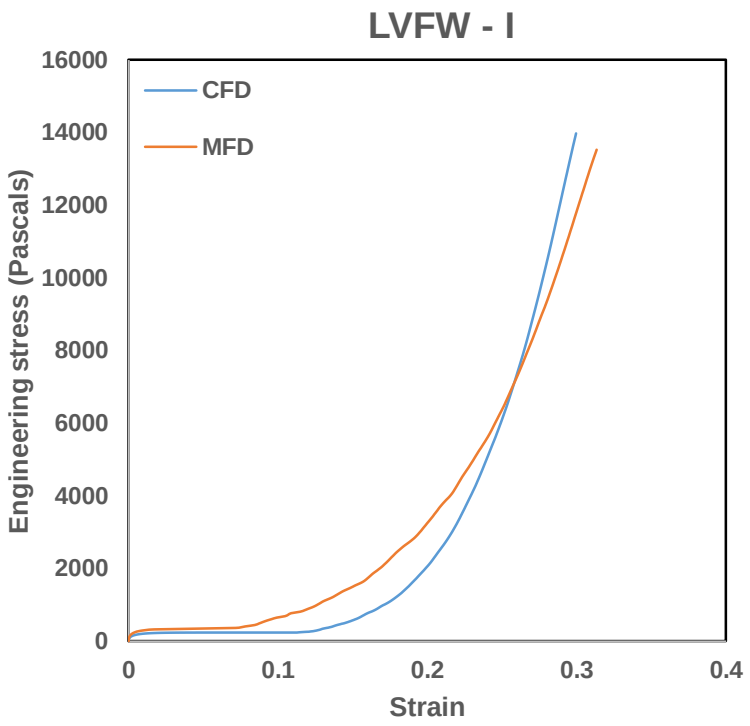
LVFW - I
CFD
MFD
Engineering stress (Pascals)
16000
14000
12000
10000
8000
6000
4000
2000
0
0
0.1
0.2
0.3
0.4
Strain

(b)

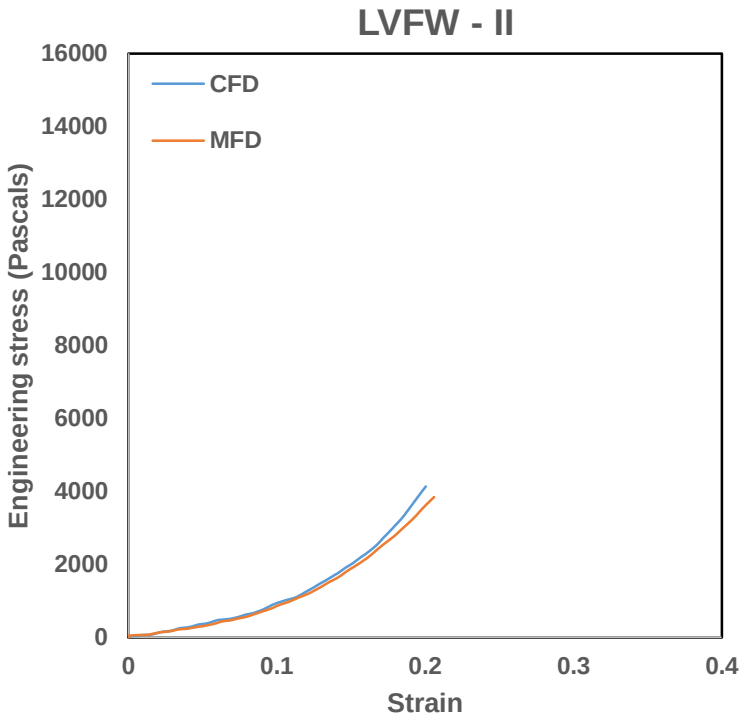
LVFW - II
CFD
MFD
Engineering stress (Pascals)
16000
14000
12000
10000
8000
6000
4000
2000
0
0
0.1
0.2
0.3
0.4
Strain

(c)

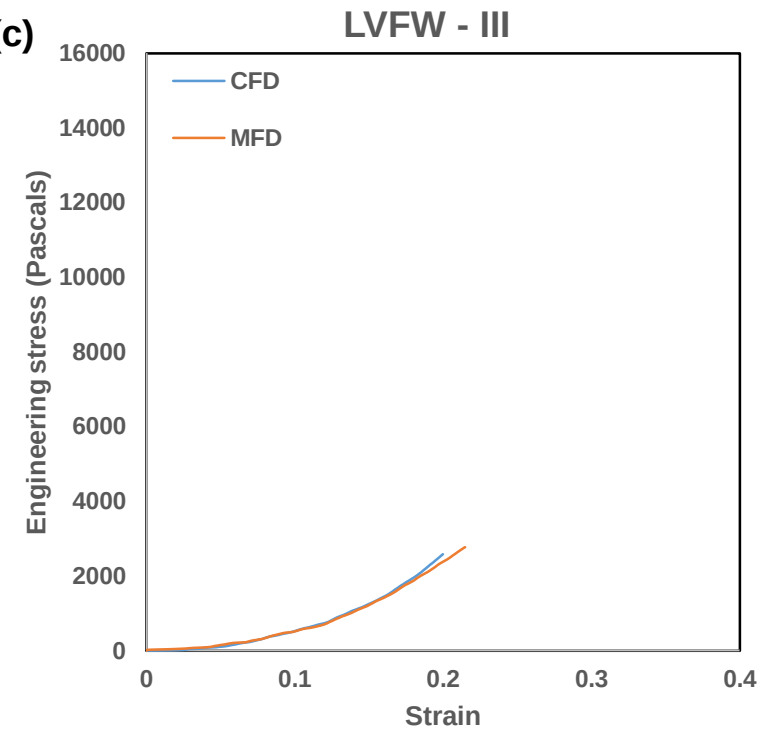
LVFW - III
CFD
MFD
Engineering stress (Pascals)
16000
14000
12000
10000
8000
6000
4000
2000
0
0
0.1
0.2
0.3
0.4
Strain

(d)

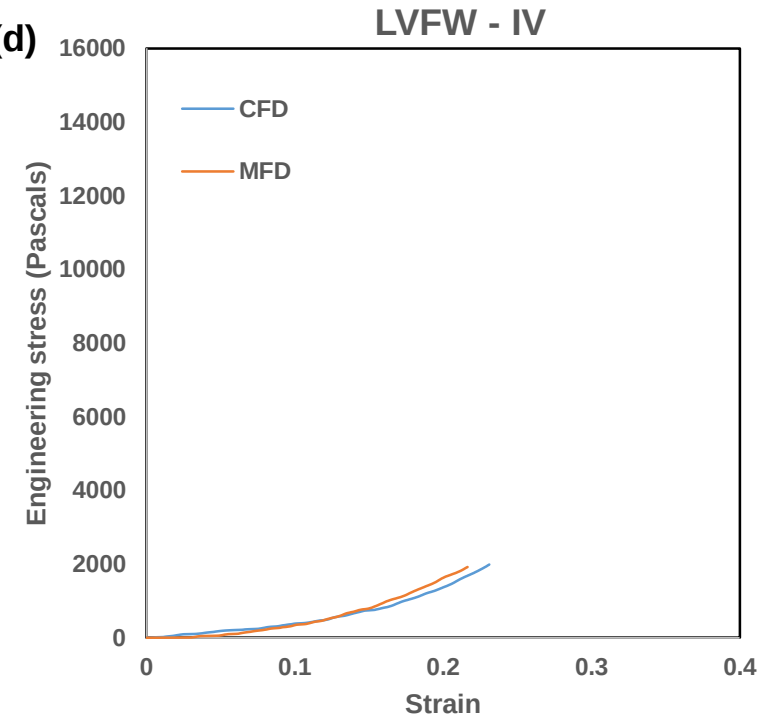
LVFW - IV
CFD
MFD
Engineering stress (Pascals)
16000
14000
12000
10000
8000
6000
4000
2000
0
0
0.1
0.2
0.3
0.4
Strain

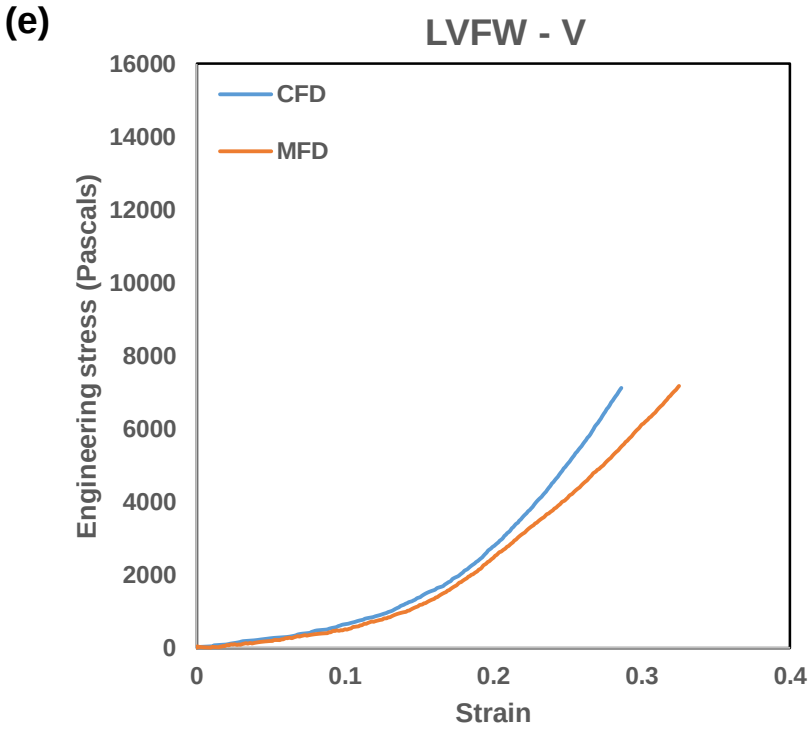

Figure 4.19: *Representing the 'passive' uniaxial tensile behaviour of the LVFW in the MFD and CFD. The specimens were stretched until failure. Five hearts were used to demonstrate the behaviour of Sample I* ***(a)****, Sample II* ***(b)****, Sample III* ***(c)****, Sample IV* ***(d)*** *and Sample V* ***(e)*** *respectively.*

(a)

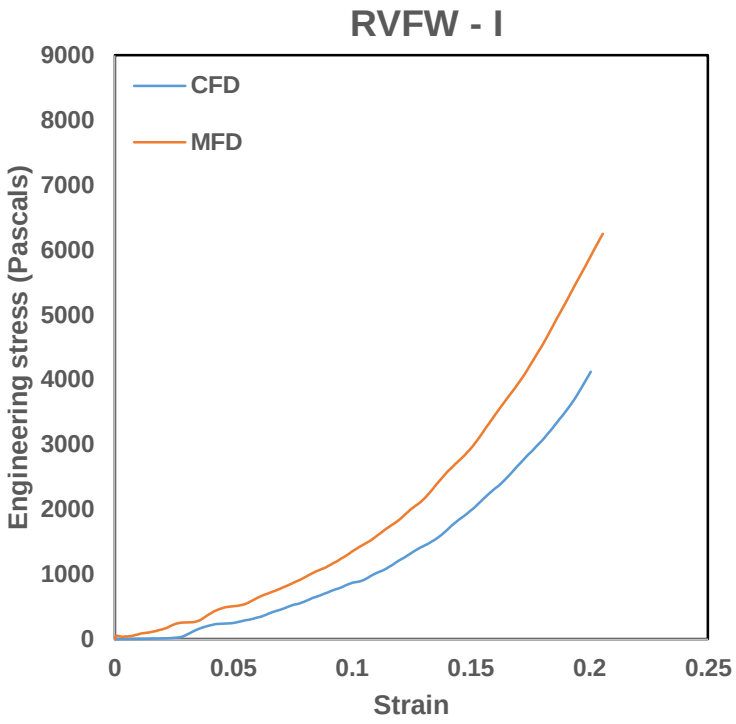
RVFW - I
CFD
MFD
Engineering stress (Pascals)
9000
8000
7000
6000
5000
4000
3000
2000
1000
0
0
0.05
0.1
0.15
0.2
0.25
Strain

(b)

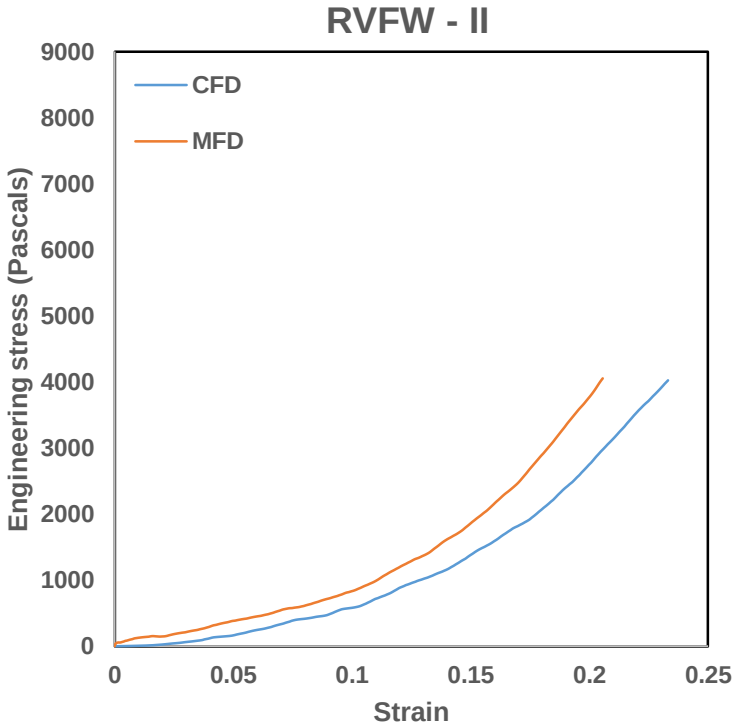
RVFW - II
CFD
MFD
Engineering stress (Pascals)
9000
8000
7000
6000
5000
4000
3000
2000
1000
0
0
0.05
0.1
0.15
0.2
0.25
Strain

(c)

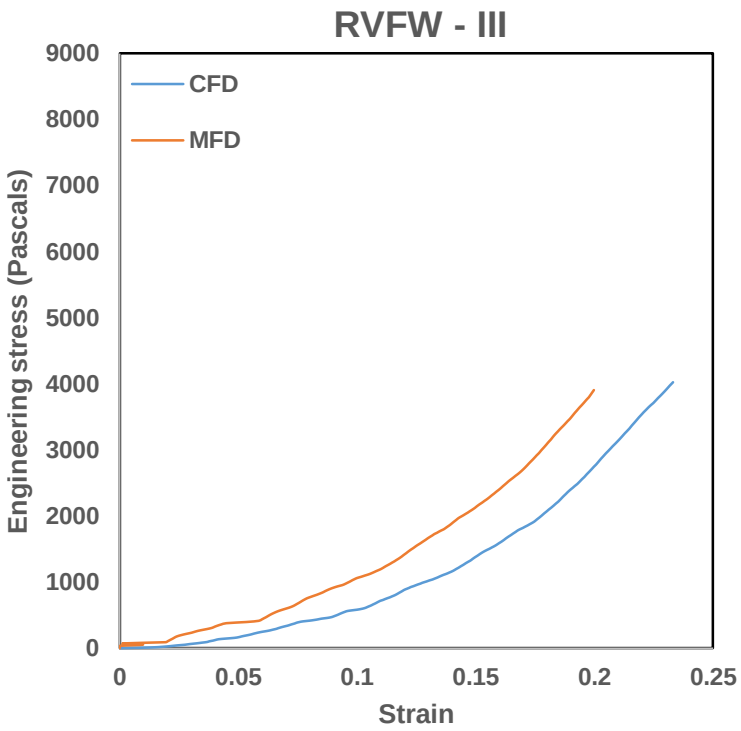
RVFW - III
CFD
MFD
Engineering stress (Pascals)
9000
8000
7000
6000
5000
4000
3000
2000
1000
0
0
0.05
0.1
0.15
0.2
0.25
Strain

(d)

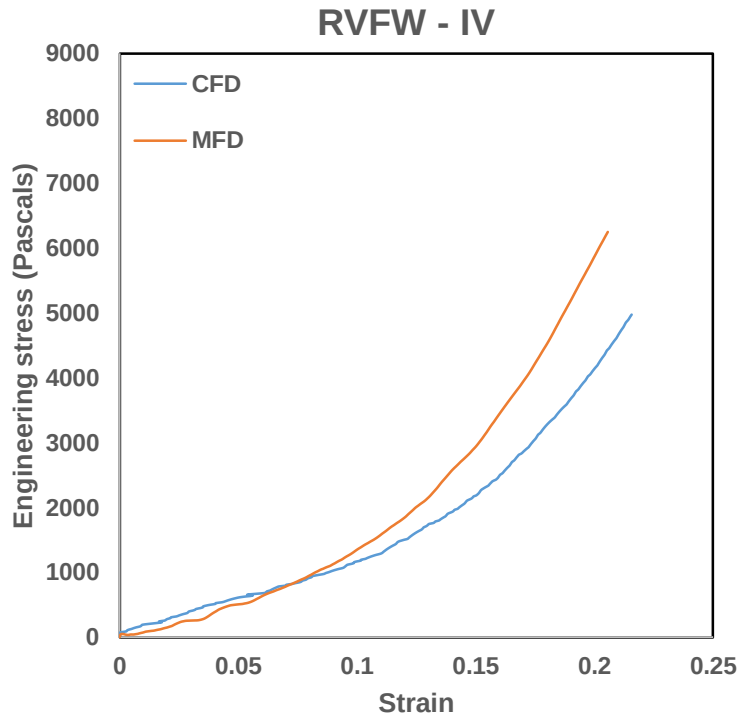
RVFW - IV
CFD
MFD
Engineering stress (Pascals)
9000
8000
7000
6000
5000
4000
3000
2000
1000
0
0
0.05
0.1
0.15
0.2
0.25
Strain

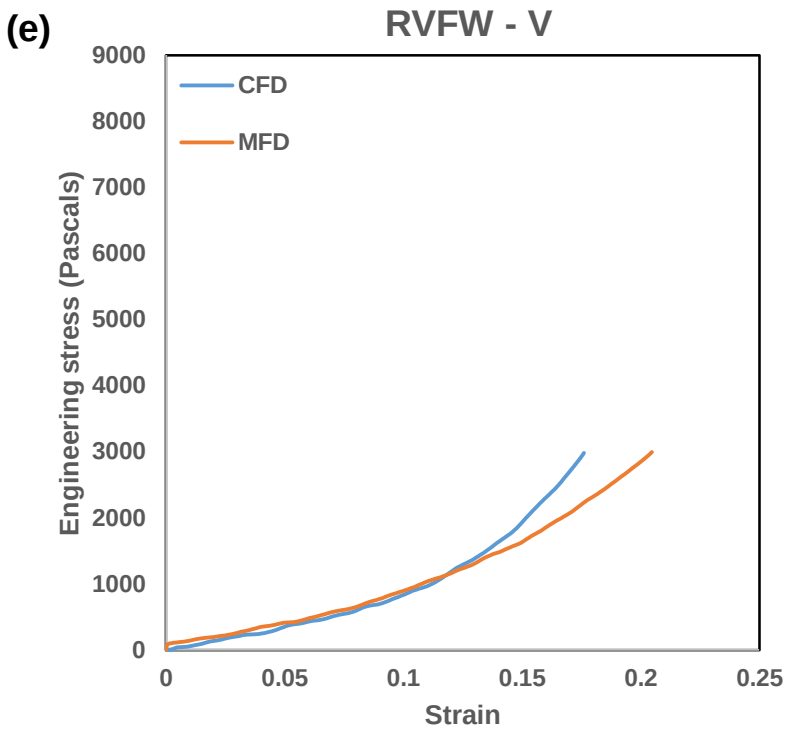

Figure 4.20: *Representing the 'passive' uniaxial tensile behaviour of the RVFW in the MFD and CFD. The specimens were stretched until failure. Five hearts were used to demonstrate the behaviour of Sample I* ***(a)****, Sample II* ***(b)****, Sample III* ***(c)****, Sample IV* ***(d)*** *and Sample V* ***(e)*** *respectively.*

(a)

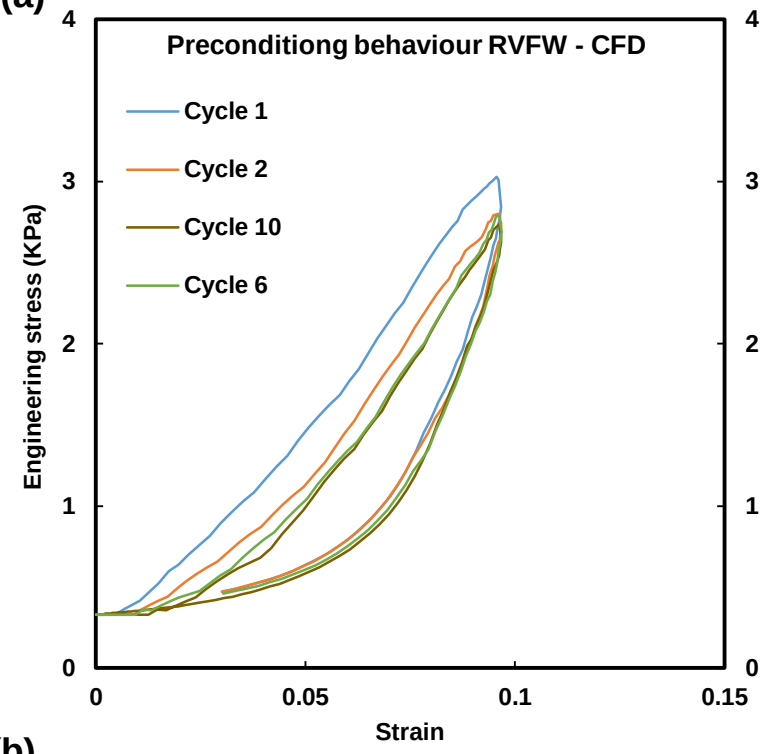
Preconditiong behaviour RVFW - CFD
Cycle 1
Cycle 2
Cycle 10
Cycle 6
Engineering stress (KPa)
Strain
0
1
2
3
4
0
0.05
0.1
0.15

(b)

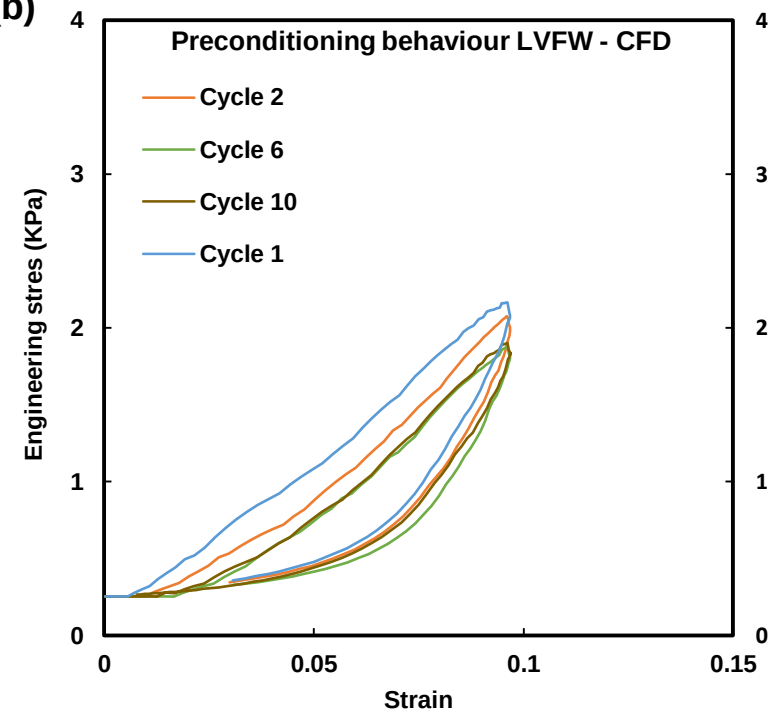
Preconditioning behaviour LVFW - CFD
Cycle 2
Cycle 6
Cycle 10
Cycle 1
Engineering stres (KPa)
Strain
0
1
2
3
4
0
0.05
0.1
0.15

(c)

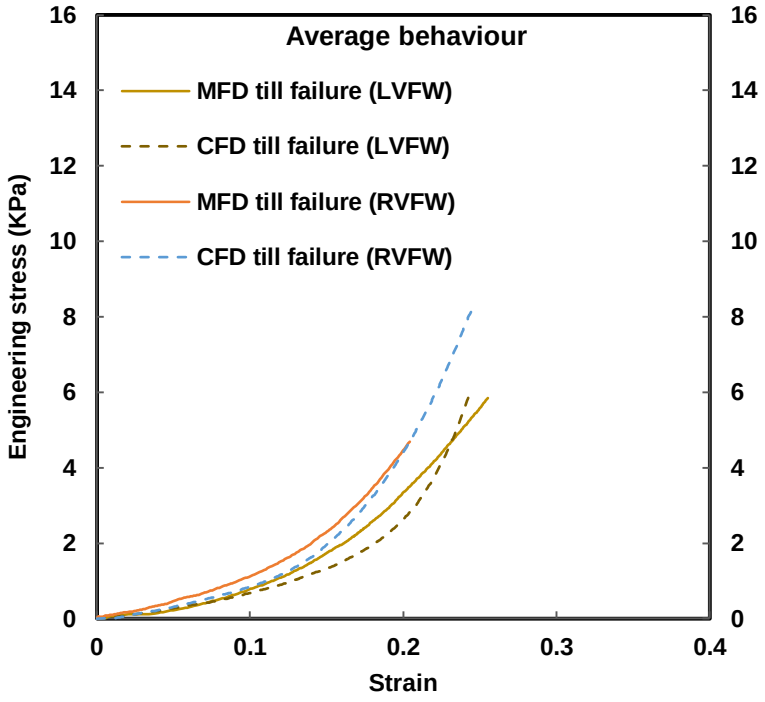
Average behaviour
MFD till failure (LVFW)
CFD till failure (LVFW)
MFD till failure (RVFW)
CFD till failure (RVFW)
Engineering stress (KPa)
Strain
0
2
4
6
8
10
12
14
16
0
0.1
0.2
0.3
0.4

(d)

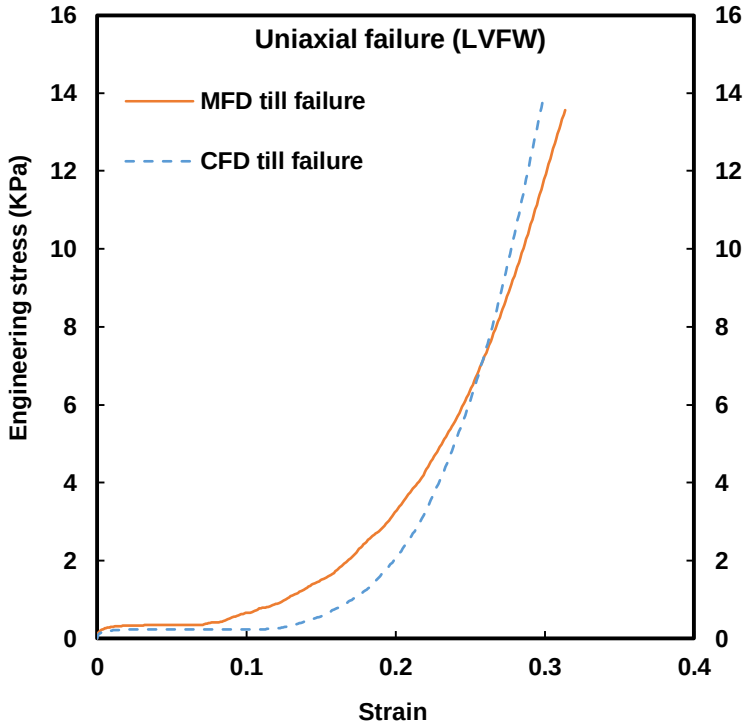
Uniaxial failure (LVFW)
MFD till failure
CFD till failure
Engineering stress (KPa)
Strain
0
2
4
6
8
10
12
14
16
0
0.1
0.2
0.3
0.4

(e)

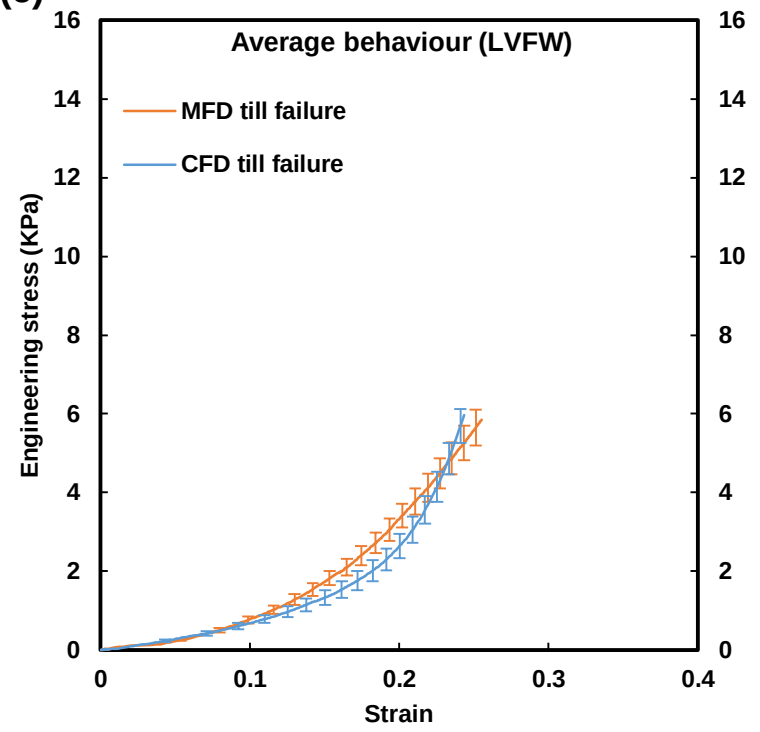
Average behaviour (LVFW)
MFD till failure
CFD till failure
Engineering stress (KPa)
Strain
0
2
4
6
8
10
12
14
16
0
0.1
0.2
0.3
0.4

(f)

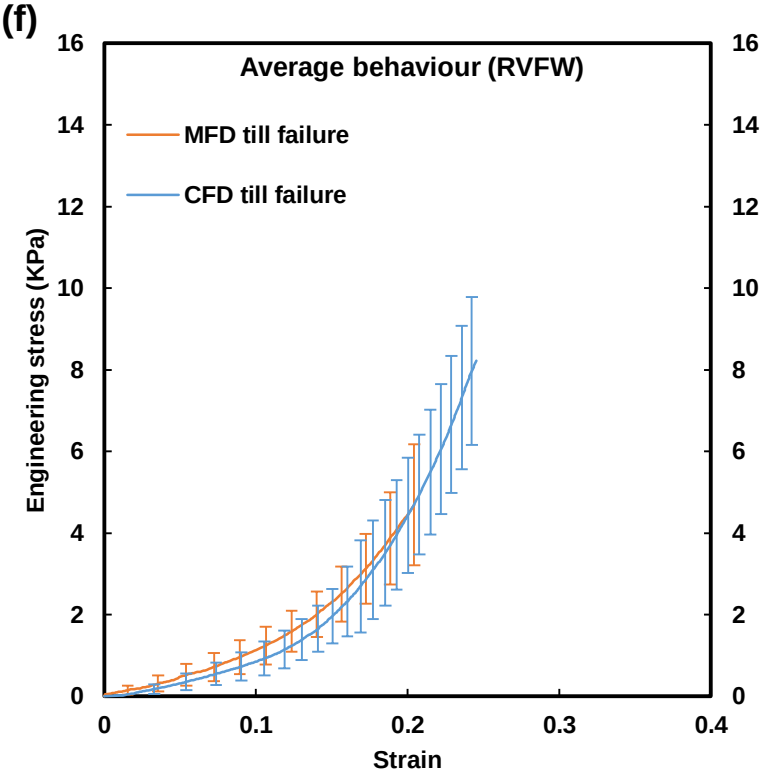
Average behaviour (RVFW)
MFD till failure
CFD till failure
Engineering stress (KPa)
Strain
0
2
4
6
8
10
12
14
16
0
0.1
0.2
0.3
0.4

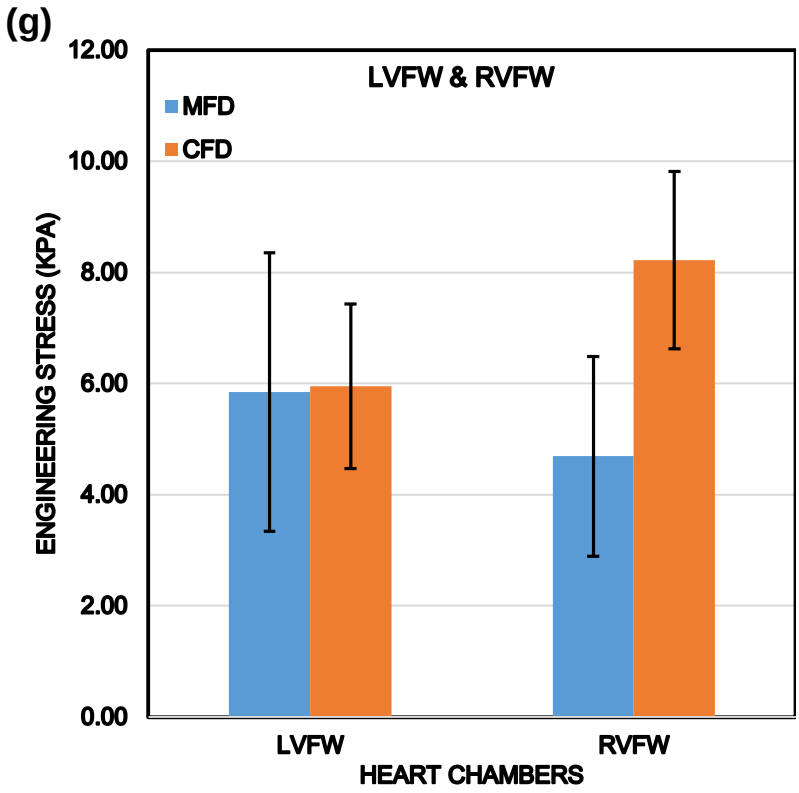

Figure 4.21: *Uniaxial cyclic behaviour of LVFW* ***(a)*** *and RVFW* ***(b)*** *in CFD.* ***(c)*** *Average 'uniaxial behaviour' of LVFW and RVFW until failure (n = 5).* ***(d)*** *Representing passive 'uniaxial behaviour' of LVFW until failure. Mean curves of the LVFW* ***(e)*** *and RVFW* ***(f)*** *(n = 5).* ***(g)*** *Column plots indicate mean failure stress in the anterior and posterior aspect of LVFW and RVFW, for MFD and CFD. Standard deviation indicated by error bars.*

Table 4.11

Average hysteresis area (J/m^3) of neonatal porcine LVFW and RVFW for uniaxial testing at 10% strain in MFD and CFD.

	Hysteresis area			
Heart regions	**MFD**	**(SD)**	**CFD**	**(SD)**
LVFW	91*	(112)	80*	(82)
RVFW	54*	(108)	43*	(93)

** One-way analysis of variance (ANOVA) revealed statistical significance between the LVFW and RVFW in the MFD and CFD $p < 0.05$.*

Table 4.12

Average failure stress values (KPa) for neonatal LVFW and RVFW for uniaxial testing: the specimens were stretched until failure.

Heart regions	**MFD**	**(SD)**	**CFD**	**(SD)**
LVFW	5.84*	(0.4)	5.95*	(0.4)
RVFW	4.69*	(1.4)	8.22*	(1.8)

** One-way analysis of variance (ANOVA) revealed statistical significance between the LVFW and RVFW in the MFD and CFD $p < 0.05$.*

4.2.2. Biaxial extension behaviour

The biaxial mechanical representatives (engineering stress vs stretch) were investigated at 30 Nm^{-1}: 30 Nm^{-1} load per unit length. LVFW and RVFW exhibited non–linear, anisotropic and viscoelastic (hysteresis formation) mechanical behaviour (Figures 4.22, 4.23 and 4.24 (a) and (b)). The RVFW was the stiffest ventricle, while the LVFW demonstrated greater viscoelasticity. The MFD exhibits stiffer behaviour in both ventricles than the CFD (Figures 4.22, 4.23 and 4.24 (a) and (b)). The LVFW exhibits mechanical - coupling between the MFD and CFD as demonstrated in Figure 4.22 (a). To highlight the specimen-to-specimen variations (Figures 4.22, 4.23), the mean engineering stress-stretch behaviour of all considered myocardial samples from LVFW (n = 5) and RVFW (n = 5) was plotted with the error bars, to identify a standard deviation in the Figures 4.24 (c) and (d). A similar qualitative behaviour (nonlinearity, anisotropy, hysteresis formation) was observed for both ventricles. The mean hysteresis area or dissipation energy per unit volume was evaluated at 30 Nm^{-1}: 30 Nm^{-1} load per unit length of both ventricles, by dividing the area enclosed by the loading and unloading curves (energy dissipation) to the area beneath the loading curve (energy input) (Tables. 4.13). The MFD exhibited the greater energy dissipation than the CFD in both ventricles. The energy dissipation was more pronounced in LVFW than the RVFW as stated in Table 4.13.

Peak engineering stress values were calculated and presented in Table 4.14 to describe the quantitative differences in both ventricles. For clarity and easy interpretation, these values were also plotted in a column chart (Figure 4.24 (e)). A significant difference exists between the RVFW and LVFW peak engineering stresses in MFD ($p = 0.0001$) and CFD ($p = 0.0001$).

(a)

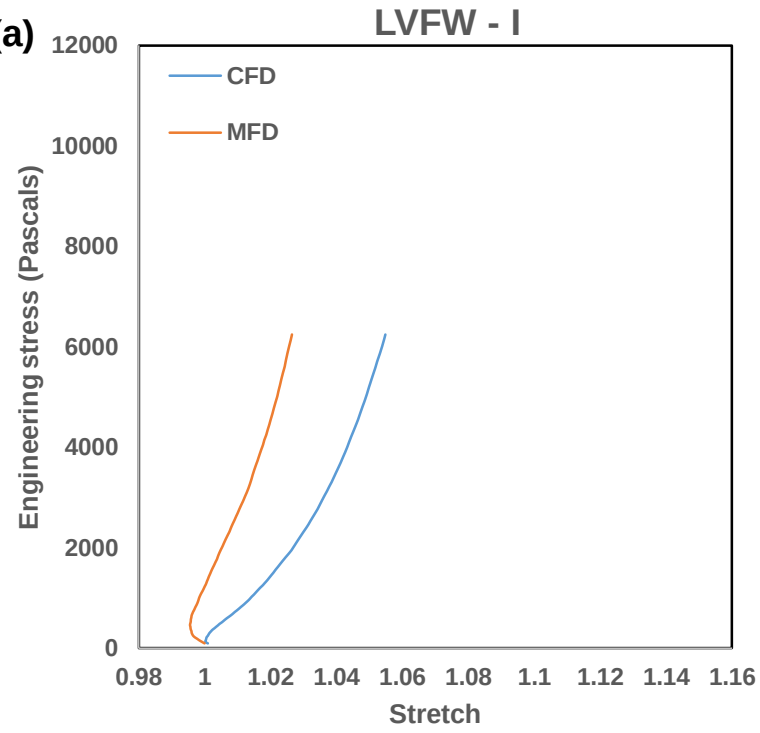
LVFW - I
CFD
MFD
Engineering stress (Pascals)
12000
10000
8000
6000
4000
2000
0
0.98
1
1.02
1.04
1.06
1.08
1.1
1.12
1.14
1.16
Stretch

(b)

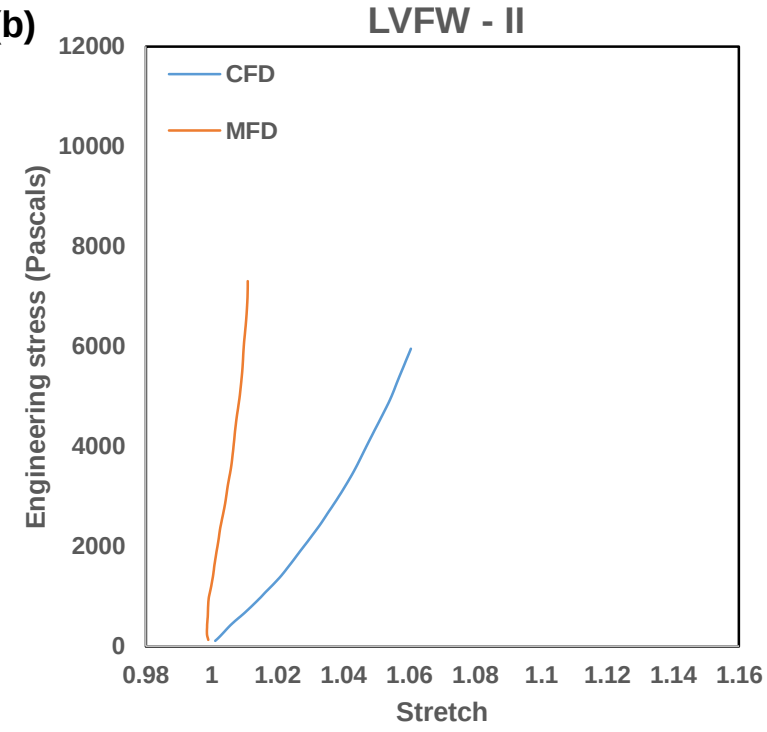
LVFW - II
CFD
MFD
Engineering stress (Pascals)
12000
10000
8000
6000
4000
2000
0
0.98
1
1.02
1.04
1.06
1.08
1.1
1.12
1.14
1.16
Stretch

(c)

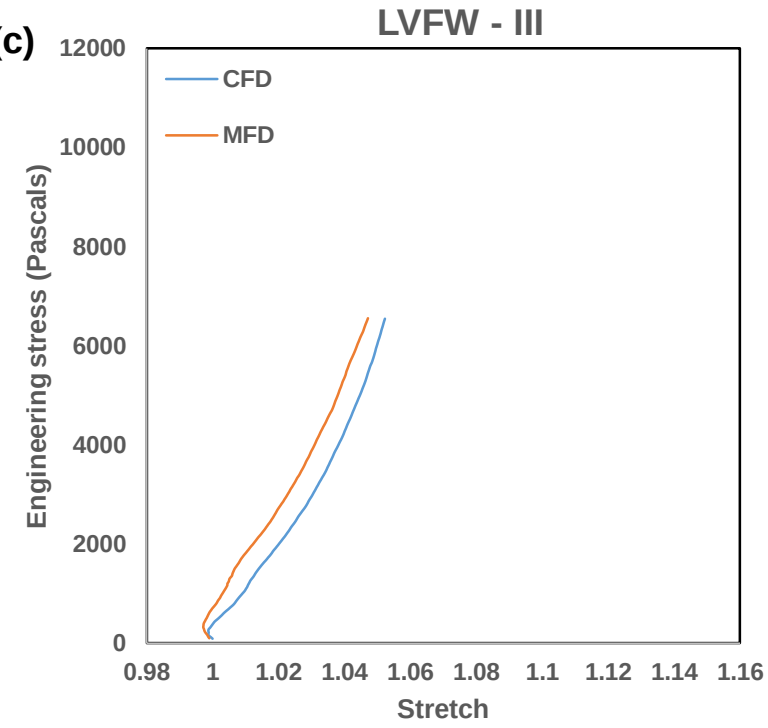
LVFW - III
CFD
MFD
Engineering stress (Pascals)
12000
10000
8000
6000
4000
2000
0
0.98
1
1.02
1.04
1.06
1.08
1.1
1.12
1.14
1.16
Stretch

(d)

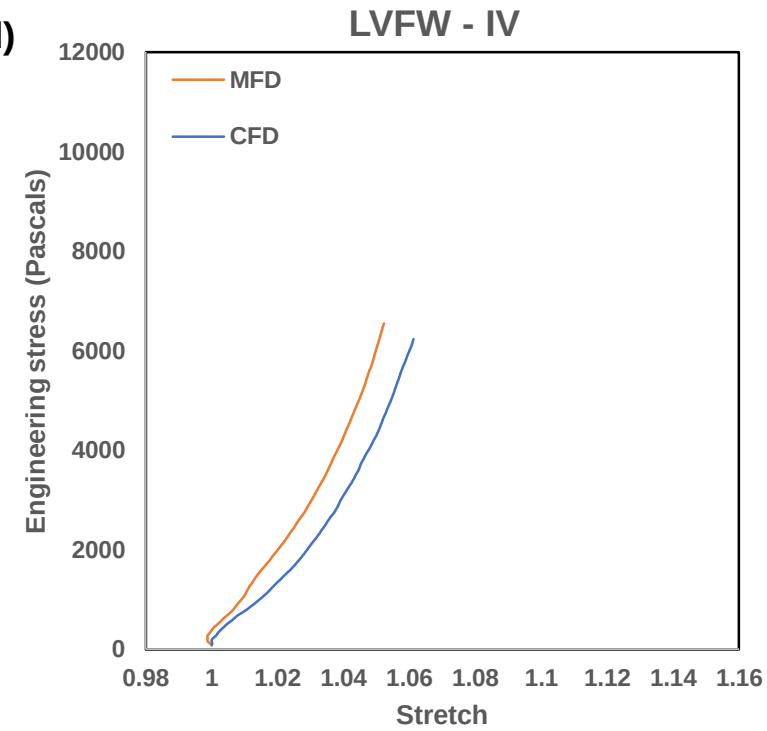
LVFW - IV
MFD
CFD
Engineering stress (Pascals)
12000
10000
8000
6000
4000
2000
0
0.98
1
1.02
1.04
1.06
1.08
1.1
1.12
1.14
1.16
Stretch

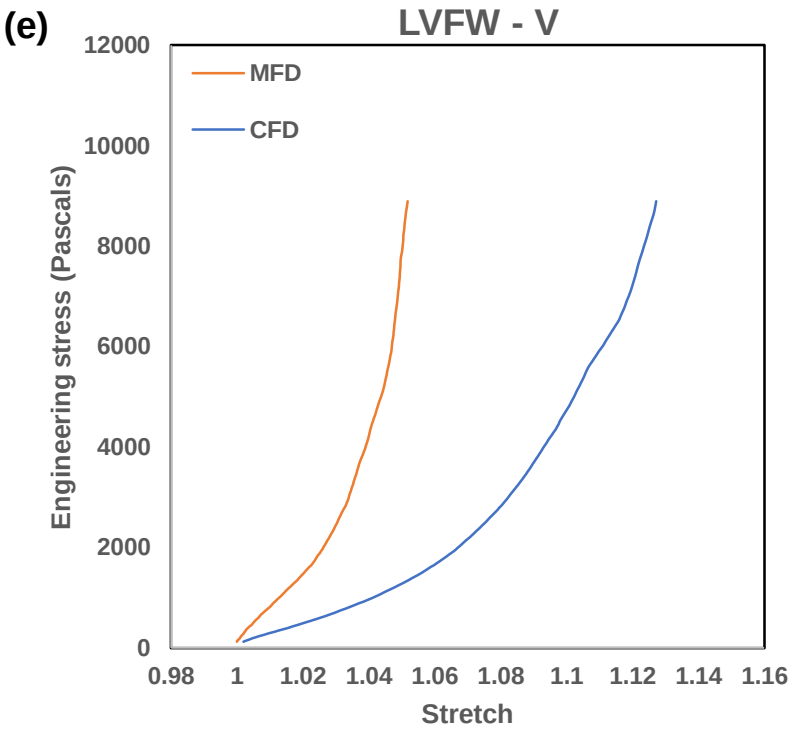

Figure 4.22: *Representing the 'passive' biaxial tensile behaviour of the LVFW in the MFD and CFD. The specimens were stretched at 30 Nm^{-1}: 30 Nm^{-1} load per unit length. Five hearts were used to demonstrate the behaviour of Sample I* ***(a)****, Sample II* ***(b)****, Sample III* ***(c)****, Sample IV* ***(d)*** *and Sample V* ***(e)*** *respectively.*

(a)

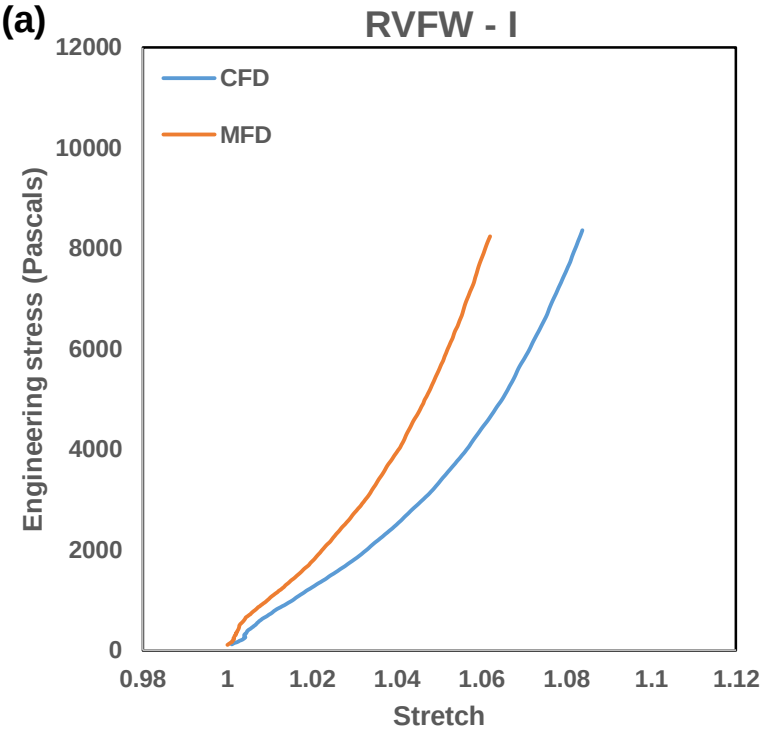
RVFW - I
CFD
MFD
Engineering stress (Pascals)
12000
10000
8000
6000
4000
2000
0
0.98
1
1.02
1.04
1.06
1.08
1.1
1.12
Stretch

(b)

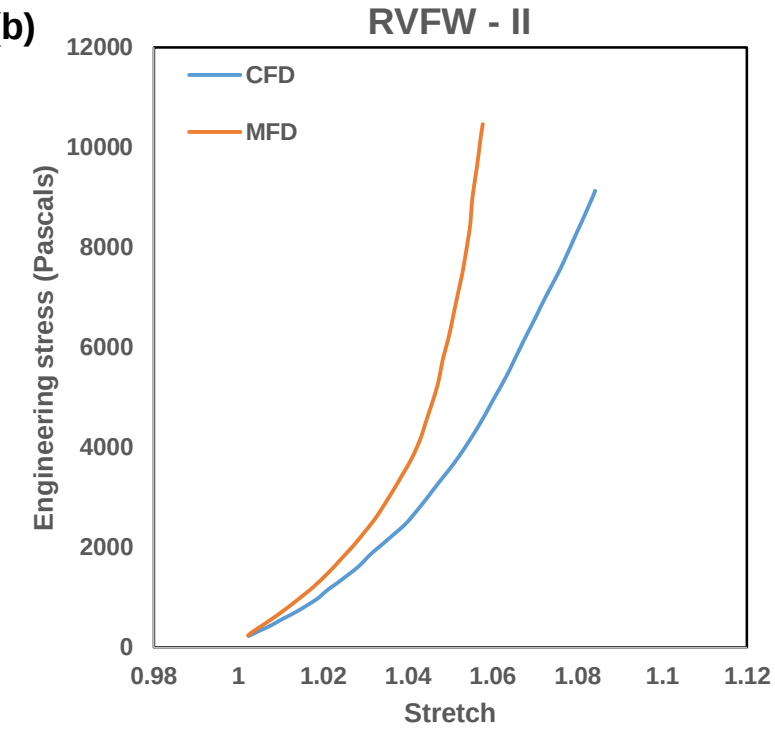
RVFW - II
CFD
MFD
Engineering stress (Pascals)
12000
10000
8000
6000
4000
2000
0
0.98
1
1.02
1.04
1.06
1.08
1.1
1.12
Stretch

(c)

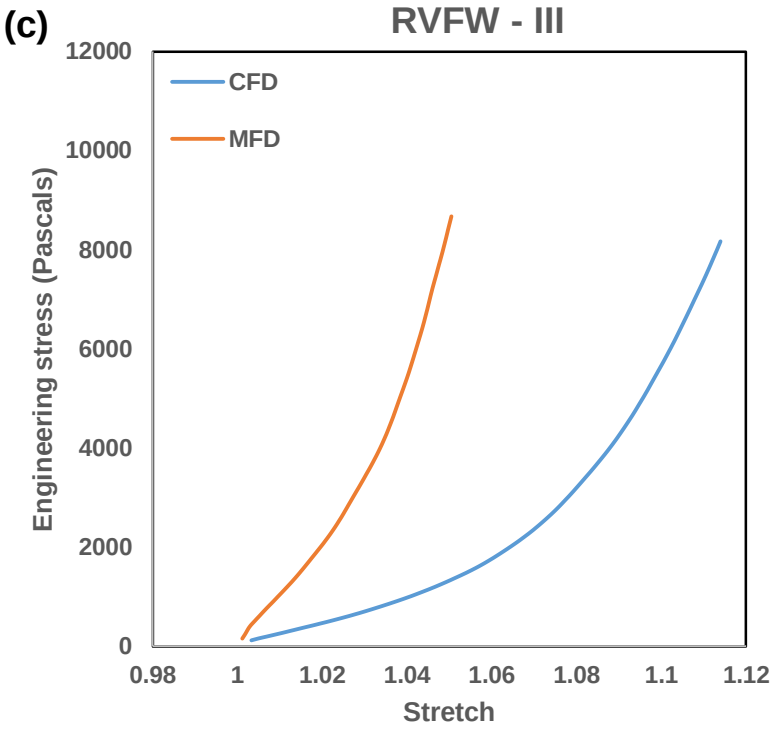
RVFW - III
CFD
MFD
Engineering stress (Pascals)
12000
10000
8000
6000
4000
2000
0
0.98
1
1.02
1.04
1.06
1.08
1.1
1.12
Stretch

(d)

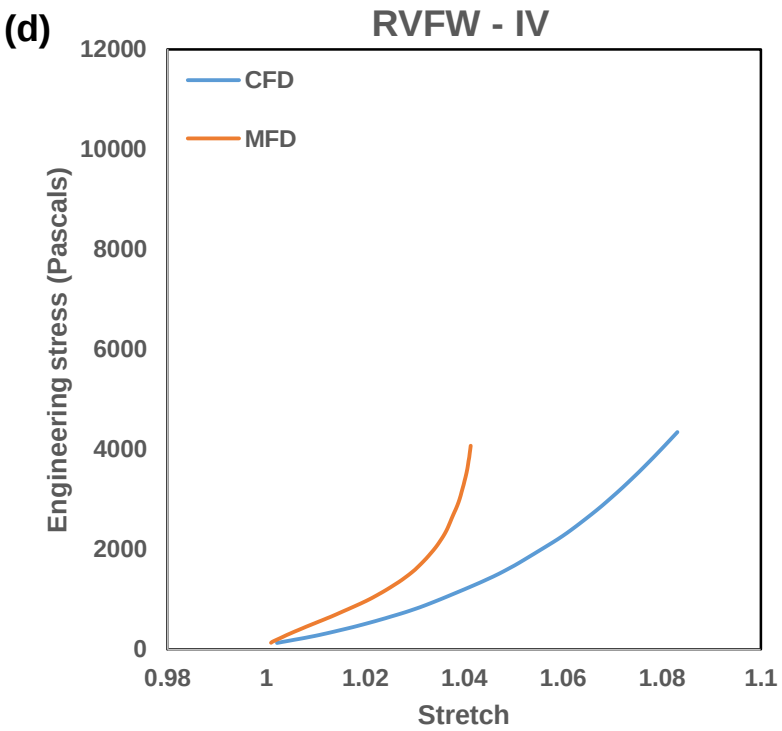
RVFW - IV
CFD
MFD
Engineering stress (Pascals)
12000
10000
8000
6000
4000
2000
0
0.98
1
1.02
1.04
1.06
1.08
1.1
Stretch

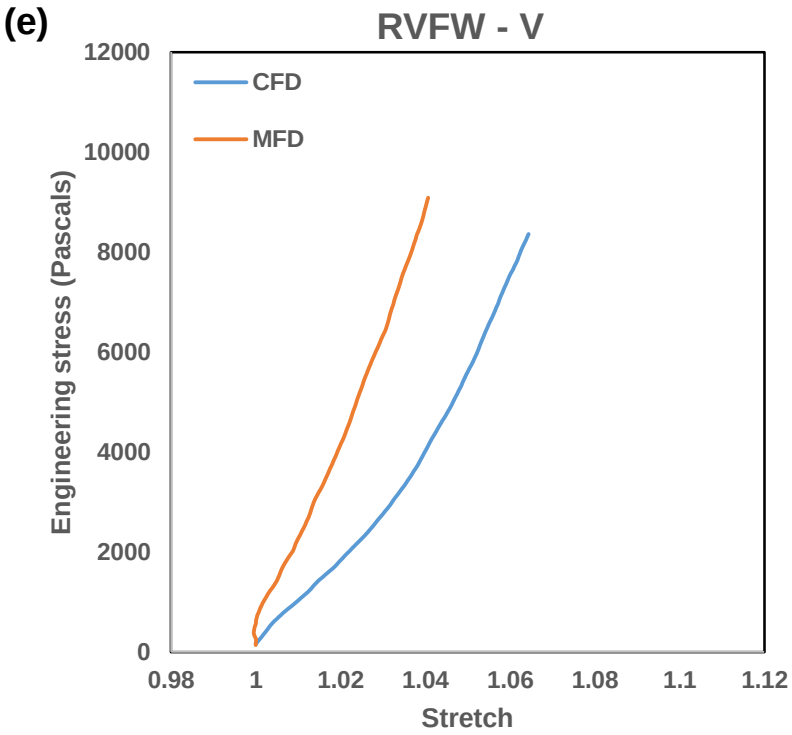

Figure 4.23: *Representing the 'passive' biaxial tensile behaviour of the RVFW in the MFD and CFD. The specimens were stretched at 30 Nm^{-1}: 30 Nm^{-1} load per unit length. Five hearts were used to demonstrate the behaviour of Sample I* ***(a)****, Sample II* ***(b)****, Sample III* ***(c)****, Sample IV* ***(d)*** *and Sample V* ***(e)*** *respectively.*

(a)

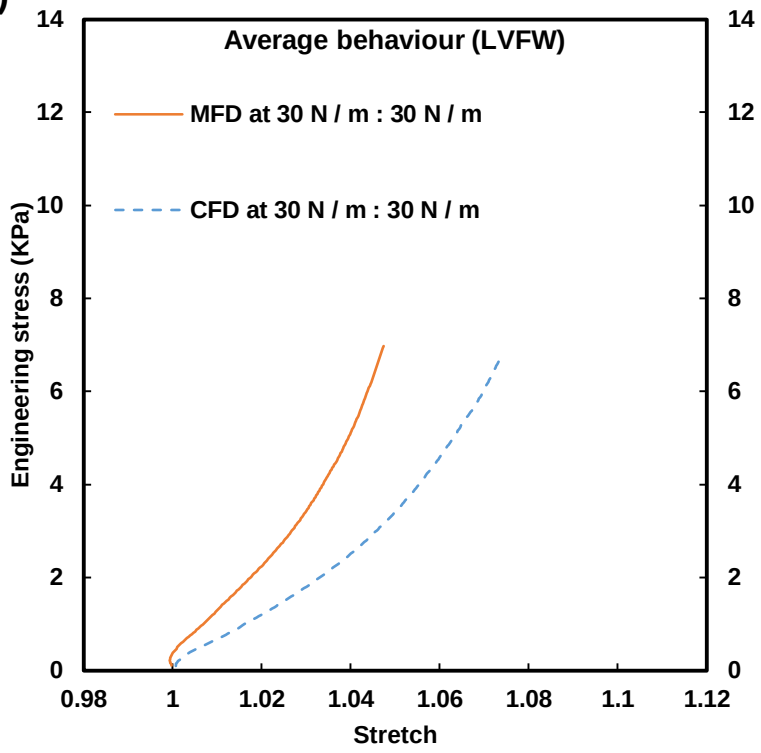
Average behaviour (LVFW)
MFD at 30 N / m : 30 N / m
CFD at 30 N / m : 30 N / m
Engineering stress (KPa)
Stretch
0
2
4
6
8
10
12
14
0.98
1
1.02
1.04
1.06
1.08
1.1
1.12

(b)

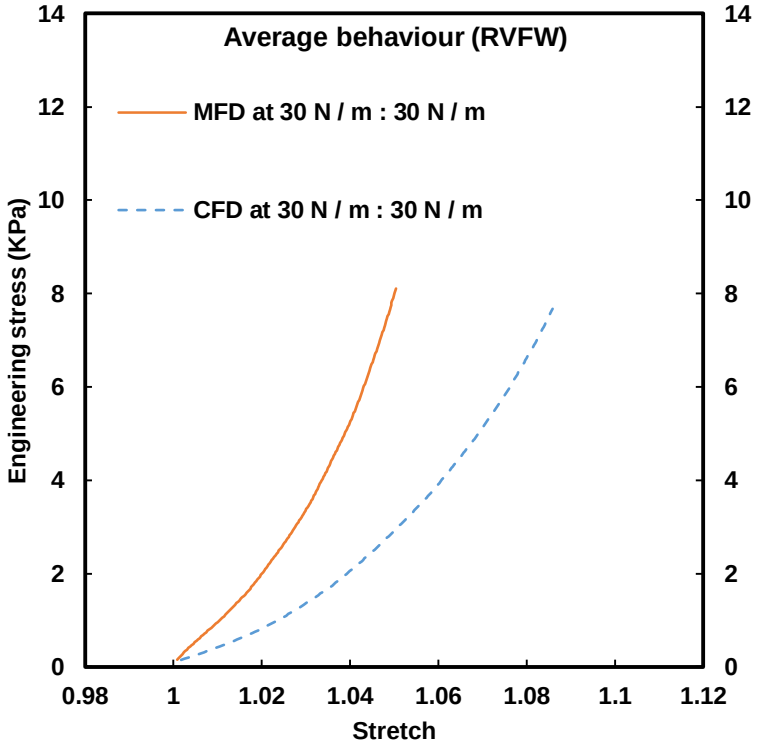
Average behaviour (RVFW)
MFD at 30 N / m : 30 N / m
CFD at 30 N / m : 30 N / m
Engineering stress (KPa)
Stretch
0
2
4
6
8
10
12
14
0.98
1
1.02
1.04
1.06
1.08
1.1
1.12

(c)

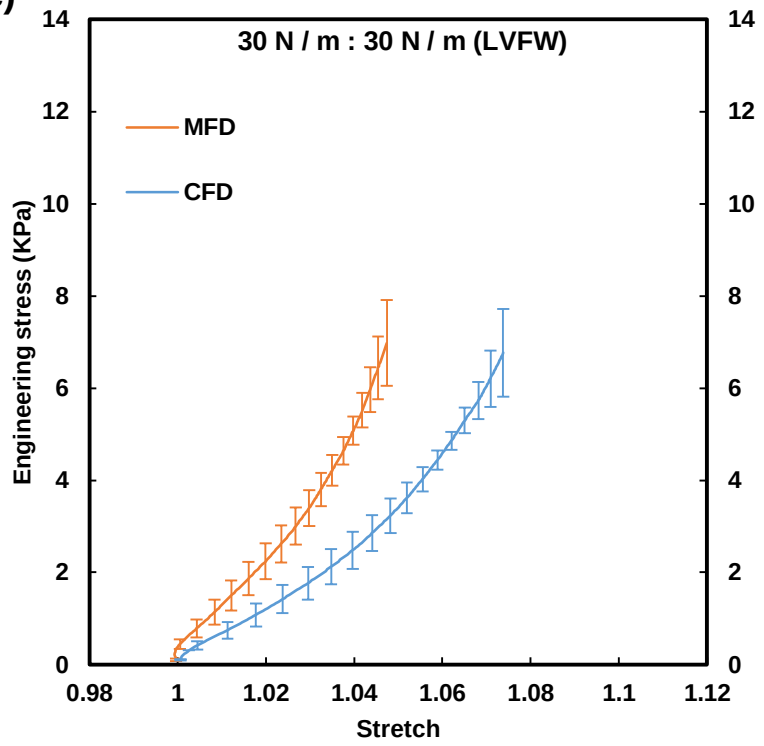
30 N / m : 30 N / m (LVFW)
MFD
CFD
Engineering stress (KPa)
Stretch
0
2
4
6
8
10
12
14
0.98
1
1.02
1.04
1.06
1.08
1.1
1.12

(d)

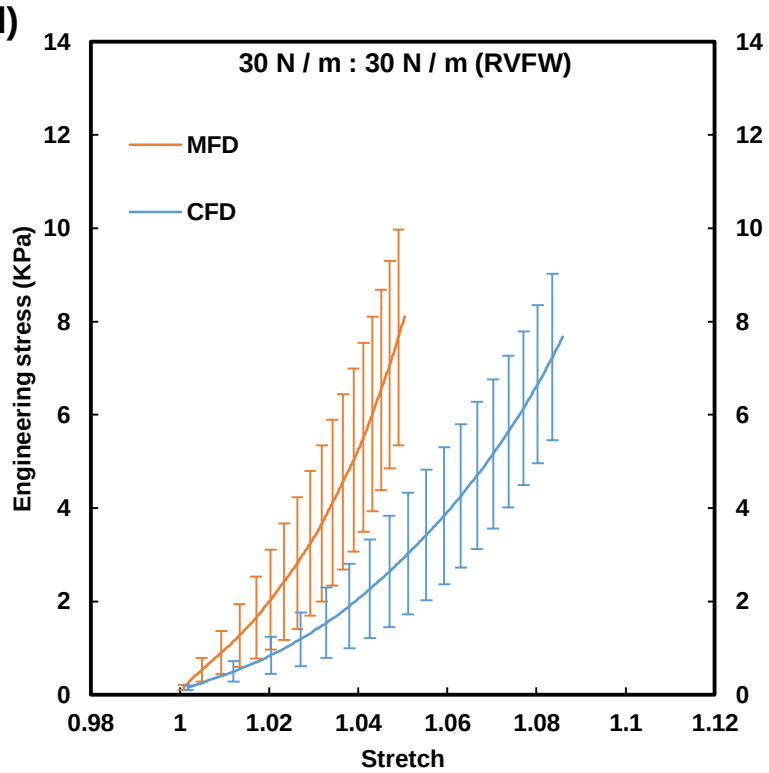
30 N / m : 30 N / m (RVFW)
MFD
CFD
Engineering stress (KPa)
Stretch
0
2
4
6
8
10
12
14
0.98
1
1.02
1.04
1.06
1.08
1.1
1.12

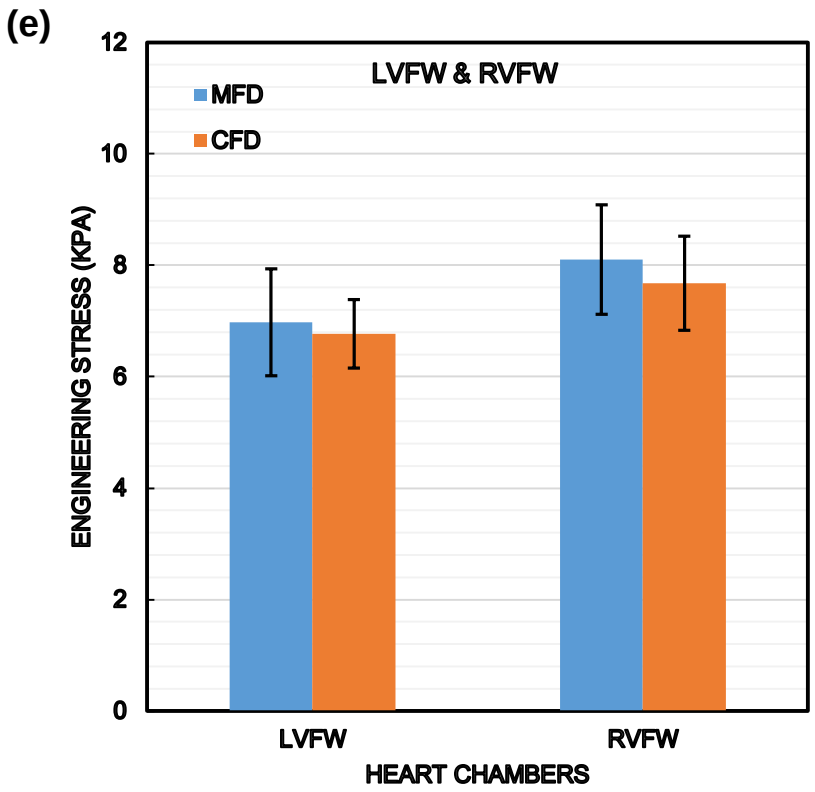

Figure 4.24: *'Average biaxial behaviour' of LVFW* ***(a)*** *and RVFW* ***(b)*** *(n = 5). Mean 'biaxial' curves of the LVFW* ***(c)*** *and RVFW* ***(d)*** *(n = 5).* ***(e)*** *Columns plot specifying the average peak Engineering stress of the LVFW and RVFW in the MFD and CFD (n = 5). Error bars describe the standard deviation.*

Table 4.13

Average hysteresis area (J/m^3) of neonatal porcine LVFW and RVFW for biaxial testing at (30:30) N / m in MFD and CFD.

	Hysteresis area			
Heart regions	**MFD**	**(SD)**	**CFD**	**(SD)**
LVFW	51	(121)	19	(76)
RVFW	48	(128)	23	(67)

* One-way analysis of variance (ANOVA) did not reveal statistical significance between the LVFW and RVFW in the MFD and CFD $p < 0.05$.

Table 4.14

Average peak engineering stress values (KPa) for neonatal porcine LVFW and RVFW for biaxial testing at (30:30) N / m in MFD and CFD.

Heart regions	**MFD**	**(SD)**	**CFD**	**(SD)**
LVFW	6.97*	(0.9)	6.77*	(0.9)
RVFW	8.11*	(2.3)	7.67*	(1.8)

* One-way analysis of variance (ANOVA) revealed statistical significance between the LVFW and RVFW in the MFD and CFD $p < 0.05$.

4.2.3. Simple shear behaviour

Hysteresis formation (energy dissipation) was prominently evident throughout the cyclic shearing behaviour, with both ventricles demonstrating increased shear (Figures 4.25 (a)–(d)). In both ventricles, the greater degree of mechanical-anisotropy and stiffness were observed at higher stain (i.e. 50%), indicating the strain-dependent behaviour of myocardial tissue (Figures 4.25 (a)–(d)). The energy dissipation was more pronounced in the anterior wall than the posterior wall in both ventricles (Table 4.15). The greater energy dissipation was observed in the RVFW when compared to the LVFW. The mean energy dissipation values for both ventricles are summarised in Table 4.15.

The representative results (shear stress vs. the amount of shear) of the anterior and posterior aspects for LVFW and RVFW are displayed in the Figures 4.26 (a)–(b)). Both ventricles demonstrated nonlinear, anisotropic, viscoelastic (hysteresis formation) behaviour. The anterior walls appeared stiffer than the posterior walls of both ventricles, while the MFD was stiffer than the CFD (Figures 4.26 (a)–(b)). The RVFW exhibited asymmetrical behaviour, possessing greater stiffness in the positive direction anteriorly and negative direction posteriorly (Figures 4.25 (c)–(d)). Conversely, both aspects of the LVFW exhibited consistent behaviour in both directions (Figures 4.25 (a)–(b)). RVFW was the stiffest ventricle in the MFD and CFD. A prominent difference in the shear behaviour (shear stress vs the amount of shear) of the anterior and posterior aspects were noted in the RVFW (4.26 (e) and (f)). The peak shear stress values were computed to perform a quantitative analysis in the anterior and posterior aspects of both ventricles. The peak shear stresses are described in Tables 4.16 and 4.17. For clarity and easy interpretation, these values were also demonstrated in terms of column plots (Figures 4.26 (g)–(i)). The results suggested that the shear properties of the

myocardial tissue are highly heterogeneous, depending on the cardiac myocytes orientation in the MFD and CFD. The greater shear stiffness was observed in the RVFW–anterior, intermediate in the LVFW–anterior and RVFW–posterior, and lowest in the LVFW–posterior. The influence of fibre direction is described in the Figures 4.26 (a)–(f)), while variations in tissue behaviour are identified statistically via a one-way analysis of variance (ANOVA) and Tukey HSD post hoc test (Table 4.18).

(a)

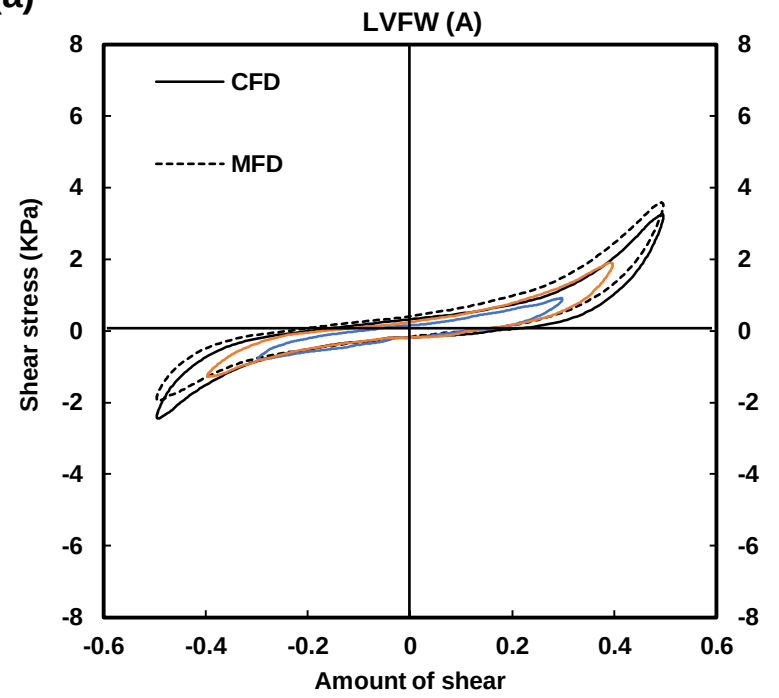
LVFW (A)
CFD
MFD
Shear stress (KPa)
Amount of shear
8
6
4
2
0
-2
-4
-6
-8
-0.6
-0.4
-0.2
0
0.2
0.4
0.6

(b)

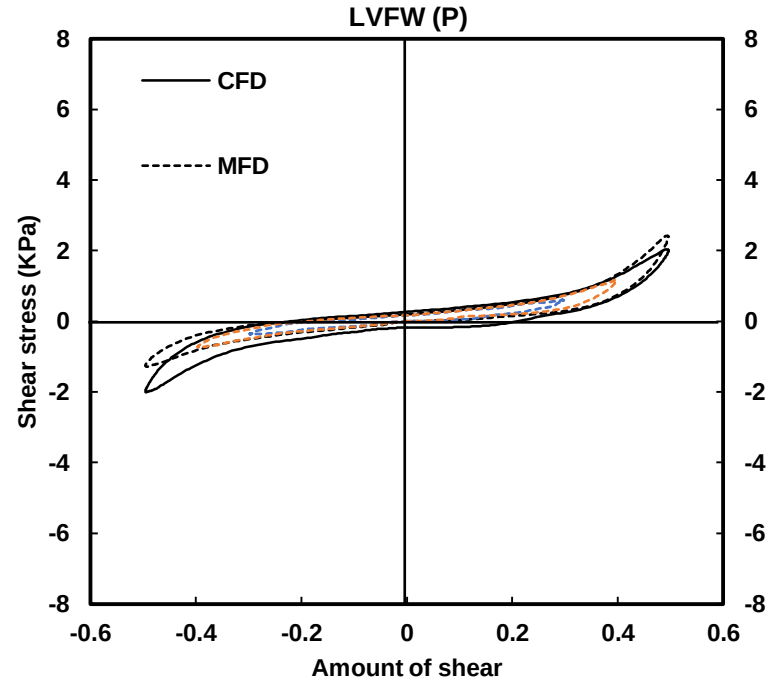
LVFW (P)
CFD
MFD
Shear stress (KPa)
Amount of shear
8
6
4
2
0
-2
-4
-6
-8
-0.6
-0.4
-0.2
0
0.2
0.4
0.6

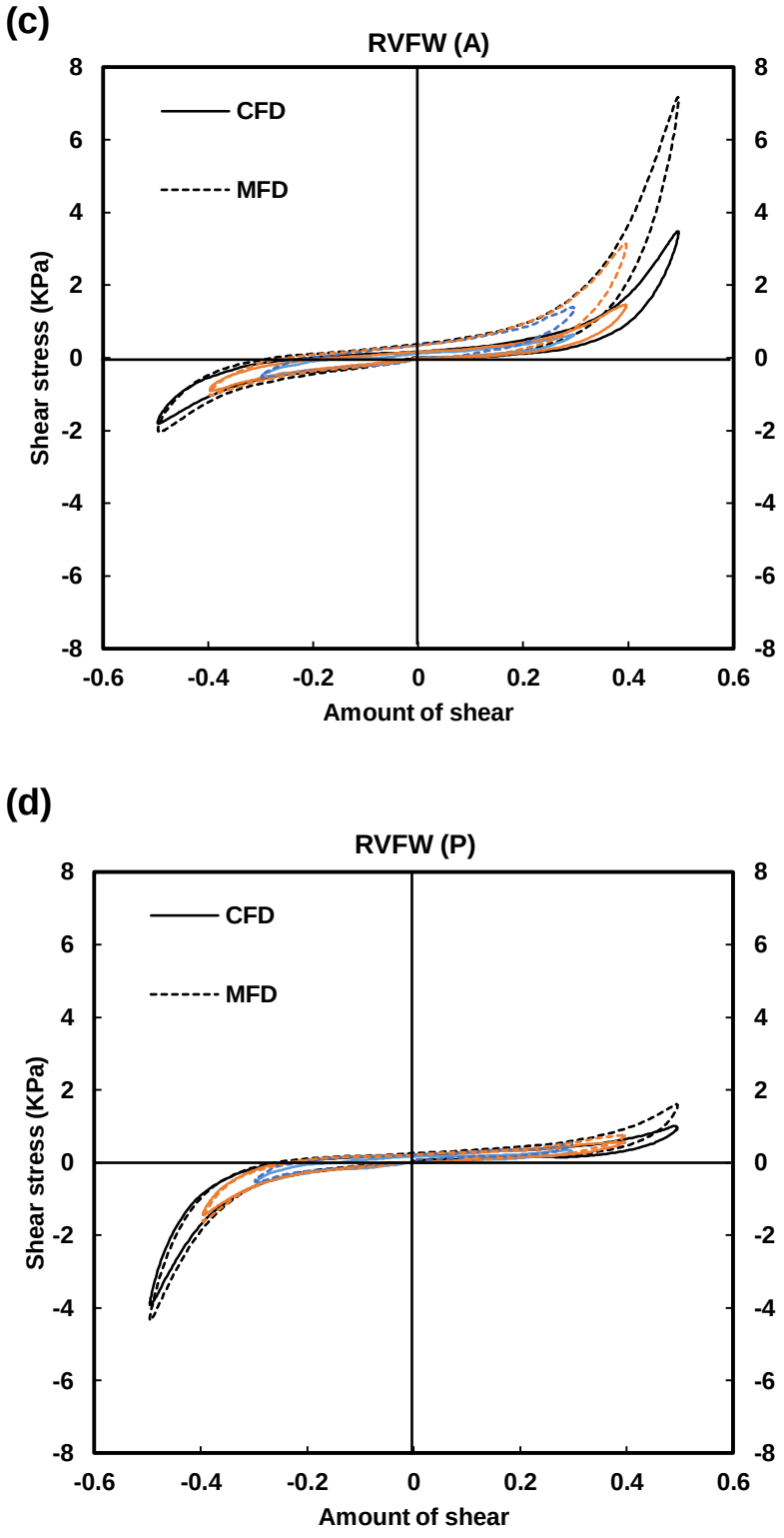

Figure 4.25: *Demonstrating passive 'simple shear' behaviour of the anterior and posterior aspects of the LVFW and RVFW in the MFD and CFD, at 30% (blue curve), 40% (orange curve) and 50% (black curve) of specimens thickness.* ***(a)*** *LVFW–anterior.* ***(b)*** *LVFW–posterior.* ***(c)*** *RVFW–anterior.* ***(d)*** *RVFW–posterior.*

(a)

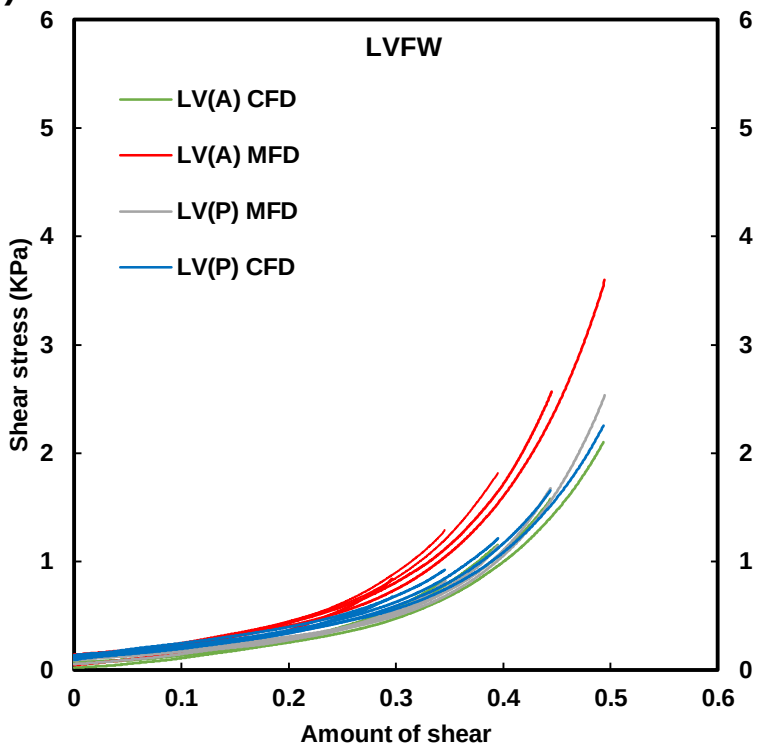
LVFW
LV(A) CFD
LV(A) MFD
LV(P) MFD
LV(P) CFD
Shear stress (KPa)
Amount of shear
0
1
2
3
4
5
6
0.1
0.2
0.3
0.4
0.5
0.6

(b)

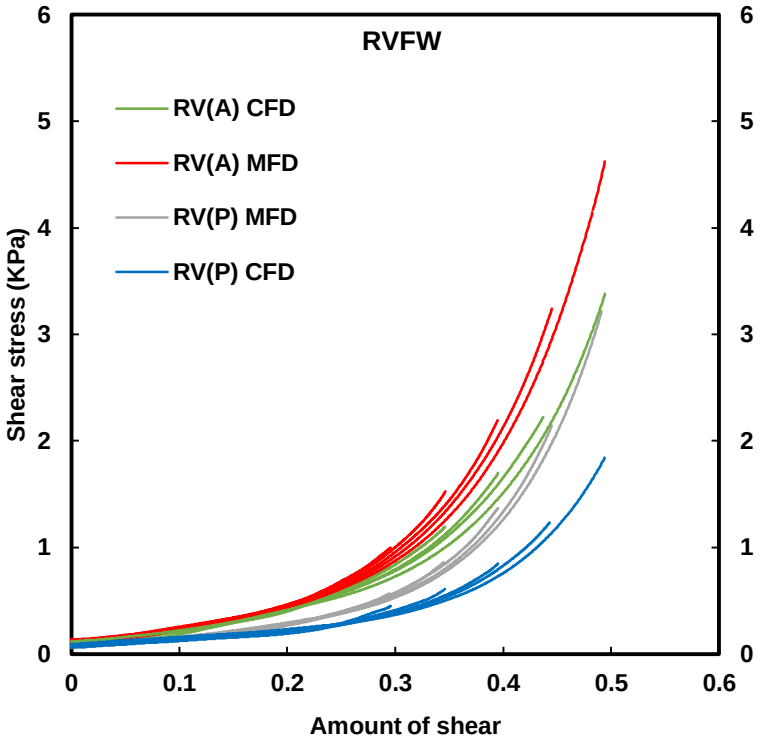
RVFW
RV(A) CFD
RV(A) MFD
RV(P) MFD
RV(P) CFD
Shear stress (KPa)
Amount of shear
0
1
2
3
4
5
6
0.1
0.2
0.3
0.4
0.5
0.6

(c)

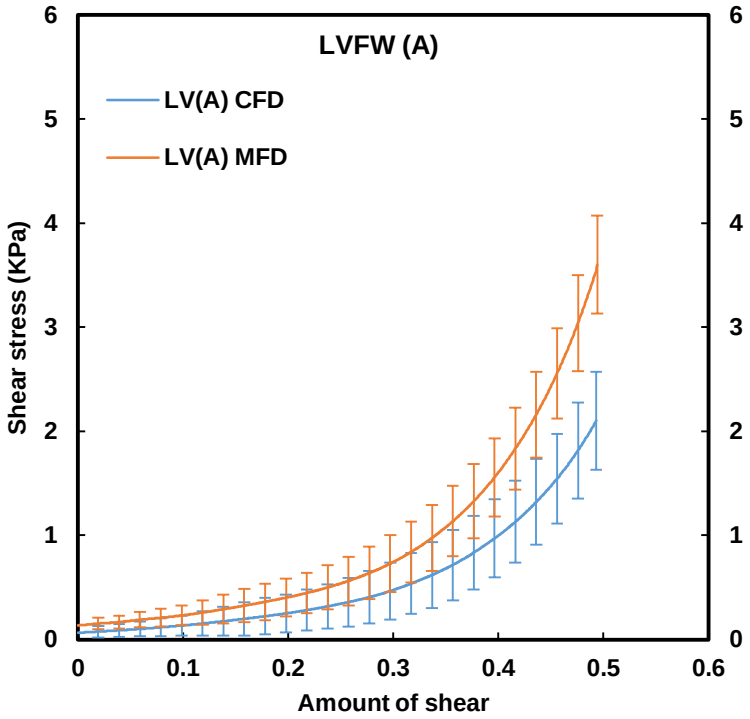
LVFW (A)
LV(A) CFD
LV(A) MFD
Shear stress (KPa)
Amount of shear
0
1
2
3
4
5
6
0
0.1
0.2
0.3
0.4
0.5
0.6

(d)

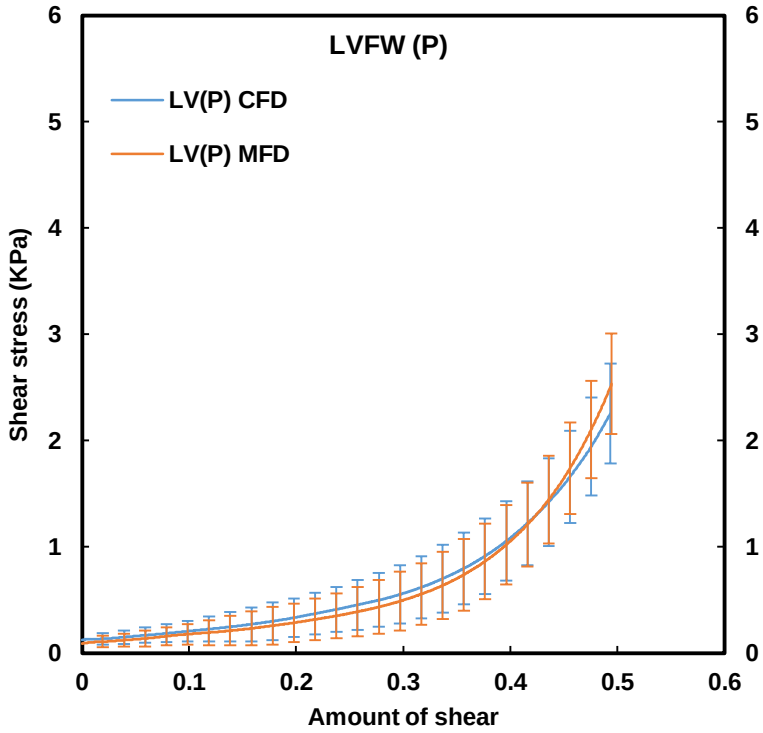
LVFW (P)
LV(P) CFD
LV(P) MFD
Shear stress (KPa)
Amount of shear
0
1
2
3
4
5
6
0
0.1
0.2
0.3
0.4
0.5
0.6

(e)

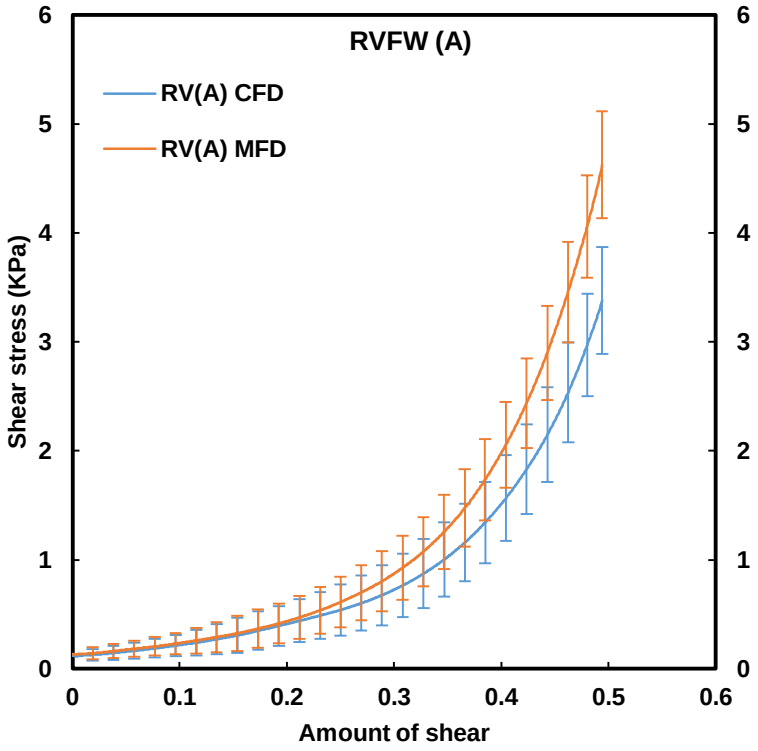
RVFW (A)
RV(A) CFD
RV(A) MFD
Shear stress (KPa)
Amount of shear
0
1
2
3
4
5
6
0.1
0.2
0.3
0.4
0.5
0.6

(f)

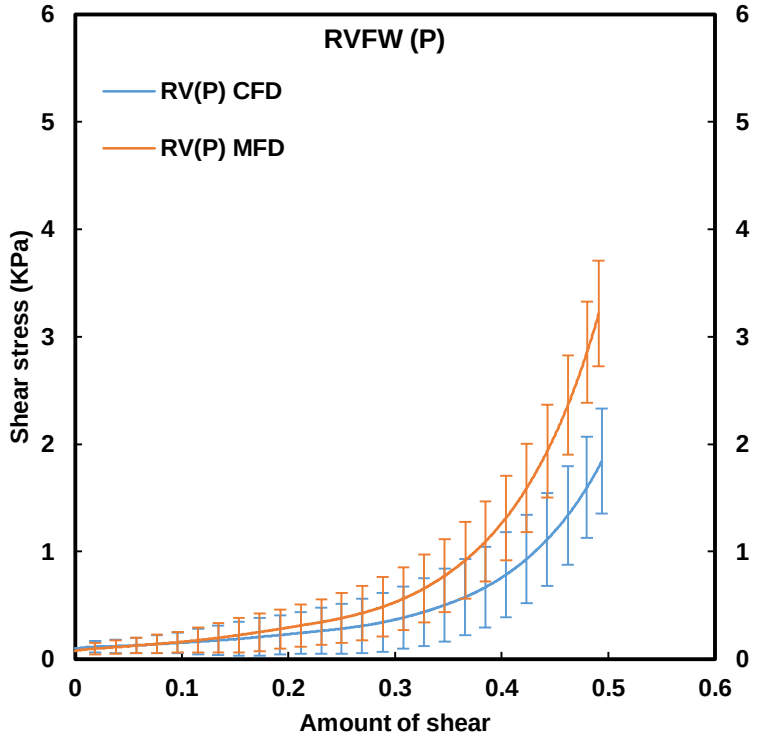
RVFW (P)
RV(P) CFD
RV(P) MFD
Shear stress (KPa)
Amount of shear
0
1
2
3
4
5
6
0.1
0.2
0.3
0.4
0.5
0.6

(g)

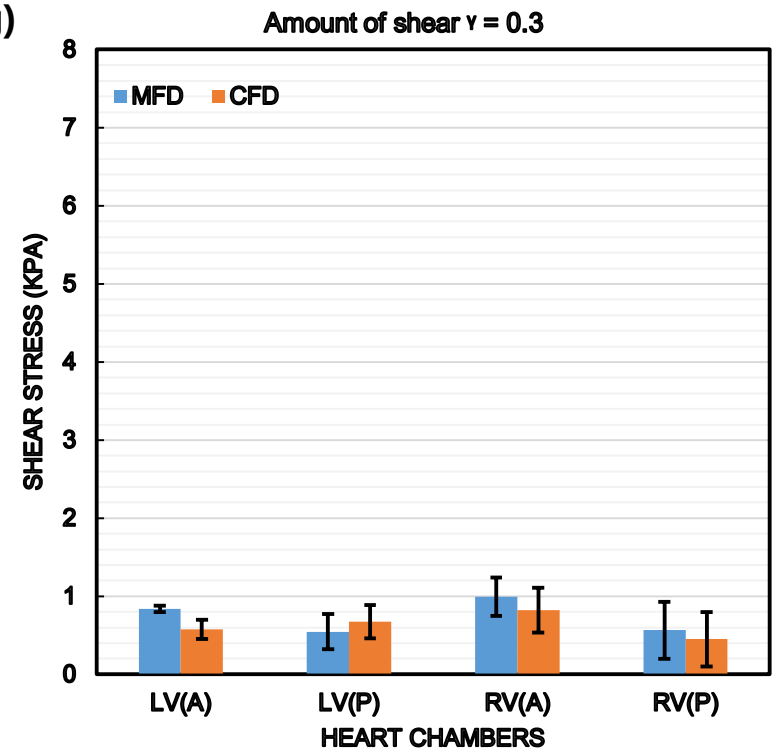
Amount of shear ɣ = 0.3
MFD
CFD
SHEAR STRESS (KPA)
0
1
2
3
4
5
6
7
8
LV(A)
LV(P)
RV(A)
RV(P)
HEART CHAMBERS

(h)

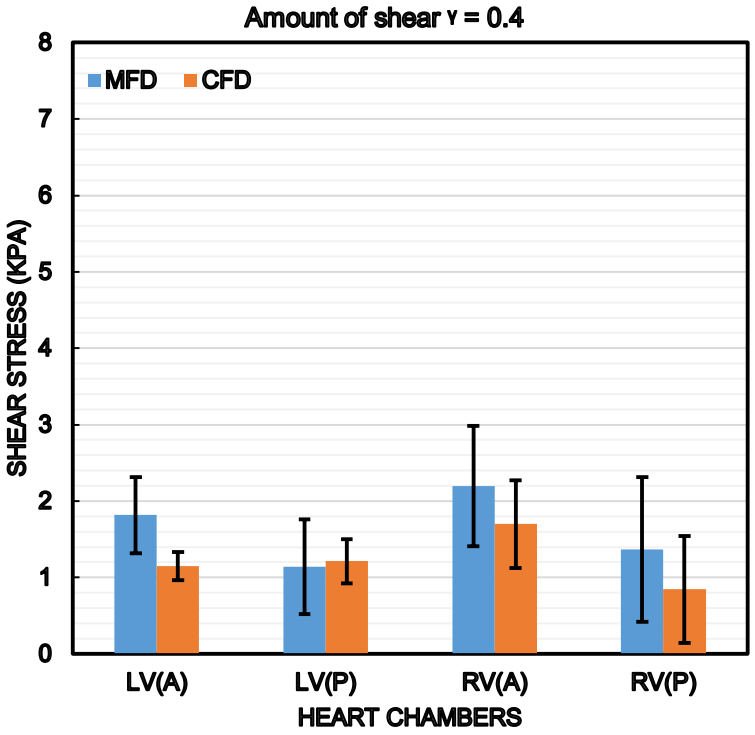
Amount of shear ɣ = 0.4
MFD
CFD
SHEAR STRESS (KPA)
0
1
2
3
4
5
6
7
8
LV(A)
LV(P)
RV(A)
RV(P)
HEART CHAMBERS

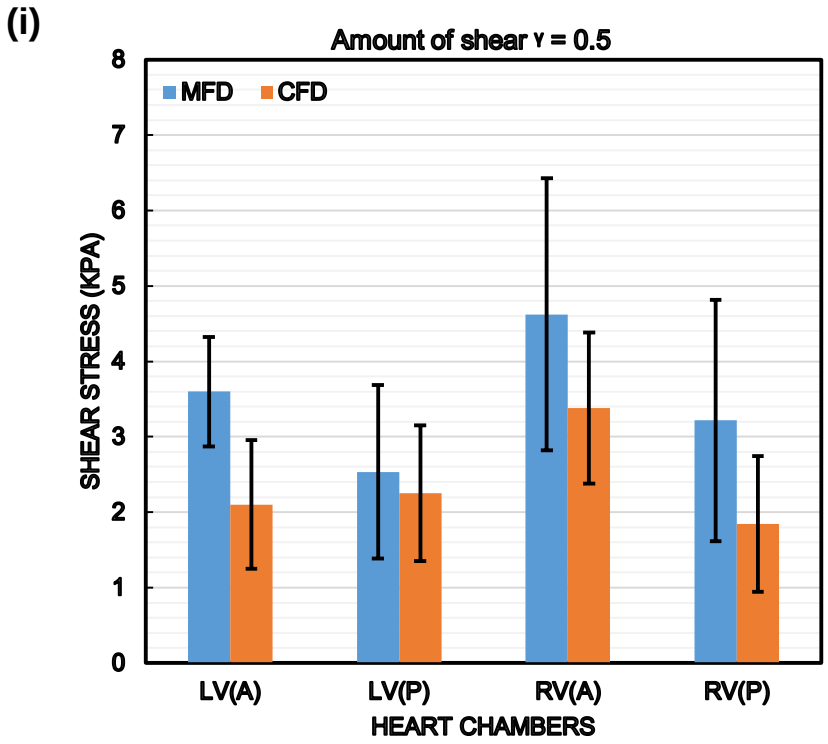

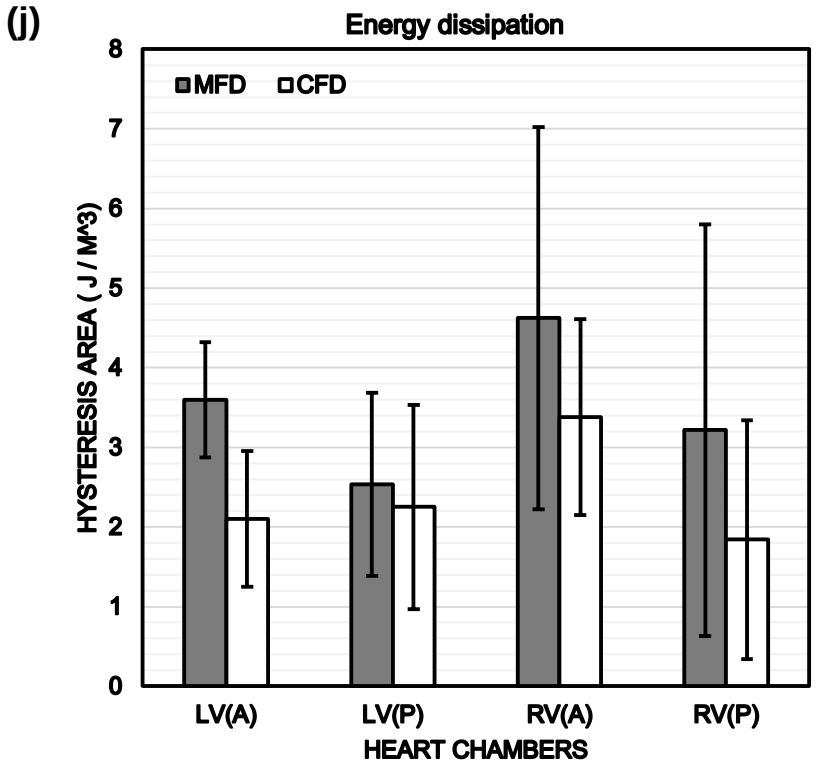

Figure 4.26: *'Mean simple shear behaviour' of anterior and posterior aspect of the LVFW* ***(a)*** *and the RVFW* ***(b)****, in the MFD and CFD at increments of 0.1, 0.2, 0.3, 0.4 and 0.5 (n = 5). LVFW–anterior* ***(c)*** *and posterior* ***(d)*** *in MFD and CFD, at an increment of 0.5. RVFW–anterior* ***(e)*** *and posterior* ***(f)*** *in MFD and CFD at an increment of 0.5.* ***(g)–(i)*** *Column plots indicate average peak shear stress in the anterior and posterior aspects of both ventricles at increments of 0.3, 0.4 and 0.5 respectively (n = 5).* ***(j)*** *Column plots demonstrating mean*

hysteresis areas in the anterior and posterior aspect of LVFW and RVFW, for MFD and CFD at an increment of 0.5 (n = 5). Error bars represent standard deviation.

Table 4.15

Average hysteresis area (J/m^3) of neonatal porcine LVFW and RVFW in the anterior and posterior aspects for simple shear testing at 0.5 increments in MFD and CFD.

	Hysteresis area			
Heart regions	**MFD**	**(SD)**	**CFD**	**(SD)**
LVFW (A)	306*	(104)	260*	(86)
LVFW (P)	201*	(17)	187*	(59)
RVFW (A)	387*	(87)	244*	(159)
RVFW (P)	208*	(117)	174*	(41)

* One-way analysis of variance (ANOVA) did not reveal statistical significance between the anterior and posterior aspects of LVFW and RVFW in the MFD and CFD $p < 0.05$.

Table 4.16

Average peak shear stress values (KPa) for the neonatal LVFW in the anterior (A) and posterior (P) aspects for simple shear testing at 30%,40%,50% amount of shear in MFD and CFD modes.

	LVFW (A)				LVFW (P)			
Increments	**MFD**	**(SD)**	**CFD**	**(SD)**	**MFD**	**(SD)**	**CFD**	**(SD)**
0.3	0.84*	(0.2)	0.57*	(0.3)	0.55*	(0.2)	0.67*	(0.2)
0.4	1.82*	(0.3)	1.15*	(0.4)	1.14*	(0.3)	1.22*	(0.4)
0.5	3.60*	(0.4)	2.10*	(0.5)	2.53*	(0.4)	2.25*	(0.5)

** One-way analysis of variance (ANOVA) revealed statistical significance between the anterior (A) and posterior (P) aspects of LVFW $p < 0.05$.*

Table 4.17

Average peak shear stress values (KPa) for the neonatal RVFW in the anterior (A) and posterior (P) aspects for simple shear testing at 30%,40%,50% amount of shear in MFD and CFD modes.

	RVFW (A)				RVFW (P)			
Increments	**MFD**	**(SD)**	**CFD**	**(SD)**	**MFD**	**(SD)**	**CFD**	**(SD)**
0.3	0.99*	(0.2)	0.82*	(0.3)	0.56*	(0.3)	0.45*	(0.4)
0.4	2.19*	(0.3)	1.69*	(0.3)	1.36*	(0.4)	0.85*	(0.4)
0.5	4.62*	(0.4)	3.38*	(0.5)	3.22*	(0.4)	1.84*	(0.5)

** One-way analysis of variance (ANOVA) revealed statistical significance between the anterior (A) and posterior (P) aspects of both ventricles $p < 0.05$.*

Table 4.18

Statistical analysis (one-way ANOVA along with Tukey HSD post hoc test) data for LVFW and RVFW in the anterior (A) and posterior (P) aspects represent: (1) LVFW (anterior and posterior) for MFD–CFD; (2) RVFW (anterior and posterior) for MFD–CFD; (3) LVFW (A) and RVFW (A) for MFD–CFD; and (4) LVFW (P) and RVFW (P) for MFD–CFD respectively. A p-value less than 0.05 considered statistically significant.

	LVFW (A)		**LVFW (P)**		**RVFW (A)**		**RVFW (P)**	
Configurations	**MFD**	**CFD**	**MFD**	**CFD**	**MFD**	**CFD**	**MFD**	**CFD**
1	0.0001	0.0001	0.0001	0.0001	-	-	-	-
2	-	-	-	-	0.0001	0.0001	0.0001	0.0001
3	0.0001	0.0001	-	-	0.002	0.01	-	-
4	-	-	0.86	0.86	-	-	0.12	0.06

4.2.4. Neonatal heart tissue behaviour under uniaxial tensile, biaxial tensile and simple shear loading modes

A quantitative analysis was performed to highlight the influence of loading conditions on the neonatal tissue mechanical behaviour. Figures 4.27 and 4.28 describe the variance in uniaxial tensile, biaxial tensile and simple shear mechanical behaviour of LVFW and RVFW in MFD and CFD. Myocardial tissue demonstrated relatively stiffer behaviour during a biaxial test, while the greater extensibility was noted during a simple shear test in the MFD and CFD of both ventricles (Figures 4.27 and 4.28). In the LVFW, almost consistent peak stress values of myocardial tissue were observed during the uniaxial tensile and biaxial tensile tests (Tables 4-10 and 4-12). Whereas, in the RVFW, small differences were observed for the peak stress values of myocardial tissue during the uniaxial tensile and biaxial tensile tests (Tables 4.12 and 4.14). In both ventricles, cardiac tissue exhibited the greater extensibility during a simple shear test (Figures 4.27 and 4.28). Meanwhile, the least extensibility in myocardial tissue was noted during a biaxial extension test in the MFD and CFD of both ventricles (Figures 4.27 and 4.28). These quantitative differences in the mechanical behaviour of myocardial tissue, suggesting that the boundary and loading conditions significantly contribute to the mechanical behaviour of cardiac tissue.

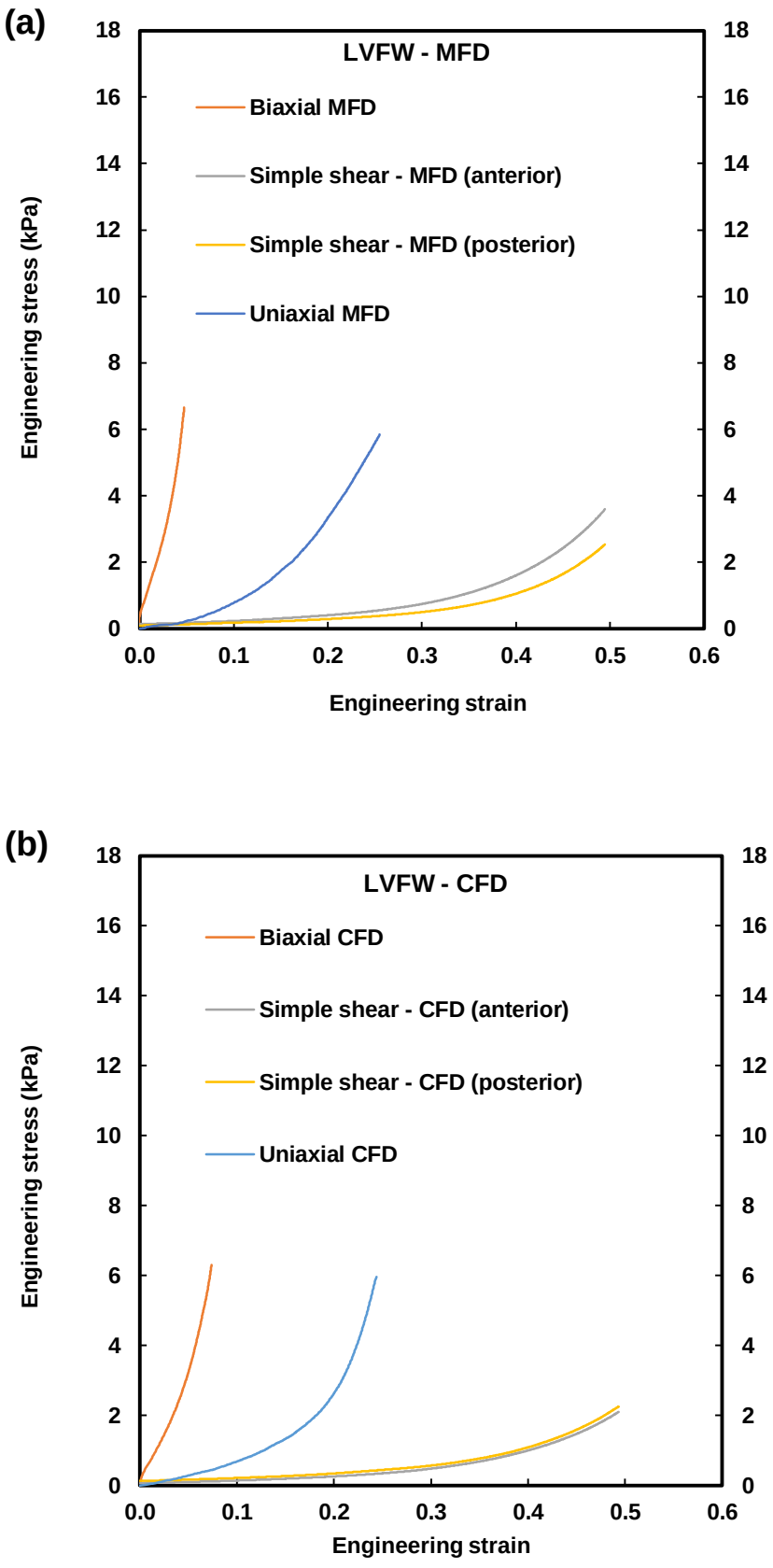

Figure 4.27: (a) *Mean curves of the LVFW (n = 5), demonstrating the mechanical behaviour under uniaxial tensile, biaxial tensile and simple shear loading modes in MFD.* ***(b)*** *Mean*

curves of the LVFW (n = 5), identifying the mechanical behaviour under uniaxial tensile, biaxial extension and simple shear loading modes in CFD.

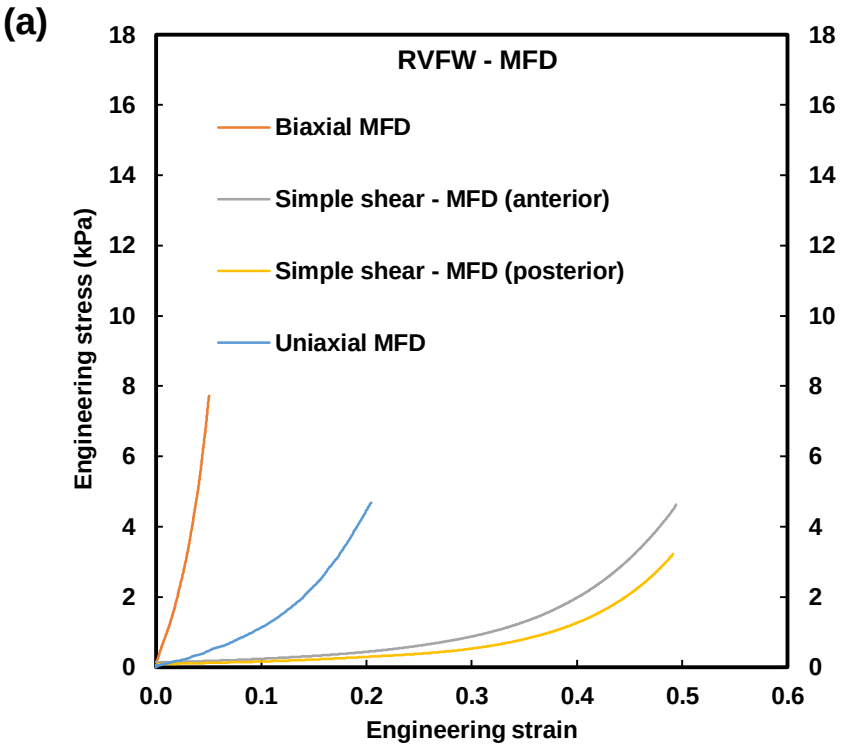

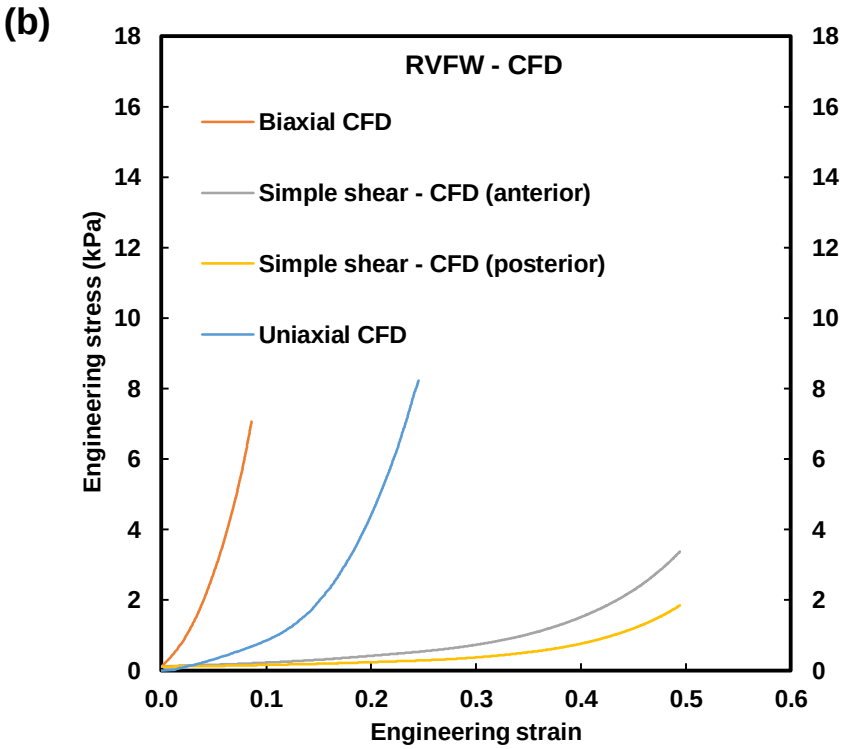

Figure 4.28: (a) *Mean curves of the RVFW (n = 5), demonstrating the mechanical behaviour under uniaxial tensile, biaxial tensile and simple shear loading modes in MFD.* ***(b)*** *Mean curves of the RVFW (n = 5), identifying the mechanical behaviour under uniaxial tensile, biaxial tensile and simple shear loading modes in CFD.*

4.4. Estimating the material parameters of neonatal ventricular myocardium

The microstructural (Fibre orientation) and biomechanical (Uniaxial tensile, biaxial tensile and simple shear) data were used with the structurally based HO – model of the myocardium (Chapter 3, Equations 3.4 & 3.5) in establishing the material parameters of the neonatal ventricular myocardium. These material parameters specifically describe neonatal ventricular myocardium and will enable simulation that more accurately reflect ventricular myocardium behaviour.

4.4.1. Objective function

To quantitatively compare the difference between fitting results and experimental data, the objective function (4.1) was introduced to present the final error to obtain reasonable parameters. The error of fit is defined as the relative difference of area-under-curve between the experimental stress-strain curves and the fitted results,

$$\mathrm{err}^{\mathrm{fit}} = \frac{\int_{\lambda_{\min}}^{\lambda_{\max}} |\sigma_i^{\mathrm{fit}} - \sigma_i^{\mathrm{exp}}| \, d\lambda}{\int_{\lambda_{\min}}^{\lambda_{\max}} \sigma_i^{\mathrm{exp}} \, d\lambda}. \qquad \text{(Eqn 4.1)}$$

A smaller value indicates a better fitting, and a value of 0 indicates a perfect fitting from the inferred parameters.

4.4.2. Fitting results with the HO model of myocardium

At first, the fibre orientation of the myocardium was not considered to obtain the fitting results, as shown in the Figures 4.29 (a), (b) and (c), indicating there are some properties of the sample that were ignored. Therefore, according to the definition of MFD and CFD and

the characteristics of fibre in the left ventricle myocardium, the cardiomyocytes rotation was adopted and set as 60° from the top to bottom of the myocardium. Using this method, the fitting results were obtained and demonstrated in the Figures 4.29 (d), (e) and (f), which was still not a good fit. The unique features in the uniaxial tension were analysed to propose the effective area ratio (an effective area in which the fibres provide stress while the excluding has no effect) to be included in obtaining the results, as shown in Figures 4.29 (g), (h) and (i), indicating the relatively better fit. Consequently, to fit different experimental data together, it is necessary to include detailed myofibre orientations and effective area ratio of the samples in question. In addition, the error in CFD was always greater than that in MFD, which may have resulted in the HO model expression that does not have the item represents CFD (normal direction).

The advantage of this experimental data is that it includes three different kinds of tests (i.e. uniaxial tensile, biaxial tensile, and simple shear), which are more likely to get realistic parameters to represent the characteristics of the myocardium, while most of the other studies have only used one or two of the tests. Therefore, it is interesting to find whether the characteristic parameters that are obtained from one or two type test can be applied to another test directly. Figures 4.30 and 4.31 indicate that the estimated parameters by fitting only one or two types of experiments could not match the remained experiments. It is, therefore, essential to include all experimental data to determine the material parameters.

The material parameters that are estimated in Figures 4.29, 4.30, and 4.31 are stated in Tables 4.19, 4.20 and 4.21. Similarly, the area error values evaluated in Figures 4.29, 4.30, and 4.31 are detailed in Tables 4.22, 4.23 and 4.24, respectively.

(a)

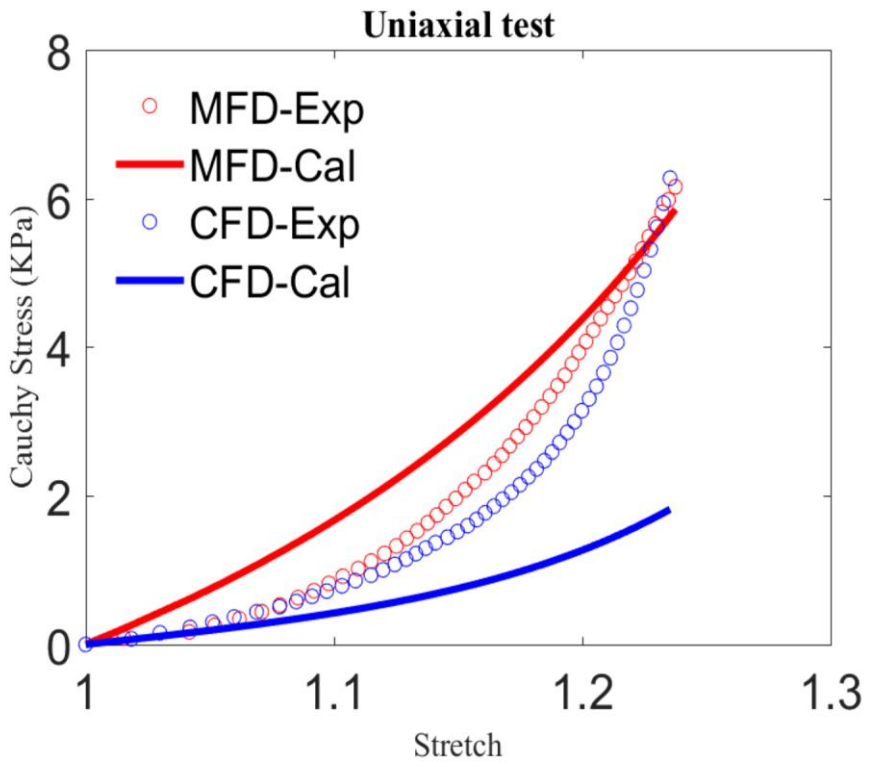
Uniaxial test
MFD-Exp
MFD-Cal
CFD-Exp
CFD-Cal
Cauchy Stress (KPa)
Stretch
0
2
4
6
8
1
1.1
1.2
1.3

(b)

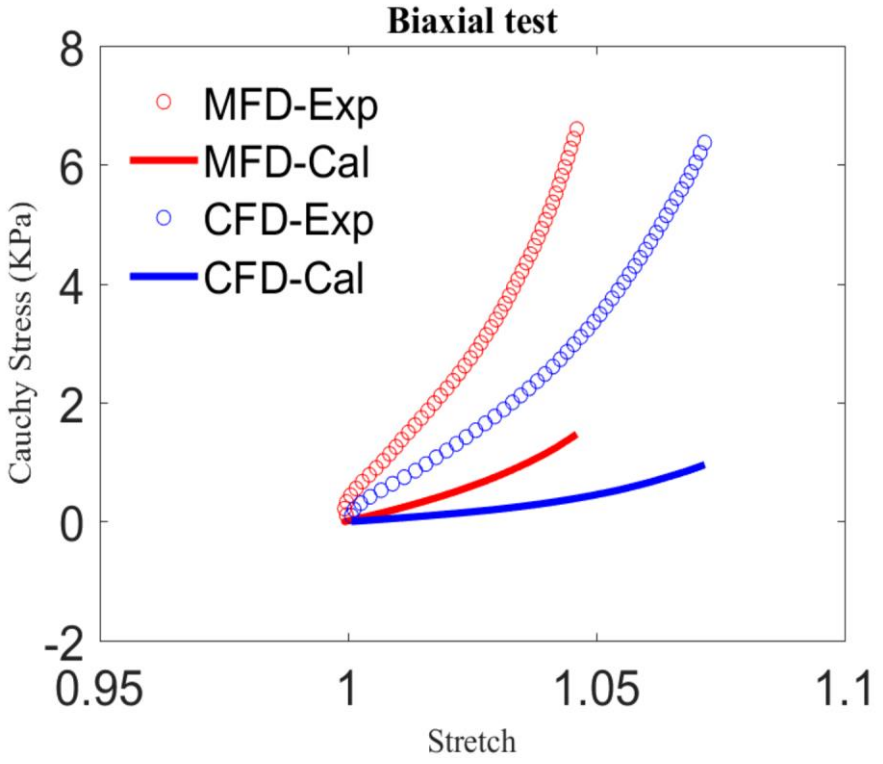
Biaxial test
MFD-Exp
MFD-Cal
CFD-Exp
CFD-Cal
Cauchy Stress (KPa)
Stretch
-2
0
2
4
6
8
0.95
1
1.05
1.1

(c)

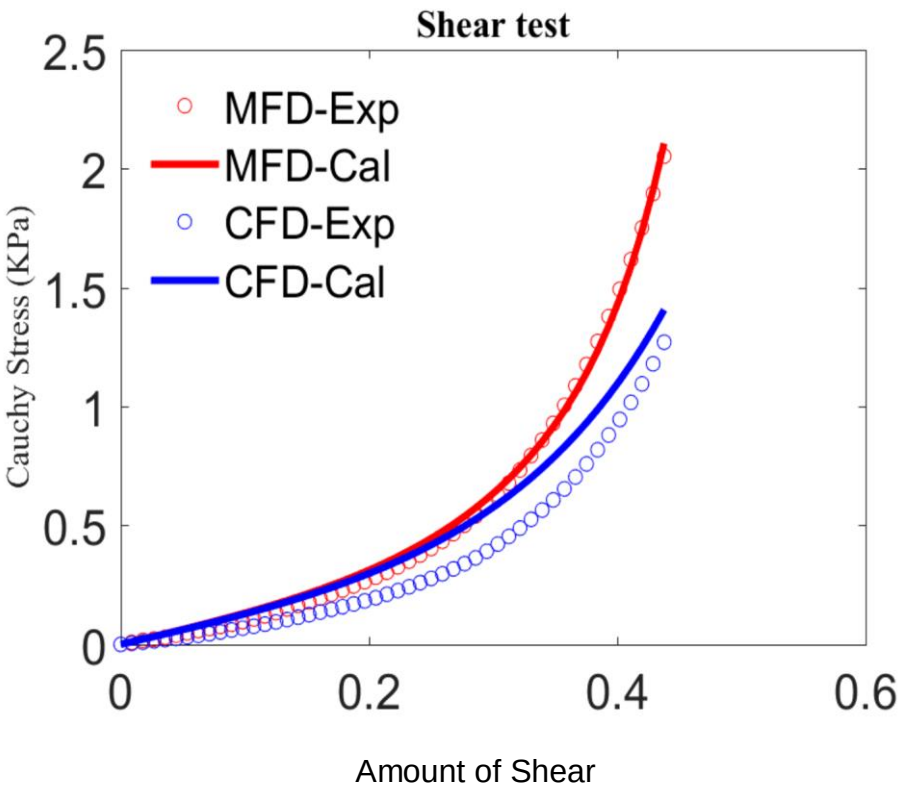
Shear test
MFD-Exp
MFD-Cal
CFD-Exp
CFD-Cal
Cauchy Stress (KPa)
2.5
2
1.5
1
0.5
0
0
0.2
0.4
0.6
Amount of Shear

(d)

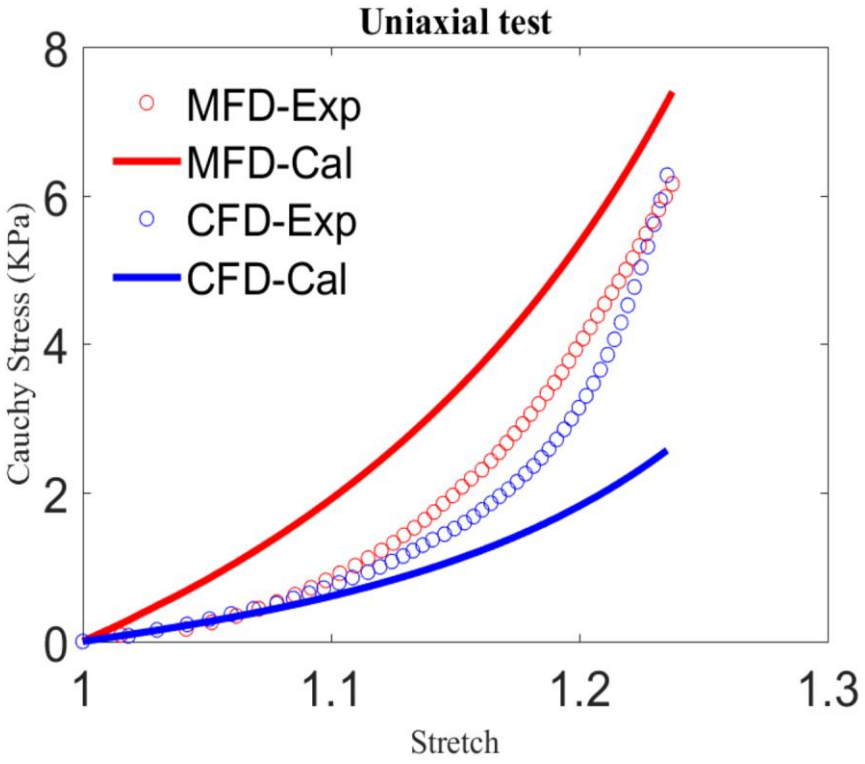
Uniaxial test
MFD-Exp
MFD-Cal
CFD-Exp
CFD-Cal
Cauchy Stress (KPa)
8
6
4
2
0
1
1.1
1.2
1.3
Stretch

(e)

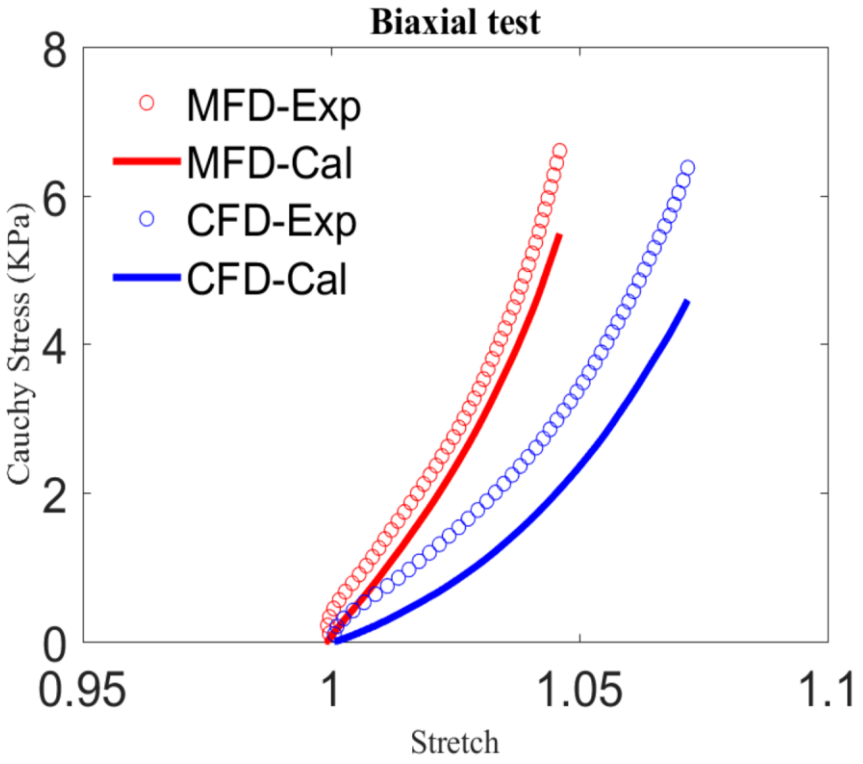
Biaxial test
MFD-Exp
MFD-Cal
CFD-Exp
CFD-Cal
Cauchy Stress (KPa)
Stretch
0
2
4
6
8
0.95
1
1.05
1.1

(f)

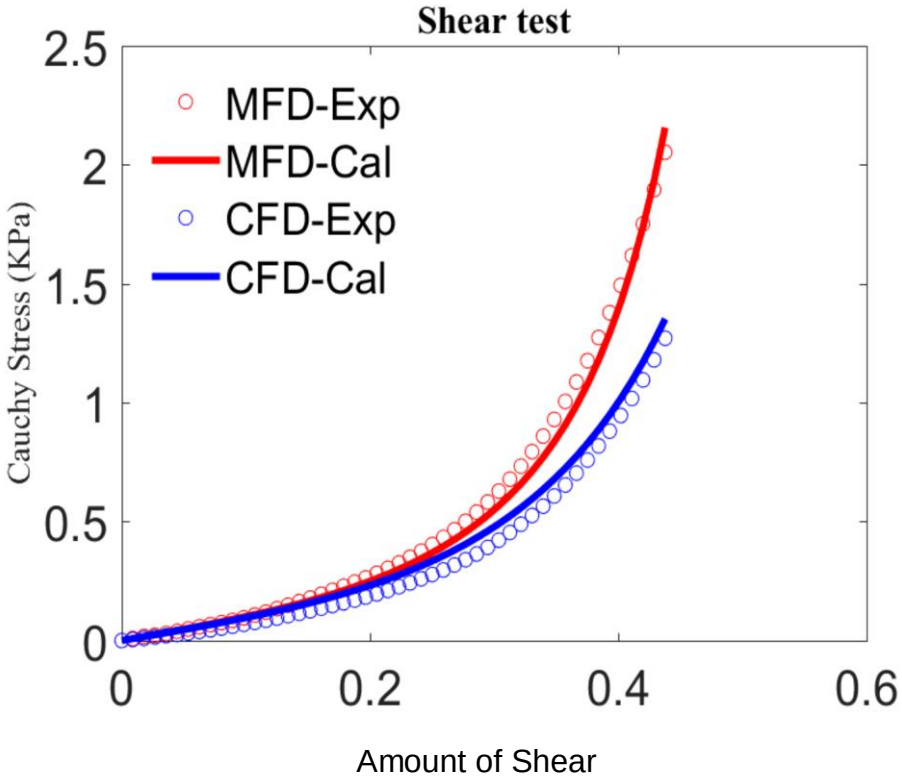
Shear test
MFD-Exp
MFD-Cal
CFD-Exp
CFD-Cal
Cauchy Stress (KPa)
Amount of Shear
0
0.5
1
1.5
2
2.5
0
0.2
0.4
0.6

(g)

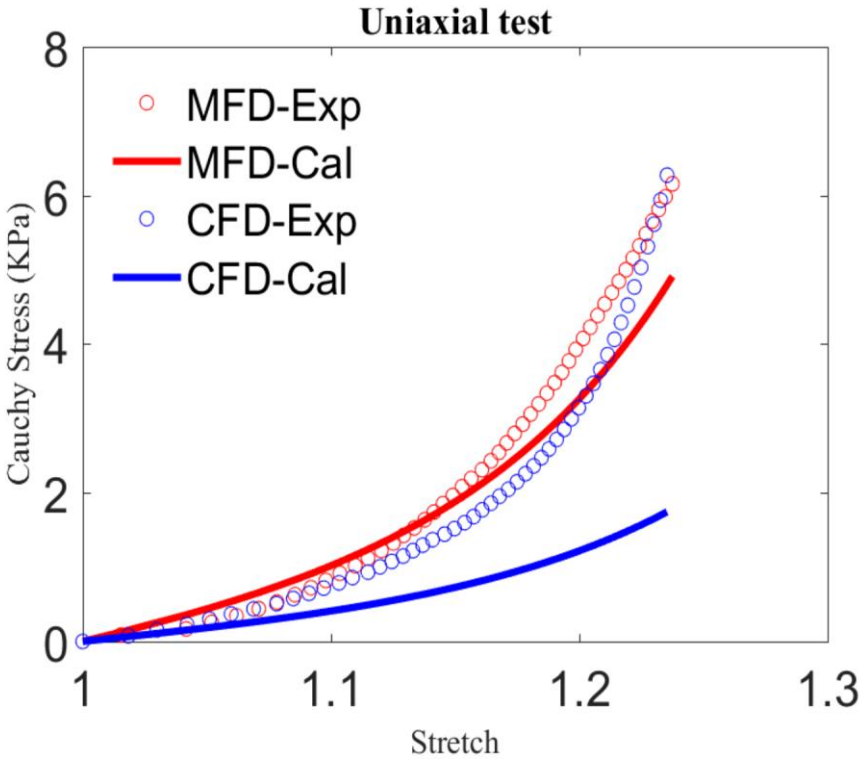
Uniaxial test
MFD-Exp
MFD-Cal
CFD-Exp
CFD-Cal
Cauchy Stress (KPa)
Stretch
0
2
4
6
8
1
1.1
1.2
1.3

(h)

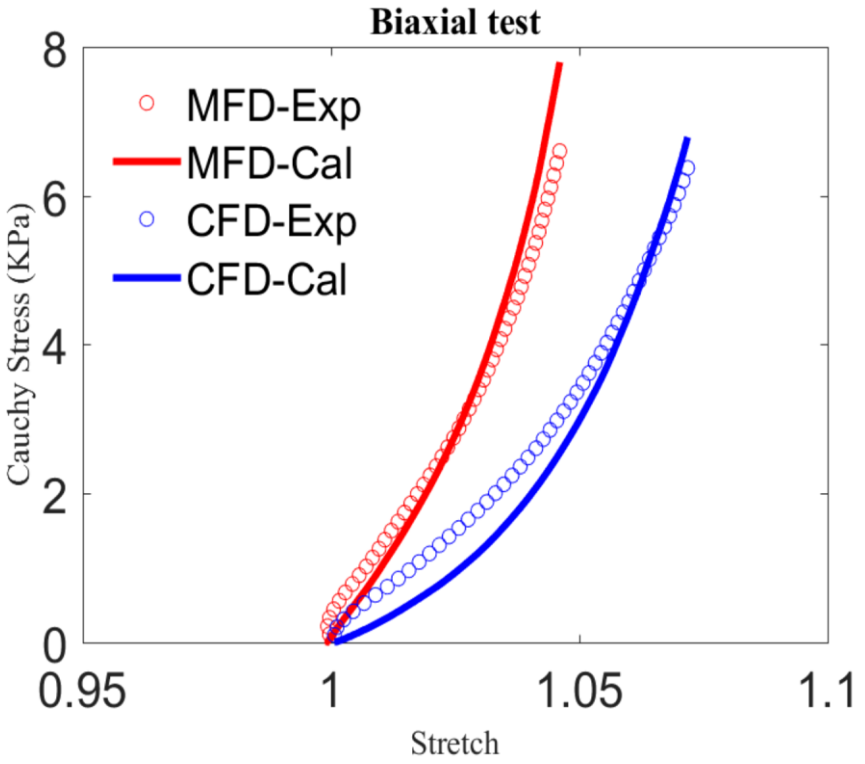
Biaxial test
MFD-Exp
MFD-Cal
CFD-Exp
CFD-Cal
Cauchy Stress (KPa)
Stretch
0
2
4
6
8
0.95
1
1.05
1.1

(i)

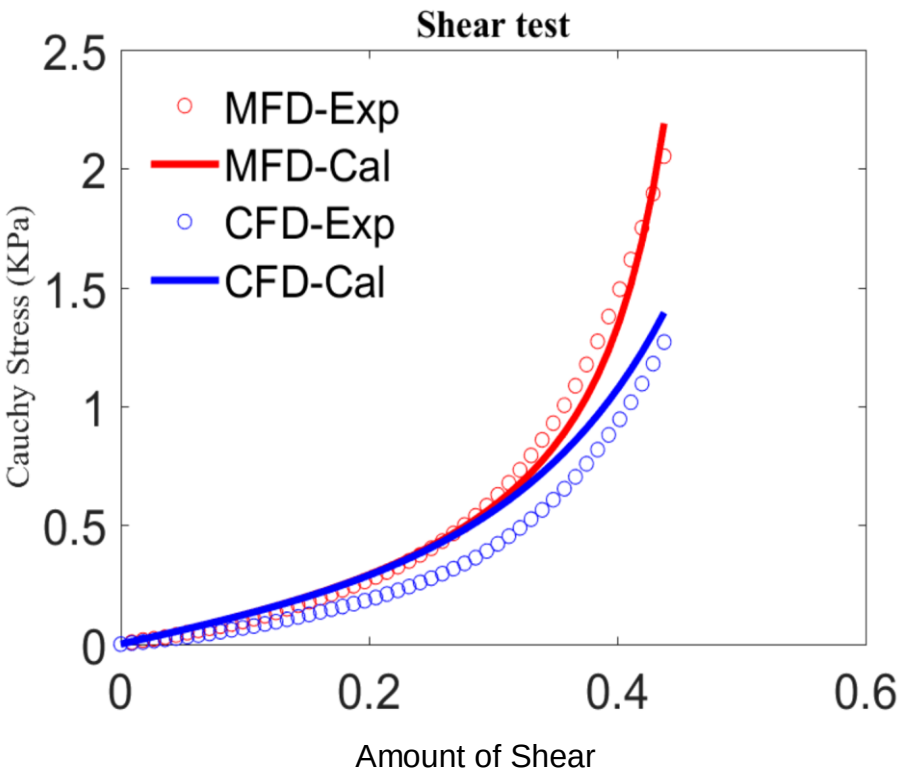
Shear test
MFD-Exp
MFD-Cal
CFD-Exp
CFD-Cal
Cauchy Stress (KPa)
Amount of Shear
0
0.5
1
1.5
2
2.5
0.2
0.4
0.6

(j)

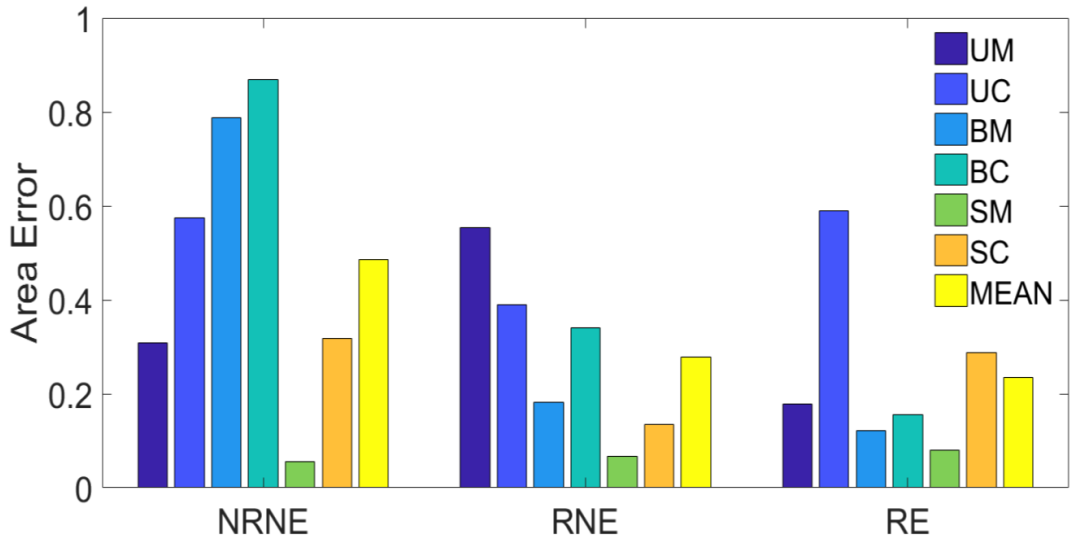
Area Error
UM
UC
BM
BC
SM
SC
MEAN
NRNE
RNE
RE
0
0.2
0.4
0.6
0.8
1

Figure 4.29: *Fit based on HO model under different assumptions between experimental data noted by Experimental-and calculating data, and noted by calculations in three types of LVFW experiments respectively.* ***(a), (b)*** *and* ***(c)*** *show the fitting when assuming there is no fibre rotation in the experimental samples;* ***(d), (e)*** *and* ***(f)*** *are the results after considering fibre rotation but no effective area;* ***(g), (h)*** *and* ***(i)*** *adopt fibre rotation and effective area.* ***(j)*** *is a comparison among different conditions. NRNE considers no fibre rotation and no effective area; RNE considers only fibre rotation and RE considers both fibre rotation and effective area. UM presents Uniaxial tension in MFD; UC presents Uniaxial tension in CFD; BM presents Biaxial tension in MFD; BC presents Biaxial tension in CFD; SM presents shear amount in MFD and SC presents shear amount in CFD.*

(a)

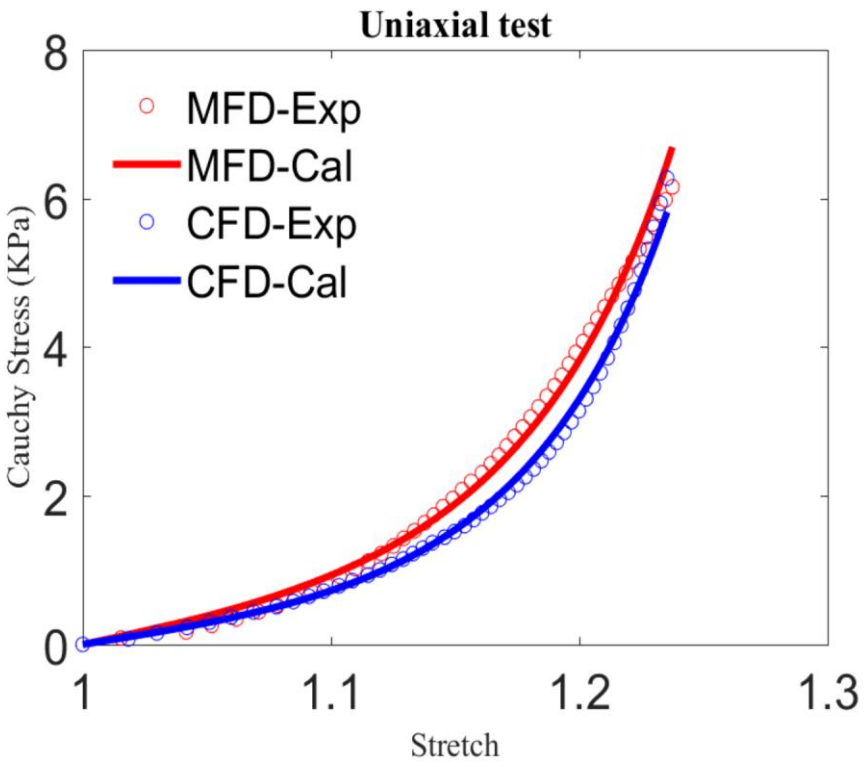
Uniaxial test
MFD-Exp
MFD-Cal
CFD-Exp
CFD-Cal
Cauchy Stress (KPa)
Stretch
0
2
4
6
8
1
1.1
1.2
1.3

(b)

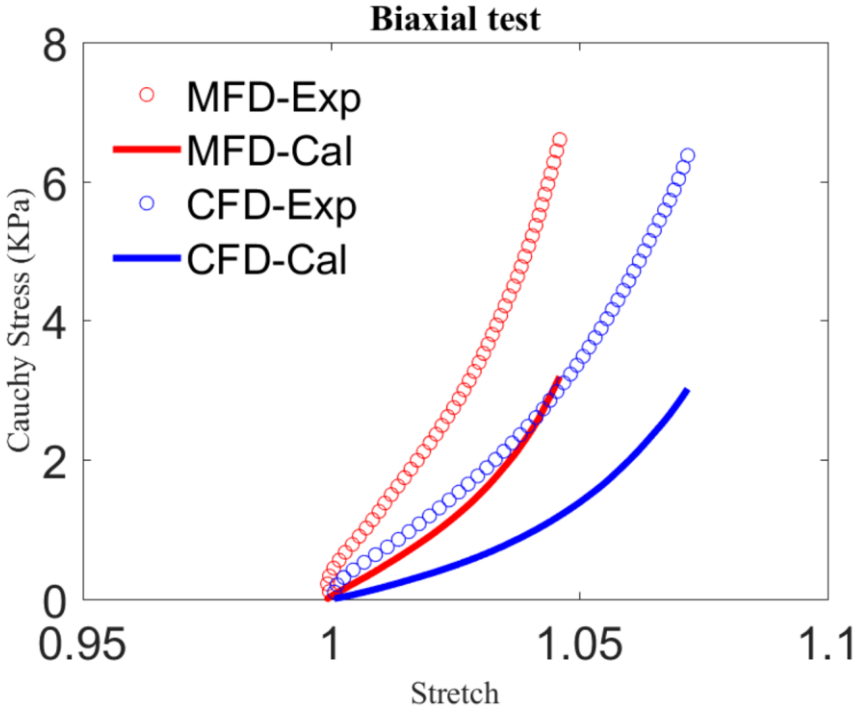
Biaxial test
MFD-Exp
MFD-Cal
CFD-Exp
CFD-Cal
Cauchy Stress (KPa)
Stretch
0
2
4
6
8
0.95
1
1.05
1.1

(c)

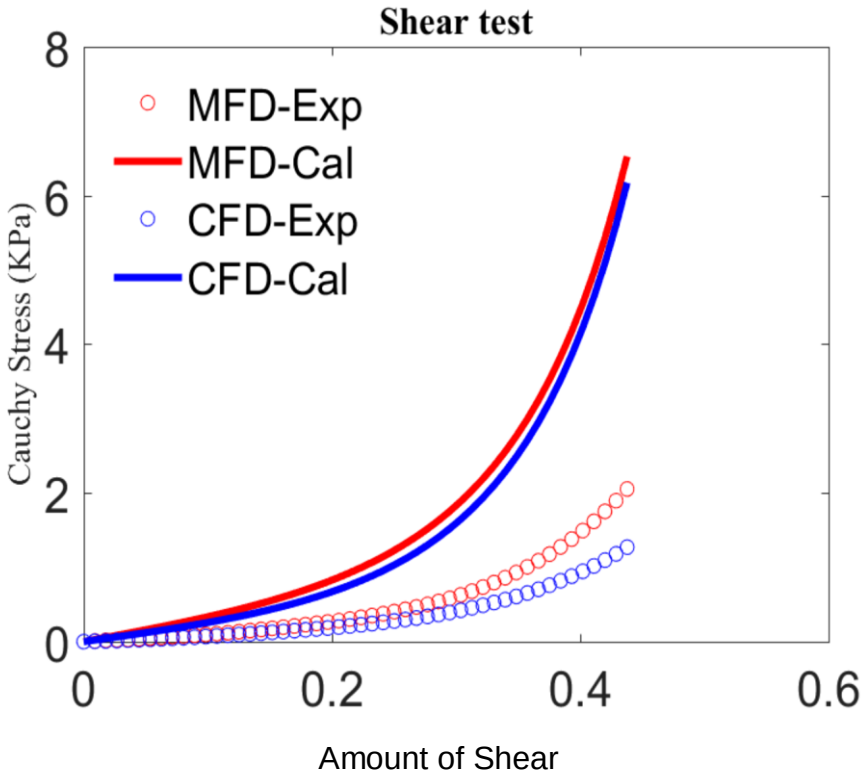
Shear test
MFD-Exp
MFD-Cal
CFD-Exp
CFD-Cal
Cauchy Stress (KPa)
0
2
4
6
8
0
0.2
0.4
0.6
Amount of Shear

(d)

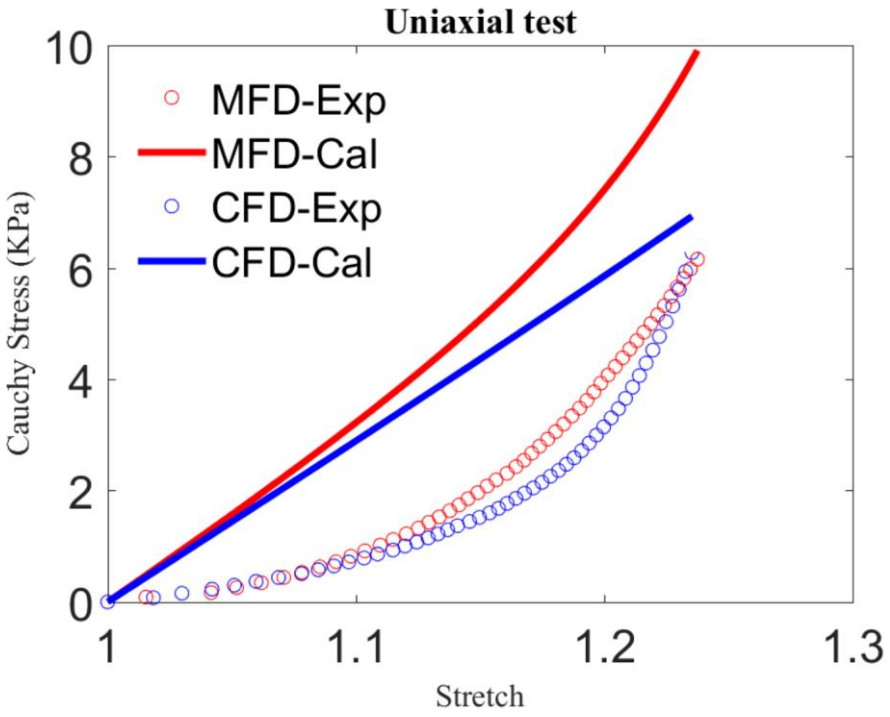
Uniaxial test
MFD-Exp
MFD-Cal
CFD-Exp
CFD-Cal
Cauchy Stress (KPa)
0
2
4
6
8
10
1
1.1
1.2
1.3
Stretch

(e)

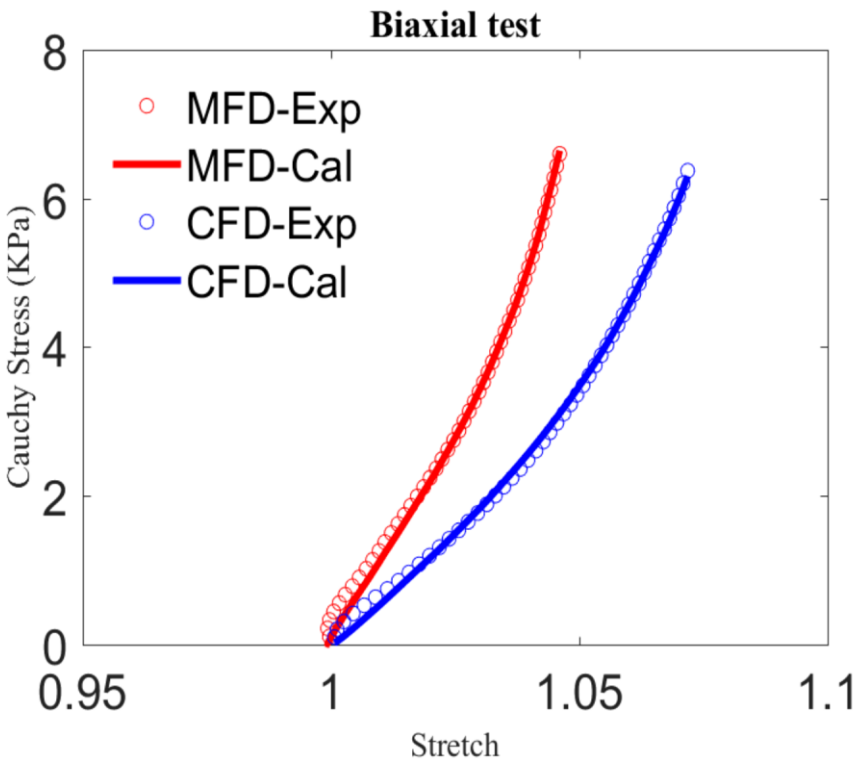
Biaxial test
MFD-Exp
MFD-Cal
CFD-Exp
CFD-Cal
Cauchy Stress (KPa)
Stretch
0
2
4
6
8
0.95
1
1.05
1.1

(f)

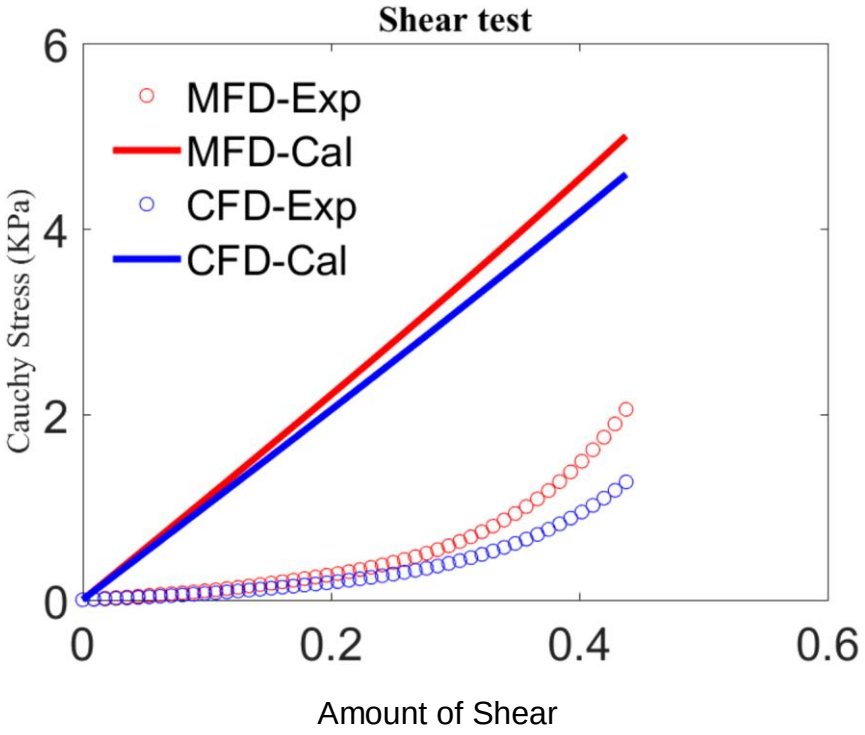
Shear test
MFD-Exp
MFD-Cal
CFD-Exp
CFD-Cal
Cauchy Stress (KPa)
Amount of Shear
0
2
4
6
0
0.2
0.4
0.6

(g)

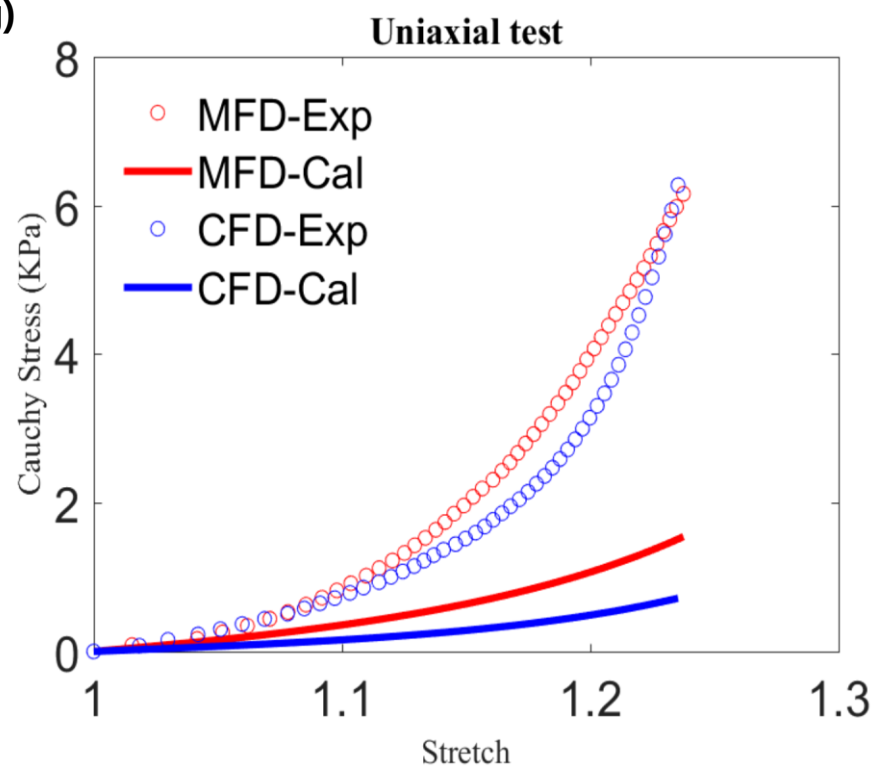
Uniaxial test
MFD-Exp
MFD-Cal
CFD-Exp
CFD-Cal
Cauchy Stress (KPa)
Stretch
0
2
4
6
8
1
1.1
1.2
1.3

(h)

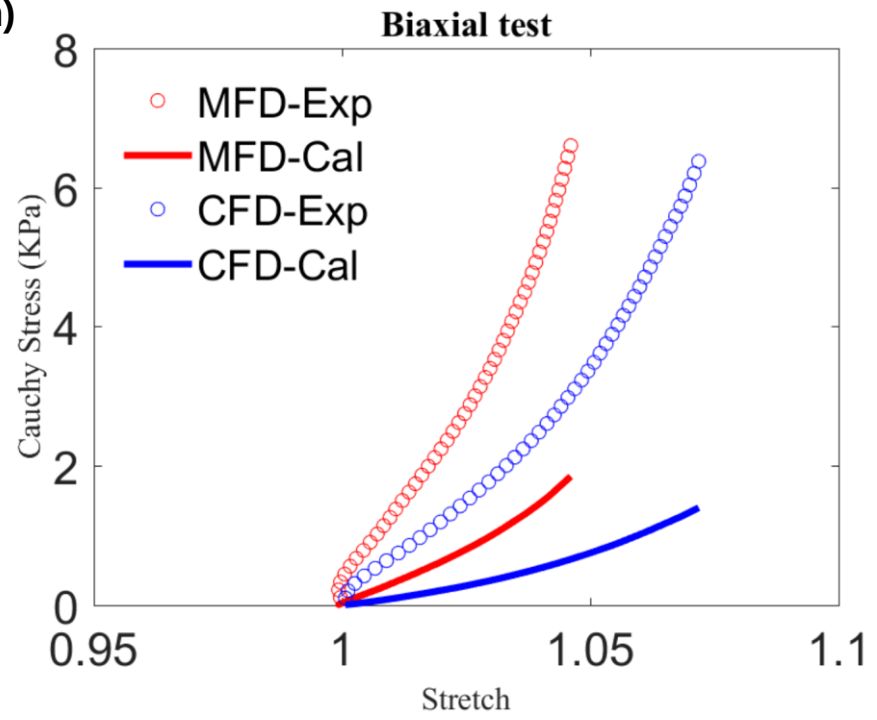
Biaxial test
MFD-Exp
MFD-Cal
CFD-Exp
CFD-Cal
Cauchy Stress (KPa)
Stretch
0
2
4
6
8
0.95
1
1.05
1.1

(i)

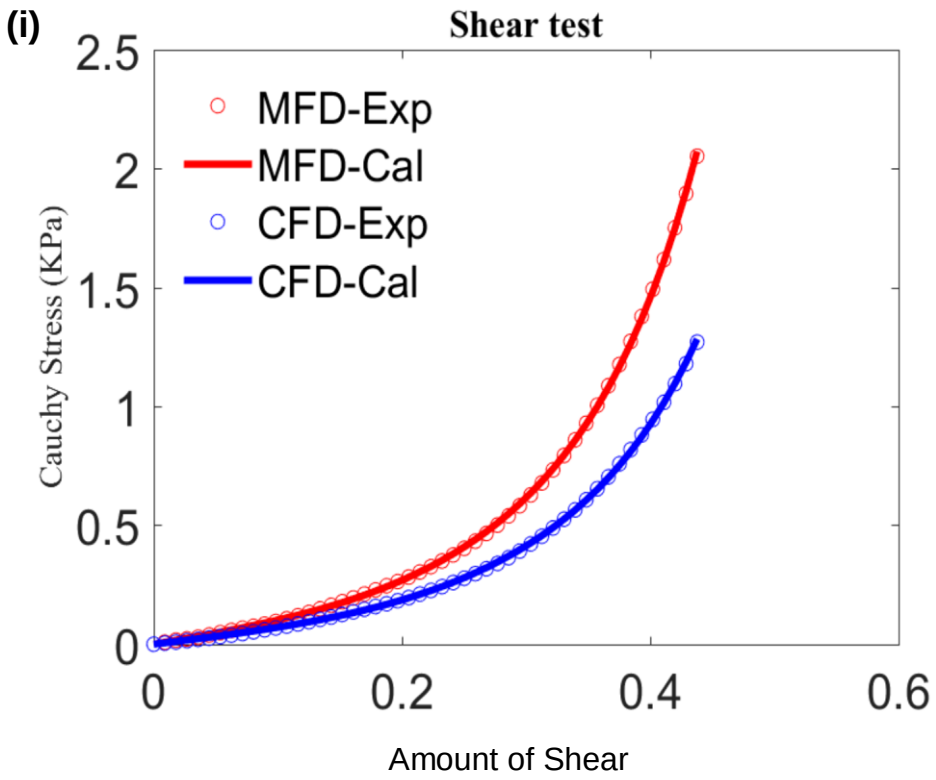
Shear test
MFD-Exp
MFD-Cal
CFD-Exp
CFD-Cal
Cauchy Stress (KPa)
2.5
2
1.5
1
0.5
0
0
0.2
0.4
0.6
Amount of Shear

(j)

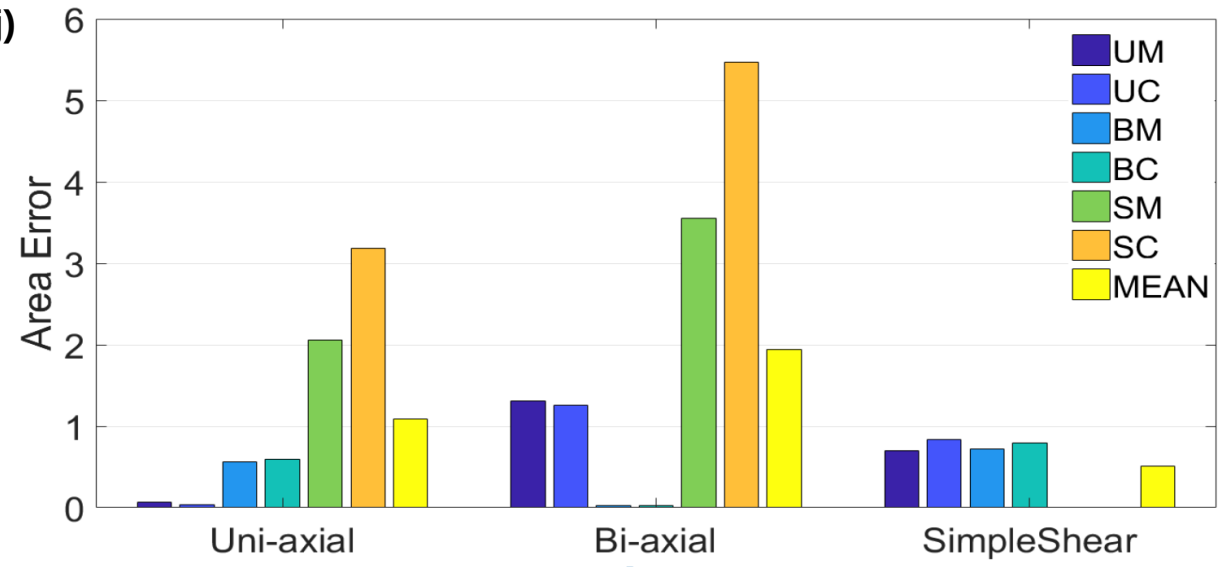
Area Error
6
5
4
3
2
1
0
UM
UC
BM
BC
SM
SC
MEAN
Uni-axial
Bi-axial
SimpleShear

Figure 4.30: *Fit based on general HO models under different fitting couples of LVFW.* ***(a), (b)*** *and* ***(c)*** *show the results by only fitting uniaxial and then apply the parameters to biaxial and simple shear;* ***(d), (e)*** *and* ***(f)*** *are only fitting biaxial data;* ***(g), (h)*** *and* ***(i)*** *fitting simple shear only.* ***(j)*** *is the area error comparison among different conditions. UM presents Uniaxial tension in MFD; UC presents Uniaxial tension in CFD; BM presents Biaxial tension in MFD; BC presents Biaxial tension in CFD; SM presents shear amount in MFD and SC presents shear amount in CFD.*

(a)

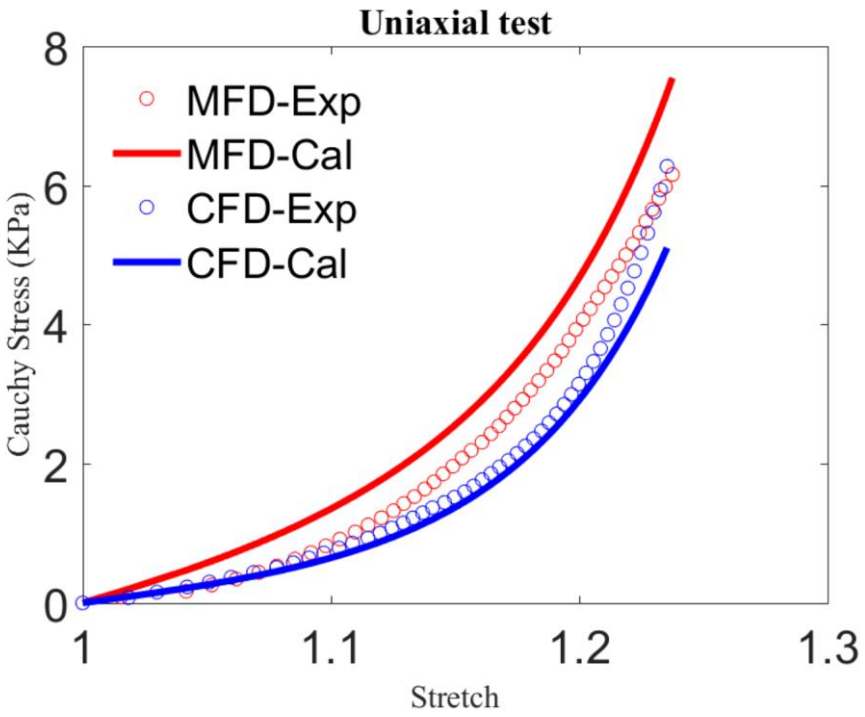
Uniaxial test
MFD-Exp
MFD-Cal
CFD-Exp
CFD-Cal
Cauchy Stress (KPa)
Stretch
0
2
4
6
8
1
1.1
1.2
1.3

(b)

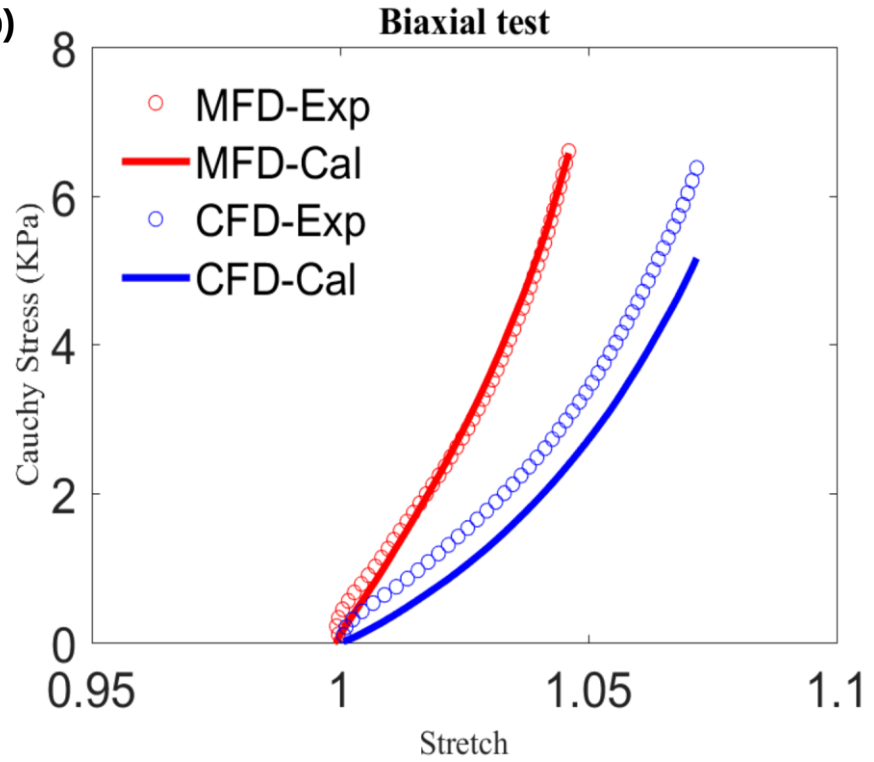
Biaxial test
MFD-Exp
MFD-Cal
CFD-Exp
CFD-Cal
Cauchy Stress (KPa)
Stretch
0
2
4
6
8
0.95
1
1.05
1.1

(c)

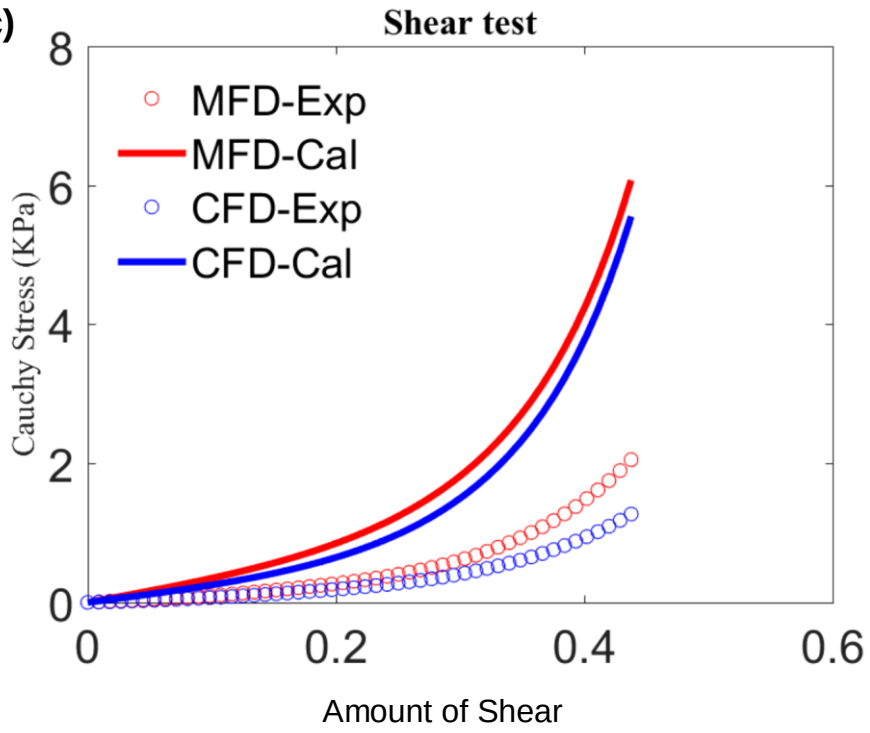
Shear test
MFD-Exp
MFD-Cal
CFD-Exp
CFD-Cal
Cauchy Stress (KPa)
0
2
4
6
8
0
0.2
0.4
0.6
Amount of Shear

(d)

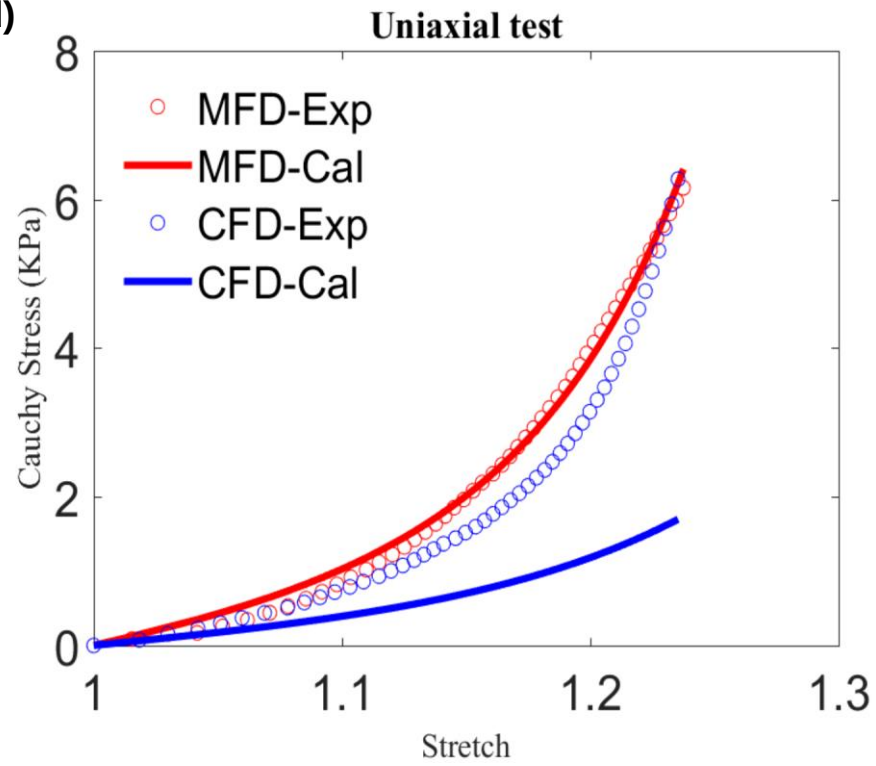
Uniaxial test
MFD-Exp
MFD-Cal
CFD-Exp
CFD-Cal
Cauchy Stress (KPa)
0
2
4
6
8
1
1.1
1.2
1.3
Stretch

(e)

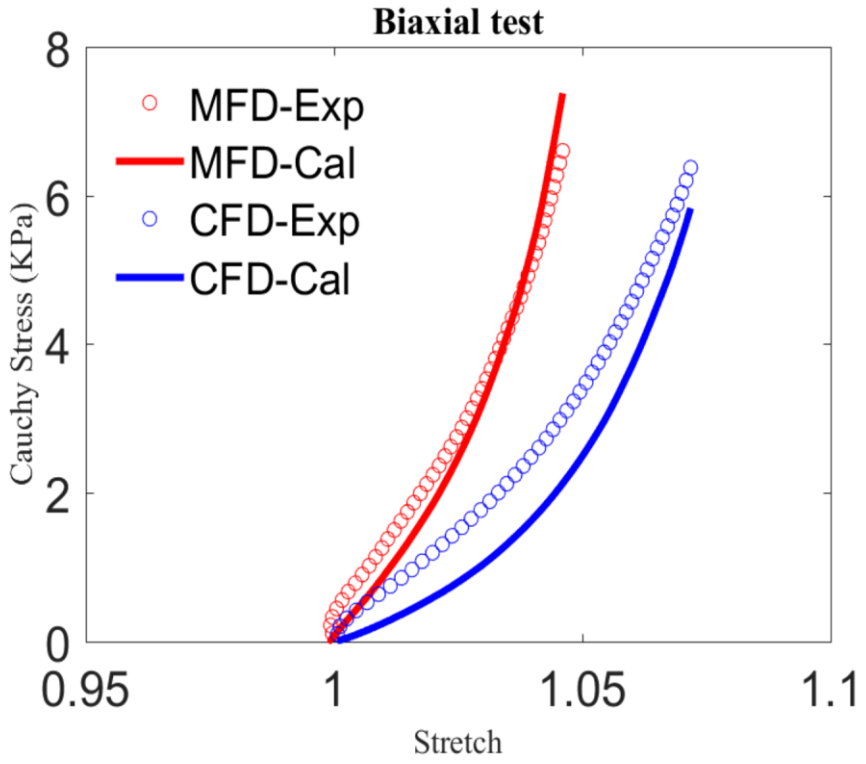
Biaxial test
MFD-Exp
MFD-Cal
CFD-Exp
CFD-Cal
Cauchy Stress (KPa)
Stretch
0
2
4
6
8
0.95
1
1.05
1.1

(f)

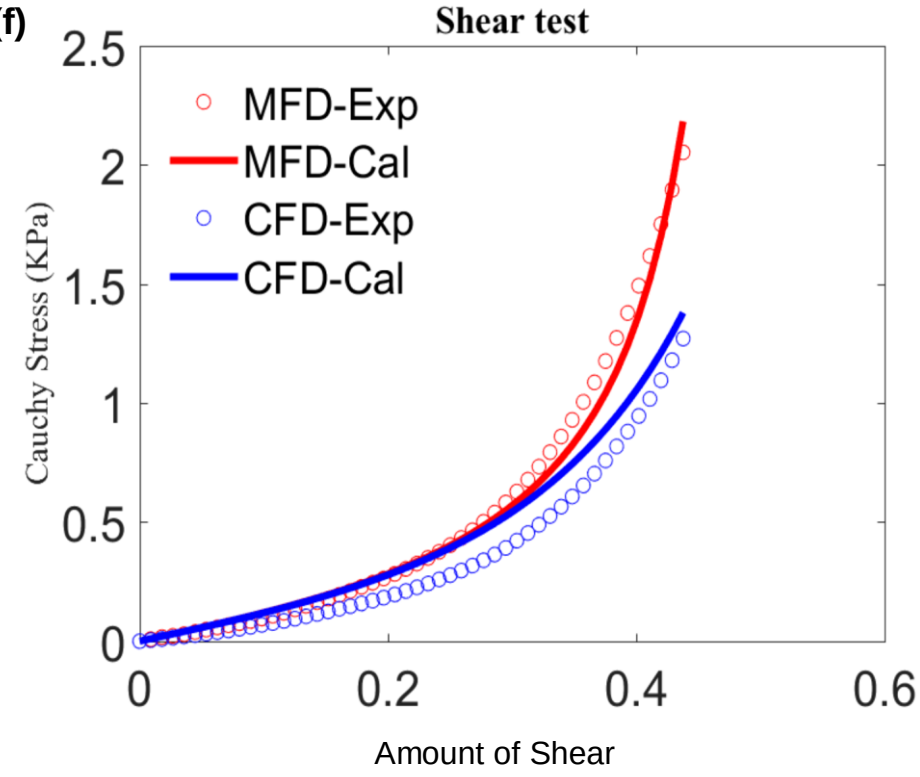
Shear test
MFD-Exp
MFD-Cal
CFD-Exp
CFD-Cal
Cauchy Stress (KPa)
Amount of Shear
0
0.5
1
1.5
2
2.5
0
0.2
0.4
0.6

(g)

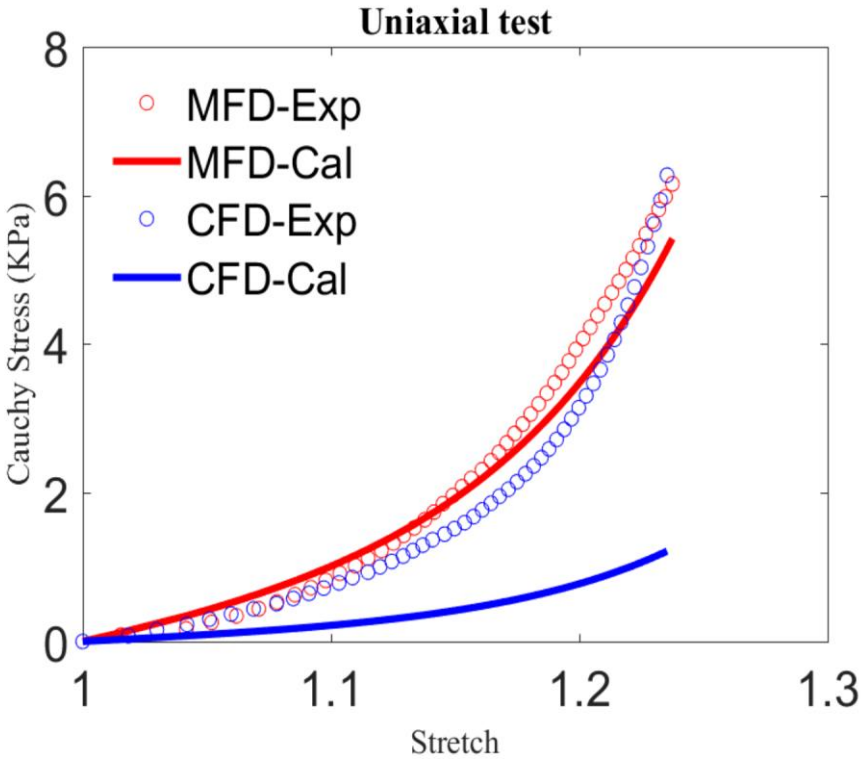
Uniaxial test
MFD-Exp
MFD-Cal
CFD-Exp
CFD-Cal
Cauchy Stress (KPa)
Stretch
0
2
4
6
8
1
1.1
1.2
1.3

(h)

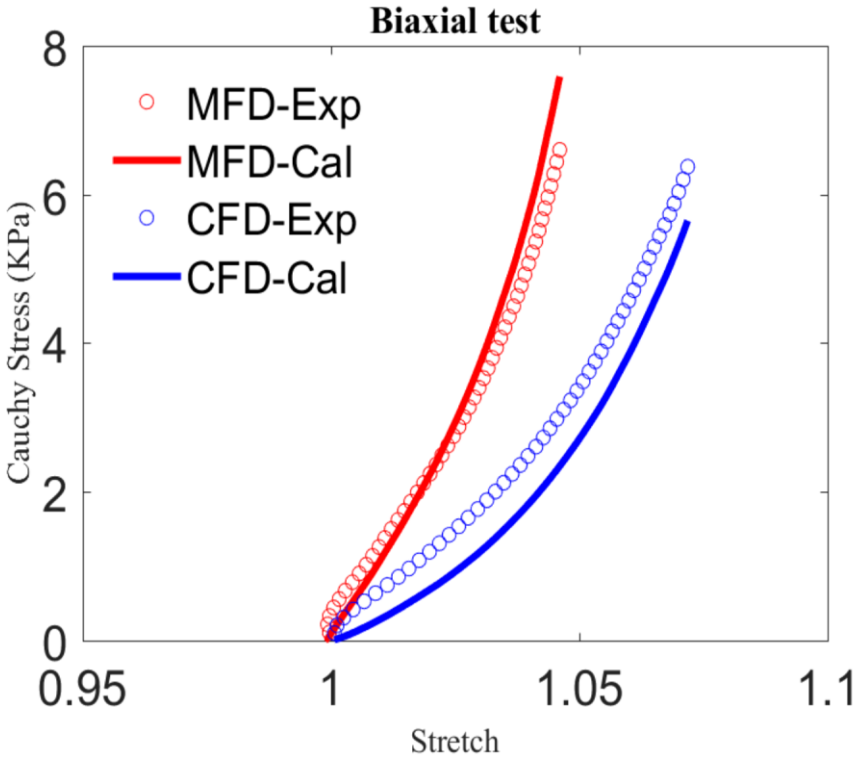
Biaxial test
MFD-Exp
MFD-Cal
CFD-Exp
CFD-Cal
Cauchy Stress (KPa)
Stretch
0
2
4
6
8
0.95
1
1.05
1.1

(i)

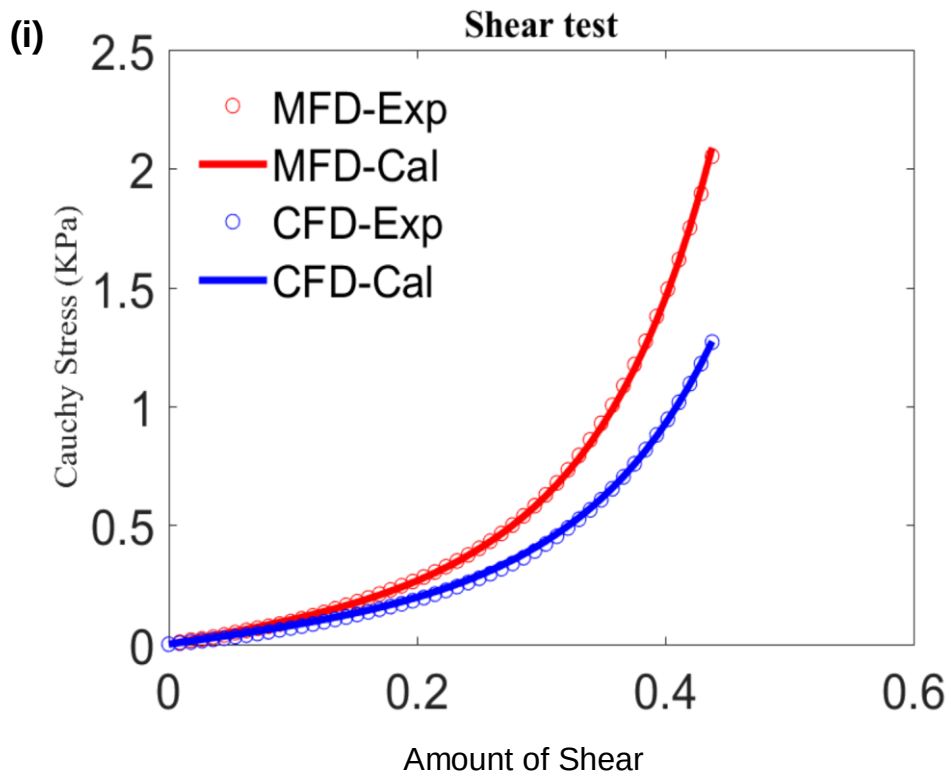
Shear test
MFD-Exp
MFD-Cal
CFD-Exp
CFD-Cal
Cauchy Stress (KPa)
Amount of Shear
0
0.5
1
1.5
2
2.5
0.2
0.4
0.6

(j)

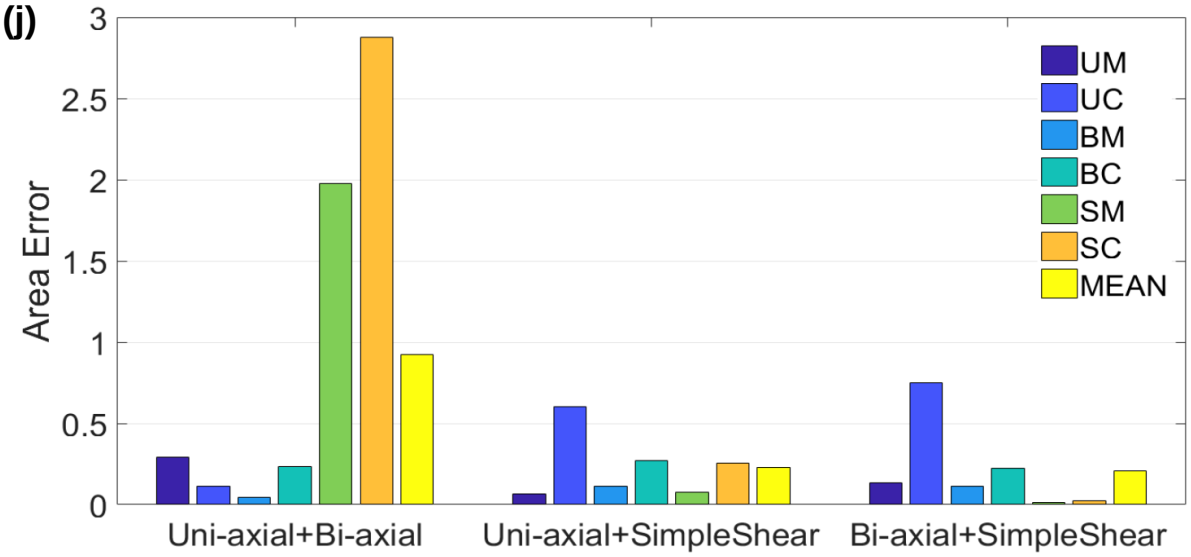
Area Error
UM
UC
BM
BC
SM
SC
MEAN
Uni-axial+Bi-axial
Uni-axial+SimpleShear
Bi-axial+SimpleShear
0
0.5
1
1.5
2
2.5
3

Figure 4.31: *Fit based on general HO model under different fitting couples of LVFW.* ***(a), (b)*** *and* ***(c)*** *show applying the parameters gotten by only fitting uniaxial and biaxial data to simple shear;* ***(d), (e)*** *and* ***(f)*** *are fitting uniaxial and simple shear and then applying the parameters to biaxial data;* ***(g), (h)*** *and* ***(i)*** *fit the biaxial and simple shear data only.* ***(j)*** *is area error comparison among different couples. UM presents Uniaxial tension in MFD; UC presents Uniaxial tension in CFD; BM presents Biaxial tension in MFD; BC presents Biaxial tension in CFD; SM presents shear amount in MFD and SC presents shear amount in CFD.*

Table 4.19: *Material parameters in Figure 4.37. RE considers both fibre rotation and effective area; RNE considers only fibre rotation and NRNE considers no fibre rotation and no effective area.*

Type	a	b	a_f	b_f	a_s	b_s	a_{fs}	b_{fs}
RE	1.144	5.049	7.897	2.766	0.001	2.585	0.013	31.930
RNE	0.895	5.886	7.172	0.001	0.001	3.235	0.099	20.958
NRNE	1.332	4.360	2.387	0.001	0.001	0.511	0.024	22.493

Table 4.20: *Material parameters in Figure 4.38, for uniaxial tensile, biaxial tensile and simple shear data.*

Type	a	b	a_f	b_f	a_s	b_s	a_{fs}	b_{fs}
Uniaxial	1.795	10.406	2.521	0.001	0.895	0.139	1.893	0.270
Biaxial	9.581	0.106	3.318	4.402	0.031	0.145	1.578	2.189
SimpleShear	0.442	5.626	2.341	1.013	1.593	15.348	0.681	10.088

Table 4.21: *Material parameters in Figure 4.39, under different fitting couples.*

Type	a	b	a_f	b_f	a_s	b_s	a_{fs}	b_{fs}
Uni+Biaxial	1.615	10.231	8.588	0.001	1.099	1.108	2.368	1.103
Uniaxial+shear	1.130	5.112	6.646	3.616	0.001	2.015	0.014	31.587
Biaxial+Shear	0.585	7.341	8.854	2.143	0.001	4.837	0.541	11.533

Table 4.22: *Area error values in Figure 4.37. RE considers both fibre rotation and effective area; RNE considers only fibre rotation and NRNE considers no fibre rotation and no effective area. UM presents Uniaxial tension in MFD; UC presents Uniaxial tension in CFD; BM presents Biaxial tension in MFD; BC presents biaxial tension in CFD; SM presents shear amount in MFD and SC presents shear amount in CFD.*

Type	UM	UC	BM	BC	SM	SC	MEAN
RE	0.092	0.601	0.110	0.217	0.076	0.260	0.226
RNE	0.640	0.359	0.240	0.450	0.062	0.134	0.314
NRNE	0.304	0.561	0.809	0.881	0.073	0.332	0.493

Table 4.23: *Area error values in Figure 4.38, for uniaxial tensile, biaxial tensile and simple shear data. UM presents Uniaxial tension in MFD; UC presents Uniaxial tension in CFD; BM presents Biaxial tension in MFD; BC presents biaxial tension in CFD; SM presents shear amount in MFD and SC presents shear amount in CFD.*

Type	UM	UC	BM	BC	SM	SC	MEAN
Uniaxial	0.064	0.035	0.567	0.598	2.060	3.186	1.085
Biaxial	1.311	1.261	0.028	0.025	3.553	5.466	1.941
SimpleShear	0.696	0.838	0.723	0.790	0.009	0.009	0.493

Table 4.24: *Area error values in Figure 4.39, under different fitting couples. UM presents Uniaxial tension in MFD; UC presents Uniaxial tension in CFD; BM presents Biaxial tension in MFD; BC presents biaxial tension in CFD; SM presents shear amount in MFD and SC presents shear amount in CFD.*

Type	UM	UC	BM	BC	SM	SC	MEAN
Uni+Biaxial	0.290	0.112	0.045	0.234	1.976	2.876	0.922
Uniaxial+Shear	0.066	0.603	0.114	0.269	0.076	0.254	0.230
Biaxial+Shear	0.132	0.752	0.115	0.226	0.013	0.022	0.210

5. DISCUSSION

This study aimed to establish material parameters that, for the first time, specifically describe neonatal ventricular myocardium and will enable simulation that more accurately reflect ventricular tissue behaviour. This will ultimately create new opportunities for researchers, bioengineers and clinicians to identify novel treatments and interventions in cases of abnormal neonatal heart functionality.

Heart tissue is known to grow and remodel in response to physiological stimulation. This means that age-specific constitutive models are of the utmost importance for an accurate analysis. Consequently, this study has focused on the interplay between the structure and function of the heart tissue at the start of this pathway. It also provides fundamental knowledge that describes the variation of collagen and myocardium fibre arrangement, and on the biomechanical behaviour of the four regions (LVFW anterior & posterior; RVFW anterior & posterior). This chapter will further discuss the translating of experimental data to numerical parameters for performing computational simulations. Finally, the clinical implications and limitations will be discussed.

5.1. Anterior and posterior LVFW

5.1.1. Structure analysis

The helical cardiomyocyte architecture of the intact heart was evaluated via 3D DT-MRI imaging, this method is consistent with the previous studies [70, 71]. Fractional anisotropy (FA) has previously been computed for neonatal and adult porcine hearts, which reflects the directional coherence of the cardiomyocytes' orientation [71]. However, *regional* FA variations have not been comprehensively documented in the neonatal porcine heart. The data that are presented here quantify the gross cardiomyocyte fibre orientation and identify the variation in FA across the three regions (i.e. base, equator and apex) in the anterior aspect (Figure 4.17 and 4.18, and Tables 4.9 and 4.10). The equator demonstrated significantly greater fibre orientation and density than the basal or apical regions (Figure 4.18). A qualitative assessment of alignment has revealed that the anterior fibres were predominantly horizontal, whereas those on the posterior surface were more diagonally-aligned (Figure 4.18).

Cardiomyocyte alignment and density in the anterior LVFW were relatively strong, with fewer extracellular spaces relative to the posterior surface (Figure 4.18). The regional differences that were observed in the cardiomyocyte orientation, changing within the anterior and posterior LVFW, may contribute to the twisting of the left ventricle during systole and diastole [192]. The left ventricle twist is defined as the relative rotation between the apex and base of the heart, while the systolic twist is defined as the wringing motion of the left ventricle, possessing a counterclockwise rotation at the apex and a clockwise rotation at the base [193, 194]. Diastolic untwisting, which is also known as torsional recoil, predominantly

occurs during isovolumic relaxation [195, 196]. This recoil mechanism is important because it determines the myocardial compliance and left ventricle suction, which in turn regulates the diastolic function of the heart [195, 196]. The anterior wall has been reported to predominantly contribute to the left ventricle twisting, when compared to the posterior wall during the systolic function of the heart [193, 194]. Thus, the greater cardiomyocyte alignment and density in the anterior wall may provide structural support and they contribute to generating the force in ejecting the blood (Figure 4.18).

The regional cardiomyocyte architecture, and thus strain distribution, is known to change during both diastole and systole, which may vary the regional (i.e. base, equator and apex) FA in the LVFW (Figures 4.17 and 4.18 and Tables 4.9 and 4.10) [57, 102, 197, 198]. In this study, FA was found to be greater in the equator than the base and apex of the anterior LVFW (equator = 0.75 vs base = 0.72 vs apex = 0.70) (Table 4.9). Moreover, it is well established that cardiomyocyte orientation changes through the thickness of LVFW. In the LVFW, the cardiomyocytes follow the path of a left-handed helix around the cavity at the subepicardial region, to circumferentially oriented in the mid-wall, and they follow the right-handed helical path at the subendocardial region [192]. These regional and transmural variations in cardiomyocyte orientation may contribute to causing the differences in the regional FA that were observed in this study (Table 4.9). In addition, cardiomyocytes are organised in small functional units, known as sheets [111]. The relative shearing between the sheets significantly contributes to the wall thinning and wall thickening during diastolic and systolic functions of the heart, which may also vary the regional FA [111, 112] (Table 4.9). A rapid increase in the LVFW FA has previously been reported during the pre-birth to 1-day postnatal period, which is probably caused by the change in cardiac workload due to the opening of pulmonary circulation and closing of ductus arteriosus and foramen ovale [70,

199]. Although the neonatal LVFW (0.72) demonstrated approximately twice the FA of equivalent adult porcine LVFW (0.42) (Table 4.9), the precise timeframe of these changes remains unclear [71]. The decreased FA in adult LVFW may be associated with the increased cardiomyocyte cross-sectional area from diastole to systole in adult tissue [200]. In addition, the relatively low FA in adult tissue is caused by the physiological hypertrophy of cardiomyocytes and an increased interstitial collagen concentration, which causes a relative expansion of the extracellular space [70]. The validity of these datasets is confirmed by a direct comparison of the LVFW FA (0.72) with that of other one-day old neonatal porcine data (0.72) [70].

A surface area analysis of histological images has quantified the greater ratio of collagen to cardiomyocytes in the posterior LVFW (0.20) when compared to the anterior LVFW (0.10) (Table 4.2). This is consistent with previous reports of higher collagen content contributing in diastolic and systolic myocardial stiffness [201-203]. This is also likely to serve in resisting myocardium deformation, preserving shape and wall thickness, and preventing a ventricular aneurysm and rupture [48, 49]. Moreover, the perimysial collagen framework is essential to maintain myocardium structural stability, which has also been reported to contribute to arranging cardiomyocyte fibres in a higher order of laminar sheet layers [92]. The greater proportion of collagen in the posterior wall is important during the diastolic function of the heart because the posterior wall has previously been reported to make a greater contribution than the anterior wall [56]. In addition, a greater change in strain has been reported in the posterior wall when compared to the anterior wall during the diastolic function [56]. Hence, the greater concentration of collagen in the posterior wall could be beneficial because the posterior wall undergoes relatively large geometrical changes versus the anterior wall during diastolic filling. The cardiomyocytes and collagen fibrils interaction

is significant in maintaining the myocardial stiffness during the cardiac cycle. At low-strains, the myocardial behaviour was governed by the cardiomyocyte fibres alone, without demonstrating any coupling between different cardiomyocyte fibre ensembles [51, 105]. Meanwhile, at higher strains, the cardiomyocyte and collagen fibril interactions have been reported to be more significant, which potentially contributes to the myocardial mechanical behaviour [51, 105]. The average surface area ratio of collagen to cardiomyocyte fibres within the anterior (0.10) and posterior (0.20) aspects of LVFW are detailed in Table 4.2.

TPEF/SHG microscopy was used to measure the cardiomyocytes' and collagen fibrils' in-plane and out-plane rotation and dispersion through 200 µm and 1022 µm depth of tissue, which encompassed the epicardium, sub-epicardium and superficial myocardium layer. The cardiomyocytes demonstrated the greater 'rate' (i.e. per unit thickness) of in-plane rotation than collagen in both the anterior (cardiomyocytes 48^0 vs collagens 41^0) and posterior (cardiomyocytes 151^0 vs collagens 129.5^0) LVFW (Tables 4.3 and 4.5). Meanwhile, both the cardiomyocytes and collagen fibrils demonstrated nearly parallel interaction within the anterior and posterior aspects of LVFW, as demonstrated in Figures 4.13–4.16. During the cardiac cycle, the cardiomyocytes possess remarkable mechanical stretch and force, which allows them to undertake the essential diastolic and systolic functions of the heart. Diastole reveals the ability of the cardiomyocytes to relax and fill with blood. The cardiomyocytes are stretched during the diastolic phase. Meanwhile, the relative shortening of the cardiomyocyte fibrils is essential to eject the blood during systole. Thus, cardiomyocytes endure changes in length and load throughout the cardiac cycle [204]. Sustaining the myocardial stiffness in both diastole and systole is of the utmost importance to resist myocardium deformation [48, 49]. Hence, the observed interaction between the cardiomyocyte and collagen fibril

ensembles provide myocardial mechanical strength and distensibility during the cardiac cycle (Figures 4.13–4.16).

The greater in-plane cardiomyocyte rotation was observed in the posterior LVFW (151.3^0) as opposed to the anterior (48^0), which may be due to the difference in ECM stiffness of the anterior (3.60 kPa) and posterior (2.53 kPa) LVFW (Table 4.3). This may also contribute to the regional nonhomogeneous behaviour of the myocardium during diastolic and systolic functions in the LVFW [56]. A lack of homogeneity in the distensibility of different regions in LVFW has been reported during the diastolic phase, which may be associated with the difference in the cardiomyocytes' anterior and posterior rotation rate (Table 4.3) [56]. These differences suggest that the posterior wall might make greater contribution to diastolic filling than the anterior wall [56]. The nonhomogeneity in regional shortening during the systolic phase has previously been reported, identifying the greater contribution of the anterior wall in systolic contraction due to the greater substrate stiffness (ECM). This would, in turn, generate greater mechanical force to eject the blood [57]. Hence, the anterior LVFW possesses greater extracellular matrix stiffness and, thus, has a smaller cardiomyocyte fibre rotation (48^0) than the posterior (151.3^0) (Table 4.3). These findings are consistent with those reported in the previous studies. This enables the correlation between the cardiomyocytes' rotation and the myocardial function to be identified. It also indicates the strong interaction between the regional cardiomyocyte rotations and mechanical performances of the heart during diastole and systole [193-196].

The greatest in-plane angular rotation rate in cardiomyocyte was identified in the sub-epicardium region. This shows that there is a significant change in fibre direction between the

epicardial to myocardial regions in both anterior and posterior LVFW (Figures 4.13–4.16). There is significant change in cardiomyocyte rotation at sub-epicardium to endocardium region within both the anterior and posterior aspects [205]. This is consistent with the findings reported in a previous study, describing that the maximum stresses occur at the inner layers of heart [205].

The cardiomyocytes exhibited the greater rate of out-plane rotation than the collagen anteriorly (cardiomyocytes 3.5^0 vs collagens 1.1^0) and posteriorly (cardiomyocytes 2.2^0 vs collagens 1.8^0) LVFW (Tables 4.4 and 4.6). Overall, cardiomyocyte rotation was markedly less when observing through the y-stacks (out-plane) of both aspects (Tables 4.3 and 4.4). The smaller out-plane rotation indicates that the cardiomyocytes were organised within the laminar sheets of the anterior and posterior LVFWs.

The collagen fibrils exhibited the greater in-plane dispersion 'rate' (i.e. per unit thickness) than the cardiomyocytes in both anterior (cardiomyocytes 11.8^0 vs collagens 27.1^0) and posterior (cardiomyocytes 12.8^0 vs collagens 14.3^0) LVFW (Tables 4.3 and 4.5). The in-plane dispersion of interstitial collagen is important because it provides myocardium structural stability and organises the cardiomyocytes architecture in a higher order of laminar sheet layers [47, 211]. Moreover, it is an essential framework for preserving the spatial registration of cardiomyocytes, such as limiting the extension of cardiomyocytes during diastole and transmitting the force and storage of energy during systole [92]. In-plane cardiomyocyte dispersion rate was greater in posterior (12.8^0) than the anterior (11.8^0), which may be associated with functionality as the posterior LVFW undergoes relatively large changes in shape and dimensions throughout the cardiac cycle (Table 4.3) [56]. Non-uniform

dimensional changes have previously been reported in the anterior and posterior LVFW during the cardiac cycle, varying through the thickness (i.e. epicardium to endocardium) of the tissue. This may be due to the differences in the cardiomyocyte and collagen fibril dispersion rate, as observed in the transmural direction of the myocardial tissue (Figures 4.13–4.16) [112]. These transmural variations in the anterior and posterior LVFW cardiomyocyte dispersion rate may contribute to changing the shearing deformation between the adjacent myocardial layers during diastole to systole [111, 212, 213]. In addition, the changes in the cardiomyocytes' and collagen fibrils' dispersion rate significantly contributes to the anterior and posterior LVFW torsional deformation. This causes the relative change in stress-strain distribution and, thus, the extent of regional-torsion in the myocardial tissue during the cardiac cycle (Figures 4.13–4.16) [214-216]. Moreover, the in-plane variations in the anterior and posterior LVFW cardiomyocyte and collagen fibril dispersion rates may contribute to supporting the interactive mechanical coupling between the cardiomyocyte and collagen fibril ensembles. This helps to sustain the in-plane stresses and deformations in myocardial tissue, as reported in the previous experimental and theoretical studies [111, 217]. To maintain the essential transmural coupling during the cardiac cycle, the cardiomyocytes and collagen fibrils significantly contribute to developing the force during systole and they prevent the overextension of left ventricle during diastole [218]. Hence, the regional cardiomyocyte and collagen fibril dispersion is important because it coordinates the global diastolic and systolic functions [133, 219].

The relatively high posterior LVFW (posterior 12.8^0 vs anterior 11.8^0) cardiomyocyte dispersion rate that was observed in our study may serve to accommodate higher concentrations of interstitial collagens, which emerges in response to the increasing workload throughout the heart's development [70, 220, 221] (Table 4.3). The interstitial collagens are

cross-linked and this provides high tensile strength, which significantly contributes to functionality during diastole [202, 203]. This preserves the myocardium shape and wall thickness, and it also prevents ventricular aneurysm and rupture [48, 49].

The cardiomyocytes exhibited a greater out-plane dispersion rate than the collagen fibrils in both the anterior (cardiomyocytes 17.8^0 vs collagens 11.2^0) and posterior (cardiomyocytes 18.8^0 vs collagens 8.4^0) LVFWs (Tables 4.4 and 4.6). The posterior (18.8^0) LVFWs exhibited the greater out-plane cardiomyocytes dispersion than the anterior (17.8^0) (Table 4.4). At higher strains, the relative dispersion of posterior LVFW cardiomyocytes may be important in providing mechanical coupling with interstitial collagen fibrils ensembles. This may contribute to sustaining the out-plane stresses and deformations [51]. These regional in- and out-plane arrangements of cardiomyocyte and collagen fibril ensembles may help to prevent the heart from bending during diastole to systole.

5.1.2. Functional analysis

The anterior and posterior LVFWs exhibited nonlinear, anisotropic, viscoelastic and heterogeneous behaviour during uniaxial tensile, biaxial tensile and simple shear loading modes (Figures 4.21, 4.24 and 4.26). These overall characteristics are consistent with those reported in adult tissue studies [104-109]. Other soft tissues also possess large deformations with nonlinear stress-strain behaviour, anisotropy, and small hysteresis [115-119]. The anterior and posterior LVFW exhibited relatively pronounced hysteresis, which identified a significant energy dissipation during uniaxial tensile, biaxial tensile and simple shear loading modes. The greater energy dissipation was observed in the mean-fibre direction (MFD) than

CFD of both aspects. Interestingly, the anterior (306 J / m^3) LVFW possessed almost 1.5 fold greater stiffness (anterior 3.60 kPa vs posterior 2.53 kPa) and energy dissipation (anterior 306 J / m^3 vs posterior 201 J / m^3) than the posterior wall tissue during the simple shear test (Tables 4.15 and 4.16). This result is consistent with our microstructural analysis, which identifies the greater ratio of cardiomyocytes to immature collagen in the anterior LVFW than the posterior. Given that a higher collagen content would typically be associated with greater stiffness in mature tissues, the less stiff behaviour that was observed in the LVFW might be related to the collagen state in a 1-day neonatal heart. This is in contrast to the intuitive mechanical contribution (i.e. stiffness) of collagen typical in mature tissues. Such difference in mechanical behaviour may in part be associated with the cross-linking mechanism of collagen fibrils, which is known to increase with age in providing high tensile strength (i.e. stiffness) to the tissue in response to the increased physiological demands of the heart [202, 203].

Uniaxial and biaxial tensile tests were performed following 10 preconditioning cycles (Figures 4.21 (a) and (b)). This method is consistent with that reported elsewhere [106, 107, 109, 114, 222-226]. During cyclic preconditioning, the greatest decrease in the hysteresis occurred during the first two preconditioning cycles, where after five cycles the tissue was stable with reproducible biomechanical behaviour (Figures 4.21 (a) and (b)). Different preconditioning configurations were used in previous studies, which mainly come from adult mammalian myocardium, ranged from 5–7 [106, 109, 222] and to 7–10 [107, 108, 114, 223, 225, 226] cycles, although five cycles for canine [107, 224] and seven for bovine [114] were reported as being sufficient.

Softening was evident during the uniaxial and biaxial cyclic preconditioning, as shown in Figures 4.21 (a) and (b). The greatest change in the stress was noted during the first two preconditioning cycles. This stress-softening behaviour is also referred to as the Mullins effect [129]. Previous studies have reported similar softening behaviour in adult myocardial tissue [130, 134, 135]. It has also been suggested that the pronounced strain softening was caused by the disruption of the perimysial collagen network, which is a consequence of the excessive shearing between adjacent myocardial muscle layers [130]. Moreover, the strain softening may occur due to changes in the collagen matrix where the cardiomyocytes are embedded [131]. In addition, strain softening may occur due to trauma to the endomysial collagen, which is a consequence of excessive stretch of the tissue [132]. Alternatively, disruption of myofilaments (such as titin, actin and myosin) may contribute to the strain softening of the neonatal cardiac walls [125, 133]. Strain softening was more pronounced during shearing than during uniaxial tensile and biaxial extension tests. This would appear indicative of the relative damage within the intra-and extracellular components in the myocardium during shearing in the anterior and posterior LVFWs. It is noted that the uniaxial (LVFW–MFD) stiffness of neonatal porcine data that is reported here (23 kPa) is approximately one-half that of the equivalent adult porcine tissue (47 kPa) [227]. Meanwhile, the neonatal porcine LVFW (140 kPa) has the approximately one-third biaxial stiffness of equivalent adult porcine (400 kPa) in the MFD [228].

The anterior and posterior LVFWs demonstrated similar mechanical trends in the positive and negative directions during simple shear tests (Figure 4.25 (a) and (b)). Hysteresis was more pronounced during shearing in the anterior and posterior LVFW than during uniaxial tensile and biaxial extension tests, as indicated in Tables 4.11, 4.13 and 4.15. The greater magnitude of energy dissipation achieved versus uniaxial tensile and biaxial extension tests

appear to be indicative of the importance of shearing within the LVFW (Tables 4.11, 4.13 and 4.15). This attribute is believed to be a consequence of the relatively high water content of myocardium (~ 80% wet weight) and affected by the muscle presence [40]. Therefore, changes in water content, such as edema, may contribute to causing alternations in the passive stiffness and viscoelasticity of the myocardium [40]. Moreover, the giant protein titin, which connects the Z line to the M line in the sarcomere, may contribute to the passive properties of the myocardium during shear deformations [124-126]. In addition, the actin–myosin interaction might help to cause the hysteresis formation [127, 128]. Although the interactions between all solids and liquids within the intracellular and extracellular components in the myocardium contribute to the hysteresis formation, their extent is currently unknown.

The anterior LVFW exhibited 1.5 fold greater anisotropy than the posterior in the MFD (Table 4.16). This is consistent with microstructural findings and indicates the greater rate of cardiomyocytes dispersion in the posterior (12.8 ^{0}) LVFW than the anterior (11.8 ^{0}). Since fibre dispersion has been reported as nonlinearly dependent on fibre alignment [39], high dispersion values correspond to less fibre alignment and, thus, a more isotropic cardiomyocyte distribution. The relationship between cardiomyocyte dispersion and mechanical anisotropy has been reported elsewhere [39, 52]. Hence, the greater degree of anisotropy in the anterior LVFW may be explained by the smaller rate of the cardiomyocytes' dispersion that is reported in our microstructural analysis (TPEF/SHG). A comparison of the stress-strain plots of this shear data to this uniaxial data highlights a similar stress, after which the MFD of myocardial tissue from both ventricles stiffens dramatically (Figures 4.21 (c) and 4.26 (c)–(f)). This is consistent with the trend that was previously reported in adult porcine cardiac tissue [113].

5.2. Anterior and posterior RVFW

5.2.1. Structural analysis

The three-dimensional cardiomyocyte tracks of the intact neonatal porcine heart were assessed from the 3D DT-MRI imaging data. Macroscopic assessment demonstrated some structural consistency with the LVFW (Figure 4.18). FA and density were again greater in the equatorial region than the base and apex (equator = 0.77 vs base = 0.74 vs apex = 0.71), with each also demonstrating significantly greater FA than the equivalent LVFW region (equator = 0.75 vs base = 0.72 vs apex = 0.70) (Figure 4.17 and Tables 4.9 and 4.10). Unlike the LVFW, both the anterior and posterior RVFW cardiomyocytes were horizontally aligned (Figure 4.18). Although FA measures have previously been used to identify microstructural changes in neonatal and adult porcine LVFW [70, 71], FA has not been reported in the neonatal RVFW. The data that are presented here consider three regions (i.e. base, equator and apex) within the anterior aspect of RVFW to identify the regional variations of FA (Figure 4.17, and Tables 4.9 and 4.10). Unlike the LVFW, cardiomyocyte alignment and density in the posterior RVFW were relatively strong with fewer extracellular spaces, as demonstrated in the Figure 4.18. Cardiomyocyte alignment and density were weaker in the anterior RVFW, as shown in Figure 4.18.

Although the RVFW FA is relatively poorly understood in the neonatal porcine heart, these data describe a marginally greater FA across all three regions (i.e. base, equator and apex) of the RVFW (equator = 0.77 vs base = 0.74 vs apex = 0.71) versus the equivalent LVFW (equator = 0.75 vs base = 0.72 vs apex = 0.70) (Tables 4.9 and 4.10). This finding resembles a previous analysis of the 1-day postnatal porcine septum, which reported a similar

proportion of cardiomyocytes associated with the LVFW and RVFW [70]. While FA in the adult porcine RVFW remains unknown, previous septal analyses demonstrated that the LVFW cardiomyocytes predominated from 5-day postnatal onwards, which presumably reflects the shifting physiological demands [70]. Moreover, it has previously been reported that the left ventricle size and weight are comparable to the right ventricle in the pig fetus but an almost 2-fold increase was reported in the left ventricle by postnatal day 14 (P14) [229, 230].

The surface area analysis of histological images quantified the greater ratio of collagen to cardiomyocytes in the posterior (0.08) compared to the anterior (0.03) RVFW, which is consistent with the previous studies (Table 4.2) [201-203]. These differences highlight the nonhomogeneous distribution of cardiomyocyte and collagen fibrils within the anterior and posterior aspects of RVFW. This is consistent with the findings reported by Holzapfel et al., which identifies that the cardiomyocyte and collagen fibrils distribution changes from region-to-region and with position through the wall (i.e. epicardium to endocardium) [38]. Figures 4.5–4.8 demonstrate that the cardiomyocytes and collagen fibrils possessed nearly planar orientation within the anterior and posterior aspects of both RVFW. This is consistent with the previous reports of their contribution in diastolic and systolic myocardial stiffness [51, 105, 201-203]. The average surface area ratio of collagen to cardiomyocyte fibres within the anterior (0.08) and posterior aspects (0.03) of RVFW, are detailed in Table 4.2.

TPEF/SHG microscopy was used to measure the cardiomyocytes' and collagen fibrils' in-plane and out-plane rotation and dispersion through 200 µm and 1022 µm depth of tissue, which encompassed the epicardium, sub-epicardium and superficial myocardium layer.

The cardiomyocytes demonstrated the greater rate of in-plane rotation than collagen in both anterior (cardiomyocytes 106^0 vs collagens 104^0) and posterior (cardiomyocytes 111^0 vs collagens 70^0) RVFW (Tables 4.3 and 4.5). The greater in-plane cardiomyocyte rotation was observed in the posterior RVFW (cardiomyocytes 111^0) as opposed to the anterior (106^0), which could be associated with the difference in ECM stiffness of the anterior (4.62 kPa) and posterior (3.22 kPa) RVFW (Table 4.3). These differences in the cardiomyocytes' rotation highlight the different biomechanical contributions of the anterior and posterior RVFWs during the diastolic and systolic functions of the heart [179]. The greatest in-plane angular cardiomyocyte rotation rate was identified in the sub-epicardium region. This means that there is a significant change in fibre direction between the epicardial to myocardial regions of the anterior and posterior RVFW. This is consistent with the findings reported for the anterior and posterior LVFW, as discussed in detail in Section 5.1 [205].

The cardiomyocytes demonstrated the greater rate of out-plane rotation than the collagen in both anterior (cardiomyocytes 8.4^0 vs collagens 2.7^0) and posterior (cardiomyocytes 6.4^0 vs collagens 1.6^0) RVFWs (Tables 4.4 and 4.6). Overall, cardiomyocyte rotation was markedly less when observing through the y-stacks (out-plane) of both anterior and posterior RVFWs (Tables 4.3 and 4.4). The smaller out-plane rotation indicates that the cardiomyocytes are organised within the laminar sheets of anterior and posterior RVFWs. The anterior RVFW possessed the greater rate of out-plane cardiomyocyte rotation through the y-stack depth than the posterior (Table 4.4).

The collagen fibrils exhibited the greater in-plane dispersion rate than the cardiomyocytes in both anterior (cardiomyocytes 8.7^0 vs collagens 13.4^0) and posterior (cardiomyocytes 12.3^0

vs collagens 22.4^0) RVFWs (Tables 4.3 and 4.5). Previous studies have reported the significant mechanical role for the perimysial collagens during the diastolic function of the heart. For example, the collagen network has been reported to work as a strain-locking system, which limits the overextension of the cardiomyocytes during diastole, to prevent a ventricular aneurysm and rupture [48, 49]. A similar function of this collagen was previously reported in the adventitia of arteries [53-55]. In addition, the in-plane dispersion of interstitial collagen is important because it provides myocardium structural stability and organises the cardiomyocytes' architecture in a higher order of laminar sheet layers [47, 211]. The posterior (12.3^0) RVFW possessed the greater rate of cardiomyocytes dispersion than the anterior (8.7^0) (Tables 4.3). In comparison to other biological structures, the heart is a paradigm of efficiency and the observed differences between the fibre dispersion rate of anterior and posterior RVFW may correlate with the functional needs of both aspects. In particular, during the systolic function in anterior RVFW, the maximum deformation has been reported to be in the MFD, which identified the maximum stress for each layer of the anterior RVFW in the MFD [231]. Hence, a greater stiffness in the MFD would contribute to supporting larger stresses. However, the maximum deformation has not been reported in the posterior MFD [231]; therefore, less anisotropic behaviour may be more mechanically constructive in the posterior RVFW mechanics.

The cardiomyocytes exhibited a greater out-plane dispersion rate than the collagen fibrils in both the anterior (cardiomyocytes 23.9^0 vs collagens 20.8^0) and posterior (cardiomyocytes 22^0 vs collagens 7.2^0) RVFW (Tables 4.4 and 4.6). The anterior (23.9^0) demonstrated the greater out-plane cardiomyocytes dispersion than the posterior (22^0) (Table 4.4). This may serve to accommodate higher concentration of interstitial collagens, which emerges in

response to the increasing workload throughout heart development [70, 220, 221]. The intestinal collagen network may help to sustain the out-plane stresses.

5.2.2. Functional analysis

The anterior and posterior RVFWs demonstrated nonlinear, anisotropic, viscoelastic and heterogeneous behaviour during uniaxial tensile, biaxial tensile and simple shear loading modes (Figures 4.21, 4.24 and 4.26). These overall characteristics are consistent with those reported in adult tissue studies [105-109, 233]. The large deformations with nonlinear stress-strain behaviour, anisotropy, and small hysteresis are a common phenomenon in soft tissue mechanics [115-119]. The anterior and posterior RVFW possessed relatively pronounced hysteresis, identifying a significant energy dissipation during uniaxial tensile, biaxial tensile and simple shear loading modes. Meanwhile, MFD exhibited the greater energy dissipation than the CFD in both anterior and posterior RVFWs. It is of significance that the anterior and posterior aspects of RVFW (anterior 387 J / m^3 vs posterior 208 J / m^3) demonstrated greater energy dissipation than the LVFW (anterior 306 J / m^3 vs posterior 201 J / m^3) during simple shear tests (Table 4.15). This indicates that the LVFW conserves more energy than the RVFW during shearing of the myocardial layers. This relative shearing between myocardial layers has previously been reported to facilitate ventricular ejection by contributing to subendocardial wall thickness during systole [111]. In addition, the relative shearing also contributes to the myocardium wall thinning during passive ventricular filling [112]. Interestingly, the anterior RVFW possessed the almost 2 fold greater stiffness (anterior 4.62 kPa vs posterior 3.22 kPa) and energy dissipation (anterior 387 J / m^3 vs posterior 208 J / m^3) than the posterior (Tables 4.15 and 4.16). This is consistent with the biomechanical behaviour of the LVFW. Our microstructural analysis indicated the greater ratio of

cardiomyocytes to immature collagen in the anterior RVFW than the posterior (Table 4.2). Given that a higher collagen content would typically be associated with greater stiffness in mature tissues, the less stiff behaviour that was observed in the posterior RVFW might be related to the collagen state in a 1-day neonatal heart. This is in contrast to the intuitive mechanical contribution (i.e. stiffness) of collagen typical in mature tissues, as discussed in Section 5.1.2.

A total of 10 preconditioning cycles were performed to account for the viscoelastic behaviour of the RVFW during uniaxial tensile and biaxial tensile tests (Figures 4.21 (a) and (b)). This method is consistent with the LVFW, as described in detail in Section 5.1 [106, 107, 109, 114, 222-226]. During cyclic preconditioning, the greatest decrease in the hysteresis occurred during the first two preconditioning cycles. After five cycles the neonatal RVFWs revealed stable and reproducible biomechanical behaviour, as demonstrated in Figures 4.21 (a) and (b)). Strain softening was observed during the uniaxial and biaxial cyclic preconditioning, as shown in Figures 4.21 (a) and (b). This is again consistent with the biomechanical behaviour of the LVFW, as discussed in detail in Section 5.1.

The anterior and posterior RVFWs demonstrated asymmetrical mechanical trends in the positive and negative directions during simple shear tests (Figure 4.25 (c) and (d)). The anterior RVFW exhibited a stiffer response in the positive direction, while the posterior RVFW had greater stiffness in the negative direction (Figure 4.25 (c) and (d)). The asymmetrical behaviour during the positive and negative cyclic shearing in RVFW indicates that the shearing behaviour of myocardial tissue is highly dependent on the local myocardial architecture. Our microstructural analyses identified the diagonal alignment of the

cardiomyocyte and collagen fibrils orientations within the anterior and posterior aspects of RVFW, which may contribute to the asymmetrical behaviour observed in the RVFWs (Figure 4.5–4.8). Hysteresis was more pronounced during shearing in the anterior and posterior RVFW than during uniaxial tensile and biaxial extension testing, as indicated in Tables 4.11, 4.13 and 4.15. This is consistent with the biomechanical behaviour of the LVFW, as discussed in detail in Section 5.1.

The anterior RVFW demonstrated 1.5 fold greater anisotropy than the posterior in MFD and CFD (Table 4.17). This is consistent with our microstructural findings and it indicates the greater rate of cardiomyocyte dispersion in the posterior (12.3 ^{0}) RVFW than the anterior (8.7 ^{0}). A nonlinear relationship has previously been reported between the cardiomyocytes dispersion and mechanical anisotropy, which means that high dispersion values correspond to less fibre alignment and, thus, a more isotropic cardiomyocyte distribution [52]. This relationship between cardiomyocyte dispersion and mechanical anisotropy has been reported elsewhere [52]. Therefore, the greater degree of anisotropy in the anterior RVFW could be associated with the smaller rate of the cardiomyocytes' dispersion, as reported in our microstructural analysis (TPEF/SHG).

5.3. Structural and biomechanical differences in neonatal and adult ventricular tissue

On an absolute scale, the extent of neonatal in-plane cardiomyocyte rotation at the sub-epicardium region appeared greater than that reported in adult porcine LVFW and RVFW [74, 75]. The anterior aspect demonstrated almost consistent cardiomyocyte rotation for both neonatal and adult LVFW, while 4-fold greater cardiomyocyte rotation was observed in the neonatal posterior LVFW (Table 4.3) [74, 75]. The anterior and posterior aspects of neonatal porcine RVFW possessed 1.5-fold greater cardiomyocyte rotation when compared to the adult porcine RVFW (Table 4.3) [74, 75].

The linearity of the timeline associated with the reducing cardiomyocyte rotation is currently unknown; hence, the cardiomyocytes may rotate within a few days of birth due to the change in stress within the tissue as a consequence of the closing of ductus arteriosus and foramen ovale [70, 199]. Furthermore, the cardiomyocytes undergo rapid growth and maturation during the early postnatal period. Increasing biomechanical force to respond to the new physiological demands is a primary factor that governs cardiomyocyte maturation [206]. This increase in mechanical force during the immediate postnatal period concurs with changes in the mechanical properties of the extracellular matrix. Cardiac workload increases rapidly after birth thanks to the opening of pulmonary circulation, which coincides with left ventricle cardiomyocyte hypertrophy, hyperplasia, and extracellular collagen deposition [23, 26, 207]. In studies of neonatal porcine, the left ventricular free wall increases in mass 4.5-fold within two weeks, cell volume increases 3.5-fold, and cellular proliferation by 0.28-fold, and the majority of tissue volume growth occurs through cellular hypertrophy [23]. During the same period, previous studies have shown the deposition of interstitial collagen undergoes a rapid increase, peaking between days 15–20 postnatal [26]. These morphological and

physiological alterations cause the relative change in stress within the tissue, and they also cause the increased extracellular matrix stiffness and mechanical stimulation, such as an increase in the stretching of the substrate. This may contribute to reducing the cardiomyocyte rotation during maturation [208-210]. Alternatively, the cardiomyocyte rotation may gradually reduce (i.e. straighten) as they align in the direction of the maximum principal stress due to the relative increase in heart workload throughout maturation and in a manner similar to the osteons of trabecular bone.

The maximum tangent shear modulus (MTM = $d\sigma/d\mathcal{E}$) at $\mathcal{E}$ = 50% (the largest strain encountered) along the MFD and CFD were computed for adult and *neonatal* LVFWs to identify the relative changes in the biomechanical properties of the tissue during maturation. The MTM of LVFW adult porcine data has previously been reported at 50% strain as ~ 28 kPa (MFD) and ~ 5 kPa (CFD) [113]. Compared to the equivalent data reported for neonatal porcine tissue in the anterior aspect (i.e. anterior ~ 7.2 kPa (MFD) and ~ 4.2 kPa (CFD) at 50% strain), this indicates that the anterior LVFW is approximately one-fourth the stiffness of mature tissue in MFD. Similarly, compared to the equivalent data reported for neonatal porcine tissue in the posterior aspect (i.e. anterior ~ 5.0 kPa (MFD) and ~ 4.5 kPa (CFD) at 50% strain), this indicates that the posterior LVFW is approximately one-sixth the stiffness of mature tissue in MFD. Hence, the observed differences between the anterior and posterior neonatal LVFW and adult porcine tissue revealed the necessity of testing neonatal tissue obtained from similar regions and this helps us to better understand the underlying differences between the neonatal and adult tissue behaviour.

5.4. Enabling more accurate neonatal cardiac simulations

As discussed in Sections 5.1 and 5.2, myocardium possessed nonlinear, anisotropic, viscoelastic and heterogeneous mechanical behaviour. A number of different approaches have been used in the literature to model the myocardium, including the constitutive models that have been used to estimate the material parameters for computational simulations. To understand the highly nonlinear mechanics of the intricate structure of the myocardium under different loading regimes, a structurally-based constitutive model is essential. Different constitutive models have been proposed in the literature that are mainly based on the assumption of transverse isotropy and, therefore, are not able to capture the orthotropic response of myocardium (as discussed in detail in Chapter 2, Section 2.5.2). Consequently, an orthotropic constitutive model is needed to precisely describe the mechanical behaviour of the myocardium. Holzapfel et al. proposed an orthotropic model that is based on a structural approach that accounts for the morphological structure through the cardiomyocytes' direction, the myocyte sheet's orientation and the sheet's normal direction, and considers the resulting macroscopic nature of the myocardium [110].

Consequently, the microstructural and biomechanical data that are reported here have been fitted to the structurally-based orthotropic Holzapfel–Ogden (HO) model of adult myocardium [110] to establish the material parameters that more accurately describe neonatal tissue behaviour (Chapter 4, Section 4.4). These material parameters will enable increased accuracy in performing computational simulations of neonatal ventricles and will enhance the understanding of fundamental underlying neonatal ventricular mechanics. In turn, this has the potential in improving the medical treatment of heart diseases, which may reduce the mortality and morbidity [8, 10-13, 15].

5.4.1 Translating experimental data to numerical parameters

To quantitatively compare the difference between fitting results and experimental data, the error was calculated using an objective function (see Eqn 5.1). The error of fit is defined as the relative difference of area-under-curve between the experimental stress-strain curves and the fitted results,

$$\mathrm{err}^{\mathrm{fit}} = \frac{\int_{\lambda_{\min}}^{\lambda_{\max}} |\sigma_i^{\mathrm{fit}} - \sigma_i^{\mathrm{exp}}| \, d\lambda}{\int_{\lambda_{\min}}^{\lambda_{\max}} \sigma_i^{\mathrm{exp}} \, d\lambda}. \qquad \text{(Eqn 5.1)}$$

A smaller value indicates a better fit, and a value of 0 indicates a perfect fit from the inferred parameters.

5.4.2. Estimating the uniaxial tensile, biaxial tensile and simple shear material parameters with HO model

The uniaxial tensile, biaxial tensile and simple shear biomechanical data of LVFW was used without considering the mean-fibre orientation of the myocardium (Figure 4.29 (a), (b) and (c)). This indicates that some properties of the sample were redundant. Therefore, to reduce the fitting error, the mean-fibre orientation of LVFW myocardium was considered according to the definition of MFD and CFD, and to the characteristics of fibre in the LVFW myocardium. The cardiomyocytes' rotation was adopted and defined as 60 $^{\circ}$ from the top to bottom of the myocardium [52]. Using this method, the fitting results were obtained and demonstrated in Figure 4.29 (d), (e) and (f). Although the fitting error was reduced, the

overall fitting remained poor. Hence, to further reduce the fitting error, the unique features in the uniaxial tension were analysed to propose the effective area ratio (as defined as the ratio of fibres contributing in the gross biomechanical stress of the sample) (Figure 4.29 (g), (h) and (i)), indicating a relatively better fit. Therefore, to fit different experimental data together, it is necessary to include detailed myofibre orientations and effective area ratio of the samples in question. It is of significance that the error of fitting results in CFD was always greater than that in MFD. This may be due to the HO model expression, which do not have an item that represents CFD (normal direction) (see Section 2.5.2 (Equation 2.6)).

The advantage of this data is that it includes three experimental tests (i.e. uniaxial tensile, biaxial tensile, and simple shear), which are more likely to get realistic parameters to represent the characteristics of the myocardium, while most of the other studies only have one or two of the tests [104, 113, 119, 135, 156]. Hence, it is interesting to determine whether or not the characteristic parameters that are obtained from one or two tests can be applied to another test directly. Figures 4.30 and 4.31 indicate that the estimated parameters by fitting only one or two types of experiments could not match the remaining experiments. It is, therefore, essential to include all of the experimental data to determine the material parameters.

5.5. Clinical implications

This study ultimately aims to create new opportunities for researchers and bioengineers to identify novel treatments and interventions in cases of abnormal neonatal heart functionality. Consequently, this work contributes the material parameters that specifically describe

neonatal cardiac tissue and enables a more accurate computational simulation of neonatal cardiac tissue behaviour.

The engineering-based computational simulations provide robust tools for performing patient-specific cardiovascular simulations and they are able to predict the consequence and effectiveness of surgical interventions. Computational modelling is increasingly used in adult cardiology to understand the behaviour of structural components and they enable the simulation of normal and pathophysiological conditions, and lead to new interventions [8, 10-13, 15]. Recently, the advances in the development of constitutive models and computing power have enabled simulations to achieve greater clinical value. In adult cardiology, patient-specific computational modelling provides a novel platform to enhance the understanding of cardiac mechanics, and assists researchers, bioengineers and clinicians to develop new interventions in improving the postoperative lives of patients [151-153]. Although a similar approach for simulation could be adopted in paediatric clinical applications, an acute lack of quantitative data describing the *neonatal tissue structure* and *biomechanical behaviour* limits the widespread use and effectiveness of these emerging techniques. Moreover, the lack of validation through experimental data potentially limits the use of computational simulations in a wide range of neonatal heart diseases.

This study has also highlighted the difference in behaviour of neonatal heart tissue and equivalent adult heart tissue (Section 5.1). These differences will likely mean that any neonatal-based studies that currently adopt adult data will be inaccurate [16-19]. Hence, there is now a need for further investigation to characterise neonatal *human* heart tissue. Our research provides the first complete set of experimental data that describe the structure and

biomechanical behaviour of neonatal porcine ventricles and can be used to estimate the material parameters with the existing HO model (Section 4.4). Because these parameters are derived from porcine tissue, they currently have the *potential* to increase the accuracy and effectiveness of neonatal cardiac simulations. However, further investigation is required to determining whether these enable more accurate simulation than the existing adult-derived parameters. This study has provided evidence of the need for future investigations to consider human neonatal tissue which, presumably, would contribute to reducing mortality and morbidity associated with neonatal heart diseases.

5.6. Limitations

While these results provide a valuable insight into neonatal cardiac tissue structure and biomechanical behaviour, it is acknowledged that an animal-based laboratory study differs from human, physiological reality. The neonatal porcine model was adopted because the adult organ is commonly used to simulate human performance given their relatively similar structure and dimensions, as described in Section 2.6. However, there are still differences that will limit the applicability of these data. While the controlled environment of a laboratory has significant advantages when investigating tissue characteristics, the need to dissect samples does create artificial boundary conditions and releases residual stresses, which may alter performance. Common protocols were followed to ensure that the tissues remained hydrated. However, there is no doubt that the deformations imposed by uniaxial tensile, biaxial tensile and simple shear testing differ from those experienced in vivo physiology of the heart. The above-mentioned factors, besides the passiveness of the heart muscle, may also contribute to the strain softening observed in this study, and may explain the softening behaviour observed at very small strains. Whilst the issues associated with in

vitro mechanical testing may limit the reliability of explicit material parameter identification, the approach used here has provided important novel data on the material response of the passive 1-day-old neonatal ventricular myocardium under Uniaxial tensile, biaxial tensile and simple shear loading modes.

The HO model that we used in this study is deduced according to the Dokos et al. experimental data [113]. While the HO model can depict the properties of these data well and it does get ideal fitting results, different experimental data have unique characteristics, as demonstrated in Section 4.2.4. This means that it may not actually be most effective for the *neonatal* LVFW myocardium under different loading modes (i.e. uniaxial tensile, biaxial tensile and simple shear). For example, in the uniaxial and biaxial tension tests (Section 3.1.2), the stretching directions are MFD (fibre direction) and CFD (normal direction) and they should be noted in the strain energy function, while the HO model does not have a normal term. Adequate adjustments could be made in the expression of HO model, based on the unique features of experiments, to obtain another specific HO model. Moreover, some errors may be due to the experiment's proposal, design and measurement, which may also contribute to the coarse fitting results. Therefore, modifications are required in the HO model to further improve the fitting of the microstructural and biomechanical data of the *neonatal* LVFW myocardium. A more specific HO model describing all three directions of myocardium (i.e. fibre (F), sheet (S) and normal (N) axes) in the strain energy function would provide a more accurate representation of the myocardial tissue behaviour, which may further improve the fitting results.

6. CONCLUSIONS

6.1. Research conclusions

This research aimed to establish the first material parameters that described neonatal ventricular myocardium, from a porcine model. It was found that:

- To fit different experimental data (i.e. uniaxial tensile, biaxial tensile and simple shear) in estimating the material parameters of the neonatal ventricular myocardium, it was necessary to include detailed myofibre orientations and the effective area ratio of the samples in question. Moreover, the fitting results identified that the characteristic parameters that were obtained from one or two tests (i.e. uniaxial tensile, biaxial tensile and simple shear) could not be associated with another test directly. It is, therefore, essential to include all of the experimental data to determine the material parameters.
- The fitting results of uniaxial tensile, biaxial tensile and simple shear tests demonstrated the greater error in CFD than that in MFD, presumably due to the HO model expression, which has no item that represents CFD (normal-direction). Hence, adequate adjustments could be made in the expression of HO model to include all three directions of the myocardium (i.e. fibre (F), sheet (S) and normal (N) axes) in the strain energy function, which may further improve the fitting results in obtaining material parameters of the neonatal ventricular myocardium.
- The surface area analysis of histological images quantified the greater ratio of collagen to cardiomyocytes in the posterior wall compared to the anterior in both ventricles. TPEF/SHG also identified the greater cardiomyocytes' rotation in the posterior wall of both ventricles. The cardiomyocytes exhibited a greater dispersion

rate out-plane, while collagen fibrils' dispersion was more pronounced through the in-plane of both ventricles.

- One-day-old porcine RVFW possessed 1.5-fold greater cardiomyocyte rotation in both the anterior and posterior wall when compared to the adult porcine RVFW. The anterior aspect demonstrated comparable cardiomyocyte rotation for both one-day-old and adult LVFW, while 4-fold greater cardiomyocyte rotation was observed in the one-day-old posterior LVFW.
- FA was found to vary between the regions (i.e. base, equator and apex) of both ventricles. The one-day-old LVFW demonstrated approximately twice the FA of equivalent adult porcine LVFW, although the precise timeframe of these changes remains unclear.
- The anterior ventricular walls were stiffest, indicating a relative difference in the substrate stiffness (ECM), which was consistent with our microstructural analysis. The one-day-old porcine tissue was also identified as exhibiting one-half the stiffness of adult porcine tissue in uniaxial testing, one-third in biaxial testing, and one-fourth stiffness in simple shear testing. These data provide both a baseline describing the microstructure and biomechanical parameters of one-day-old porcine tissue and an indication as to the relative change in the tissue morphometry and characteristics that occur during maturation.

This research study has identified the difference in behaviour of neonatal heart tissue and equivalent adult heart tissue. These differences will likely mean that any neonatal-based studies that currently adopt adult data will be inaccurate. This research study also provides the first complete set of experimental data that describe the structure and biomechanical behaviour of neonatal porcine ventricles and can be used to estimate the material parameters

with the existing HO model. Meanwhile, adequate modifications are required in the HO model, with relevant changes in the strain energy function to further improve the fitting results in obtaining the material parameters of the one-day-old porcine ventricular myocardium. However, the estimated material parameters in this research study will enable a simulation that more accurately reflect neonatal ventricular tissue behaviour. This will ultimately create new opportunities for researchers, bioengineers and clinicians to identify novel treatments and interventions in cases of abnormal neonatal heart functionality.

6.2. Future work

6.2.1 Development of modified HO model

The existing HO model for adult myocardium did not demonstrate the ideal fitting results with the one-day neonatal data, indicating the need to develop *age-specific* constitutive models based on the growth and remodelling of the heart during maturation. These constitutive models will improve the effectiveness of computational simulations in understanding the fundamental underlying the ventricular mechanics during maturation, which is a necessary in the improvement of medical treatment of heart diseases.

6.2.2 Establishing a new model that encompasses growth and remodelling

It is recognised that this neonatal data represents only a ‘snapshot’ of the heart behaviour during the earliest phase of a complex growth and remodelling pathway. Moreover, significant changes in the structure and biomechanical characteristics have been identified by

comparing the one-day-old porcine data to the adult. Hence, future work has been planned to develop a new G&R (growth and remodelling) based constitutive law that will enable prediction of the age-specific, viscoelastic properties.

6.2.2.1. Aims and objectives of future work

The future work will aim to:

1. Characterise the G&R-dependent, viscoelastic constituent parameters of cardiac tissue in a validated animal model.
2. Develop a viscoelastic-based constituent model that enables prediction of macroscopic, age-specific tissue behaviour.

These aims will be realised through the achievement of seven objectives, as follows:

1. Verify the six G&R stages selected for the porcine heart model spanning neonate to adulthood (with a focus on maturation) and establish the equivalent human age by performing ratiometric biomarker analysis.

2. Quantify the critical microstructural parameters for constitutive modelling across the six G&R-stages, within the anterior and posterior aspect of both ventricles (i.e. fractional anisotropy; fibre rotation; fibre dispersion).

3. Quantify the biomechanical parameters that are critical for constitutive viscoelasticity modelling across the 6 G&R-stages within the anterior and posterior aspect of both ventricles (open angle, biaxial, simple shear, and stress relaxation).

4. Estimate the apparent growth tensor $\mathbf{F}^{g}$ and its evolution by registering ventricular shapes at different times reconstructed from in vivo and ex vivo images.
5. Model age-related G&R in cardiac structure and biomechanical function, and then correlate their changes with the biochemical biomarkers and maturation relative to humans.

6. Collect in vivo porcine data (p-v curve, blood pressure) to enable hypothesis-testing.

7. Hypotheses-test maturation-related G&R laws in the porcine heart using different growth driven mechanisms (stress, strain).

7. REFERENCES

[1] H. Oertel, S. Krittian, Modelling the human cardiac fluid mechanics, KIT Scientific Publishing2011.

[2] G.A. Holzapfel, R.W. Ogden, Constitutive modelling of passive myocardium: a structurally based framework for material characterization, Philosophical transactions. Series A, Mathematical, physical, and engineering sciences 367(1902) (2009) 3445-75.

[3] A.S. Go, D. Mozaffarian, V.L. Roger, E.J. Benjamin, J.D. Berry, M.J. Blaha, S. Dai, E.S. Ford, C.S. Fox, S. Franco, H.J. Fullerton, C. Gillespie, S.M. Hailpern, J.A. Heit, V.J. Howard, M.D. Huffman, S.E. Judd, B.M. Kissela, S.J. Kittner, D.T. Lackland, J.H. Lichtman, L.D. Lisabeth, R.H. Mackey, D.J. Magid, G.M. Marcus, A. Marelli, D.B. Matchar, D.K. McGuire, E.R. Mohler, 3rd, C.S. Moy, M.E. Mussolino, R.W. Neumar, G. Nichol, D.K. Pandey, N.P. Paynter, M.J. Reeves, P.D. Sorlie, J. Stein, A. Towfighi, T.N. Turan, S.S. Virani, N.D. Wong, D. Woo, M.B. Turner, Heart disease and stroke statistics--2014 update: a report from the American Heart Association, Circulation 129(3) (2014) e28-e292.

[4] M. Nichols, N. Townsend, R. Luengo-Fernandez, J. Leal, A. Gray, P. Scarborough, M. Rayner, European heart network, European society of cardiology, Brussels, Sophia Antipolis (2012).

[5] <https://www.bhf.org.uk/>).

[6] H. Dolk, M. Loane, E. Garne, The prevalence of congenital anomalies in Europe, Advances in experimental medicine and biology 686 (2010) 349-64.

[7] H. Dolk, M. Loane, E. Garne, G. European Surveillance of Congenital Anomalies Working, Congenital heart defects in Europe: prevalence and perinatal mortality, 2000 to 2005, Circulation 123(8) (2011) 841-9.

[8] S. Dokos, I.J. LeGrice, B.H. Smaill, J. Kar, A.A. Young, A Triaxial-Measurement Shear-Test Device for Soft Biological Tissues, Journal of biomechanical engineering 122(5) (2000) 471-478.

[9] T.S. Eriksson, A.J. Prassl, G. Plank, G.A. Holzapfel, Modeling the dispersion in electromechanically coupled myocardium, International journal for numerical methods in biomedical engineering 29(11) (2013) 1267-84.

[10] T.S. Eriksson, A. Prassl, G. Plank, G.A. Holzapfel, Influence of myocardial fiber/sheet orientations on left ventricular mechanical contraction, Mathematics and Mechanics of Solids (2013) 1081286513485779.

[11] M.P. Nash, A.V. Panfilov, Electromechanical model of excitable tissue to study reentrant cardiac arrhythmias, Progress in biophysics and molecular biology 85(2-3) (2004) 501-22.

[12] S. Niederer, L. Mitchell, N. Smith, G. Plank, Simulating human cardiac electrophysiology on clinical time-scales, Frontiers in physiology 2 (2011) 14.

[13] T.P. Usyk, J.H. Omens, A.D. McCulloch, Regional septal dysfunction in a three-dimensional computational model of focal myofiber disarray, American journal of physiology. Heart and circulatory physiology 281(2) (2001) H506-14.

[14] S.T. Wall, J.C. Walker, K.E. Healy, M.B. Ratcliffe, J.M. Guccione, Theoretical impact of the injection of material into the myocardium: a finite element model simulation, Circulation 114(24) (2006) 2627-35.

[15] G.A. Holzapfel, J.A. Niestrawska, R.W. Ogden, A.J. Reinisch, A.J. Schriefl, Modelling non-symmetric collagen fibre dispersion in arterial walls, Journal of the Royal Society, Interface 12(106) (2015).

[16] S. Giannico, F. Hammad, A. Amodeo, G. Michielon, F. Drago, A. Turchetta, R. Di Donato, S.P. Sanders, Clinical outcome of 193 extracardiac Fontan patients: the first 15 years, Journal of the American College of Cardiology 47(10) (2006) 2065-73.

[17] E. Petrossian, V.M. Reddy, D.B. McElhinney, G.P. Akkersdijk, P. Moore, A.J. Parry, L.D. Thompson, F.L. Hanley, Early results of the extracardiac conduit Fontan operation, The Journal of thoracic and cardiovascular surgery 117(4) (1999) 688-96.

[18] T. Shinoka, C. Breuer, Tissue-engineered blood vessels in pediatric cardiac surgery, The Yale journal of biology and medicine 81(4) (2008) 161-6.

[19] M.L. Lindsey, D.K. Goshorn, C.E. Squires, G.P. Escobar, J.W. Hendrick, J.T. Mingoia, S.E. Sweterlitsch, F.G. Spinale, Age-dependent changes in myocardial matrix metalloproteinase/tissue inhibitor of metalloproteinase profiles and fibroblast function, Cardiovascular research 66(2) (2005) 410-419.

[20] H. Kurobe, M.W. Maxfield, C.K. Breuer, T. Shinoka, Concise review: tissue-engineered vascular grafts for cardiac surgery: past, present, and future, Stem cells translational medicine 1(7) (2012) 566-71.

[21] C.J. Cote, A practice of anesthesia for infants and children, WB Saunders Company1993.

[22] R.G. Cox, Smith's Anesthesia for Infants and Children - Eighth Edition, Canadian Journal of Anesthesia/Journal canadien d'anesthésie 58(10) (2011) 973.

[23] C.J. Beinlich, C.J. Rissinger, H.E. Morgan, Mechanisms of rapid growth in the neonatal pig heart, J Mol Cell Cardiol 27(1) (1995) 273-81.

[24] N.S. Assali, N. Sehgal, S. Marable, Pulmonary and ductus arteriosus circulation in the fetal lamb before and after birth, The American journal of physiology 202 (1962) 536-40.

[25] G.S. Dawes, J.C. Mott, J.G. Widdicombe, Closure of the foramen ovale in newborn lambs, The Journal of physiology 128(2) (1955) 384-395.

[26] W. Carver, L. Terracio, T.K. Borg, Expression and accumulation of interstitial collagen in the neonatal rat heart, Anat Rec 236(3) (1993) 511-20.

[27] P. Anversa, J.M. Capasso, Cellular basis of aging in the mammalian heart, Scanning microscopy 5(4) (1991) 1065-73; discussion 1073-4.

[28] C.R. Gazoti Debessa, L.B. Mesiano Maifrino, R. Rodrigues de Souza, Age related changes of the collagen network of the human heart, Mechanisms of Ageing and Development 122(10) (2001) 1049-1058.

[29] C.T. Nguyen, C.S. Hall, M.J. Scott, Q. Zhu, J. Marsh, S.A. Wickline, Age-related alterations of cardiac tissue microstructure and material properties in Fischer 344 rats, Ultrasound in Medicine & Biology 27(5) (2001) 611-619.

[30] B. Aigner, S. Renner, B. Kessler, N. Klymiuk, M. Kurome, A. Wünsch, E. Wolf, Transgenic pigs as models for translational biomedical research, Journal of molecular medicine 88(7) (2010) 653-664.

[31] G.W. Almond, Research applications using pigs, Veterinary Clinics of North America: food animal practice 12(3) (1996) 707-716.

[32] A. Bassols, C. Costa, P.D. Eckersall, J. Osada, J. Sabria, J. Tibau, The pig as an animal model for human pathologies: A proteomics perspective, Proteomics. Clinical applications 8(9-10) (2014) 715-31.

[33] S.A. Book, L.K. Bustad, The fetal and neonatal pig in biomedical research, Journal of animal science 38(5) (1974) 997-1002.

[34] D. Cooper, Y. Ye, L. Rolf Jr, N. Zuhdi, The pig as potential organ donor for man, Xenotransplantation, Springer1991, pp. 481-500.

[35] W.R. Douglas, Of pigs and men and research, Origins of life and evolution of biospheres 3(3) (1972) 226-234.

[36] Y. Luo, L. Lin, L. Bolund, T.G. Jensen, C.B. Sørensen, Genetically modified pigs for biomedical research, Journal of inherited metabolic disease 35(4) (2012) 695-713.

[37] P. Vodicka, K. Smetana, Jr., B. Dvorankova, T. Emerick, Y.Z. Xu, J. Ourednik, V. Ourednik, J. Motlik, The miniature pig as an animal model in biomedical research, Annals of the New York Academy of Sciences 1049 (2005) 161-71.

[38] G.A. Holzapfel, R.W. Ogden, Constitutive modelling of passive myocardium: a structurally based framework for material characterization, 2009.

[39] G. Sommer, D. Haspinger, M. Andra, M. Sacherer, C. Viertler, P. Regitnig, G.A. Holzapfel, Quantification of Shear Deformations and Corresponding Stresses in the Biaxially Tested Human Myocardium, Ann Biomed Eng 43(10) (2015) 2334-48.

[40] J.D. Humphrey, Cardiovascular Solid Mechanics: Cells, Tissues, and Organs, Springer New York2013.

[41] J.W. Holmes, T.K. Borg, J.W. Covell, Structure and mechanics of healing myocardial infarcts, Annual review of biomedical engineering 7 (2005) 223-53.

[42] H. Ashikaga, J.W. Covell, J.H. Omens, Diastolic dysfunction in volume-overload hypertrophy is associated with abnormal shearing of myolaminar sheets, American journal of physiology. Heart and circulatory physiology 288(6) (2005) H2603-10.

[43] I.J. LeGrice, B.H. Smaill, L.Z. Chai, S.G. Edgar, J.B. Gavin, P.J. Hunter, Laminar structure of the heart: ventricular myocyte arrangement and connective tissue architecture in the dog, The American journal of physiology 269(2 Pt 2) (1995) H571-82.

[44] E.A. Woodcock, S.J. Matkovich, Cardiomyocytes structure, function and associated pathologies, The International Journal of Biochemistry & Cell Biology 37(9) (2005) 1746-1751.

[45] W.J. Karlon, A.D. McCulloch, J.W. Covell, J.J. Hunter, J.H. Omens, Regional dysfunction correlates with myofiber disarray in transgenic mice with ventricular expression

of ras, American journal of physiology. Heart and circulatory physiology 278(3) (2000) H898-906.

[46] A. Palit, S.K. Bhudia, T.N. Arvanitis, V. Sherwood, S. Wayte, G.A. Turley, M.A. Williams, Effect of fibre orientation on diastolic mechanics of human ventricle, Conference proceedings : ... Annual International Conference of the IEEE Engineering in Medicine and Biology Society. IEEE Engineering in Medicine and Biology Society. Annual Conference 2015 (2015) 6523-6.

[47] K.T. Weber, Y. Sun, S.C. Tyagi, J.P. Cleutjens, Collagen network of the myocardium: function, structural remodeling and regulatory mechanisms, Journal of molecular and cellular cardiology 26(3) (1994) 279-292.

[48] R. Dawson, G. Milne, R.B. Williams, Changes in the collagen of rat heart in copper-deficiency-induced cardiac hypertrophy, Cardiovasc Res 16(10) (1982) 559-65.

[49] S.M. Factor, T.F. Robinson, R. Dominitz, S.H. Cho, Alterations of the myocardial skeletal framework in acute myocardial infarction with and without ventricular rupture. A preliminary report, The American journal of cardiovascular pathology 1(1) (1987) 91-7.

[50] Circulation Research Thematic Synopsis Cardiac Myocyte Biology and Function, Circulation research 111(9) (2012) e232-e251.

[51] R. Avazmohammadi, M.R. Hill, M.A. Simon, W. Zhang, M.S. Sacks, A novel constitutive model for passive right ventricular myocardium: evidence for myofiber-collagen fiber mechanical coupling, Biomech Model Mechanobiol 16(2) (2017) 561-581.

[52] G. Sommer, A.J. Schriefl, M. Andra, M. Sacherer, C. Viertler, H. Wolinski, G.A. Holzapfel, Biomechanical properties and microstructure of human ventricular myocardium, Acta biomaterialia 24 (2015) 172-92.

[53] G.A. Holzapfel, G. Sommer, C.T. Gasser, P. Regitnig, Determination of layer-specific mechanical properties of human coronary arteries with nonatherosclerotic intimal thickening

and related constitutive modeling, American Journal of Physiology - Heart and Circulatory Physiology 289(5) (2005) H2048-H2058.

[54] G. Sommer, P. Regitnig, L. Költringer, G.A. Holzapfel, Biaxial mechanical properties of intact and layer-dissected human carotid arteries at physiological and supraphysiological loadings, American Journal of Physiology - Heart and Circulatory Physiology 298(3) (2010) H898-H912.

[55] C.A.J. Schulze-Bauer, P. Regitnig, G.A. Holzapfel, Mechanics of the human femoral adventitia including the high-pressure response, American Journal of Physiology - Heart and Circulatory Physiology 282(6) (2002) H2427-H2440.

[56] Z.N. Zhou, S.J. Dong, E.R. Smith, J.V. Tyberg, Differences in distensibility between the anterior and posterior walls of the left ventricle in dogs, Canadian journal of physiology and pharmacology 69(3) (1991) 334-40.

[57] Y. Goto, B.K. Slinker, M.M. LeWinter, Nonhomogeneous left ventricular regional shortening during acute right ventricular pressure overload, Circulation research 65(1) (1989) 43-54.

[58] J. Chen, S.K. Lee, W.R. Abd-Elgaliel, L. Liang, E.Y. Galende, R.J. Hajjar, C.H. Tung, Assessment of cardiovascular fibrosis using novel fluorescent probes, PloS one 6(4) (2011) e19097.

[59] G. Klein, A. Schaefer, D. Hilfiker-Kleiner, D. Oppermann, P. Shukla, A. Quint, E. Podewski, A. Hilfiker, F. Schroder, M. Leitges, H. Drexler, Increased collagen deposition and diastolic dysfunction but preserved myocardial hypertrophy after pressure overload in mice lacking PKCepsilon, Circulation research 96(7) (2005) 748-55.

[60] K. Schenke-Layland, U.A. Stock, A. Nsair, J. Xie, E. Angelis, C.G. Fonseca, R. Larbig, A. Mahajan, K. Shivkumar, M.C. Fishbein, W.R. MacLellan, Cardiomyopathy is associated

with structural remodelling of heart valve extracellular matrix, European heart journal 30(18) (2009) 2254-65.

[61] X. Chen, O. Nadiarynkh, S. Plotnikov, P.J. Campagnola, Second harmonic generation microscopy for quantitative analysis of collagen fibrillar structure, Nature protocols 7(4) (2012) 654-69.

[62] W.R. Zipfel, R.M. Williams, W.W. Webb, Nonlinear magic: multiphoton microscopy in the biosciences, Nature biotechnology 21(11) (2003) 1369-77.

[63] V. Caorsi, C. Toepfer, M.B. Sikkel, A.R. Lyon, K. MacLeod, M.A. Ferenczi, Non-linear optical microscopy sheds light on cardiovascular disease, PloS one 8(2) (2013) e56136.

[64] A.J. Pope, G.B. Sands, B.H. Smaill, I.J. LeGrice, Three-dimensional transmural organization of perimysial collagen in the heart, American Journal of Physiology-Heart and Circulatory Physiology 295(3) (2008) H1243-H1252.

[65] K.A. Faraj, V.M. Cuijpers, R.G. Wismans, X.F. Walboomers, J.A. Jansen, T.H. van Kuppevelt, W.F. Daamen, Micro-computed tomographical imaging of soft biological materials using contrast techniques, Tissue engineering. Part C, Methods 15(3) (2009) 493-9.

[66] B.D. Metscher, MicroCT for comparative morphology: simple staining methods allow high-contrast 3D imaging of diverse non-mineralized animal tissues, BMC Physiology 9(1) (2009) 11.

[67] B.D. Metscher, MicroCT for developmental biology: a versatile tool for high-contrast 3D imaging at histological resolutions, Developmental dynamics : an official publication of the American Association of Anatomists 238(3) (2009) 632-40.

[68] N.S. Jeffery, R.S. Stephenson, J.A. Gallagher, J.C. Jarvis, P.G. Cox, Micro-computed tomography with iodine staining resolves the arrangement of muscle fibres, Journal of biomechanics 44(1) (2011) 189-92.

[69] M.T. Wu, W.Y. Tseng, M.Y. Su, C.P. Liu, K.R. Chiou, V.J. Wedeen, T.G. Reese, C.F. Yang, Diffusion tensor magnetic resonance imaging mapping the fiber architecture remodeling in human myocardium after infarction: correlation with viability and wall motion, Circulation 114(10) (2006) 1036-45.

[70] L. Zhang, J. Allen, L. Hu, S.D. Caruthers, S.A. Wickline, J. Chen, Cardiomyocyte architectural plasticity in fetal, neonatal, and adult pig hearts delineated with diffusion tensor MRI, American Journal of Physiology - Heart and Circulatory Physiology 304(2) (2013) H246-H252.

[71] S. Zhang, J.A. Crow, X. Yang, J. Chen, A. Borazjani, K.B. Mullins, W. Chen, R.C. Cooper, R.M. McLaughlin, J. Liao, The correlation of 3D DT-MRI fiber disruption with structural and mechanical degeneration in porcine myocardium, Ann Biomed Eng 38(10) (2010) 3084-95.

[72] S. Javani, M. Gordon, A.N. Azadani, Biomechanical Properties and Microstructure of Heart Chambers: A Paired Comparison Study in an Ovine Model, Annals of Biomedical Engineering 44(11) (2016) 3266-3283.

[73] M.S. Sirry, J.R. Butler, S.S. Patnaik, B. Brazile, R. Bertucci, A. Claude, R. McLaughlin, N.H. Davies, J. Liao, T. Franz, Characterisation of the mechanical properties of infarcted myocardium in the rat under biaxial tension and uniaxial compression, J Mech Behav Biomed Mater 63 (2016) 252-264.

[74] F.J. Vetter, S.B. Simons, S. Mironov, C.J. Hyatt, A.M. Pertsov, Epicardial fiber organization in swine right ventricle and its impact on propagation, Circulation research 96(2) (2005) 244-51.

[75] D.D. Streeter, D.L. Bassett, An engineering analysis of myocardial fiber orientation in pig's left ventricle in systole, The Anatomical Record 155(4) (1966) 503-511.

[76] E. Avolio, I. Rodriguez-Arabaolaza, H.L. Spencer, F. Riu, G. Mangialardi, S.C. Slater, J. Rowlinson, V.V. Alvino, O.O. Idowu, S. Soyombo, A. Oikawa, M.M. Swim, C.H.T. Kong, H. Cheng, H. Jia, M.T. Ghorbel, J.C. Hancox, C.H. Orchard, G. Angelini, C. Emanueli, M. Caputo, P. Madeddu, Expansion and Characterization of Neonatal Cardiac Pericytes Provides a Novel Cellular Option for Tissue Engineering in Congenital Heart Disease, Journal of the American Heart Association: Cardiovascular and Cerebrovascular Disease 4(6) (2015) e002043.

[77] M.P. Bal, W.B. de Vries, P. Steendijk, P. Homoet-van der Kraak, F.R. van der Leij, J. Baan, M.F.M. van Oosterhout, F. van Bel, Histopathological Changes of the Heart After Neonatal Dexamethasone Treatment: Studies in 4-, 8-, and 50-Week-Old Rats, Pediatric Research 66 (2009) 74.

[78] N. Bursac, M. Papadaki, R.J. Cohen, F.J. Schoen, S.R. Eisenberg, R. Carrier, G. Vunjak-Novakovic, L.E. Freed, Cardiac muscle tissue engineering: toward an in vitro model for electrophysiological studies, American Journal of Physiology - Heart and Circulatory Physiology 277(2) (1999) H433-H444.

[79] A.H. Cheema, S.H. Gilani, Cardiac myopathies in neonatal lambs: histological and histochemical studies, Biology of the neonate 34(1-2) (1978) 84-91.

[80] C. Llanos, D.M. Friedman, A. Saxena, P.M. Izmirly, C.-E. Tseng, R. Dische, R.G. Abellar, M. Halushka, R.M. Clancy, J.P. Buyon, Anatomical and pathological findings in hearts from fetuses and infants with cardiac manifestations of neonatal lupus, Rheumatology 51(6) (2012) 1086-1092.

[81] T. Tirilomis, M. Bensch, R. Waldmann-Beushausen, F.A. Schoendube, Myocardial histology and outcome after cardiopulmonary bypass of neonatal piglets, Journal of cardiothoracic surgery 10 (2015) 170.

[82] T.H. Chen, S.W. Liu, M.R. Chen, K.H. Cho, T.Y. Chen, P.H. Chu, Y.Y. Kao, C.H. Hsu, K.M. Lin, Neonatal Death and Heart Failure in Mouse with Transgenic HSP60 Expression, Biomed Res Int 2015 (2015) 539805.

[83] A.J. Pope, G.B. Sands, B.H. Smaill, I.J. LeGrice, Three-dimensional transmural organization of perimysial collagen in the heart, American journal of physiology. Heart and circulatory physiology 295(3) (2008) H1243-h1252.

[84] G.S. He, S.H. Liu, Physics of nonlinear optics, World Scientific Publishing Co Inc1999.

[85] H. Liu, W. Qin, Y. Shao, Z. Ma, T. Ye, T. Borg, B.Z. Gao, Myofibrillogenesis in live neonatal cardiomyocytes observed with hybrid two-photon excitation fluorescence-second harmonic generation microscopy, Journal of biomedical optics 16(12) (2011) 126012-1260124.

[86] H. Liu, Y. Shao, W. Qin, R.B. Runyan, M. Xu, Z. Ma, T.K. Borg, R. Markwald, B.Z. Gao, Myosin filament assembly onto myofibrils in live neonatal cardiomyocytes observed by TPEF-SHG microscopy, Cardiovascular Research 97(2) (2013) 262-270.

[87] C. Williams, K.P. Quinn, I. Georgakoudi, L.D. Black Iii, Young developmental age cardiac extracellular matrix promotes the expansion of neonatal cardiomyocytes in vitro, Acta biomaterialia 10(1) (2014) 194-204.

[88] P.J. Campagnola, L.M. Loew, Second-harmonic imaging microscopy for visualizing biomolecular arrays in cells, tissues and organisms, Nature biotechnology 21(11) (2003) 1356-60.

[89] P.J. Campagnola, M.D. Wei, A. Lewis, L.M. Loew, High-resolution nonlinear optical imaging of live cells by second harmonic generation, Biophysical journal 77(6) (1999) 3341-9.

[90] R.M. Williams, W.R. Zipfel, W.W. Webb, Interpreting second-harmonic generation images of collagen I fibrils, Biophysical journal 88(2) (2005) 1377-86.

[91] R. Lacomb, O. Nadiarnykh, S.S. Townsend, P.J. Campagnola, Phase Matching considerations in Second Harmonic Generation from tissues: Effects on emission directionality, conversion efficiency and observed morphology, Optics communications 281(7) (2008) 1823-1832.

[92] A.J. Pope, G.B. Sands, B.H. Smaill, I.J. LeGrice, Three-dimensional transmural organization of perimysial collagen in the heart, American Journal of Physiology - Heart and Circulatory Physiology 295(3) (2008) H1243-H1252.

[93] A.A. Holmes, D.F. Scollan, R.L. Winslow, Direct histological validation of diffusion tensor MRI in formaldehyde-fixed myocardium, Magnetic resonance in medicine 44(1) (2000) 157-61.

[94] D. Rohmer, A. Sitek, G.T. Gullberg, Reconstruction and visualization of fiber and laminar structure in the normal human heart from ex vivo diffusion tensor magnetic resonance imaging (DTMRI) data, Investigative radiology 42(11) (2007) 777-789.

[95] L. Zhukov, A.H. Barr, Heart-muscle fiber reconstruction from diffusion tensor MRI, IEEE Visualization, 2003. VIS 2003., 2003, pp. 597-602.

[96] J. Dou, T.G. Reese, W.Y. Tseng, V.J. Wedeen, Cardiac diffusion MRI without motion effects, Magnetic resonance in medicine 48(1) (2002) 105-14.

[97] J. Dou, W.Y. Tseng, T.G. Reese, V.J. Wedeen, Combined diffusion and strain MRI reveals structure and function of human myocardial laminar sheets in vivo, Magnetic resonance in medicine 50(1) (2003) 107-13.

[98] W.Y. Tseng, T.G. Reese, R.M. Weisskoff, T.J. Brady, V.J. Wedeen, Myocardial fiber shortening in humans: initial results of MR imaging, Radiology 216(1) (2000) 128-39.

[99] W.Y. Tseng, T.G. Reese, R.M. Weisskoff, V.J. Wedeen, Cardiac diffusion tensor MRI in vivo without strain correction, Magnetic resonance in medicine 42(2) (1999) 393-403.

[100] C.F. Westin, S.E. Maier, H. Mamata, A. Nabavi, F.A. Jolesz, R. Kikinis, Processing and visualization for diffusion tensor MRI, Medical image analysis 6(2) (2002) 93-108.

[101] J.G. Malcolm, M.E. Shenton, Y. Rathi, Filtered multitensor tractography, IEEE transactions on medical imaging 29(9) (2010) 1664-75.

[102] L.A. McGill, A.D. Scott, P.F. Ferreira, S. Nielles-Vallespin, T. Ismail, P.J. Kilner, P.D. Gatehouse, R. de Silva, S.K. Prasad, A. Giannakidis, D.N. Firmin, D.J. Pennell, Heterogeneity of Fractional Anisotropy and Mean Diffusivity Measurements by In Vivo Diffusion Tensor Imaging in Normal Human Hearts, PloS one 10(7) (2015) e0132360.

[103] C. Mekkaoui, P. Porayette, M.P. Jackowski, W.J. Kostis, G. Dai, S. Sanders, D.E. Sosnovik, Diffusion MRI tractography of the developing human fetal heart, PloS one 8(8) (2013) e72795.

[104] L.L. Demer, F.C. Yin, Passive biaxial mechanical properties of isolated canine myocardium, The Journal of physiology 339 (1983) 615-30.

[105] M.R. Hill, M.A. Simon, D. Valdez-Jasso, W. Zhang, H.C. Champion, M.S. Sacks, Structural and mechanical adaptations of right ventricle free wall myocardium to pressure overload, Ann Biomed Eng 42(12) (2014) 2451-65.

[106] J.D. Humphrey, R.K. Strumpf, F.C.P. Yin, Determination of a Constitutive Relation for Passive Myocardium: II.—Parameter Estimation, Journal of biomechanical engineering 112(3) (1990) 340-346.

[107] V.P. Novak, F.C. Yin, J.D. Humphrey, Regional mechanical properties of passive myocardium, Journal of biomechanics 27(4) (1994) 403-12.

[108] M.S. Sacks, C.J. Chuong, Biaxial Mechanical Properties of Passive Right Ventricular Free Wall Myocardium, Journal of biomechanical engineering 115(2) (1993) 202-205.

[109] F.C. Yin, R.K. Strumpf, P.H. Chew, S.L. Zeger, Quantification of the mechanical properties of noncontracting canine myocardium under simultaneous biaxial loading, Journal of biomechanics 20(6) (1987) 577-89.

[110] G.A. Holzapfel, R.W. Ogden, Constitutive modelling of passive myocardium: a structurally based framework for material characterization, Philosophical Transactions of the Royal Society A: Mathematical, Physical and Engineering Sciences 367(1902) (2009) 3445-3475.

[111] I.J. LeGrice, Y. Takayama, J.W. Covell, Transverse shear along myocardial cleavage planes provides a mechanism for normal systolic wall thickening, Circulation research 77(1) (1995) 182-93.

[112] H.M. Spotnitz, W.D. Spotnitz, T.S. Cottrell, D. Spiro, E.H. Sonnenblick, Cellular basis for volume related wall thickness changes in the rat left ventricle, Journal of Molecular and Cellular Cardiology 6(4) (1974) 317-331.

[113] S. Dokos, B.H. Smaill, A.A. Young, I.J. LeGrice, Shear properties of passive ventricular myocardium, American journal of physiology. Heart and circulatory physiology 283(6) (2002) H2650-9.

[114] H. Ghaemi, K. Behdinan, A.D. Spence, In vitro technique in estimation of passive mechanical properties of bovine heart: Part I. Experimental techniques and data, Medical Engineering & Physics 31(1) (2009) 76-82.

[115] G.A. Holzapfel, G. Sommer, P. Regitnig, Anisotropic mechanical properties of tissue components in human atherosclerotic plaques, Journal of biomechanical engineering 126(5) (2004) 657-65.

[116] G. Sommer, P. Regitnig, L. Koltringer, G.A. Holzapfel, Biaxial mechanical properties of intact and layer-dissected human carotid arteries at physiological and supraphysiological

loadings, American journal of physiology. Heart and circulatory physiology 298(3) (2010) H898-912.

[117] G.A. Holzapfel, G. Sommer, C.T. Gasser, P. Regitnig, Determination of layer-specific mechanical properties of human coronary arteries with nonatherosclerotic intimal thickening and related constitutive modeling, American journal of physiology. Heart and circulatory physiology 289(5) (2005) H2048-58.

[118] G. Sommer, M. Eder, L. Kovacs, H. Pathak, L. Bonitz, C. Mueller, P. Regitnig, G.A. Holzapfel, Multiaxial mechanical properties and constitutive modeling of human adipose tissue: a basis for preoperative simulations in plastic and reconstructive surgery, Acta biomaterialia 9(11) (2013) 9036-48.

[119] G. Sommer, A. Schriefl, G. Zeindlinger, A. Katzensteiner, H. Ainodhofer, A. Saxena, G.A. Holzapfel, Multiaxial mechanical response and constitutive modeling of esophageal tissues: Impact on esophageal tissue engineering, Acta biomaterialia 9(12) (2013) 9379-91.

[120] J.D. Humphrey, R.K. Strumpf, F.C. Yin, Biaxial mechanical behavior of excised ventricular epicardium, The American journal of physiology 259(1 Pt 2) (1990) H101-8.

[121] T. Kang, J.D. Humphrey, F.C. Yin, Comparison of biaxial mechanical properties of excised endocardium and epicardium, The American journal of physiology 270(6 Pt 2) (1996) H2169-76.

[122] R.J. Okamoto, M.J. Moulton, S.J. Peterson, D. Li, M.K. Pasque, J.M. Guccione, Epicardial suction: a new approach to mechanical testing of the passive ventricular wall, Journal of biomechanical engineering 122(5) (2000) 479-87.

[123] A.D. McCulloch, B.H. Smaill, P.J. Hunter, Regional left ventricular epicardial deformation in the passive dog heart, Circulation research 64(4) (1989) 721-33.

[124] M.R. Rehorn, A.K. Schroer, S.S. Blemker, The passive properties of muscle fibers are velocity dependent, Journal of biomechanics 47(3) (2014) 687-93.

[125] K. Wang, R. McCarter, J. Wright, J. Beverly, R. Ramirez-Mitchell, Viscoelasticity of the sarcomere matrix of skeletal muscles. The titin-myosin composite filament is a dual-stage molecular spring, Biophysical journal 64(4) (1993) 1161-77.

[126] T. Toursel, L. Stevens, H. Granzier, Y. Mounier, Passive tension of rat skeletal soleus muscle fibers: effects of unloading conditions, Journal of applied physiology (Bethesda, Md. : 1985) 92(4) (2002) 1465-72.

[127] M. Linari, L. Lucii, M. Reconditi, M.E. Casoni, H. Amenitsch, S. Bernstorff, G. Piazzesi, V. Lombardi, A combined mechanical and X-ray diffraction study of stretch potentiation in single frog muscle fibres, The Journal of physiology 526 Pt 3 (2000) 589-96.

[128] D.E. Rassier, W. Herzog, Considerations on the history dependence of muscle contraction, Journal of applied physiology (Bethesda, Md. : 1985) 96(2) (2004) 419-27.

[129] L. Mullins, N.R. Tobin, Theoretical Model for the Elastic Behavior of Filler-Reinforced Vulcanized Rubbers, Rubber Chemistry and Technology 30(2) (1957) 555-571.

[130] J.L. Emery, J.H. Omens, A.D. McCulloch, Strain softening in rat left ventricular myocardium, Journal of biomechanical engineering 119(1) (1997) 6-12.

[131] J.B. Caulfield, T.K. Borg, The collagen network of the heart, Laboratory investigation; a journal of technical methods and pathology 40(3) (1979) 364-72.

[132] D.A. MacKenna, J.H. Omens, A.D. McCulloch, J.W. Covell, Contribution of collagen matrix to passive left ventricular mechanics in isolated rat hearts, The American journal of physiology 266(3 Pt 2) (1994) H1007-18.

[133] H.L. Granzier, T.C. Irving, Passive tension in cardiac muscle: contribution of collagen, titin, microtubules, and intermediate filaments, Biophysical journal 68(3) (1995) 1027-1044.

[134] J. Emery, J. Omens, O. Mathieu-Costello, A. McCulloch, Structural mechanisms of acute ventricular strain softening, Int J Cardiovasc Med Sci 1 (1998) 241-250.

[135] J.L. Emery, J.H. Omens, A.D. McCulloch, Biaxial mechanics of the passively overstretched left ventricle, The American journal of physiology 272(5 Pt 2) (1997) H2299-305.

[136] W.A. Linke, V.I. Popov, G.H. Pollack, Passive and active tension in single cardiac myofibrils, Biophysical journal 67(2) (1994) 782-92.

[137] W.A. Linke, M.L. Bartoo, M. Ivemeyer, G.H. Pollack, Limits of titin extension in single cardiac myofibrils, Journal of muscle research and cell motility 17(4) (1996) 425-38.

[138] M.S. Kellermayer, S.B. Smith, C. Bustamante, H.L. Granzier, Mechanical fatigue in repetitively stretched single molecules of titin, Biophysical journal 80(2) (2001) 852-63.

[139] R. Kirton, A. Taberner, P. Nielsen, A. Young, D. Loiselle, Strain softening behaviour in nonviable rat right-ventricular trabeculae, in the presence and the absence of butanedione monoxime, Experimental physiology 89(5) (2004) 593-604.

[140] M. Helmes, K. Trombitas, T. Centner, M. Kellermayer, S. Labeit, W.A. Linke, H. Granzier, Mechanically driven contour-length adjustment in rat cardiac titin's unique N2B sequence: titin is an adjustable spring, Circulation research 84(11) (1999) 1339-52.

[141] X. Wang, P. Lin, Q. Yao, C. Chen, Development of small-diameter vascular grafts, World journal of surgery 31(4) (2007) 682-9.

[142] E. Petrossian, V.M. Reddy, K.K. Collins, C.B. Culbertson, M.J. MacDonald, J.J. Lamberti, O. Reinhartz, R.D. Mainwaring, P.D. Francis, S.P. Malhotra, D.B. Gremmels, S. Suleman, F.L. Hanley, The extracardiac conduit Fontan operation using minimal approach extracorporeal circulation: early and midterm outcomes, The Journal of thoracic and cardiovascular surgery 132(5) (2006) 1054-63.

[143] C.P. Twine, A.D. McLain, Graft type for femoro-popliteal bypass surgery, The Cochrane database of systematic reviews (5) (2010) CD001487.

[144] J.A. Dearani, G.K. Danielson, F.J. Puga, H.V. Schaff, C.W. Warnes, D.J. Driscoll, C.D. Schleck, D.M. Ilstrup, Late follow-up of 1095 patients undergoing operation for complex congenital heart disease utilizing pulmonary ventricle to pulmonary artery conduits, The Annals of thoracic surgery 75(2) (2003) 399-410; discussion 410-1.

[145] K.A. Holst, J.A. Dearani, H.M. Burkhart, H.M. Connolly, C.A. Warnes, Z. Li, H.V. Schaff, Risk factors and early outcomes of multiple reoperations in adults with congenital heart disease, The Annals of thoracic surgery 92(1) (2011) 122-8; discussion 129-30.

[146] M. Homann, J.C. Haehnel, N. Mendler, S.U. Paek, K. Holper, H. Meisner, R. Lange, Reconstruction of the RVOT with valved biological conduits: 25 years experience with allografts and xenografts, European journal of cardio-thoracic surgery : official journal of the European Association for Cardio-thoracic Surgery 17(6) (2000) 624-30.

[147] B. Wang, A. Borazjani, M. Tahai, A.L. Curry, D.T. Simionescu, J. Guan, F. To, S.H. Elder, J. Liao, Fabrication of cardiac patch with decellularized porcine myocardial scaffold and bone marrow mononuclear cells, Journal of biomedical materials research. Part A 94(4) (2010) 1100-10.

[148] A.J. Engler, S. Sen, H.L. Sweeney, D.E. Discher, Matrix elasticity directs stem cell lineage specification, Cell 126(4) (2006) 677-89.

[149] J. Guan, F. Wang, Z. Li, J. Chen, X. Guo, J. Liao, N.I. Moldovan, The stimulation of the cardiac differentiation of mesenchymal stem cells in tissue constructs that mimic myocardium structure and biomechanics, Biomaterials 32(24) (2011) 5568-80.

[150] F. Wang, J. Guan, Cellular cardiomyoplasty and cardiac tissue engineering for myocardial therapy, Advanced drug delivery reviews 62(7-8) (2010) 784-97.

[151] Y. Bazilevs, V.M. Calo, Y. Zhang, T.J. Hughes, Isogeometric fluid–structure interaction analysis with applications to arterial blood flow, Computational Mechanics 38(4-5) (2006) 310-322.

[152] C.A. Figueroa, I.E. Vignon-Clementel, K.E. Jansen, T.J. Hughes, C.A. Taylor, A coupled momentum method for modeling blood flow in three-dimensional deformable arteries, Computer methods in applied mechanics and engineering 195(41-43) (2006) 5685-5706.

[153] C. Long, M.C. Hsu, Y. Bazilevs, J. Feinstein, A. Marsden, Fluid–structure interaction simulations of the Fontan procedure using variable wall properties, International journal for numerical methods in biomedical engineering 28(5) (2012) 513-527.

[154] G. Holzapfel, Nonlinear solid mechanics: a continuum approach for engineering. 2000, West Sussex, England: John Wiley & Sons, Ltd.

[155] J.D. Humphrey, F.C. Yin, On constitutive relations and finite deformations of passive cardiac tissue: I. A pseudostrain-energy function, Journal of biomechanical engineering 109(4) (1987) 298-304.

[156] J.D. Humphrey, R.K. Strumpf, F.C. Yin, Determination of a constitutive relation for passive myocardium: II. Parameter estimation, Journal of biomechanical engineering 112(3) (1990) 340-6.

[157] R.C. Kerckhoffs, P.H. Bovendeerd, J.C. Kotte, F.W. Prinzen, K. Smits, T. Arts, Homogeneity of cardiac contraction despite physiological asynchrony of depolarization: a model study, Ann Biomed Eng 31(5) (2003) 536-47.

[158] J.M. Guccione, A.D. McCulloch, L.K. Waldman, Passive material properties of intact ventricular myocardium determined from a cylindrical model, Journal of biomechanical engineering 113(1) (1991) 42-55.

[159] K.D. Costa, P.J. Hunter, J.S. Wayne, L.K. Waldman, J.M. Guccione, A.D. McCulloch, A three-dimensional finite element method for large elastic deformations of ventricular myocardium: II--Prolate spheroidal coordinates, Journal of biomechanical engineering 118(4) (1996) 464-72.

[160] A. Horowitz, Y. Lanir, F.C. Yin, M. Perl, I. Sheinman, R.K. Strumpf, Structural three-dimensional constitutive law for the passive myocardium, Journal of biomechanical engineering 110(3) (1988) 200-7.

[161] J.E. Bischoff, E.A. Arruda, K. Grosh, A Microstructurally Based Orthotropic Hyperelastic Constitutive Law, Journal of Applied Mechanics 69(5) (2002) 570-579.

[162] K.D. Costa, J.W. Holmes, A.D. McCulloch, Modelling cardiac mechanical properties in three dimensions, Philosophical Transactions of the Royal Society of London. Series A: Mathematical, Physical and Engineering Sciences 359(1783) (2001) 1233.

[163] H. Schmid, M.P. Nash, A.A. Young, P.J. Hunter, Myocardial material parameter estimation-a comparative study for simple shear, Journal of biomechanical engineering 128(5) (2006) 742-50.

[164] D.J. Schneider, T.K. Nordt, B.E. Sobel, Stimulation by proinsulin of expression of plasminogen activator inhibitor type-I in endothelial cells, Diabetes 41(7) (1992) 890-895.

[165] F. Wyler, M. Rutishauser, G. Stalder, DISTRIBUTION OF CARDIAC-OUTPUT AND ORGAN BLOOD-FLOW IN THE MINIPIG, AN EXPERIMENTAL ANIMAL FOR HEMODYNAMIC RESEARCH, European Journal of Cardiology, ELSEVIER SCIENCE BV PO BOX 211, 1000 AE AMSTERDAM, NETHERLANDS, 1979, pp. 327-328.

[166] J. Litten-Brown, A. Corson, L. Clarke, Porcine models for the metabolic syndrome, digestive and bone disorders: a general overview, Animal 4(6) (2010) 899-920.

[167] M. Hubert, I. Salazkin, J. Desjardins, G. Blaise, Cardiopulmonary bypass surgery in swine: a research model, Journal of Experimental Animal Science 42(3) (2003) 135-149.

[168] M.E. Weaver, G.A. Pantely, J.D. Bristow, H.D. Ladley, A quantitative study of the anatomy and distribution of coronary arteries in swine in comparison with other animals and man, Cardiovascular research 20(12) (1986) 907-917.

[169] F. White, S. Carroll, A. Magnet, C. Bloor, Coronary collateral development in swine after coronary artery occlusion, Circulation research 71(6) (1992) 1490-1500.

[170] M. Kyllar, J. Štembírek, I. Putnová, L. Stehlik, S. Odehnalova, M. Buchtová, Radiography, computed tomography and magnetic resonance imaging of craniofacial structures in pig, Anatomia, histologia, embryologia 43(6) (2014) 435-452.

[171] C. Maaske, N. Booth, T. Nielsen, Experimental right heart failure in swine, Swine in Biomedical Research 377 (1966).

[172] H. Rowsell, J. Mustard, M. Packham, W. Dodds, The hemostatic mechanism and its role in cardiovascular disease of swine, Swine in Biomedical Research 365 (1966).

[173] E. Glauser, Advantages of piglets as experimental animals in pediatric research, Experimental medicine and surgery 24(2) (1966) 181-190.

[174] M. Wehling, Translational medicine: science or wishful thinking?, Journal of translational medicine 6(1) (2008) 31.

[175] D.N. Atochin, P.L. Huang, Endothelial nitric oxide synthase transgenic models of endothelial dysfunction, Pflügers Archiv-European Journal of Physiology 460(6) (2010) 965-974.

[176] Y. Hao, H. Yong, C. Murphy, D. Wax, M. Samuel, A. Rieke, L. Lai, Z. Liu, D. Durtschi, V. Welbern, Production of endothelial nitric oxide synthase (eNOS) over-expressing piglets, Transgenic research 15(6) (2006) 739-750.

[177] R.S. Prather, Targeted genetic modification: xenotransplantation and beyond, Cloning and stem cells 9(1) (2007) 17-20.

[178] S.J. Crick, M.N. Sheppard, S.Y. HO, L. Gebstein, R.H. Anderson, Anatomy of the pig heart: comparisons with normal human cardiac structure, The Journal of Anatomy 193(1) (1998) 105-119.

[179] R.P. Faizan Ahmad, Jun Liao, Shwe Soe1, Michael D Jones, Jonathan Miller, Parker Berthelson, Daniel Enge, Katherine M. Copeland, Samar Shaabeth, Richard Johnston, Ian Maconochie, Peter S.Theobald, Biomechanical properties and microstructure of neonatal porcine ventricles, Journal of the Mechanical Behavior of Biomedical Materials (2018).

[180] Z.Q. Liu, Scale space approach to directional analysis of images, Applied optics 30(11) (1991) 1369-73.

[181] S. Fliegener, M. Luke, P. Gumbsch, 3D microstructure modeling of long fiber reinforced thermoplastics, Composites Science and Technology 104 (2014) 136-145.

[182] N. Reznikov, R. Almany-Magal, R. Shahar, S. Weiner, Three-dimensional imaging of collagen fibril organization in rat circumferential lamellar bone using a dual beam electron microscope reveals ordered and disordered sub-lamellar structures, Bone 52(2) (2013) 676-683.

[183] N. Reznikov, R. Shahar, S. Weiner, Three-dimensional structure of human lamellar bone: the presence of two different materials and new insights into the hierarchical organization, Bone 59 (2014) 93-104.

[184] A.J. Woolley, H.A. Desai, M.A. Steckbeck, N.K. Patel, K.J. Otto, In situ characterization of the brain–microdevice interface using device capture histology, Journal of neuroscience methods 201(1) (2011) 67-77.

[185] D.P. Lobo, A.M. Wemyss, D.J. Smith, A. Straube, K.B. Betteridge, A.H. Salmon, R.R. Foster, H.E. Elhegni, S.C. Satchell, H.A. Little, Direct detection and measurement of wall shear stress using a filamentous bio-nanoparticle, Nano research 8(10) (2015) 3307-3315.

[186] W. Sun, S. Chang, D.C. Tai, N. Tan, G. Xiao, H. Tang, H. Yu, Nonlinear optical microscopy: use of second harmonic generation and two-photon microscopy for automated quantitative liver fibrosis studies, Journal of biomedical optics 13(6) (2008) 064010.

[187] M.S. Sirry, J.R. Butler, S.S. Patnaik, B. Brazile, R. Bertucci, A. Claude, R. McLaughlin, N.H. Davies, J. Liao, T. Franz, Infarcted rat myocardium: Data from biaxial tensile and uniaxial compressive testing and analysis of collagen fibre orientation, Data in brief 8 (2016) 1338-43.

[188] B. Wang, M.E. Tedder, C.E. Perez, G. Wang, A.L. de Jongh Curry, F. To, S.H. Elder, L.N. Williams, D.T. Simionescu, J. Liao, Structural and biomechanical characterizations of porcine myocardial extracellular matrix, Journal of materials science. Materials in medicine 23(8) (2012) 1835-47.

[189] J.S. Grashow, A.P. Yoganathan, M.S. Sacks, Biaixal stress-stretch behavior of the mitral valve anterior leaflet at physiologic strain rates, Ann Biomed Eng 34(2) (2006) 315-25.

[190] J.S. Grashow, M.S. Sacks, J. Liao, A.P. Yoganathan, Planar biaxial creep and stress relaxation of the mitral valve anterior leaflet, Ann Biomed Eng 34(10) (2006) 1509-18.

[191] J.D. Humphrey, R.K. Strumpf, F.C. Yin, Determination of a constitutive relation for passive myocardium: I. A new functional form, Journal of biomechanical engineering 112(3) (1990) 333-9.

[192] M. Takeuchi, H. Nakai, M. Kokumai, T. Nishikage, S. Otani, R.M. Lang, Age-related changes in left ventricular twist assessed by two-dimensional speckle-tracking imaging, Journal of the American Society of Echocardiography 19(9) (2006) 1077-1084.

[193] L.A. Taber, M. Yang, W.W. Podszus, Mechanics of ventricular torsion, Journal of biomechanics 29(6) (1996) 745-52.

[194] F.A. Tibayan, F. Rodriguez, F. Langer, M.K. Zasio, L. Bailey, D. Liang, G.T. Daughters, N.B. Ingels, Jr., D.C. Miller, Alterations in left ventricular torsion and diastolic recoil after myocardial infarction with and without chronic ischemic mitral regurgitation, Circulation 110(11 Suppl 1) (2004) Ii109-14.

[195] F.E. Rademakers, M.B. Buchalter, W.J. Rogers, E.A. Zerhouni, M.L. Weisfeldt, J.L. Weiss, E.P. Shapiro, Dissociation between left ventricular untwisting and filling. Accentuation by catecholamines, Circulation 85(4) (1992) 1572-81.

[196] S.J. Dong, P.S. Hees, C.O. Siu, J.L. Weiss, E.P. Shapiro, MRI assessment of LV relaxation by untwisting rate: a new isovolumic phase measure of tau, American journal of physiology. Heart and circulatory physiology 281(5) (2001) H2002-9.

[197] W.Y. Lew, M.M. LeWinter, Regional comparison of midwall segment and area shortening in the canine left ventricle, Circulation research 58(5) (1986) 678-91.

[198] L.K. Waldman, D. Nosan, F. Villarreal, J.W. Covell, Relation between transmural deformation and local myofiber direction in canine left ventricle, Circulation research 63(3) (1988) 550-62.

[199] A.M. Rudolph, Fetal and neonatal pulmonary circulation, The American review of respiratory disease 115(6 Pt 2) (1977) 11-8.

[200] J. Chen, W. Liu, H. Zhang, L. Lacy, X. Yang, S.-K. Song, S.A. Wickline, X. Yu, Regional ventricular wall thickening reflects changes in cardiac fiber and sheet structure during contraction: quantification with diffusion tensor MRI, American Journal of Physiology-Heart and Circulatory Physiology 289(5) (2005) H1898-H1907.

[201] T.K. Borg, J.B. Caulfield, The collagen matrix of the heart, Fed Proc 40(7) (1981) 2037-2041.

[202] K.T. Weber, W.A. Clark, J.S. Janicki, S.G. Shroff, Physiologic versus pathologic hypertrophy and the pressure-overloaded myocardium, Journal of cardiovascular pharmacology 10 Suppl 6 (1987) S37-50.

[203] K.T. Weber, J.S. Janicki, S.G. Shroff, R. Pick, C. Abrahams, R.M. Chen, R.I. Bashey, Collagen compartment remodeling in the pressure overloaded left ventricle, Journal of Applied Cardiology 3(1) (1988) 37-46.

[204] V. Sequeira, L.L. Nijenkamp, J.A. Regan, J. van der Velden, The physiological role of cardiac cytoskeleton and its alterations in heart failure, Biochimica et biophysica acta 1838(2) (2014) 700-22.

[205] I. Mirsky, Left ventricular stresses in the intact human heart, Biophysical journal 9(2) (1969) 189-208.

[206] O. Hudlicka, M.D. Brown, Postnatal growth of the heart and its blood vessels, Journal of vascular research 33(4) (1996) 266-87.

[207] F.J. Clubb, Jr., S.P. Bishop, Formation of binucleated myocardial cells in the neonatal rat. An index for growth hypertrophy, Laboratory investigation; a journal of technical methods and pathology 50(5) (1984) 571-7.

[208] J.G. Jacot, H. Kita-Matsuo, K.A. Wei, H.S. Chen, J.H. Omens, M. Mercola, A.D. McCulloch, Cardiac myocyte force development during differentiation and maturation, Annals of the New York Academy of Sciences 1188 (2010) 121-7.

[209] M. Tallawi, R. Rai, A.R. Boccaccini, K.E. Aifantis, Effect of substrate mechanics on cardiomyocyte maturation and growth, Tissue engineering. Part B, Reviews 21(1) (2015) 157-65.

[210] J.G. Jacot, A.D. McCulloch, J.H. Omens, Substrate Stiffness Affects the Functional Maturation of Neonatal Rat Ventricular Myocytes, Biophysical journal 95(7) (2008) 3479-3487.

[211] M.L. Burgess, J.C. McCrea, H.L. Hedrick, Age-associated changes in cardiac matrix and integrins, Mechanisms of ageing and development 122(15) (2001) 1739-1756.

[212] K.D. Costa, Y. Takayama, A.D. McCulloch, J.W. Covell, Laminar fiber architecture and three-dimensional systolic mechanics in canine ventricular myocardium, The American journal of physiology 276(2 Pt 2) (1999) H595-607.

[213] Y. Takayama, K.D. Costa, J.W. Covell, Contribution of laminar myofiber architecture to load-dependent changes in mechanics of LV myocardium, American journal of physiology. Heart and circulatory physiology 282(4) (2002) H1510-20.

[214] P.H. Bovendeerd, J.M. Huyghe, T. Arts, D.H. van Campen, R.S. Reneman, Influence of endocardial-epicardial crossover of muscle fibers on left ventricular wall mechanics, Journal of biomechanics 27(7) (1994) 941-51.

[215] F.E. Rademakers, W.J. Rogers, W.H. Guier, G.M. Hutchins, C.O. Siu, M.L. Weisfeldt, J.L. Weiss, E.P. Shapiro, Relation of regional cross-fiber shortening to wall thickening in the intact heart. Three-dimensional strain analysis by NMR tagging, Circulation 89(3) (1994) 1174-82.

[216] J. Rijcken, P.H.M. Bovendeerd, A.J.G. Schoofs, D.H. van Campen, T. Arts, Optimization of Cardiac Fiber Orientation for Homogeneous Fiber Strain During Ejection, Annals of Biomedical Engineering 27(3) (1999) 289-297.

[217] T. Arts, K.D. Costa, J.W. Covell, A.D. McCulloch, Relating myocardial laminar architecture to shear strain and muscle fiber orientation, American journal of physiology. Heart and circulatory physiology 280(5) (2001) H2222-9.

[218] N.B. Ingels, Jr., Myocardial fiber architecture and left ventricular function, Technology and health care : official journal of the European Society for Engineering and Medicine 5(1-2) (1997) 45-52.

[219] T.F. Robinson, L. Cohen-Gould, S.M. Factor, Skeletal framework of mammalian heart muscle. Arrangement of inter- and pericellular connective tissue structures, Laboratory investigation; a journal of technical methods and pathology 49(4) (1983) 482-98.

[220] J.E. Bishop, G. Lindahl, Regulation of cardiovascular collagen synthesis by mechanical load, Cardiovasc Res 42(1) (1999) 27-44.

[221] K.T. Weber, J.S. Janicki, S.G. Shroff, R. Pick, R.M. Chen, R.I. Bashey, Collagen remodeling of the pressure-overloaded, hypertrophied nonhuman primate myocardium, Circulation research 62(4) (1988) 757-65.

[222] D.H. Lin, F.C. Yin, A multiaxial constitutive law for mammalian left ventricular myocardium in steady-state barium contracture or tetanus, Journal of biomechanical engineering 120(4) (1998) 504-17.

[223] K.B. Gupta, M.B. Ratcliffe, M.A. Fallert, L.H. Edmunds, Jr., D.K. Bogen, Changes in passive mechanical stiffness of myocardial tissue with aneurysm formation, Circulation 89(5) (1994) 2315-26.

[224] M.S. Sacks, C.J. Chuong, Biaxial mechanical properties of passive right ventricular free wall myocardium, Journal of biomechanical engineering 115(2) (1993) 202-5.

[225] P. Wang, F. Zhu, N.H. Lee, K. Konstantopoulos, Shear-induced interleukin-6 synthesis in chondrocytes: roles of E prostanoid (EP) 2 and EP3 in cAMP/protein kinase A- and PI3-K/Akt-dependent NF-kappaB activation, The Journal of biological chemistry 285(32) (2010) 24793-804.

[226] D. Valdez-Jasso, M.A. Simon, H.C. Champion, M.S. Sacks, A murine experimental model for the mechanical behaviour of viable right-ventricular myocardium, The Journal of physiology 590(18) (2012) 4571-84.

[227] D. Perie, N. Dahdah, A. Foudis, D. Curnier, Multi-parametric MRI as an indirect evaluation tool of the mechanical properties of in-vitro cardiac tissues, BMC cardiovascular disorders 13 (2013) 24.

[228] B. Wang, G. Wang, F. To, J.R. Butler, A. Claude, R.M. McLaughlin, L.N. Williams, A.L. de Jongh Curry, J. Liao, Myocardial scaffold-based cardiac tissue engineering: application of coordinated mechanical and electrical stimulations, Langmuir : the ACS journal of surfaces and colloids 29(35) (2013) 11109-17.

[229] D. Guerreiro, S.C. Lennox, R.H. Anderson, Postnatal development of the pig heart, Cardiovasc Res 14(11) (1980) 675-9.

[230] A. Hislop, L. Reid, Weight of the left and right ventricle of the heart during fetal life, Journal of Clinical Pathology 25(6) (1972) 534-536.

[231] C.J. Chuong, M.S. Sacks, G. Templeton, F. Schwiep, R.L. Johnson, Jr., Regional deformation and contractile function in canine right ventricular free wall, The American journal of physiology 260(4 Pt 2) (1991) H1224-35.

[232] G. Sommer, A.J. Schriefl, M. Andrä, M. Sacherer, C. Viertler, H. Wolinski, G.A. Holzapfel, Biomechanical properties and microstructure of human ventricular myocardium, Acta biomaterialia 24 (2015) 172-192.

[233] L.L. Demer, F.C. Yin, Passive biaxial mechanical properties of isolated canine myocardium, The Journal of physiology 339 (1983) 615-630.

8. APPENDIX

A.1. Masson's Trichrome stained histological images of the anterior and posterior aspects in the LVFW and RVFW

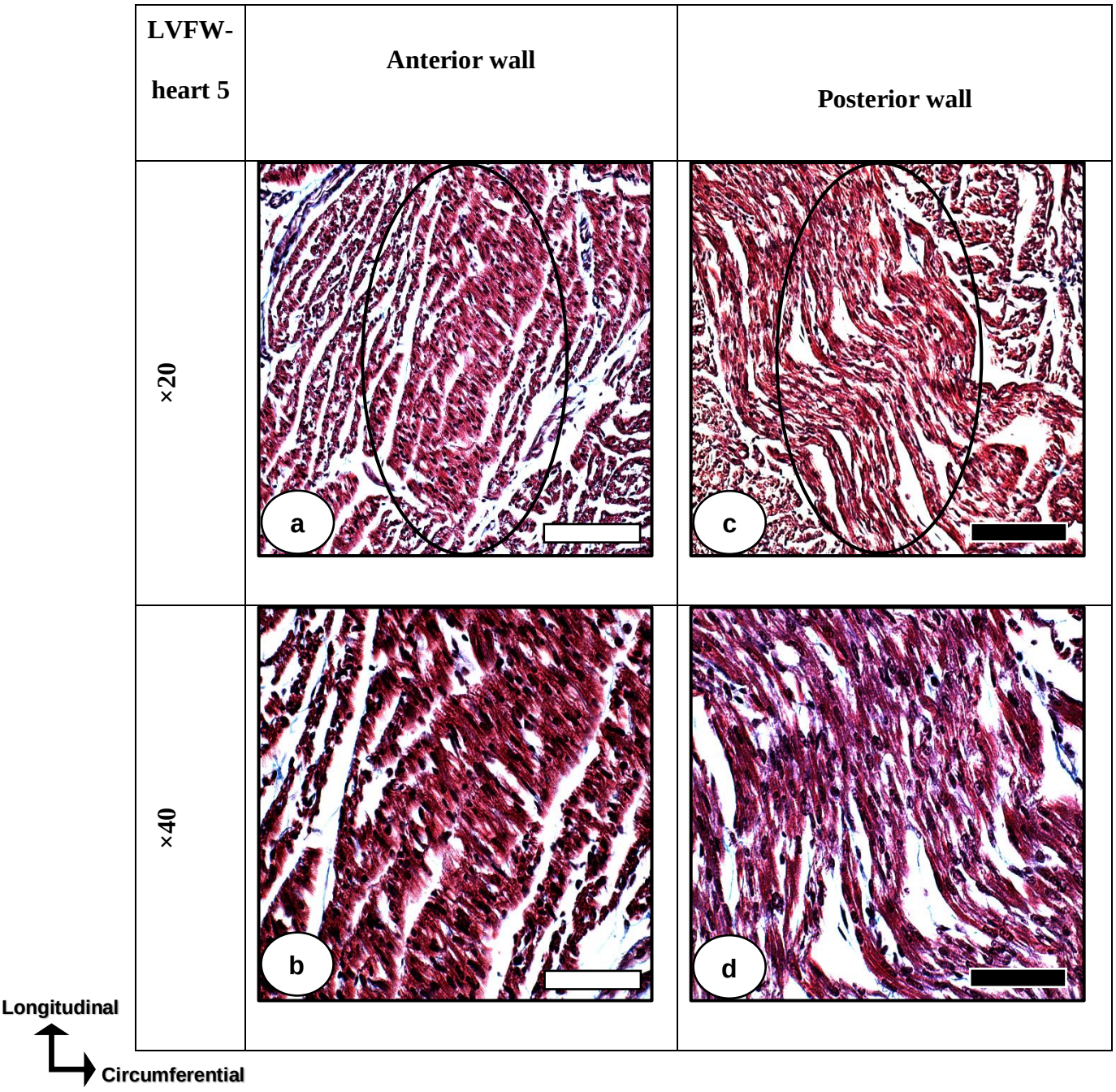

Figure A.1.1: *Masson's trichrome staining images of the neonatal porcine ventricles, sectioned in the plane perpendicular to the transmural direction (i.e. in-plane), and viewed at × 20 and × 40 magnification.* ***(a–b)*** *LVFW–anterior, demonstrating circumferentially aligned fibres.* ***(c–d)*** *LVFW–posterior, describing longitudinally aligned fibres. Principal or preferred fibre angles are detailed in Table 4.1. The scale bar at* ***×20*** *=100 µm and at* ***×40*** *=50µm, respectively.*

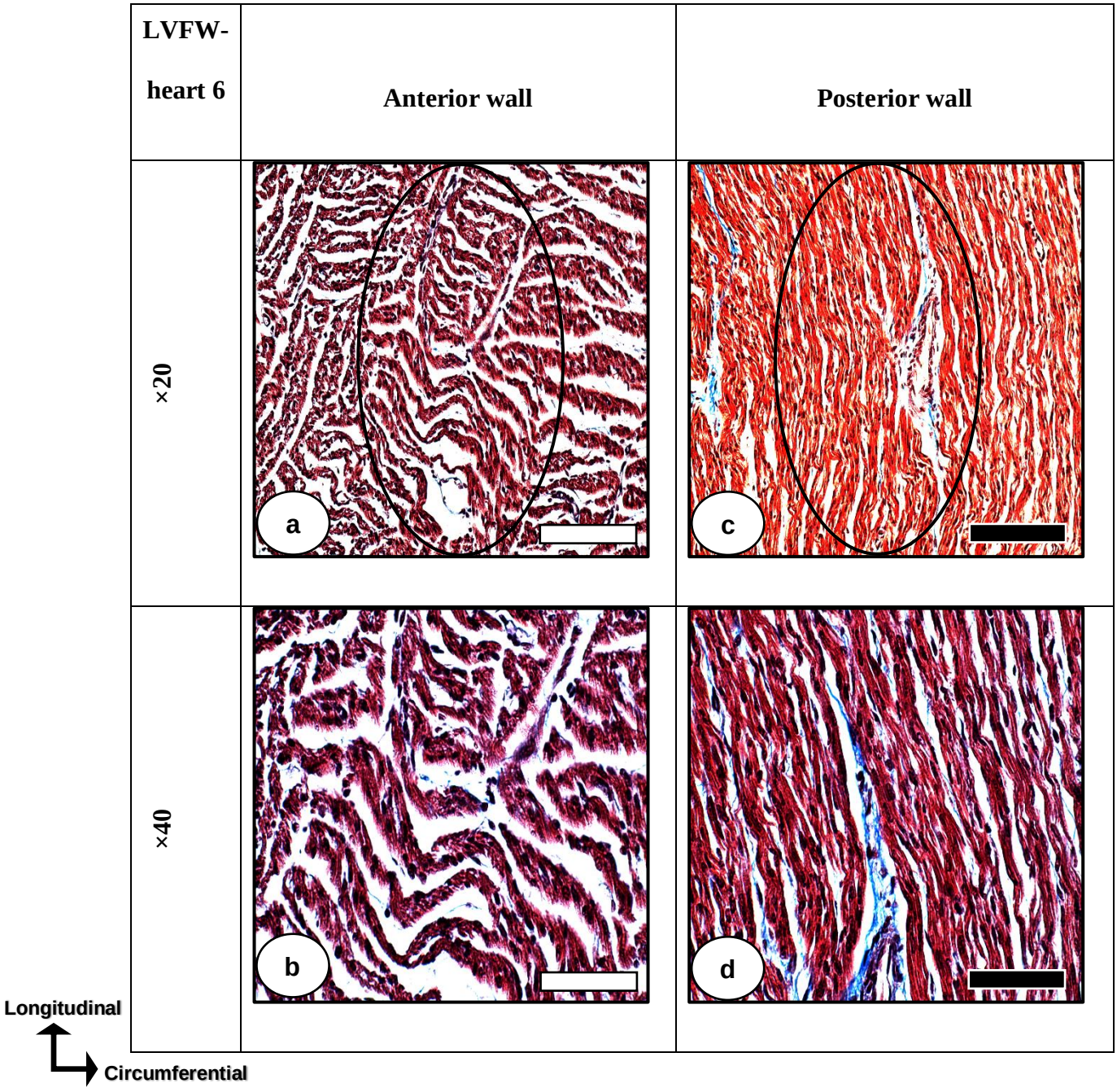

Figure A.1.2: *Masson's trichrome staining images of the neonatal porcine ventricles, sectioned in the plane perpendicular to the transmural direction (i.e. in-plane), and viewed at × 20 and × 40 magnification.* ***(a–b)*** *LVFW–anterior, demonstrating circumferentially aligned fibres.* ***(c–d)*** *LVFW–posterior, describing longitudinally aligned fibres. Principal or preferred fibre angles are detailed in Table 4.1. The scale bar at* ***×20*** *=100 µm and at* ***×40*** *=50µm, respectively.*

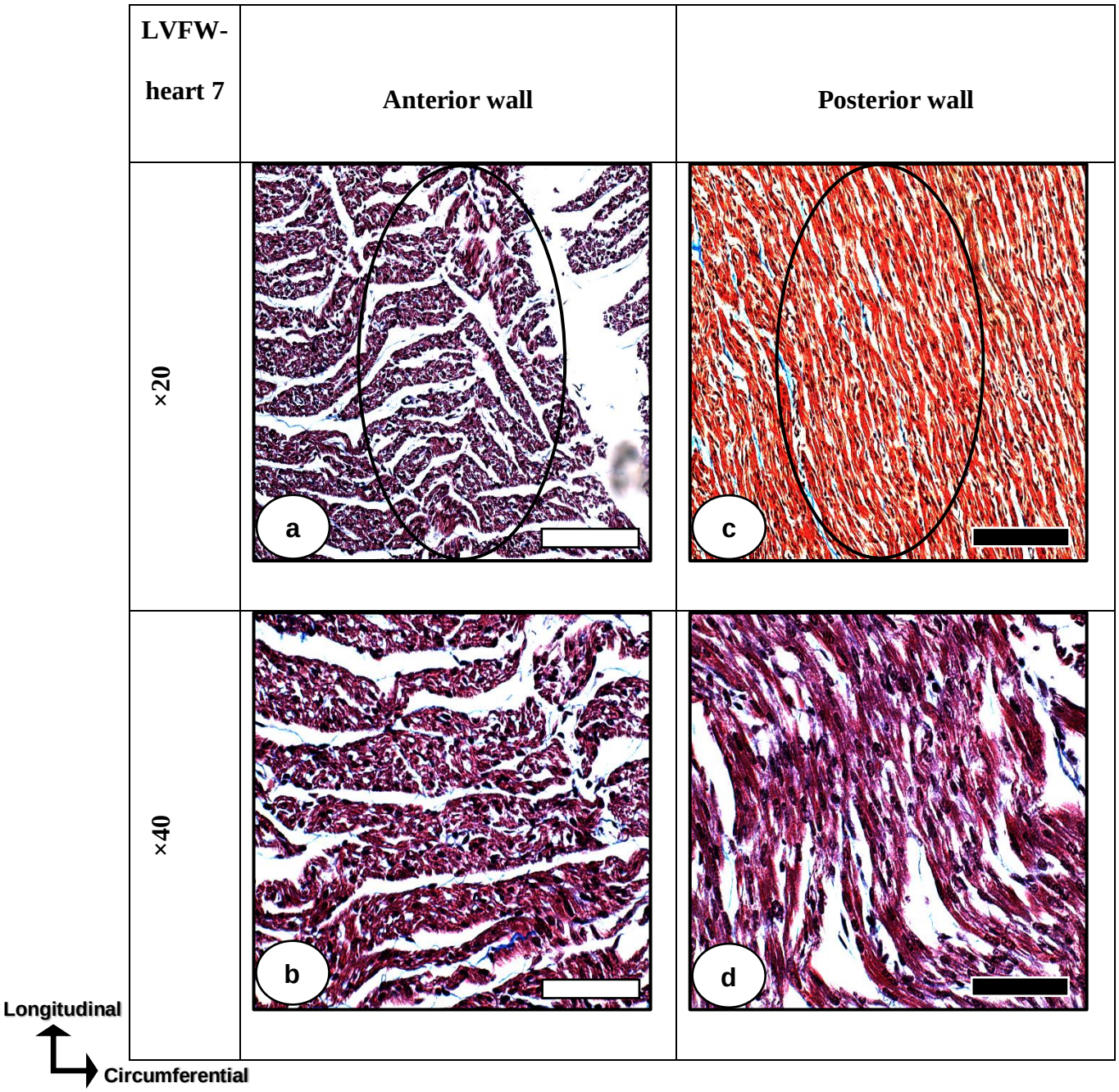

Figure A.1.3: *Masson's trichrome staining images of the neonatal porcine ventricles, sectioned in the plane perpendicular to the transmural direction (i.e. in - plane), and viewed at × 20 and × 40 magnification.* ***(a–b)*** *LVFW–anterior, demonstrating circumferentially aligned fibres.* ***(c–d)*** *LVFW–posterior, describing longitudinally aligned fibres. Principal or preferred fibre angles are detailed in Table 4.1. The scale bar at* ***×20*** *=100 µm and at* ***×40*** *=50µm, respectively.*

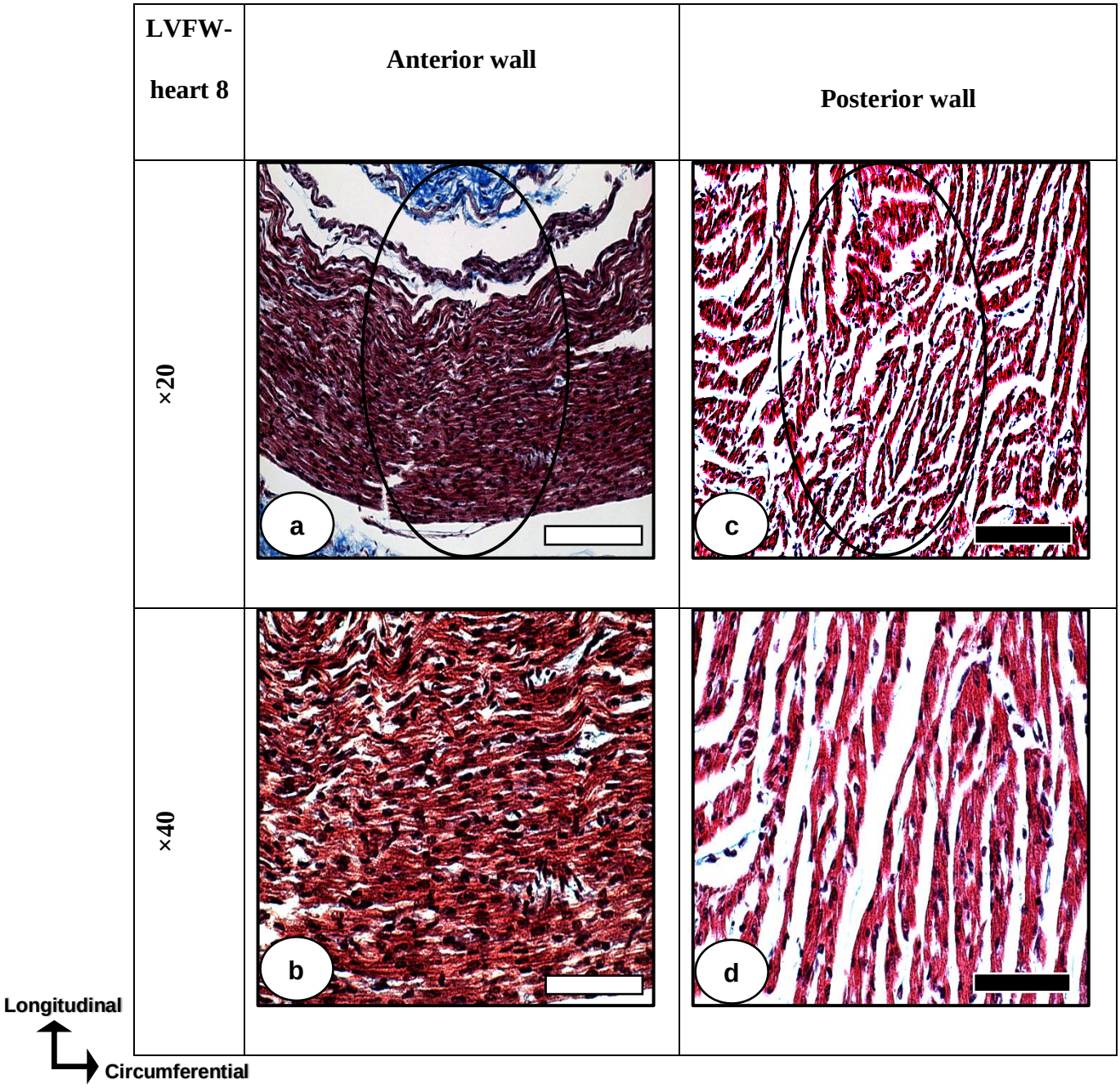

Figure A.1.4: *Masson's trichrome staining images of the neonatal porcine ventricles, sectioned in the plane perpendicular to the transmural direction (i.e. in - plane), and viewed at × 20 and × 40 magnification.* ***(a–b)*** *LVFW–anterior, demonstrating circumferentially aligned fibres.* ***(c–d)*** *LVFW–posterior, describing longitudinally aligned fibres. Principal or preferred fibre angles are detailed in Table 4.1. The scale bar at* ***×20*** *=100 µm and at* ***×40*** *=50µm, respectively.*

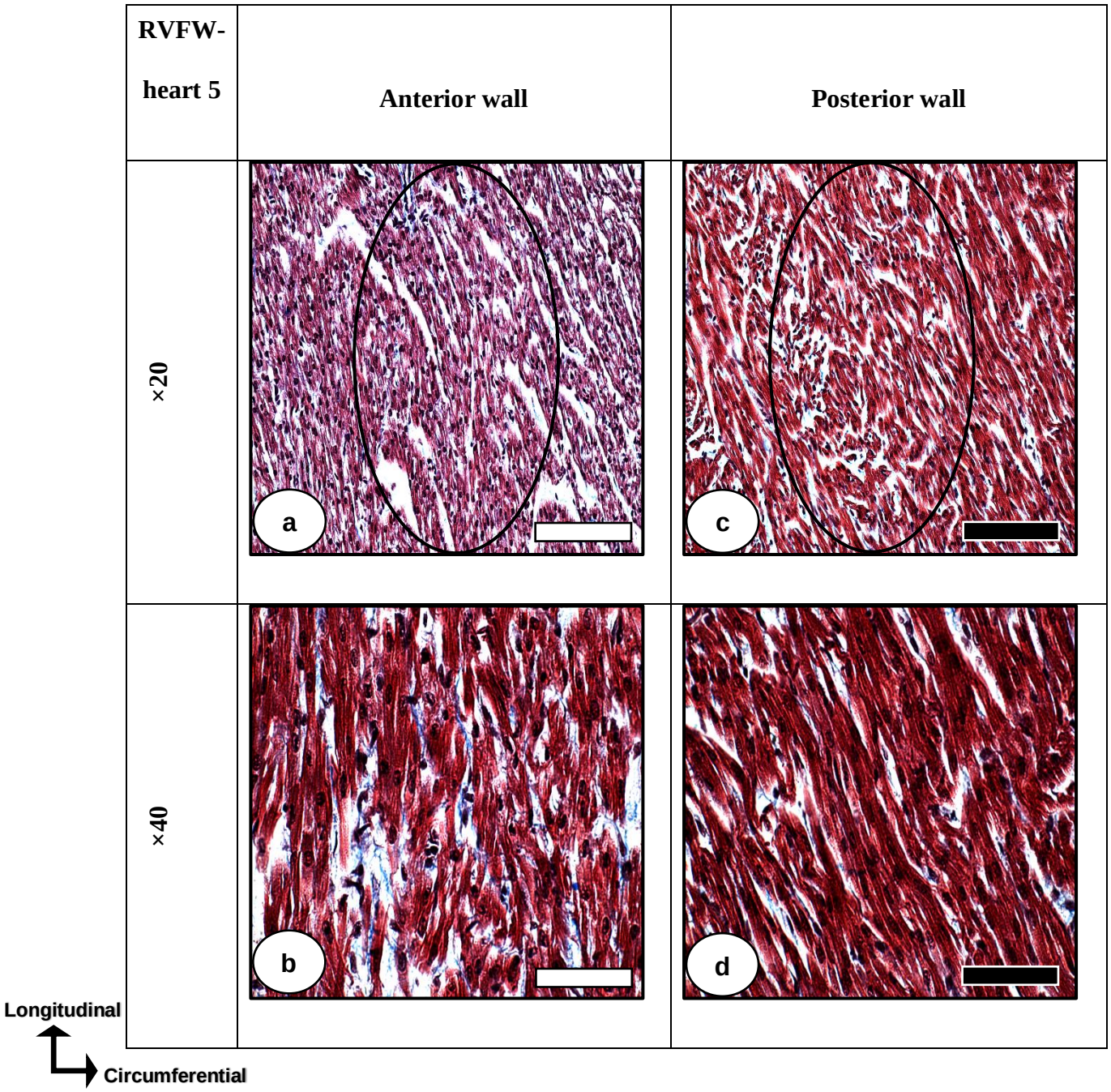

Figure A.1.5: *Masson's trichrome staining images of the neonatal porcine ventricles, sectioned in the plane perpendicular to the transmural direction (i.e. in-plane), and viewed at × 20 and × 40 magnification. The RVFW–anterior* ***(a–b)*** *and posterior* ***(c– d)*** *aspects demonstrated almost symmetrical fibre alignment, with the former having greater concentration and alignment of muscle fibres. Principal or preferred fibre angles are detailed in Table 4.1. The scale bar at* ***×20*** *=100 µm and at* ***×40*** *=50µm, respectively.*

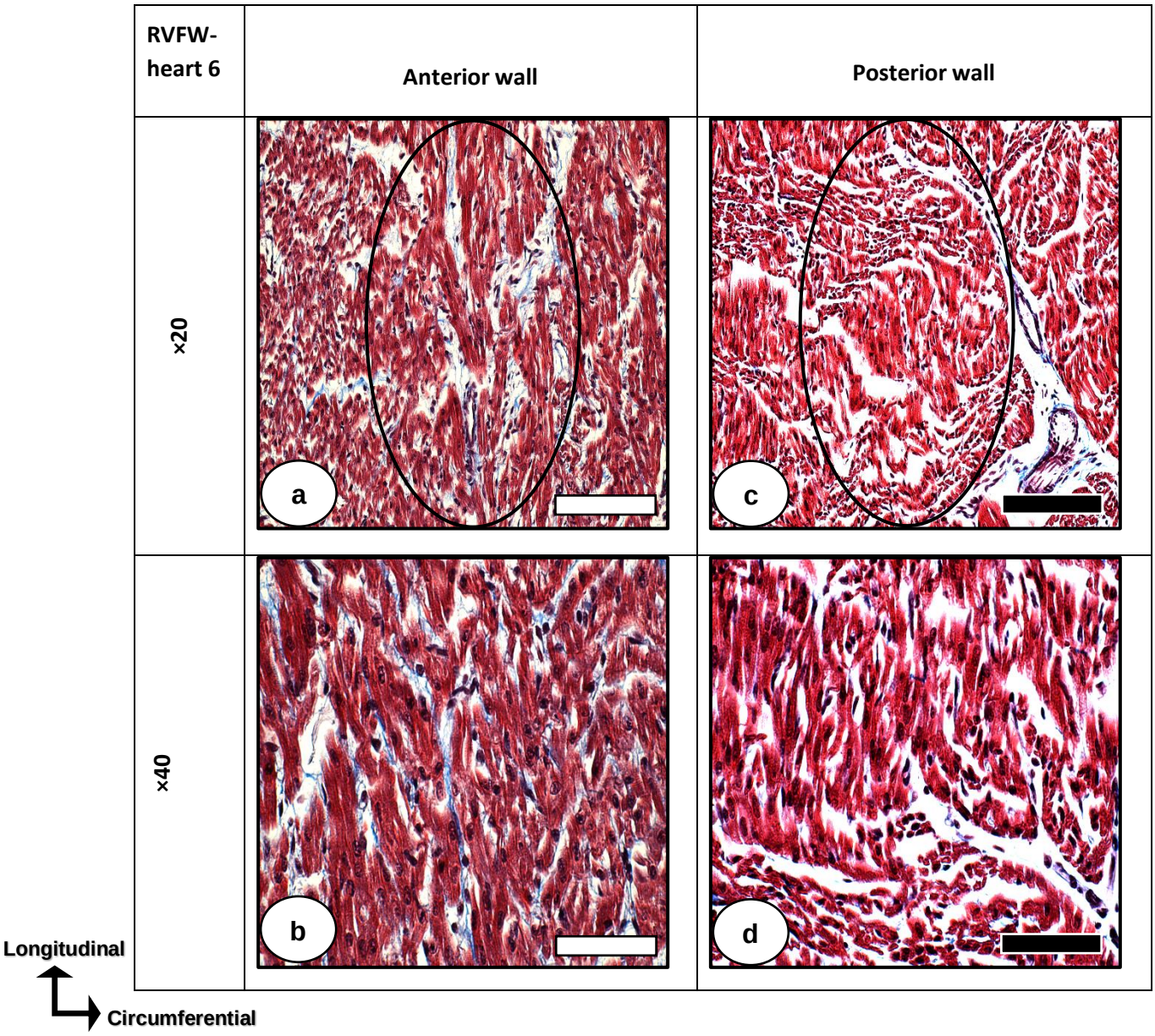

Figure A.1.6: *Masson's trichrome staining images of the neonatal porcine ventricles, sectioned in the plane perpendicular to the transmural direction (i.e. in-plane), and viewed at × 20 and × 40 magnification. The RVFW–anterior* ***(a–b)*** *and posterior* ***(c–d)*** *aspects demonstrated almost symmetrical fibre alignment, with the former having greater concentration and alignment of muscle fibres. Principal or preferred fibre angles are detailed in Table 4.1. The scale bar at* ***×20*** *=100 µm and at* ***×40*** *=50µm, respectively.*

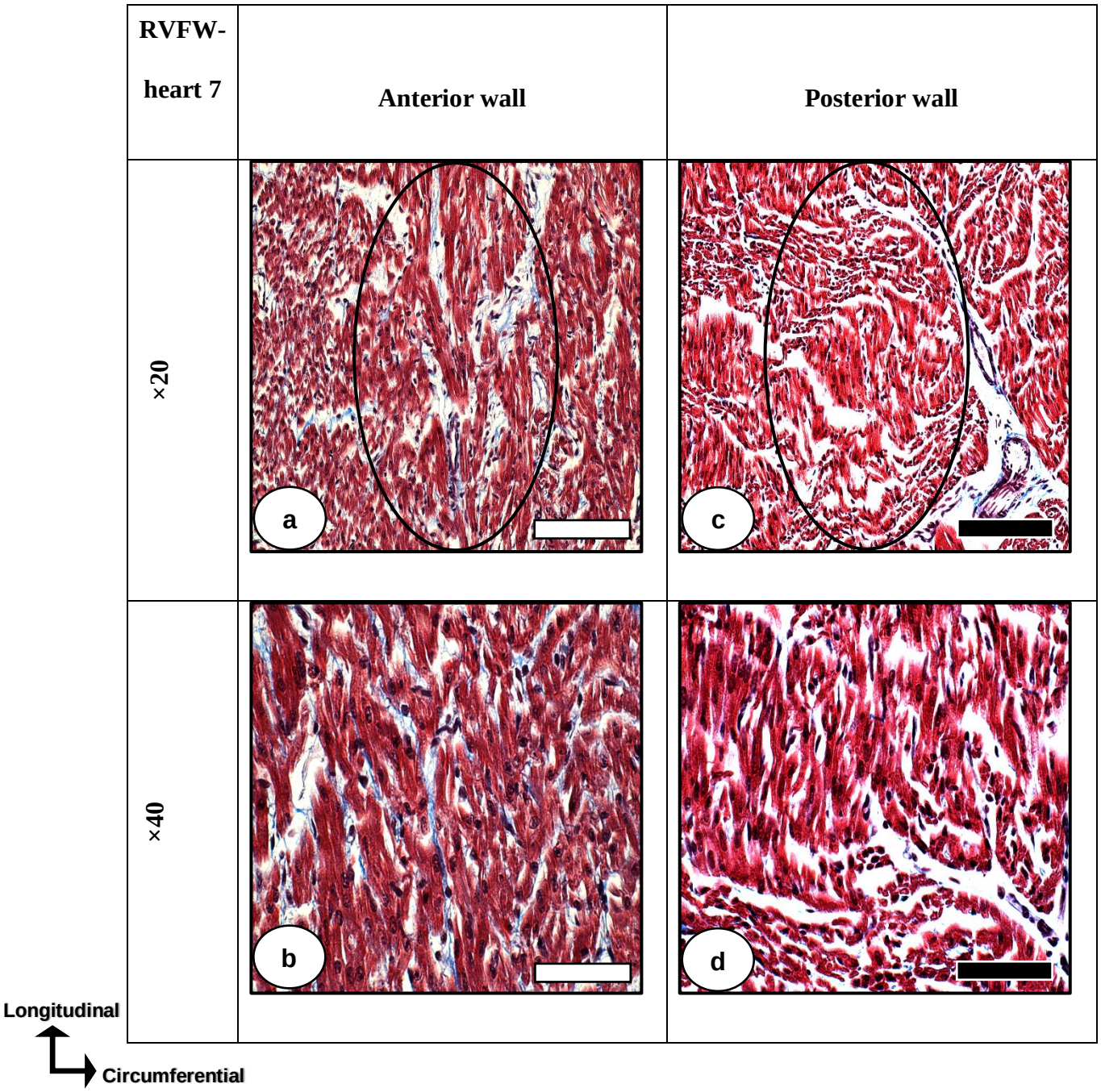

Figure A.1.7: *Masson's trichrome staining images of the neonatal porcine ventricles, sectioned in the plane perpendicular to the transmural direction (i.e. in-plane), and viewed at × 20 and × 40 magnification. The RVFW–anterior* ***(a–b)*** *and posterior* ***(c–d)*** *aspects demonstrated almost symmetrical fibre alignment, with the former having greater concentration and alignment of muscle fibres. Principal or preferred fibre angles are detailed in Table 4.1. The scale bar at* ***×20*** *=100 µm and at* ***×40*** *=50µm, respectively.*

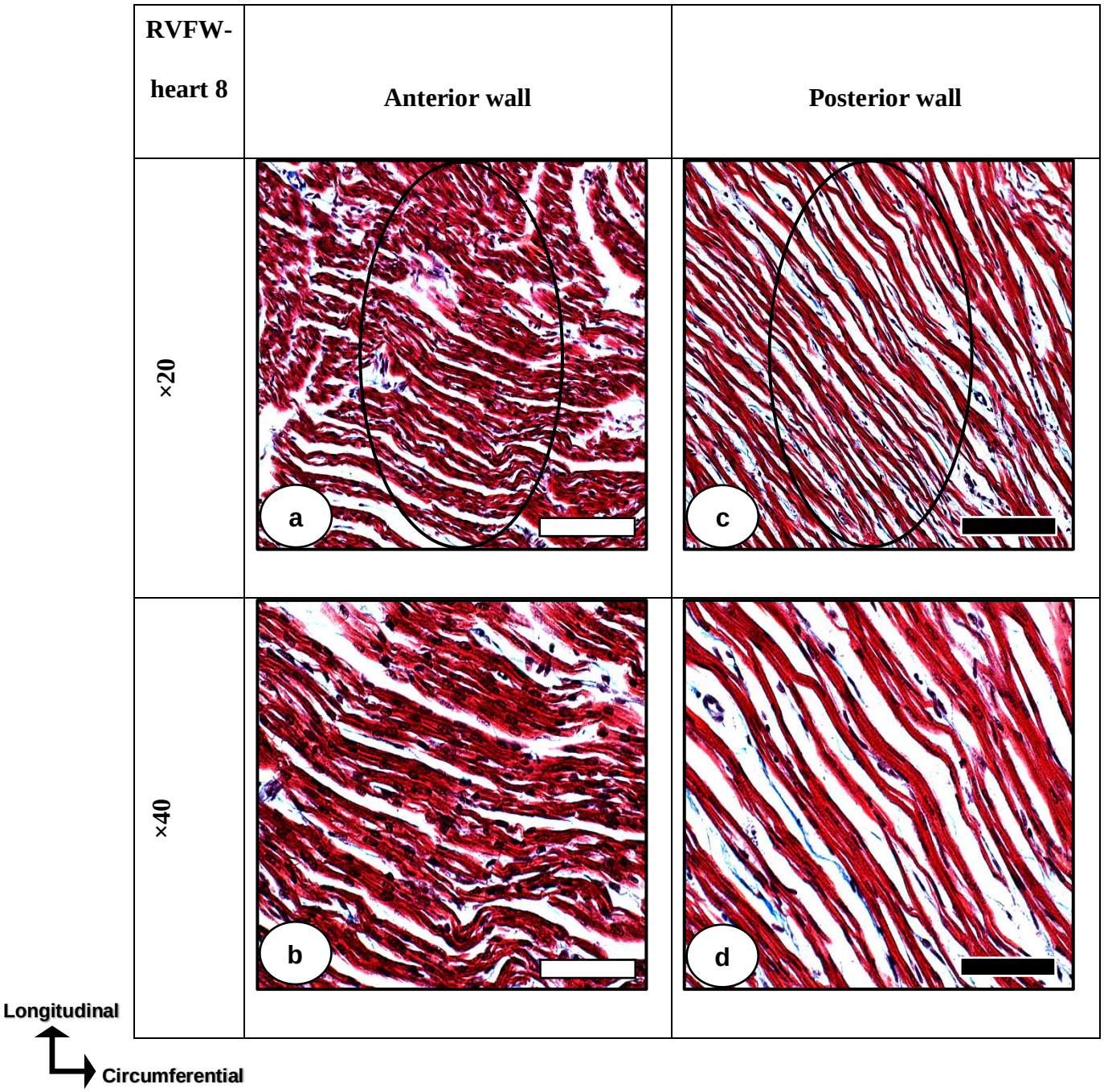

Figure A.1.8: *Masson's trichrome staining images of the neonatal porcine ventricles, sectioned in the plane perpendicular to the transmural direction (i.e. in-plane), and viewed at × 20 and × 40 magnification. The RVFW–anterior* ***(a–b)*** *and posterior* ***(c–d)*** *aspects demonstrated almost symmetrical fibre alignment, with the former having greater concentration and alignment of muscle fibres. Principal or preferred fibre angles are detailed in Table 4.1. The scale bar at* ***×20*** *=100 µm and at* ***×40*** *=50µm, respectively.*

A.2. Matlab code for fitting the experimental data with the HO model of the myocardium

```
clear all;close all;

global exp_data1  exp_data2 exp_data3;
global exp_data4  exp_data5 exp_data6 exp_data7 exp_data8;
global keyword keyword2 keyword3 record iter;
%global para

%choose the keywrods
keywrods_str1={'All_Together','Uniaxial_MFD+CFD','Biaxial_MFD+CFD','Shear_MFD+CFD'
};
[s,v] = listdlg('PromptString','Select a file:',...
                'SelectionMode','single',...
                'ListString',keywrods_str1);
keyword = keywrods_str1{s};

keywrods_str2={'Fibre_Rotation','No_Fibre_Rotation'};
[s,v] = listdlg('PromptString','Select a file:',...
                'SelectionMode','single',...
                'ListString',keywrods_str2);
keyword2 = keywrods_str2{s};

keywrods_str3={'Effective_area','No_Effective_area'};
[s,v] = listdlg('PromptString','Select a file:',...
                'SelectionMode','single',...
                'ListString',keywrods_str3);
keyword3 = keywrods_str3{s};

%input the experiment data
load('Exp_Data_Cau');

%allocate data according to the data frameffffff
%uniaxial
exp_data1(:,1)=unim(:,1);
exp_data1(:,2)=unim(:,2);
exp_data2(:,1)=unic(:,1);
exp_data2(:,2)=unic(:,2);
%biaxial
exp_data3(:,1)=biam(:,1);
exp_data3(:,2)=biam(:,2);
exp_data4(:,1)=biac(:,1);
exp_data4(:,2)=biac(:,2);
```

```
%shear anterior
exp_data5(:,1)=shemA(:,1);
exp_data5(:,2)=shemA(:,2)-shemA(1,2);
exp_data6(:,1)=shecA(:,1);
exp_data6(:,2)=shecA(:,2)-shecA(1,2);
%shear posterior
exp_data7(:,1)=shemP(:,1);
exp_data7(:,2)=shemP(:,2);
exp_data8(:,1)=shecP(:,1);
exp_data8(:,2)=shecP(:,2);

% call the remodeling program
%for iter=1:10
%   iter=1;
Remodeling;
%end
```

A.3. Refereed journal article - I

Faizan Ahmad, R. Prabhu, Jun Liao, Shwe Soe, Michael D Jones, Jonathan Miller, Parker Berthelson, Daniel Enge, Katherine M. Copeland, Samar Shaabeth, Richard Johnston, Ian Maconochie, Peter S.Theobald. **'**Biomechanical properties and microstructure of neonatal porcine ventricles', *Journal of the Mechanical Behavior of Biomedical Materials.*

doi: 10.1016/j.jmbbm.2018.07.038.

A.4. Refereed journal article - II

Faizan Ahmad, S Soe, N White, R Johnston, I Khan, J Liao, M Jones, R Prabhu, I Maconochie, P Theobald. 'Region-specific microstructure in the neonatal ventricles of a porcine model', *Annals of Biomedical Engineering*.

https://doi.org/10.1007/s10439-018-2089-4

A.5. Peer-reviewed conference abstract - I

Faizan Ahmad, S Soe, P Skacel, R Johnston, I Maconochie, P Theobald 2016. 'Biaxial and shear properties of immature porcine heart tissue', 2nd Workshop on Soft Tissue Modelling, Glasgow.

Biaxial and shear properties of immature porcine heart tissue

F. Ahmad[1], S. Soe[1], P. Skacel[2], R. Johnson[3], I. Maconochie[4], P. Theobald[1]

[1] School of Engineering, Cardiff University, UK, CF24 3AA.

[2] *Institute of Solid Mechanics, Mechatronics and Biomechanics, Brno University of Technology, Czech Republic*

[3] *College of Engineering, Swansea University, UK, SA2 8PP*

[4] *Paediatric Emergency Department, St Mary's Hospital, Imperial College NHS Healthcare Trust, UK, W2 1NY.*

Accurately quantifying the mechanical properties of biological tissue is critical to further enhance biomechanical and mathematical models used to predict the consequence of injury, illness and intervention. This study attempts to develop a localised knowledge of cardiac tissue, exploring the anterior and posterior walls of the four chambers. Tissue samples (18mm x 18mm) were dissected from the above regions in two immature (<18 months) porcine hearts, acquired fresh from a butcher. Samples were subjected to extension (0.33mms^{-1}) comparable to in vivo conditions on a custom-built machine, to investigate the elastic behaviour, biaxial and pure shear moduli. The data demonstrated anisotropic, nonlinear and heterogeneous behaviour across the anterior and posterior walls of each chamber (Table 1). Considering each tissue sample to consist of two layers (i.e. that the endocardium was too thin to test and so deemed consistent with the myocardium), the tissue is stiffer circumferentially than longitudinally in all chambers during biaxial test. Pure shear testing of right and left ventricles demonstrates longitudinal stiffness anteriorly, and circumferential stiffness posteriorly. Right and left atria are stiffer in circumferential direction likewise in biaxial test. From these data it can be deduced that the mechanical response in cardiac tissue appears dependent on the micro-level fibre orientation, that fibre orientation appears to vary throughout wall thickness, and that the anterior and posterior walls of the same chamber have different fibre orientations. It is anticipated that these data will ultimately prove useful to other bio-mechanical and mathematical researchers seeking to perform macro- and micro-scopic cardiac simulations.

	Moduli (Biaxial) / kPa				**Moduli (Pure Shear) / kPa**			
	Circumferential		Longitudinal		Circumferential		Longitudinal	
	Anterior	Posterior	Anterior	Posterior	Anterior	Posterior	Anterior	Posterior
Right	33.44	25.64	17.86	24.16	26.16	26.42	27.40	24.49
Left	53.87	51.19	46.86	22.62	47.45	58.20	50.47	51.45
Right	16.78		14.47		13.77		13.65	
Left	14.45		13.78		13.53		13.35	

Table 1 – Data describing the biaxial and pure shear moduli in immature porcine cardiac tissue.

A.6. Peer-reviewed conference abstract – II

Debao Guan, **Faizan Ahmad**, Peter Theobald, Shwe Soe, Hao Gao, Xiaoyu Luo 2018. 'Fitting Various Experimental Data from Neonatal Porcine Myocardium Based on the HO Model', Frontiers of simulations and experimentation for personalised cardiovascular management and treatment, London.

Fitting Various Experimental Data from Neonatal Porcine Myocardium Based on the HO Model

Debao Guan[1], Faizan Ahmad[2], Peter Theobald[2], Hao Gao[1], Xiaoyu Luo[1]

[1] *School of mathematics & statistics, University of Glasgow, UK, G12 8QQ*

[2] School of Engineering, Cardiff University, UK, CF24 3AA

Biomechanical cardiac modelling relies essentially on the knowledge of constitutive laws and the corresponding myocardial material properties. It has been showed [1] that bi-axial test data with different loading protocols and simple shear test data at different specimen orientations were required to capture adequately the direction-dependent nonlinear material response of myocardium. In this work, we estimated myocardial parameters from neonatal porcine by combining 3 different types of experimental tests that were the uni-axial tensile, bi-axial tensile and the simple shear tests. The myocardium has a highly laminar structure forming local orthotropic material axes, the myofibre direction f, the sheet direction s, and the normal direction n. Biomechanical experiments were performed by the Cardiff team, samples were harvested from neonatal porcine hearts. In the uni-axial experiments, samples were stretched along f direction and then n direction. In the bi-axial test, samples were stretched simultaneously along f and n. Finally, samples were sheared in fs plane along f direction, then in ns plane along n direction. The constitutive law developed by Holzapfel and Ogden (HO) [1] was used to fit the three experiments together, which has four invariants. When fitting to the three experiments, we considered the myofibre rotation from endocardium to epicardium rather than a uni-direction in other studies during the fitting process, and the ratio of effective myofibre contribution in the uni-axial sample. We found that the estimated parameters by fitting only one or two types of experiments could not match the remained experiments, therefore, it is necessary to include all necessary experimental data to determine the material parameters. Importantly, to fit different experimental data together, it is necessary to include detailed myofibre orientations of the samples in question.

References

[1] Holzapfel G A, Ogden R W. Constitutive modelling of passive myocardium: a structurally based framework for material characterization. Philos Trans A Math Phys Eng Sci 2009, 367(1902): 3445-3475.

A.7. Peer-reviewed conference abstract – III

Amanda Davies, **Faizan Ahmad,** Peter Theobald, Richard Hugtenburg, Richard Johnston 2018. 'A Novel MRI Method for Vertebral Strength', British Renal Society, Winchester.

A Novel MRI Method for Vertebral Strength

Amanda Davies[1], Faizan Ahmad[2], Peter Theobald[2], Richard Hugtenburg[1], Richard Johnston[1]

[1] *College of Engineering, Swansea University, UK, SA2 8PP*

[2] School of Engineering, Cardiff University, UK, CF24 3AA

Vertebral fractures are twice as common as any other fracture in osteoporosis (OP) patients and are typically a first indicator of the disease. However, the lack of a direct, non-invasive method to assess mechanical strength prevents prospective identification of vertebrae likely to fracture. Dual-energy x-ray absorptiometry (DXA) is the gold standard technique, calculating areal bone mineral density (aBMD) which is used with clinical factors to estimate fracture risk (NICE, 2012). DXA is limited by the overlap observed in T-scores in individuals with and without fracture (B. McCreadie, 2000). A magnetic resonance imaging-based (MRI) technique, "***fine***SA", has been reported that can non-invasively quantify fine structures (B.A.J. Evans; et al, 2012, J. Rafferty; et al, 2016) and this study explores its potential to provide a more accurate measure of fracture resistance.

The L1-L3 lumbar vertebrae were excised from deer of the same herd (n=11) culled for the meat industry (approximately 24 months old). Each sample underwent the ***fine***SA method (Siemens 3T Magnetom Skyra, Swansea University), microCT (Nikon XT H 225, Swansea University), DXA (Horizon A machine, Singleton Hospital) and compression testing (Instron, Cardiff University). Two spinal segments were excluded from analysis due to poor quality data then Pearson's correlation coefficient and multiple regression performed using MATLAB (2011b).

The ***fine***SA metric was strongly correlated ($r=-0.86$, $p=0.003$) with mechanical strength and this relationship was stronger than that observed for aBMD ($r=0.71$, $p=0.03$). Non-significant correlations were observed between microCT measurements and mechanical strength. Multiple regression showed that adding the ***fine***SA metric to aBMD in the model increases the percentage of variance in mechanical strength explained from 50% to 78% ($p = 0.01$).

This study provides early evidence that ***fine***SA could provide a more accurate method to predict fracture occurrence by closely approximating mechanical strength. Further work is required to progress towards clinical trials, with an initial application of this novel approach potentially include oncology patients, where MRI is in routine use and an appreciation of mechanical strength has even greater significance.